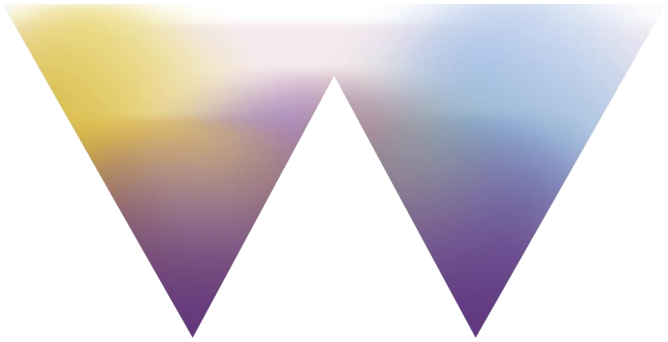

WARWICK

THE UNIVERSITY OF WARWICK

Thermo-electrochemistry of Boron Doped Diamond from Fundamentals to Application

by

Lingcong Meng

Thesis

Submitted to the University of Warwick

for the degree of

Doctor of Philosophy

Department of Chemistry

September 2016

To my family,

Table of contents

List of figures

List of tables

Acknowledgements

First I would like to thank my supervisors, Prof. Julie Macpherson and Prof. Mark Newton for their help and guidance over the last four years. It is their guidance, encouragement and advice during my Ph.D. studies that help me to manage all the projects and the thesis.

I am thankful to Warwick Chancellors International scholarship for providing funding for my Ph.D. studies and Element Six for providing all the diamond samples.

Thanks to Warwick Electrochemistry and Interface Group members past and present for their help. I would like to particularly mention Dr. James Iacobini for his help during my 1st year Ph.D. and Dr. Max Joseph for the helpful discussions. A special thanks to members in office A105, Jenny Webb, Jon Newland, Tania Read, liz Oseland, Zoë Ayres, Haytham Hussein, Sam Cobb, Mareike Herrmann and members in office C113, Rob Johnson, Lee Simcox, Roy Meyler, Guohui Zhang, Rehab Botros and Sophie Kinnear.

Finally I would like to thank my parents, sisters and Sharel, without your encouragement and support, I would not have achieved so much.

Declaration

I confirm that this thesis has not been submitted for a degree at another university and I declare that the work contained in this thesis is my own except where carried out in collaboration, as outlined below.

Chapter 3, the COMSOL modelling was built by myself with the help of Dr. Max Joseph (PDRA in the group); Chapter 4, the TEM image was taken with the help of Mr. Steve Hindmarsh (Warwick Physics); Chapter 6, surface modification of gold electrodes was conducted by Lee Simcox (MAS CDT project student) and myself. The DNA was provided by Dr. Rob Johnson (University of Utah, US) and XPS data was collected by either Dr. Marc Walker (Warwick Physics) or Miss Zoë Ayres (Ph.D. student in the group). TFAAD synthesis was carried out with the help of Dr. Andrew Marsh (Warwick Chemistry).

Parts of this thesis have been published or to be submitted, as detailed below:

Lingcong Meng, James G. Iacobini, Maxim B. Joseph, Julie V. Macpherson and Mark E. Newton. Laser heated boron doped diamond electrodes: effect of temperature on outer sphere electron transfer processes. *Faraday discussions*, 172 (2014): 421-438.

Lingcong Meng, Jon Ustarroz, Julie V. Macpherson and Mark E. Newton. Elucidating the Electrodeposition Mechanism of Lead/Lead Oxide Nanocrystallite Formation in Aqueous Solution, under review in *Journal of Materials Chemistry A.*

Lingcong Meng, Julie V. Macpherson and Mark E. Newton. Laser heated boron doped diamond microelectrode: the effect of temperature on the removal of fouling caused by dopamine oxidation, *in preparation*.

Abstract

Boron doped diamond (BDD), due to its exceptional electrochemical response (extended solvent window and low background current) and thermal properties (large thermal diffusivity and extreme resistance to thermal ablation), is investigated as the electrode material for thermoelectrochemical studies. A pulsed infrared (IR) laser technique is used to heat the electrode from the back (non-solution) side. The non-isothermal pulsed technique enables mass transport to be more readily controlled as opposed to isothermal heating approaches such as a water bath.

The effect of temperature on fundamental electrochemical processes, such as mass transport, electron transfer (ET) kinetics and thermodynamics of both outer sphere and inner sphere redox mediators is investigated on both BDD macro- and micro- electrodes. The effective temperature increase at electrode surface can be determined both experimentally and theoretically using finite element models. Enhanced mass transport and ET process at elevated temperatures, in addition to the temperature coefficient of the redox mediators, play a crucial role in the temperature dependent electrochemical response.

Thermoelectrochemical studies are extended to an electroactive species which forms a solid structure after electrolysis. In particular, the cathodic electrodeposition of lead/lead oxide (Pb/PbO) under non-isothermal heating conditions in nitrate containing solutions is investigated. The effect of deposition potential, time, dissolved oxygen content and temperature are explored to understand the mechanism for the synthesis of crystalline PbO “plate” structures, and the role of electrodeposited Pb.

Further work explores the effect of temperature on an electroactive species which upon electrolysis forms a solid product which fouls the electrode surface. Using a BDD microelectrode it is possible to show how temperature can be used to minimise the effect of surface blocking after the oxidation of a neurotransmitter, dopamine, which is known to lead to electrode fouling.

Finally, proof of concept studies are undertaken to assess the suitability of a thermoelectrochemical approach to the detection of single nucleotide polymorphism (SNP) in deoxyribonucleic acid (DNA). Initial studies investigate immobilisation strategies for both (in separate experiments) electrochemically active self-assembled monolayers (SAM) and redox-labelled double stranded DNA on gold and BDD electrodes.

Abbreviations

Symbol	Abbreviation
AC	Alternating current
AFM	Atomic force microscopy
BDD	Boron doped diamond
CV	Cyclic voltammetry
CVD	Chemical vapour deposition
DAQ	Data acquisition
DCM	Dichloromethane
DI	Deionised
DNA	Deoxyribonucleic acid
DOS	Density of state
DPPA	Diphenyl phosphoryl azide
DPV	Differential pulse voltammetry
dsDNA	Double stranded DNA
EBSD	Electron backscatter diffraction
EDX	Energy-dispersive X-ray
FCC	Face centred cubic
FEM	Finite element modelling
FE-SEM	Field emission scanning electron microscopy
HET	Heterogeneous electron transfer
HFCVD	Hot filament chemical vapour deposition
HOPG	Highly oriented pyrolytic graphite
HPHT	High pressure high temperature

IHP	Inner Helmholtz plane
IR	Infrared
ITO	Indium tin oxide
LSV	Linear sweep voltammetry
LOD	Limit of detection
MB	Methylene blue
MCH	Mercaptohexanol
MD	Molecular dynamic
MPCVD	Microwave plasma chemical vapour deposition
NEA	Negative electron affinity
NDC	Non-diamond carbon
NP	Nanoparticle
SAED	Selected area electron diffraction
SAM	Self-assembled monolayer
SCE	Saturated calomel electrode
SEM	Scanning electron microscopy
SHE	Standard hydrogen electrode
SIMS	Secondary ion mass spectrometry
SNP	Single nucleotide polymorphism
ssDNA	Single stranded DNA
SSMCC	Sulphosuccinimidyl-4-(N-maleimidomethyl)cyclohexane-1-carboxylate
OCP	Open circuit potential
OHP	Outer Helmholtz plane
pBDD	Polycrystalline BDD

PTFE	Polytetrafluoroethylene
t-BOC	tert-butyloxycarbonyl
TEM	Transmission electron microscopy
TFA	Trifluoroacetic acid
TPV	Temperature pulsed voltammetry
TFAAD	Trifluoroacetamide-protected 1-aminodec-1-ene
UV	Ultraviolet
VMD	Visual molecule dynamics
XPS	X-ray photoelectron spectroscopy

Glossary of terms

Symbol	Abbreviation
α	Bond angel
α_c	Charge transfer coefficient
α_D	Thermal diffusivity
η	Overpotential
λ	Electron tunnelling parameter
κ	Thermal conductivity
μ	Viscosity
∇^2	Laplace operator
∇	Grad operator
Γ	Surface coverage
ρ	Density
β	Temperature coefficient
θ	Contact angel
L	C-C bond length
A	Electrode area
a	Radius of electrode
$[B]$	Boron concentration
C_{ox}	Concentration of oxidised species
C_{red}	Concentration of reduced species
C_p	Heat capacity
d	Length of the alkyl chain
D_R	Diffusion coefficient of species R

E	Electrode potential
$E_{1/2}$	Half wave potential
E_0	Standard electrode potential
E_a	Impurity acceptor level
E_F	Fermi level
E_p^a	Anodic peak potential
E_p^c	Cathodic peak potential
ΔE_p	Peak separation
F	Faradaic constant
f_z	Volume force
g	Gravitational constant
i	Faradic current
i_{lim}	Limiting current
i_s	Shoulder current
i_p^a	Anodic peak current
i_p^c	Cathodic peak current
j	Flux
k_0	Heterogeneous standard rate constant
k_b	Electron transfer rate of the backward reaction
k_B	Boltzmann constant
k_f	Electron transfer rate of the forward reaction
k_t	Mass transport rate
k_r	Electron transfer rate constant
n	Number of electrons transferred
p	Pressure

P_{d}	Laser power density
P_{con}	Pressure constraint point
R	Gas constant
$[R]_{\mathrm{bulk}}$	Concentration of species R in bulk solution
ΔS	Change in entropy
T	Temperature
ΔT	Temperature change
v	Scan rate

Chapter 1: Introduction

1.1 Boron doped diamond (BDD)

Diamond is a well-known gemstone that has attracted scientists' attention because of its extraordinary properties. Diamond is known as the hardest material (70 - 100 GPa),[1] and as a result it has found application in the oil and gas industry as a drilling tool.[2] It also exhibits very high thermal conductivity (2200 W m^{-1} K^{-1}),[1] making it an excellent material in electronics, where it is employed as a heat sink.[3] Diamond has other properties such as the ability to transmit light over a very wide frequency range from deep ultraviolet (UV) to far infrared (IR).[4] It also has an exceptional acoustic response,[5] making it an ideal candidate for use in optics[6] and high quality loudspeakers.

The demand for diamond has been increasing over the years, but natural diamond mined from the ground is costly. The synthesis of diamond began as early as 1954 by Tracy Hall,[7] which not only enabled diamond to be grown to demand but it offered a means of controlling the amount of impurity present in the diamond lattice by optimising the growth parameters. The two major methodologies to grow diamond are the high pressure high temperature (HPHT) approach[8] and the chemical vapour deposition (CVD) technique.[9] Diamond in its pure form is an electrical insulator (electrical resistivity of 10^{13} Ω cm).[4] Controlled amounts of impurity can be introduced to the diamond lattice by both HPHT and CVD. The two main doping elements in CVD diamond are boron (B) and nitrogen (N). The former makes diamond a p-type semi-conductor or a conductor depending on the boron doping

level.[10] The latter makes diamond a deep donor n-type semi-conductor.[11] Both have found their chemical and physical applications.

Attention has been paid to the electrical conductivity property of boron doped diamond (BDD) by electrochemists, since it can be a candidate as an electrode material.[12] Recent research has shown that BDD exhibits a superior electrochemical response compared to metal and traditional carbon electrodes, such as an extended potential window,[13] low capacitance,[13] resistance to fouling[14] and chemical inertness.[15] The quality of synthetic BDD, in the form of thin film (attached to a growth substrate) or free standing, depends on the growth conditions employed. Boron doping level, sp^2 carbon content and surface termination are all of importance in terms of the electrochemical response of BDD, so the process of BDD synthesis is crucial in terms of quality control and associated electrochemical response.

1.1.1 Synthesis of BDD

Natural diamond is formed in the earth's mantle under high pressure and high temperature conditions, as shown in the phase diagram in Figure 1.1. In the laboratory, HPHT conditions can be replicated (Figure 1.1) to precipitate small diamond grains from molten metal solvent, eventually forming larger synthetic diamond. This process normally requires a pressure of 4 to 10 GPa and a temperature of above 1400 ^{o}C.[16] The dimension of diamond grown under HPHT conditions normally ranges from nanometre to millimetre,[4] with the predominant application in cutting industry.

Since the first attempt to grow diamond using CVD in 1955 by Eversole,[17] significant progress in diamond synthesis has been made.[18-20] The CVD process

requires a mixture of a carbonaceous gas (such as methane, 1-5 %) and hydrogen gas (95-99 %) flowing into a reactor. Chemical reactions happen at about 1 cm above an inert substrate.[9] High energy plasma, generated either by a hot filament (HFCVD) or a microwave (MPCVD), is applied to decompose the carbonaceous gas (methane) and hydrogen gas. The temperature of the plasma is normally above 2000 °C (Figure 1.1). To synthesize BDD, a small amount of a boron containing source, such as B_2H_6 is added into the reactor.[21]

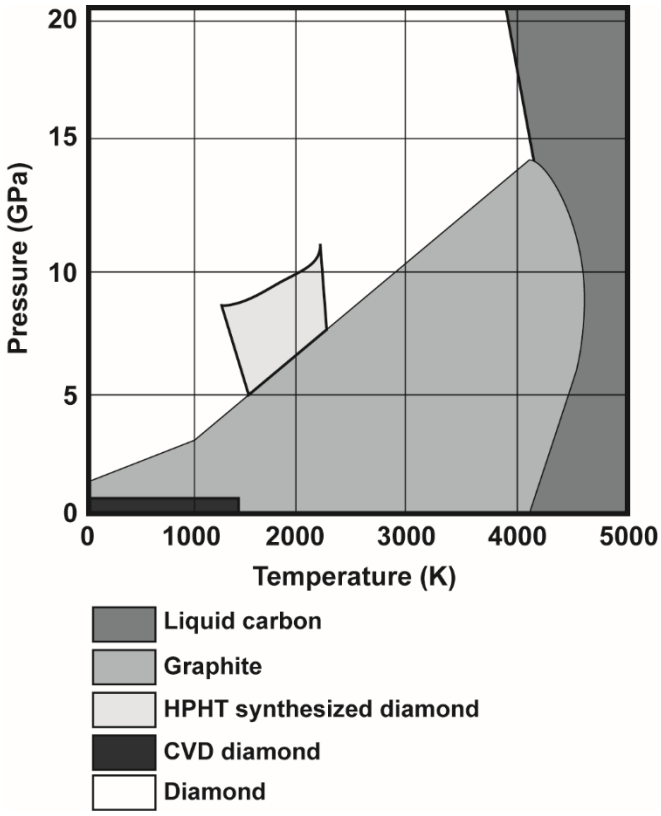

Figure 1.1: Phase diagram for graphite and diamond.[22] Figure illustrates the pressure and temperature relationship for diamond synthesis.

In CVD after decomposition of the gaseous chemical species by a plasma, diamond structure nucleation and growth takes place on the growth substrate.[23] Typical growth substrates include diamond,[18] Si[24] and various metals, such as Nb,[25]

W.[26] Prior to growth the substrate is typically seeded with diamond particles. The high energy plasma generates both carbon containing radicals, *e.g.* $CH_3^{\bullet}$, and atomic hydrogen. The latter plays a significant role in preventing the formation of graphitic carbon (sp^2 carbon). Surface radical sites (carbon-hydrogen bonds, typical on the seeded diamond) react with gas phase carbon radicals, building the sp^3 diamond lattice, layer by layer from the growth surface. If the activated boron radical is present, BDD will be produced as a result of replacing carbon atoms by boron atoms in the diamond lattice. CVD diamond growth rates can range from 0.1-15 μm h^{-1} depending on the deposition conditions.[27]

During CVD, small crystallites of diamond firstly nucleate on the seeds and then grow to form a film of diamond on the substrate with different grains merging together. Eventually a polycrystalline structure is formed which is shown in Figure 1.2a and b. Note the grain size increases as the film thickness increases. An scanning electron microscopy (SEM) image of thin film CVD diamond is shown in Figure 1.2c. It can be seen that diamond grains vary in size (nanometre to micrometre) and different crystalline orientations are observed. By carefully controlling the growth conditions and chosen substrates, synthetic diamond can be single crystalline[28, 29] (employs a single crystal growth substrate) or polycrystalline,[30] thin film[31, 32] or free standing, *i.e.* removed from the growth substrate.[29]

Figure 1.2d shows an SEM image of a freestanding polycrystalline BDD after the growth face has been polished. It can be seen the grain size is in the micrometre range. And the contrast in the SEM image indicates differences in the boron doping level, where darker intensity corresponds to more heavily doped

regions of the BDD surface.[33] Diamond materials used in the work presented in this thesis are growth face polished, polycrystalline and freestanding.

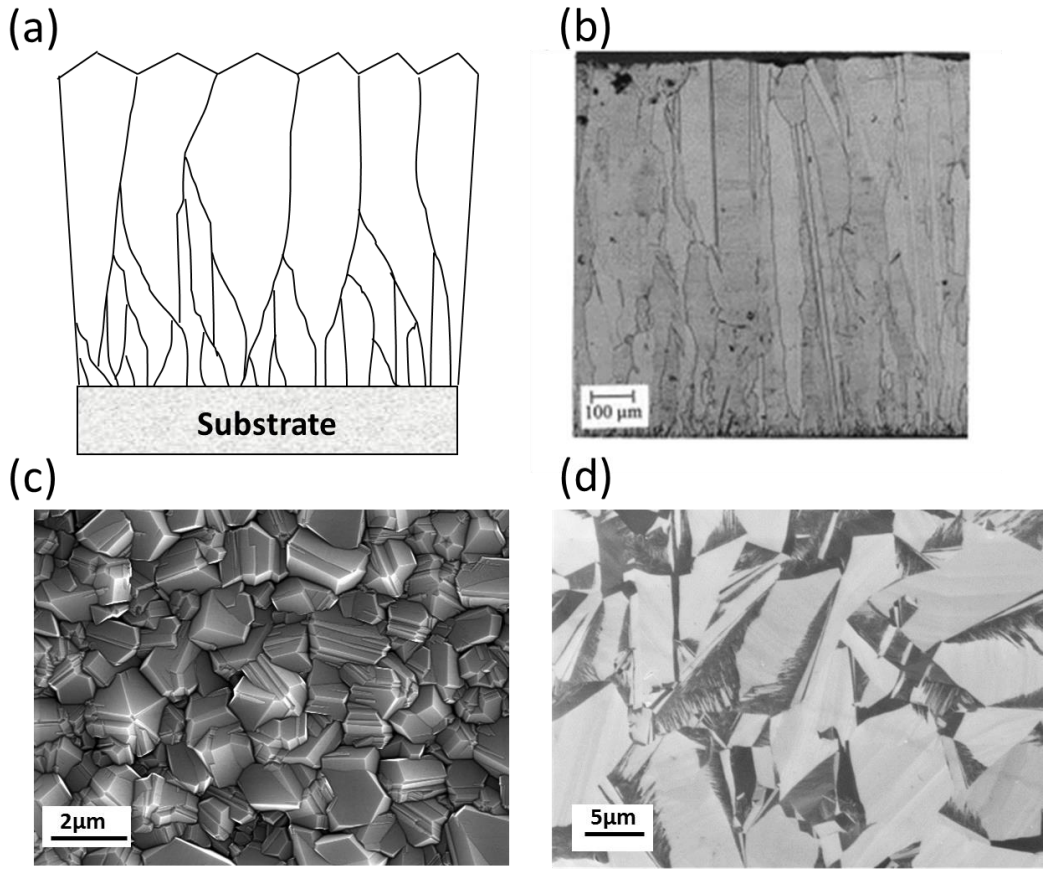

Figure 1.2: (a) Schematic and (b) SEM image of cross section of CVD-grown diamond.[34] SEM image of (c) an as-grown CVD polycrystalline diamond and (d) a 'polished' growth side microcrystalline BDD. Contrast in the SEM image indicates the differences in the boron doping level. Darker intensity corresponds to more heavily doped regions of the BDD surface.

1.1.2 Structure and property of diamond

Diamond is an allotrope of carbon, with a typical type of face centred cubic (FCC) lattice composed of sp^3 carbon atoms. The unit cell of diamond consists of

two FCC unit cells, one of which moves ¼ of the diagonal length towards the diagonal direction of the Bravais lattice,[9] shown in Figure 1.3.

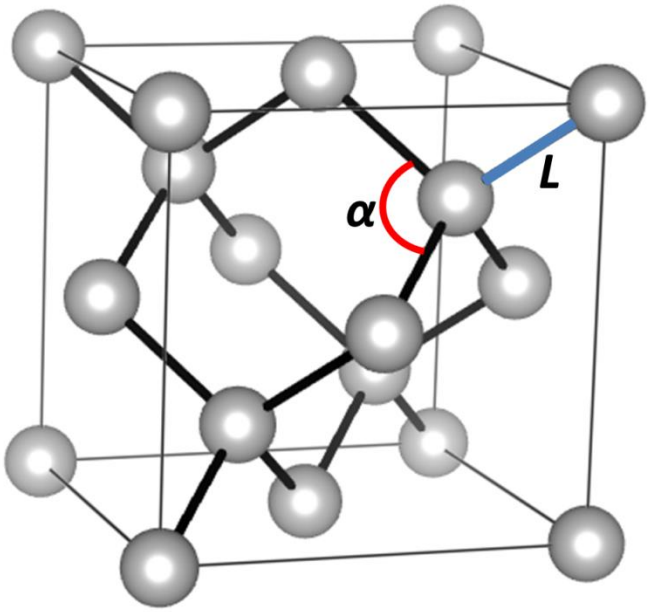

Figure 1.3: Illustration of the atomic structure of diamond. α is the C-C-C bond angle and L represents the C-C bond length.

In diamond, the carbon atoms form four sp^3 hybrid orbitals, therefore each carbon atom is surrounded by four carbon atoms in the form of covalent bonding, resulting in a tetrahedral arrangement. The C-C bond length, *L*, is 0.154 nm with a C-C-C angle, α, of 109.5^{o}. With the rigid and covalent sp^3 bonding, diamond exhibits exceptional properties, which are summarised in Table 1.1.

Table 1.1: Properties of diamond[1]

Properties	Value
Hardness (GPa)	70-100
Thermal conductivity (W m^{-1} K^{-1})	2200
Thermal expansion coefficient (ppm K^{-1}) at 300 K	1.0 ± 0.1
Transparency (λ)	226 nm – 500 μm
Band gap (eV)	5.47

1.1.3 Structure and electrical properties of BDD

Intrinsic diamond is a good electrical insulator due to the wide band gap that separating the valence and conduction band; 5.47 eV at 300 K,[1] as shown in Figure 1.4a. Findings have shown that hydrogen termination introduces a "surface conductivity" property into intrinsic diamond in the presence of water.[35] The most common method to synthesise conducting diamond is impurity doping, which modifies the band structure by introducing impurity levels in between the conduction and valence band. Nitrogen doping introduces a deep nitrogen donor level, 1.7 eV below the conduction band.[36]

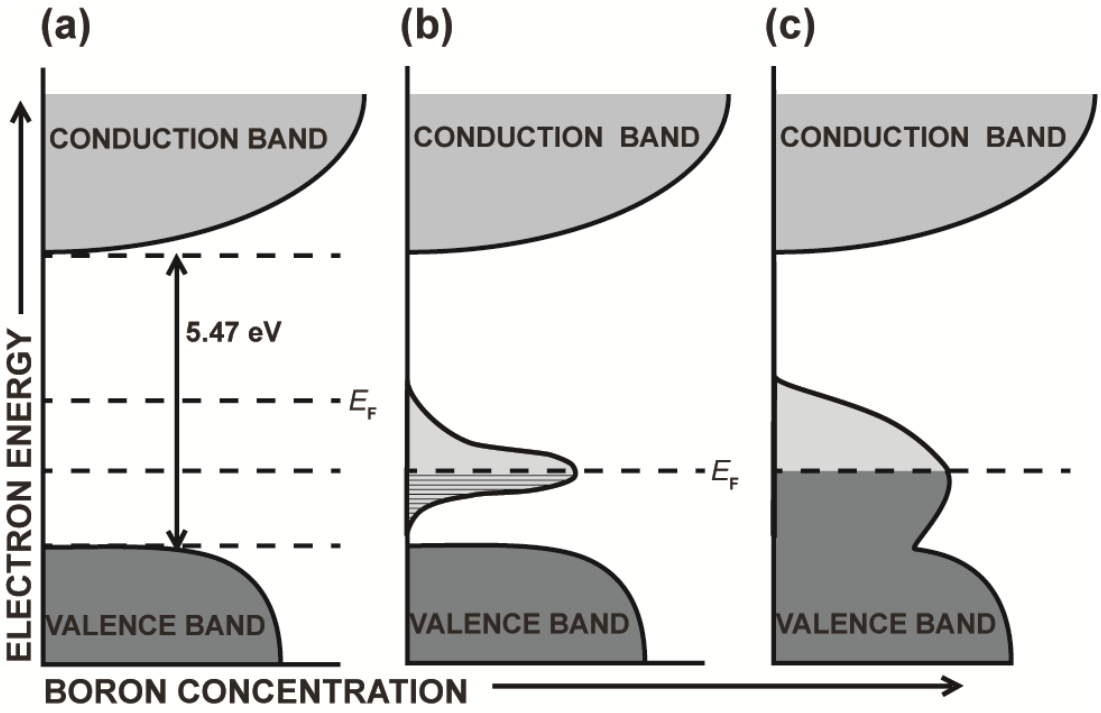

Figure 1.4: Schematic of the band structures for (a) intrinsic, (b) moderate boron doped diamond and (c) heavily boron doped diamond. E_F represents the Fermi level. Moderate boron concentration introduces an impurity band above the valence band, whereas heavily doped diamond shows overlapping between the impurity and valence bands.

Derived from its density (3.5 g cm^{-3}), diamond contains 1.8×10^{23} C atoms cm^{-3}. The boron atom has three electrons in its valence orbital; whereas the carbon atom has four electrons. When a carbon atom in diamond lattice is replaced by a boron atom, a hole is introduced, resulting in an impurity level, E_a, lying about 0.37 eV above the valence band,[37] shown in Figure 1.4a. The atomic concentration of boron, [*B*] in diamond can be measured by secondary ion mass spectrometry (SIMS).[38] When [*B*] < 10^{17} atoms cm^{-3}, BDD exhibits semi-conductive behaviour, which means a large activation energy is needed to excite electron from the valence band to the impurity levels.[39]

Moderate boron concentration in the range of 10^{18}-10^{19} atoms cm^{-3} results in reduced boron spacing in the diamond lattice and overlapping of the wave function of holes bound to impurity sites. Conduction is due to nearest-neighbour hopping.[40, 41] The impurity level evolves into a 'band',[42] and the activation energy needed to excite electron is reduced, as shown in Figure 1.4b. The resistivity of moderately boron doped diamond decreases with temperature,[43] which shows typical semi-conductive behaviour. As [*B*] increases to above 10^{20} atoms cm^{-3} (*i.e.* 1 boron atom in 1000 carbon atoms), BDD exhibits semi-metallic behaviour,[42] as the activation energy for exciting electrons will be zero, indicating the overlap of the impurity 'band' with the valence band, illustrated in Figure 1.4c. The resistivity of semi-metallic BDD is as low as 0.001 Ω cm and increases with temperature, similar to the behaviour of metals.[43] The resistivity of BDD, plotted as a function of boron concentration, is shown in Figure 1.5.

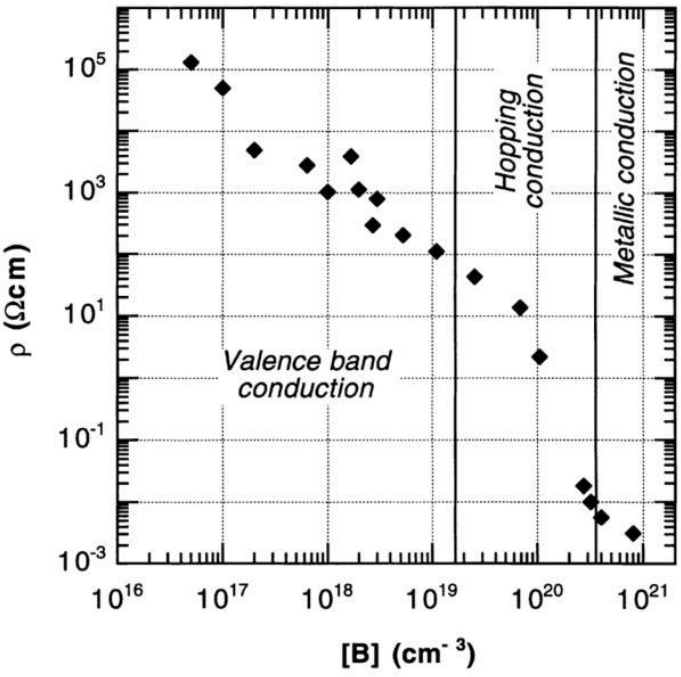

Figure 1.5: Room temperature resistivity of BDD as a function of boron doping concentration.[43]

1.2 Electrochemistry theory

1.2.1 Dynamic electrochemistry

The study of electron transfer reactions across an interface, often between an electrode and redox species in solution, under the application of an external potential is referred as dynamic electrochemistry.[44-46] The electrode is normally a solid conducting material, across which charge transfer occurs. For example, consider a simple redox reaction:

$$O + ne^- \underset{k_b}{\overset{k_f}{\rightleftarrows}} R \qquad (1.1)$$

where k_f and k_b are the reaction rate constants of the forward and backward reactions respectively. When there is no external driving force applied to reaction 1.1, the system will be at equilibrium and the rates for the forward and backward reaction are the same, where:

$$k_f = k_b = k_0 \tag{1.2}$$

where k_0 is the heterogeneous standard rate constant. An external driving force will disturb the equilibrium of this reaction. Factors affecting the electrode reaction include electron transfer kinetics and transport of redox species between the bulk solution and the electrode surface, as illustrated in Figure 1.6. k_t and k_r represent the mass transport coefficient and electron transfer rate constant, respectively. The former reflects the rate of reactant species travelling from the bulk solution to the electrode surface; the latter determines the charge transfer rate across the electrode surface. The overall reaction rate of the electrochemical reaction is determined by whichever is the slowest step in the process.

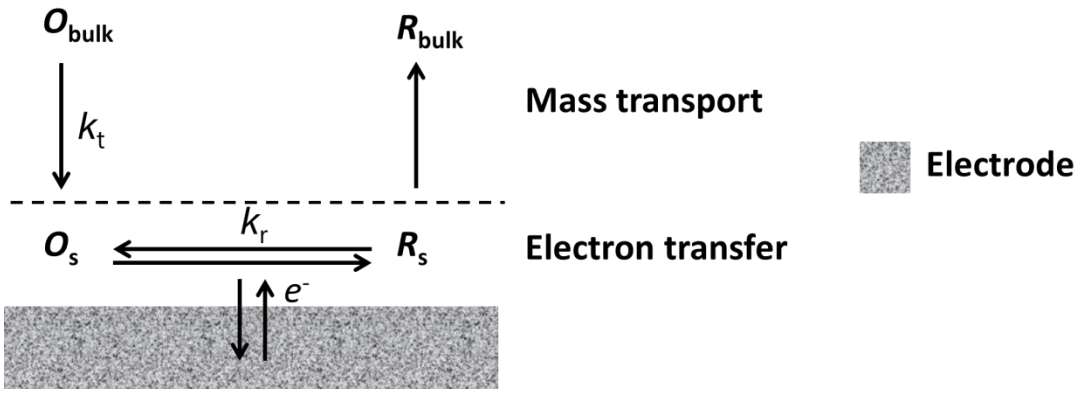

Figure 1.6: Electrode dynamic of a general electrochemical reaction; O_{bulk} and R_{bulk} are the concentration of O and R in bulk solution, whereas O_s and R_s are the concentration of O and R at the electrode surface. k_t and k_r represent mass transport coefficient and electron transfer rate constant, respectively.

1.2.1.1 Electron transfer kinetics

The faradic current, *i*, at the electrode is proportional to the flux of species at the electrode surface, *j*

$$i = nAFj \tag{1.3}$$

where *n* is the number of electrons transferred per redox specie, *A* is the area of the electrode, *F* is Faraday's constant and *j* is defined by:

$$j = k_f C_{ox} - k_b C_{red} \tag{1.4}$$

where k_f and k_b have an exponential dependence on the electrode overpotential, η,

$$\eta = E - E^o \tag{1.5}$$

$$k_f = k^0 e^{\frac{-\alpha n F \eta}{RT}} \tag{1.6}$$

$$k_b = k^0 e^{\frac{(1-\alpha)nF\eta}{RT}} \quad (1.7)$$

where α is the charge transfer coefficient, E is the electrode potential, E^0 is the standard potential, and R is the gas constant. Substituting equations 1.6 and 1.7 into 1.4 produces the Butler-Volmer equation: [45]

$$i = nAFk_0 \left[C_{ox} e^{\frac{-\alpha nF\eta}{RT}} - C_{red} e^{\frac{(1-\alpha)nF\eta}{RT}} \right] \quad (1.8)$$

1.2.1.2 Mass transport

In a dynamic electrochemical system, reactant species close to the electrode surface are consumed, resulting in the product species. Understanding the transport of reactant species between the bulk and the electrode surface becomes essential. Mass transport can be attributed to three modes: diffusion, convection and migration.[45]

Diffusion is the movement of species due to concentration distributions in a system; species tend to reach homogeneous composition within the system. All dynamic electrochemical systems have diffusion operating due to the removal of reactant and generation of product at the surface of the electrode. Diffusion in an electrochemical cell involves the reactant species moving from a region of high concentration (the bulk) to a region of low concentration (the electrode surface); with the product species moving in the opposite direction. The concentration profile developed during an electrochemical reaction varies depending on electrode size and geometry, which is shown in Figure 1.7. Planar diffusion can be found at a macroelectrode, *i.e.* an electrode with a diameter in the millimetre and above range, whereas a hemispherical diffusion profile can be seen at a microelectrode with

diameter in micrometre range. Note that for a microelectrode the diffusional flux (number of molecules reaching the surface per unit time per unit area) towards the electrode is greatly increased, due to the significant contribution of radial diffusion. This provides the possibility to probe fast electrode kinetic information.

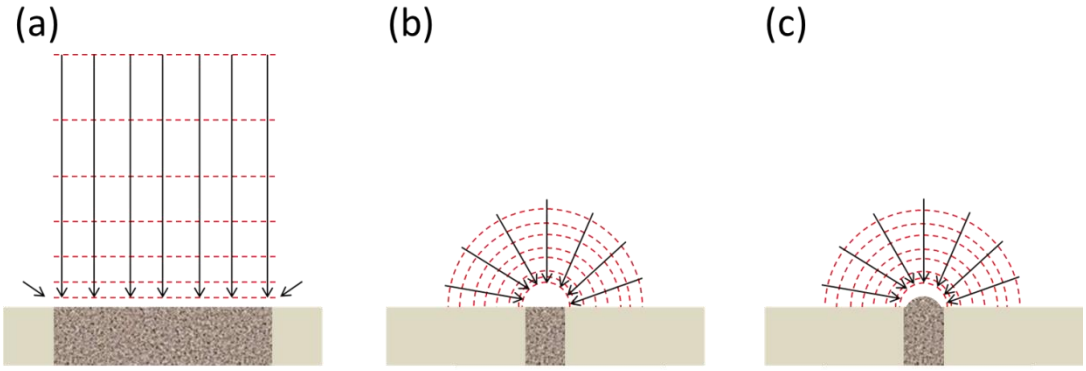

Figure 1.7: Schematic of diffusion profile of different sized electrodes: (a) macroelectrode, (b) inlaid microelectrode, (c) hemispherical microelectrode.

Migration is the movement of charge resulting from an electrical field. In an electrochemical cell, a potential is applied to the electrode, generating an electrical gradient in the solution. Charge carriers, such as reactant species, will tend to move toward certain electrodes according to the electrical field. Thus, complex mass transport, which is hard to interpret, will be obtained due to the interplay of migration and diffusion in an electrochemical cell. To avoid the effect of migration, a supporting electrolyte is added to the solution, providing sufficient charge carriers and shrinking the size of the double layer at the electrode/electrolyte interface.[44] The supporting electrolyte is chosen as a chemically and electrochemically inert salt, *e.g.* KNO_3 or KCl. The concentration is usually 100 times the concentration of the reactant species.[46, 47] The addition of supporting electrolyte also provides other

benefits including (1) an increase to the solution conductivity[47] and (2) a more stable ionic strength resulting from the high concentration of supporting electrolyte.[47]

Forced movement of solution species is termed convection. The external driving force can be mechanical or thermal. An example of controlled convection is the rotating disk electrode,[48] where the working electrode is rotated at a certain rate and an increased flux of reactant species towards the electrode surface is obtained. An example of uncontrolled convection is stirring. For a controlled electrochemical experiment, the contribution of convective mass transport is usually minimised by conducting experiments in stationary solution under ambient conditions at atmospheric pressure (1 atm).

1.2.1.3 Cyclic voltammetry

One of the most common and simple electrochemical technique is voltammetry, *i.e.* the measurement of electrode current as a function of applied potential, as illustrated in Figure 1.8a. In Figure 1.8a, a voltage, E_1, is applied to the electrode which changes linearly with time and reaches E_2. The current flowing through the electrode is measured. The plot of current *vs* potential is termed linear sweep voltammetry (LSV). If the potential is followed by a reserve sweep to its original value E_1 or a different value, resulting in a triangular potential cycle, the plot of current *vs* potential is cyclic voltammetry (CV).[45, 49] The scan rate varies from 1 mV s^{-1} to 100 V s^{-1}. The resulting peak shaped CV from a disk macroelectrode is illustrated in Figure 1.8b.

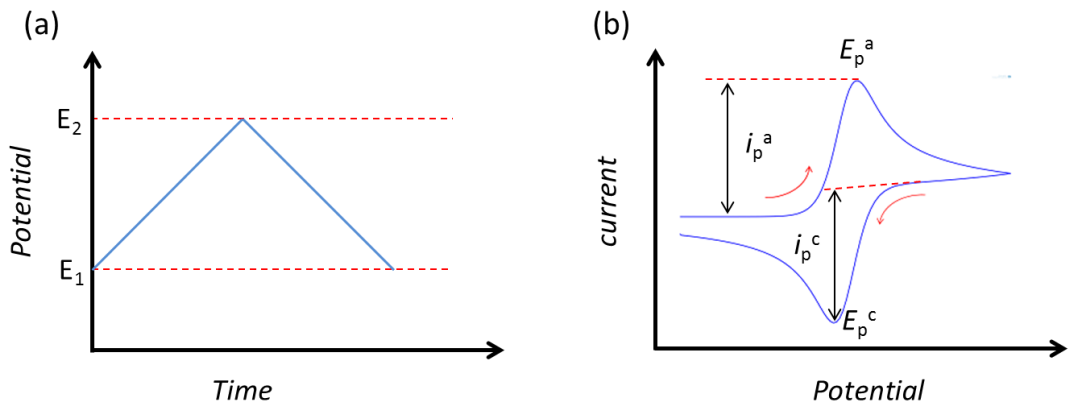

Figure 1.8: Schematics of CV for an oxidation process at a macrodisk electrode. (a) Applied potential waveform; (b) Resulting voltammogram. The potential is swept from E_1 to E_2 and then back to E_1. E_p^a and E_p^c are the anodic and cathodic peak potentials and i_p^a and i_p^c are the anodic and cathodic peak currents respectively.

The potential applied to the electrochemical system is scanned from E_1, where no electron transfer process happens and no faradic current is observed, to a value which is great enough to drive the electron transfer process of *R* to *O*, resulting in an increase in current. Species *R* is consumed and *O* is generated at the electrode surface. As the potential approaches E_2, the faradic current rises approximately exponentially due to the increase in k_r until the anodic current reaches a peak i_p^a at potential of E_p^a, after which the current drops. The current response reflects the relative rates of electron transfer and mass transport. The decreased current indicates the rate of mass transport cannot compete with the rate of electron transfer. On reaching E_2, the potential is then scanned backwards, reducing *O*, formed at the electrode surface, to *R*. The resulting cathodic current in the opposite sense is observed with a cathodic peak current, i_p^c, at E_p^c, after which the current decreases in magnitude. The peak separation, ΔE_p,

$$\Delta E_p = E_p^a - E_p^c \tag{1.9}$$

is equal to 59/n mV for a reversible (diffusion limited) reaction at 298.15 K derived from the Nernst equation. The value of $i_p{}^a$ for the forward sweep can be described by Randles-Sevcik equation:[50]

$$i_p^a = (2.69 \times 10^5) n^{\frac{3}{2}} A D_R^{\frac{1}{2}} [R]_{bulk} v^{\frac{1}{2}} \tag{1.10}$$

for a reversible process at 298.15 K, where A is the area of the electrode, D_R is the diffusion coefficient of species R, $[R]_{bulk}$ is the concentration of species R in bulk solution, v is the scan rate in V s^{-1}. In the case of an electron transfer kinetically limited CV, an extended ΔE_p (> 59/n mV) is observed.

A steady state limiting current is obtained in a microelectrode CV (or a macroelectrode operated under convective mass transport conditions). A typical disk microelectrode CV is illustrated in Figure 1.9. Due to the reduced electrode area, the CV of a microelectrode has a few different features compared to the macroelectrode. This includes (1) a steady state current due to the enhanced mass transport rate as a result of the hemispherical diffusion; (2) Reduced current size due to the smaller electrode area. The steady state limiting current, i_{lim}, is determined by:

$$i_{lim} = 4naFD_R[R]_{bulk} \tag{1.11}$$

where a is the radius of the microelectrode. For a reversible process in a microelectrode system,

$$E_{3/4} - E_{1/4} = \frac{59}{n}\ mV \tag{1.12}$$

where $E_{3/4}$ and $E_{1/4}$ is the potential at current values equals to ¾ and ¼ of i_{lim}, respectively.[51]

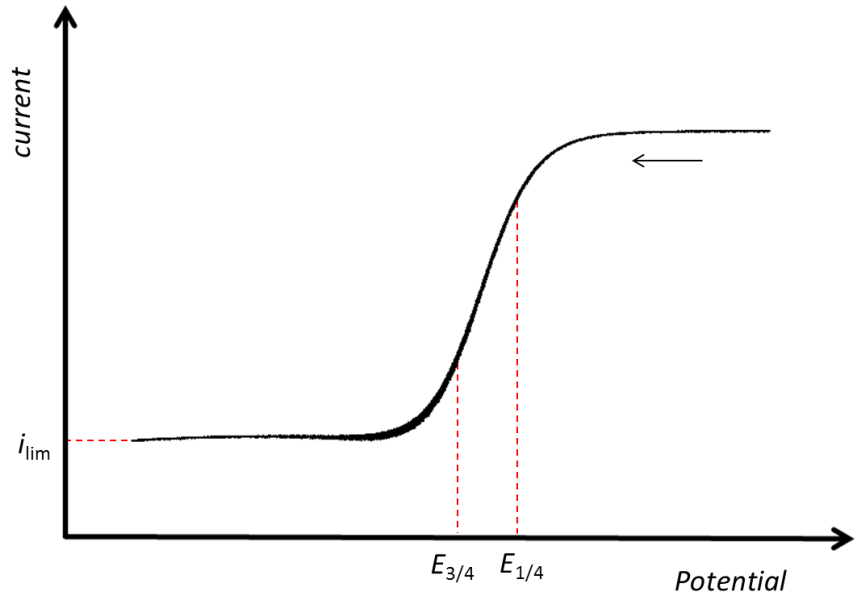

Figure 1.9: CV of a microdisk electrode. i_{lim} is the limiting current, $E_{3/4}$ and $E_{1/4}$ is the potential at current values equals to ¾ and ¼ of i_{lim}, respectively.

1.2.1.4 Outer and inner sphere electron transfer[45, 52-54]

Charge ordering at the electrode/electrolyte interface is often described as an electrical double layer.[55] The electrical double layer has dimensions in the range of nanometres depending on the charge concentrations in solution. It can be simply described as two layers of charges associating (that associated with the electrode and the solution) at the electrode/electrolyte interface. Therefore, a capacitance exists across the double layer. The model established by Helmholtz and further developed by Grahame[56, 57] assumed the excess charge on the electrode is neutralised by a monolayer of ions with opposite charge in the solution, *i.e.* desolvated 'absorbed' ions and solvated ions. The centre of these desolvated absorbed ions is defined as the

inner Helmholtz plane (IHP), whilst the centre of the solvated redox molecules is defined as the outer Helmholtz plane (OHP). The structure of the electrical double layer is depicted in Figure 1.10.

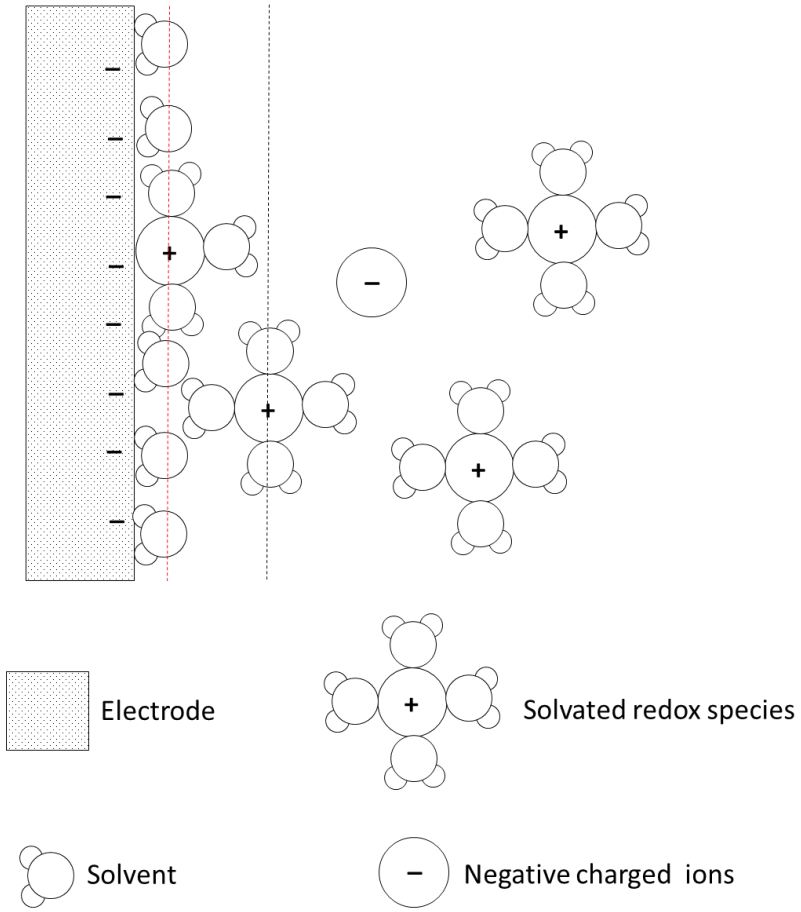

Figure 1.10: Model of electrical double layer. Red dash line and black dash line represent the IHP and OHP, respectively.[45]

Heterogeneous electron transfer (HET) at the electrode/electrolyte interface can be affected by the electrode material chosen and also the chemical nature of the reactant species themselves. HET is classified into two classes: 'outer sphere' and 'inner sphere', illustrated in Figure 1.11.

For outer sphere electron transfer reactions, shown in Figure 1.11a, electrons transfer through tunnelling between the electrode and reactant species across at least one layer of solvent.[45] As a result, outer sphere redox mediators are insensitive to the electrode material. Examples of outer sphere redox mediator include $Ru(NH_3)_6^{3+}$/ $Ru(NH_3)_6^{2+}$ and derivatives of ferrocene.[58, 59]

Inner sphere electron transfer reaction involves strong interaction of reactants, intermediates or products with the electrode surface, as illustrated in Figure 1.11b. Thus, inner sphere redox species often specifically absorb (bind) to the electrode surface and are therefore sensitive to electrode materials and even the heterogeneity within the same electrode. For example, polycrystalline Pt electrode showed distinct activities towards oxygen reduction reaction from different facets with the (111) facet showing the fastest electron transfer rate.[60] The kinetics of inner sphere electron transfer is thus electrode material dependent.

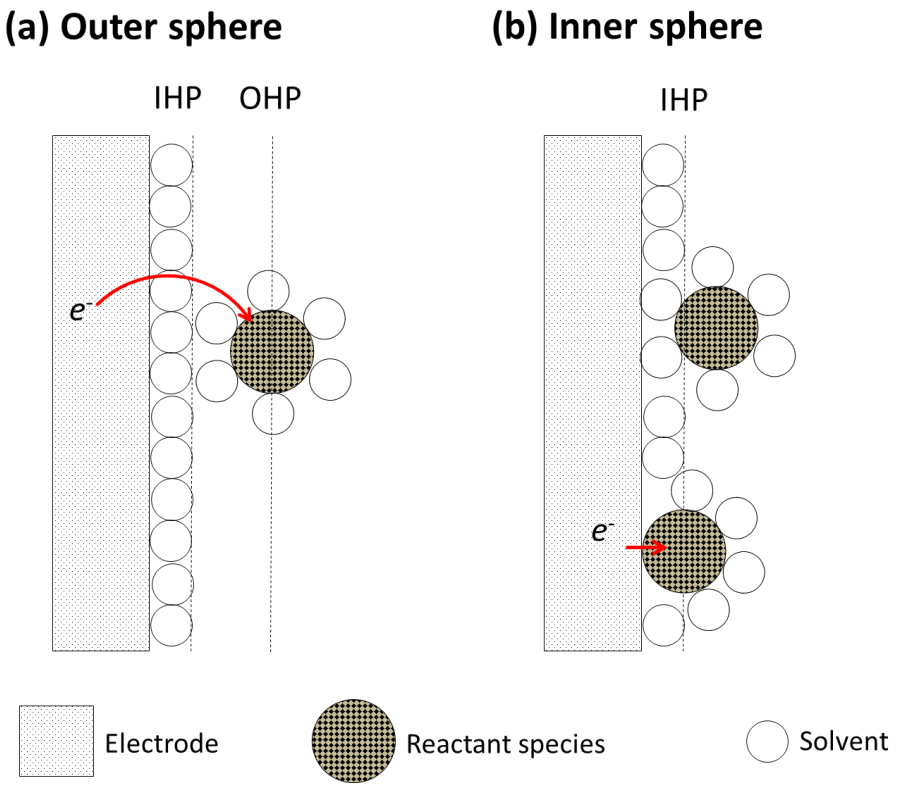

Figure 1.11: Schematic of an electrode/electrolyte interface for (a) an outer sphere reaction and (b) an inner sphere reaction. IHP and OHP represent the inner- and outer- Helmholtz planes, respectively.

1.2.2 Electrode blocking

Surface blocking in its general meaning is the accumulation of material on a solid surface, which in return, affects its functionality. This concept can be extended to the electrode/electrolyte interface. Here the absorption and accumulation of reactants, intermediates or products on the electrode surface lead to the following effects: (1) layer formation;[61, 62] (2) changes in electrode capacitance;[63] (3) hindered electron transfer process.[64]

Self-assembled monolayer (SAM)[65-67] formation is one of most common approaches for forming layers on an electrode surface and has been used for *e.g.*

corrosion protection on electrodes[68] and surface functionalisation.[69] Surface polymerisation of molecules, such as polyaniline[70] is also a common approach for effective layer formation on electrode surfaces and preventing electrode corrosion. Preparation and application of SAM will be discussed in section 1.4.1.

In electrochemical sensing, especially bio-sensing, inhibition of electron transfer processes, as a result of surface absorption of species, is disadvantageous as it is detrimental to the sensitivity and stability of the electrode.[64, 71] In the field of bio-sensing, neurotransmitters such as dopamine and serotonin are well known surface fouling inner-sphere redox mediators. For example, the oxidation of dopamine, shown in Figure 1.12, happens through a complex 2-electron 2-proton process [72-74] at neutral pH environment and leads to the product, dopaminequinone, which spontaneously forms leucodopaminechrome. Finally, polymerisation of melanin-like compound is formed on the electrode surface, which suppresses the electron transfer process. Surface fouling phenomena for the oxidation of dopamine has been found in both metal electrodes, such as gold (Au),[75] platinum (Pt)[76] and conventional carbon electrodes, such as glassy carbon.[77]

Approaches to enhance the catalytic activity (prevent surface fouling) of electrode materials towards bio-molecules include: (1) modified electrodes and (2) electrode polarisation. Sensitivity for the oxidation of dopamine[77-79] and serotonin[79, 80] has been improved by modifying glassy carbon electrode with Au nanoparticles (NPs)[78, 79, 81] or carbon nanotubes.[77, 82] Anodic or cathodic polarisation has been employed to either remove phenolic films deposited on Pt electrode[83] or reduce fouling at BDD electrodes[84] and carbon nanotube modified microelectrodes.[85]

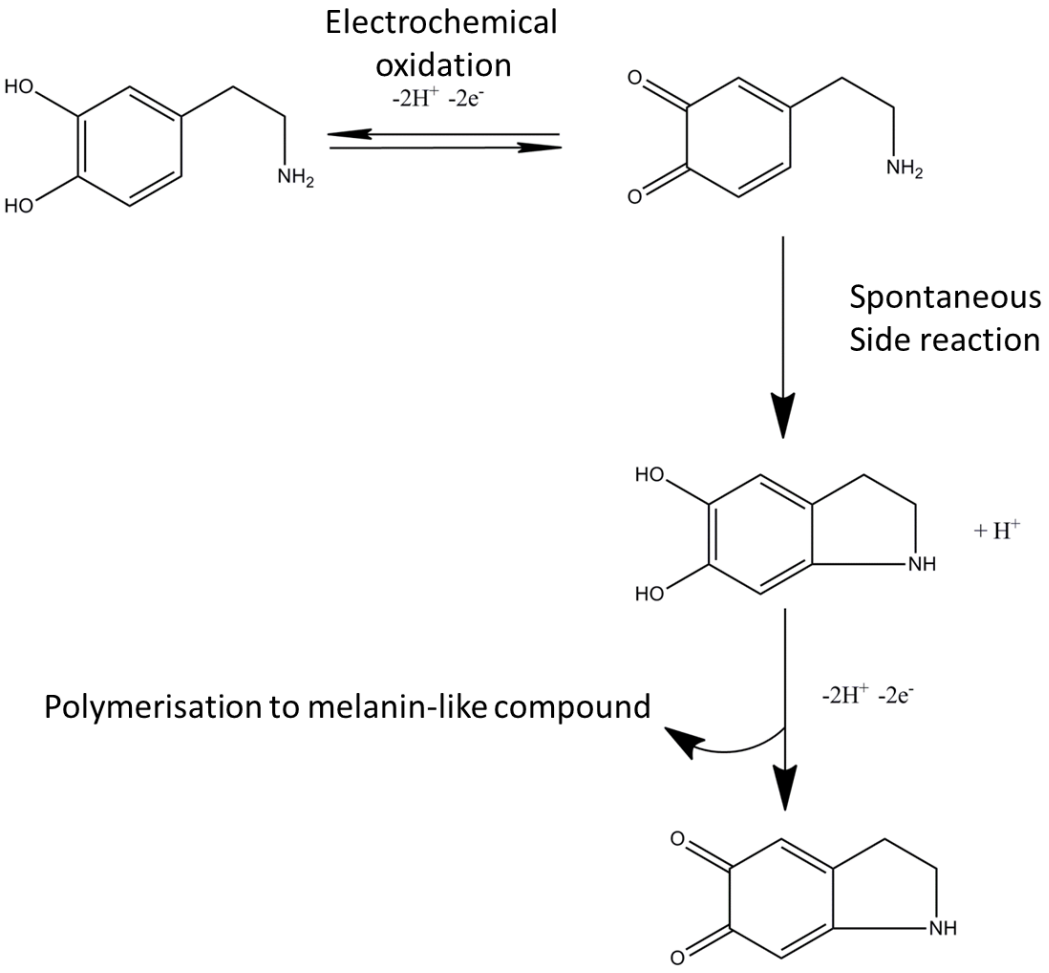

Figure 1.12: Oxidation schematic of dopamine at neutral pH showing the side reactions that lead to surface fouling.

1.3 Electrochemical characterisation of BDD

The first report on conducing diamond as an electrode material highlighted the low capacitance and wide potential window.[86] Since then conducting diamond has gained great interests and Swain et al[87, 88] comprehensively documented the electrochemical response of high quality BDD, including low background current, chemical stability, wide solvent window and chemical inertness. BDD, as an

electrode material, has been explored for a variety of electrochemical applications, such as oxygen reduction reactions,[89-91] and detecting trace metals (Pb,[92-94] Cu,[92] Hg[95, 96]) in solution. Further applications of BDD electrodes are described comprehensively in recent reviews[97, 98] and in section 1.6.

High quality BDD exhibits very low background current ($\leq$ 10 µF cm^{-2})[34] compared to conventional metal electrodes, such as Pt, Au (~ 30 µF cm^{-2})[99] and carbon electrodes, such as glassy carbon, carbon fibre. Thus, BDD is a good candidate for electrochemical trace metal detection, providing improved electroanalytical sensitivity compared to conventional electrodes.[100] The reported low capacitance is due to (1) low density of states (DOS)[101, 102] near Fermi level, (2) the chemical stability of the sp^3 diamond structure and the lack of higher order oxide groups on the electrode surface and (3) negligible surface processes, *i.e.* surface oxidation and reduction.

The solvent window is defined by the potential range in both the anodic and cathodic directions in which it is possible to carry out electrochemical reactions without the electrolysis of water taking place. BDD exhibits an extended solvent window. This is due to the chemically inert nature of the sp^3 structure. As water electrolysis is an inner sphere reaction, see section 1.2.1.4, catalytic sites on the BDD surface are needed for the oxidation and reduction of water molecules.[103] One of the advantages of the extended solvent window is the possibility to study a wide range of redox reactions which happen at extreme potentials (especially for outer sphere redox couples). Moreover, the chemically inert nature results in an increased resistance to fouling, which gives BDD potential applications in the detection of

biological species, such as dopamine, which are known to foul significantly at electrode surfaces constructed from other materials.[104-106]

'High quality' BDD means there is minimal non-diamond carbon (NDC), such as sp^2 carbon and graphitic carbon, embedded in the diamond structure. NDC exists mainly in the grain boundary or defect sites of CVD diamond. Thus the amount of NDC is larger in microcrystalline BDD compared to single crystal BDD due to the increased density of grain boundaries. NDC incorporated in BDD affects the electrochemical response as either it provides more active sites for inner sphere reactions[107, 108] or it is reactive itself, leading to an increased background current,[109, 110] decreased solvent window and more susceptible to fouling.[111] NDC content in diamond can be characterised by Raman spectroscopy.[112, 113]

The surface termination of diamond affects not only its electrochemical response, especially for inner sphere reactions,[52] but the wetting properties of the surface. The two main surface terminations on BDD are hydrogen and oxygen. As-grown CVD diamond is hydrogen terminated due to the presence of hydrogen gas in the CVD growth process. Oxygen terminated diamond can be generated by alumina polishing,[109] oxygen plasma treatment,[114, 115] anodic polarisation[116-118] or hot acid treatment.[119] The oxygen-containing groups introduced on the surface include hydroxyl, ether and carbonyl, with the relative amounts depending on the crystallographic orientations present.[120]

The surface wetting properties of diamond with water after hydrogen and oxygen termination are very different, as shown in Figure 1.13. The former shows a hydrophobic nature, whereas the latter leads to a hydrophilic surface. Contact angle

for hydrogen terminated diamond is normally above 65°, whereas for oxygen termination it is below 65°.[34] Another interesting feature of the hydrogen terminated diamond surface is the property of negative electron affinity (NEA),[121-123] which is essential for the photochemical modification of the diamond surface.[124] Hydrogen termination of diamond results in the vacuum level lying below (- 1.1 eV) the conduction band (NEA), whereas oxygen terminated diamond exhibits positive electron affinity, where vacuum level lies above (+ 1.7 eV) the conduction band.[121] Surface modification of BDD will be discussed in detail in section 1.6.2.

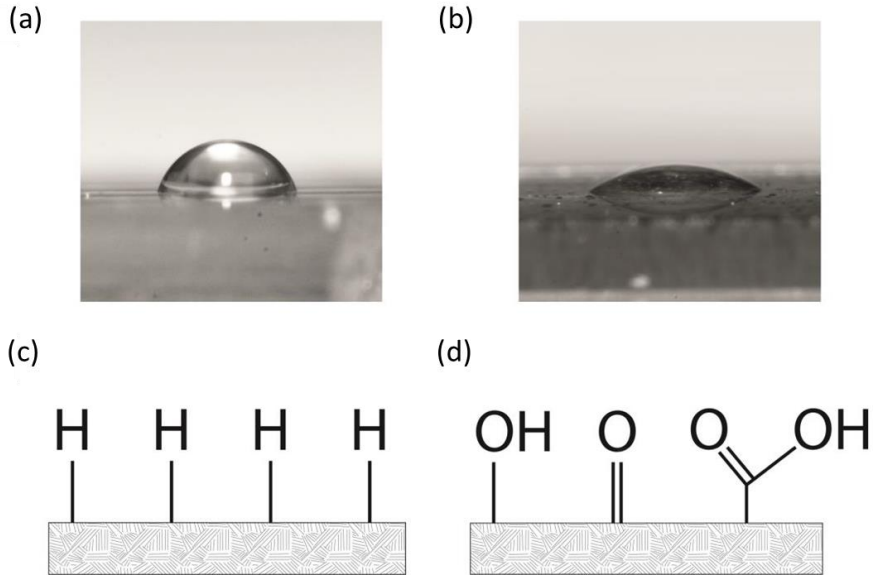

Figure 1.13: Comparison of the contact angle of a water droplet on (a) a hydrogen terminated diamond surface and (b) an oxygen terminated diamond surface. (c) and (d) illustrate the surface terminal groups on hydrogen and oxygen terminated diamond surfaces, respectively.[34]

1.4 Surface bound electrochemistry

1.4.1 Self-assembled monolayer

SAM is a monolayer of molecules assembled on a surface by either chemical or physical bonding. The most common approach[66, 125] employed is the immobilisation of alkanethiols (structure can be written as $HS(CH_2)_nX$), which contains a thiol head group (HS-) and a tail functional group(X-), on a metal surface, such as Au. *n* is the number of methylene units in the alkanethiols molecule. The general structure of an alkanethiols on Au surface is illustrated in Figure 1.14. The formation of the SAM on Au surface is through the interaction between the thiol group and the Au surface, as described in the following reaction:[126]

$$RS\text{-}H + Au \rightarrow RS\text{-}Au + H^+ + e^- \quad (1.13)$$

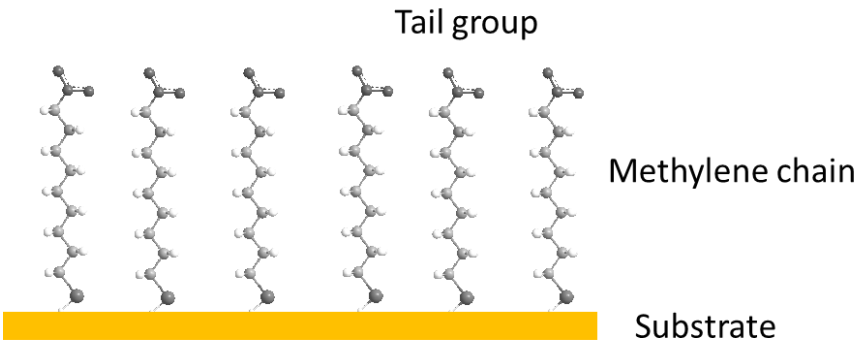

Figure 1.14: Structure of a SAM formed on Au surface[66]

The electrochemistry of SAM provides a number of advantages, including (1) easy preparation; (2) a wide range of functionalities of the tail group and (3) the ability to study surface confined electrochemistry. The quality of the SAM on electrode surface, such as density, alkanethiols length and tilt angle, can be accessed

via an electrochemical approach by attaching a redox probe at the tail end.[67, 127, 128] SAM based biosensors have been developed to detect DNA[129, 130] and enzymes.[131, 132]

1.4.2 Electrochemistry of redox active SAM

The study of electron transfer using redox labelled SAM modified electrodes has drawn interests in recent years and the electron transfer rate constant, k_{ET}^0, for a densely packed surface, has been found to follow the equation:[128, 133]

$$k_{ET}^0 = k_0 e^{(-\lambda d)} \tag{1.14}$$

where k_0 is the electron transfer rate constant for redox species in bulk solution, λ is the tunnelling parameter, and d is the length of the alkyl chain separating the redox active probe (on the tail of the SAM) and the electrode surface. The tunnelling parameter is typically between 0.85 and 1.1 $Å^{-1}$,[134, 135] resulting in a large decrease in k_{ET}^0 with increasing the length of alkyl chain. For example, for a λ value of 1 $Å^{-1}$ and d value of 1 nm, the electron transfer rate constant is about one million times smaller than that in the absence of SAM, indicating the strong blocking effect of the SAM on the electrode surface.

1.5 High temperature electrochemistry

High temperature electrochemistry, also known as thermoelectrochemistry, is the expansion of electrochemistry with the addition of a new variable, temperature. Temperature plays a crucial role in electrochemical reactions, and affects mass transport, electron transfer kinetics and thermodynamics.[136]

1.5.1 Development of thermoelectrochemistry

Isothermal and non-isothermal approaches are employed for thermoelectrochemical experiments. The former is the conventional method, where the electrochemical cell, including both electrodes and solution, is heated to a specific temperature using *e.g.* a water bath or an autoclave.[137] The drawback of the isothermal approach includes: (1) potential variation due to heated reference electrode and (2) uncontrolled or uneven temperature distribution within the electrochemical cell.[138] Whereas in the latter the working electrode **only** is heated, leaving all the other elements at ambient conditions. This leads to a temperature gradient between the working electrode and the surroundings. Both continuous and pulsed heating techniques can be applied in non-isothermal cells.

1.5.2 Approaches for non-isothermal electrochemical cell

Non-isothermal set-ups require a fast localised temperature change, resulting in a temperature gradient between the electrode surface and the surrounding solution. Early work included heated flow-through arrangements,[139, 140] where a solution stream flows through a preheated unit, in which the electrodes were placed. Kinetics investigations of the $Fe^{2+/3+}$ redox mediator have been carried out using this system.[141]

A somewhat different approach to establish the non-isothermal cell is techniques which generate a small 'hot spot' at the electrode/electrolyte interface which can be switched on and off rapidly. One methods used to generate a 'hot spot' in close vicinity of the electrode surface is focused microwave heating,[142] illustrated in Figure 1.15. The electrochemical cell is placed in a microwave oven, where a long

wire with a noble metal end (micrometre size) acts as the working electrode and also serves as an 'antenna', receiving the microwave oscillation energy. Thus a hot solution spot close to the metal end will be generated. Fast temperature change is achieved by carefully tuning the focused microwave setup. The drawbacks of the microwave heating include: (1) the uncontrolled warming-up of the solution as the electrochemical cell is located inside the microwave oven and (2) limitations over electrode size.[143]

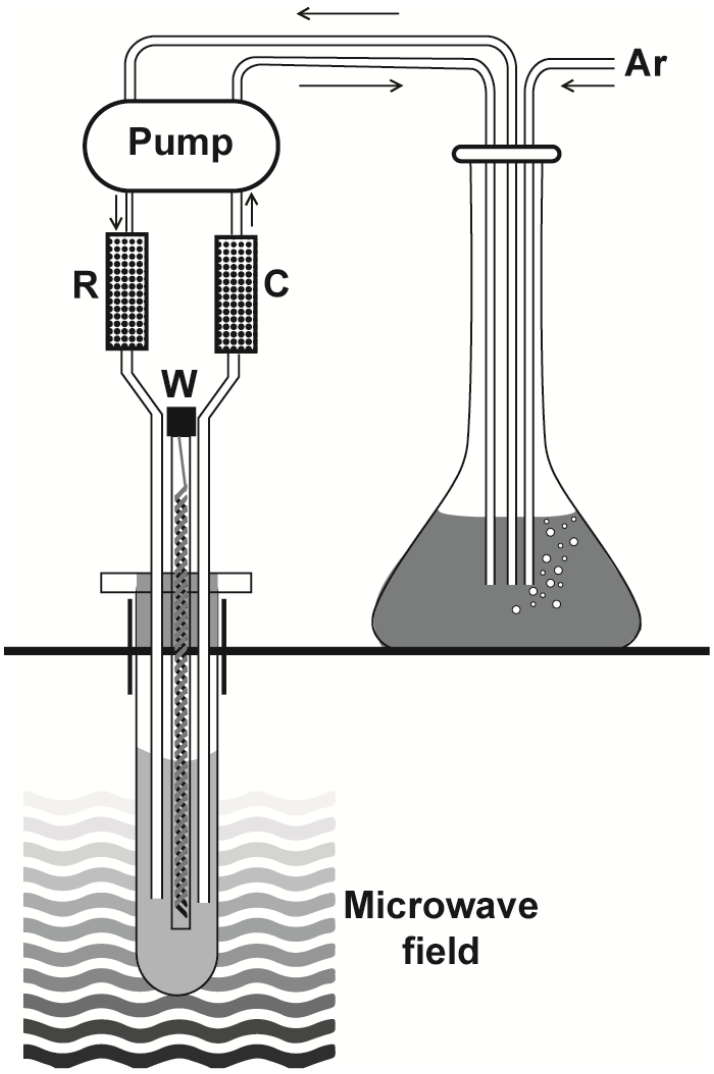

Figure 1.15: Electrochemical cell for in-situ microwave voltammetry[144]

A different non-isothermal technique is directly heating the electrode itself instead of generating a 'hot spot' close to electrode surface. This can be achieved by resistive wire heating (Joule heating)[145-147] and laser heating.[148, 149] Resistive wire heating involves the application of an alternating current (AC) to thin metallic wire electrodes, resulting in a local temperature increase at the electrode surface. Early work by Gabrielli et al[150] introduced only a small temperature jump of a few Kelvin to avoid AC distortion of the electrochemical signal. Since then, resistive wire heating has been developed to avoid AC distortion by using a symmetrical setup,[151] where the centre of the thin metal wire is connected to a potentiostat as working electrode. The setup is illustrated in Figure 1.16. The two AC components with opposite sign will be generated at both ends, but the distortion will be avoided at the centre. Recent developments to avoid the distortion include 'bridge' arrangements, where the compensation of the distortion signal is carried out by introducing two inductive elements as branches of the bridge.[152]

Resistive wire heating has become a well-established technique due to its short heating-up and cooling-down periods. However, resistive wire heating is limited to Pt, Ag and Au microelectrodes. Resistive heated macrostructures, such as screen printed electrodes, ITO electrodes and paste electrodes, have also been employed but in continuous heating mode as pulsed heating is less effective due to the high thermal resistance of these materials.[138]

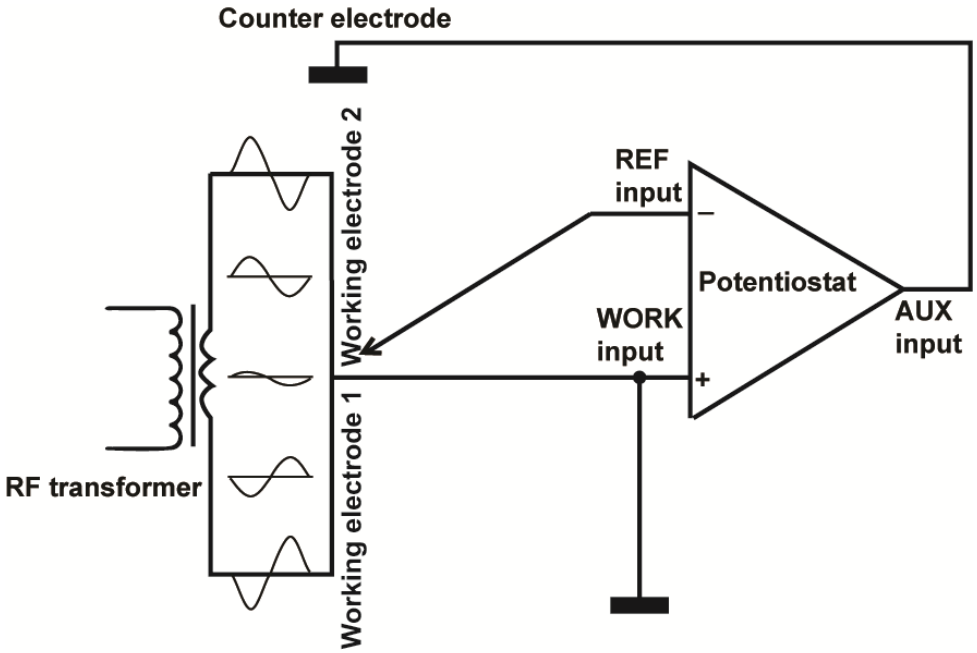

Figure 1.16: Distortion of potentiostat measuring circuit by AC heating and its compensation made by employment of a symmetrical arrangement.[151]

Laser heating is another approach for generating non-isothermal cell. The laser beam can either be focused on the rear of the electrode or from the electrolyte side (laser beam passes through solution). In the former case, energy will generate an exclusively thermal effect, and electrode materials with good thermal conductivity are therefore required so that heat can propagate to the solution side rapidly. In the latter case energy loss is experienced as the beam passes through the solution, moreover there is the possibility for photo-electrochemical reactions to be induced.[153]

Temperature rise at the electrode surface can be well above the boiling point of water depending on the power of laser[154] and the heating and cooling processes are relatively fast when employing pulsed heating approaches.[155] However, consideration must be given to the nature of light source (UV, visible or IR) and the

absorptivity of the electrode materials (absorption coefficient of light). Disadvantages of laser heating on metal and conventional carbon electrodes include: (1) increased surface roughness after laser heating, resulting in uncontrolled surface area, for example, it has been shown that even after mild laser treatments (power density, P_d > 1.5 W cm^{-2}) a Pt electrode surface roughens,[154] (2) surface oxide formation.[156]

1.5.3 Applications of high temperature electrochemistry

1.5.3.1 Analytical and stripping analysis

Locally induced temperature changes have been shown to improve the detection sensitivity of an electrode due to the increased mass transport of reactant species towards the electrode surface.[157] Electrode heating also acts to increase the electron transfer kinetics of species.[158] For example, research shows the limit of detection towards the reduction of dissolved oxygen in water has been enhanced at heated Pt microelectrodes, and the sluggish response of oxygen reduction has been accelerated.[159] Stripping analysis with focused microwave heating has been employed in trace metal detections, such as lead,[93, 160] palladium[161] and cadmium.[162]

1.5.3.2 Biosensors

Precise temperature control is crucial in the DNA hybridisation and denaturation processes. Hybridisation, where a single stranded DNA interacts with its complementary target stranded DNA in solution, is temperature sensitive. An single nucleotide polymorphism (SNP) is a DNA sequence variation occurring commonly within a population, where one nucleotide base has been substituted for

another. Detecting SNPs in DNA is extremely important for genomic research as SNPs often lead to debilitating genetic disorders. There are different methods to detect SNPs but many are reliant on the basic premise that the melting temperature of SNP-containing DNA is lower than SNP-free DNA because of the instability of mismatched base pairs. Thus, careful and precise temperature control is required for discriminating SNPs in DNA duplex. Redox labelled DNA has been used for electrochemical detection of the hybridisation process at heated carbon paste electrodes[163] and SNP in DNA duplex at a heated gold electrode.[164] Heated electrodes have also been utilised to distinguish two or more closely related compounds *e.g.* glucose and maltose at an enzymatic biosensor,[165] where multiple linear temperature dependences for the oxidation of both molecules were obtained to discriminate between glucose and maltose.

1.5.3.3 Switchable passive layers

In electrochemistry, passivation of an electrode surface by either forming oxide layer or deposition of reactants, intermediates and products is common. Passive layers formed on the electrode surface hinder electron transfer, resulting in reduced (or zero) current response. For example, after anodic polarisation, gold electrodes experienced oxidised layer formation in acid, neutral and alkaline solution, suppressing electron transfer for the oxidation of ferrocene at the electrode surface.[166] Reports found that pulsed heating shifted the onset potential positively for passive layer formation enabling efficient electron transfer.[166] In this case, the electrode reaction could be switched 'on' and 'off' depending on the applied temperature, providing a controllable surface response.[166]

1.6 Application of BDD as an electrode material

1.6.1 Metal deposition and trace metal detection

BDD is an ideal supporting substrate for catalytic materials due to its relatively low background current. Various metals, such as Au,[167, 168] Pt[169, 170] Pb[171] of different morphologies (NPs [142, 144] islands or films[171]) have been deposited on the BDD electrode and been employed for catalytic applications. For example, Pt NPs modified BDD has shown superior electrocatalytic activity towards methanol oxidation.[169] Trace metal detection employing BDD is another promising area. This process involves a pre-concentration step, *i.e.* trace metal ions in solution are firstly reduced and deposited on an electrode surface and then a subsequent stripping step is implemented, whereby deposited metal is oxidised. The measured stripping current (or charge passed) is used to quantify the concentration of metal ions in solution. Low detection limits in parts per billion (ppb) range have been reported with the BDD electrode for different metals, such as Pb[94, 172] and Hg.[95] The wide solvent window of BDD is also of advantage as it allows detection of a variety of metals, surpassing other electrode materials with narrow potential windows. For example, a comparison between BDD and Hg electrodes for the detection of various metals (Zn^{2+}, Cd^{2+}, Pb^{2+}, Cu^{2+}) has been conducted and BDD electrode shows superior limit of detection.[172]

1.6.2 Surface functionalisation

There has been a great interest in modifying solid surfaces with biomolecules due to their potential for use in biosensors. Due to its exceptional physical and

chemical properties, such as chemical inertness and biocompatibility, diamond has been an ideal candidate for bio-sensing applications (such as the detection of enzyme, DNA, protein).[173] Covalent grafting is known as a reliable approach for the formation of robust and stable bio-interfaces and progress has been made for the development of controllable and reliable covalent grafting of different functional groups on the diamond surface. These approaches include chemical,[174] photochemical,[175, 176] and in the case of BDD, electrochemical modification.[177, 178] CVD diamond, straight from the growth chamber is hydrogen terminated (section 1.1.1). Hydrogen terminated diamond can be modified by either electrochemical reduction of aryldiazonium salt or photochemical attachment of organic alkene molecules using 254 nm UV light due to the property of NEA, described in sections 1.6.2.1 and 1.6.2.2,[179] respectively.

1.6.2.1 Electrochemical reduction of aryldiazonium salt

Since the first report on the electrochemical modification of a diamond surface by electrochemical reduction of aryldiazonium salt by McCreery et al[180] in 1999, a wide range of functional groups such as -COOH, -NO_2,[180, 181] have been introduced to the diamond surface, enabling further bio-sensing applications.

Aryldiazonium cations exhibit a strong electron-withdrawing property, resulting in their easy reduction and immobilisation on the diamond surface.[182] The mechanism of electrochemical reduction of aryldiazonium salt is illustrated in Figure 1.17a. The ability to reduce nitro aryldiazonium salt onto diamond surface makes DNA bio-modification possible, as the nitro group can be reduced to a primary

amine group, to which a DNA molecule is covalently bonded through a bifunctional linker,[183] illustrated in Figure 1.17b.

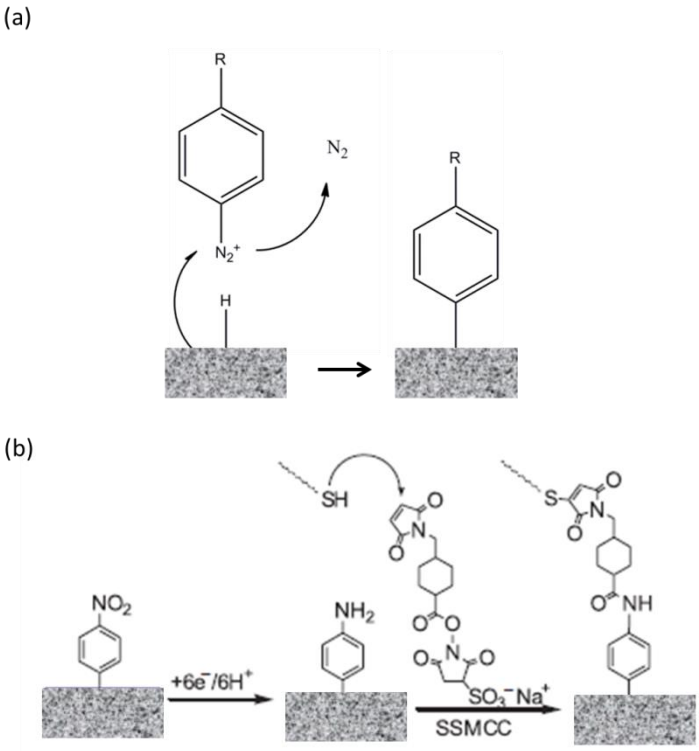

Figure 1.17: (a) Electrochemical reduction of aryldiazonium salt on a diamond surface, R=NO_2, COOH, CN, Cl, etc.[184] *(b) Schematic of covalent linking thiolated DNA molecule on the diamond surface using 4-(N-maleimidomethyl)-cyclohexane-1-carboxylate (SSMCC) as bifunctional linker.*[183]

While the electrochemical reduction of the aryldiazonium salt is a convenient way to modify the diamond surface, it has experienced drawbacks such as multilayer formation.[184] The phenyl radical species, formed during the electrochemical reduction process, reacts not only with the diamond, but also with the phenyl ring immobilised on the surface, resulting in the formation of multilayers. Multilayer formation hinders electron transfer processes and results in electrode blocking (section 1.2.2).

1.6.2.2 Photochemical modification

Photochemical modification of hydrogen terminated diamond with alkene-containing organic molecules was developed by Hamers and co-workers.[185] The modification process employed an UV (λ = 254 nm) light irradiating on hydrogen terminated diamond surface, which was covered by a liquid thin film of alkene-containing molecules under inert atmosphere.

Hamers et al[175] proposed the following mechanisms for photochemical modification, as illustrated in Figure 1.18a. The photochemical modification process is initiated by the photoejection of an electron either by (1) excitation from near the Fermi level to the conduction band followed by diffusion and emission to liquid phase, or (2) direct photoemission from the valence band to the liquid phase due to the NEA properties of hydrogen terminated diamond.

The most commonly used alkene-containing molecules are aminodec-1-ene protected with a trifluoroacetamide functional group (TFAAD) and tert-butyloxycarbonyl (t-BOC) protected ω-unsaturated aminoalkane (10-N-Boc-amino-dec-1-ene). After photoemission of an electron into the liquid phase, liquid phase anion radicals abstract H from the C-H bond on the diamond surface, resulting in surface active sites for covalent bonding alkene-containing molecules. Photochemical modification has been employed for covalent immobilisation of DNA on the diamond surface. It showed superior stability (over 30 hybridisation and denaturation cycles[185]) compared to other solid surfaces, such as Au, Si and glassy carbon (Figure 1.18b).

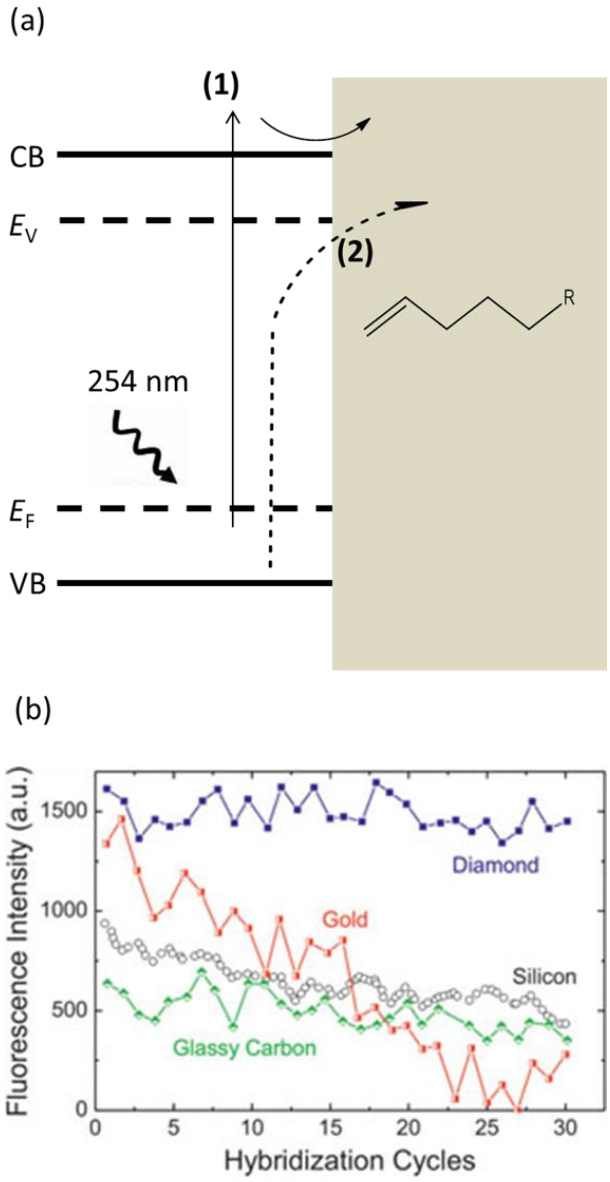

Figure 1.18: (a) Proposed mechanism for injection of electron from diamond into the liquid phase. Pathway (1) excitation from near Fermi level to conduction band followed by diffusion and emission to liquid phase (solid line); pathway (2) direct photoemission from valence band to liquid phase (dashed line). VB and CB represent valence and conduction bands; E_F and E_v are the Fermi level and vacuum level, respectively. (b) Comparison of hybridisation stability of DNA on different surfaces after 30 cycles.

1.6.2.3 Surface modification of oxygen terminated diamond

Recent development has shown that oxygen terminated diamond is also accessible for covalent modification. Surface modification of an oxygen terminated diamond surface employing a copper (I) catalysed cycloaddition of azides and alkynes which is shown in Figure 1.19. subsequent DNA immobilisation is carried out on the diamond surface to detect the hybridisation and denaturation processes via electrochemical impedance technique, and a detection limit of 1 nM DNA has been reported.[186]

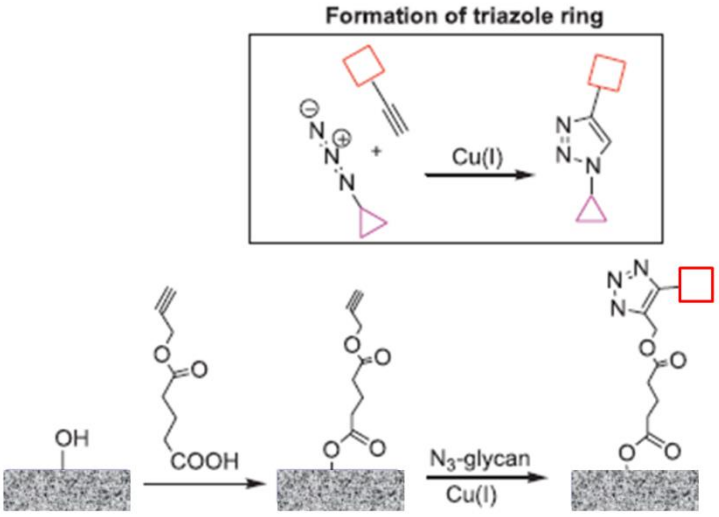

Figure 1.19: Copper 'click' chemistry on diamond for the formation of glycan-modified diamond surface.[186]

1.7 Aims and objectives

This thesis is based primarily on investigating the use of high quality BDD with thermal heating and exploring electrochemical applications in areas such as metal/metal oxide deposition, electrode fouling and surface modification. To date

there has been no studies which look to combine high quality freestanding BDD with high temperature (laser heating) electrochemical studies. BDD is the ideal material for thermoelectrochemistry due to its thermal stability, high thermal conductivity, *ca.* 600 W m^{-1} K^{-1} at 300 K,[187] and high thermal diffusivity, which is approximately 2-3 times higher than that of the copper. We employ a pulsed laser set-up, heating from the backside of BDD to avoid solution heating effects. Chapter 2 outlines the experimental detail and the characterisation techniques.

In chapter 3 the effect of temperature on the electrochemical response of two simple outer sphere redox couples ($Ru(NH_3)_6^{3+/2+}$ and $IrCl_6^{2-/3-}$) on an IR laser pulse heated BDD macroelectrode is examined. The temperature increase at the electrode surface is determined using both thermopotentiometry and finite element simulation. CVs for electrolysis of the two mediators are recorded and interpreted both qualitatively and quantitatively by taking into account temperature induced shifts in formal potential, mass transport and electron transfer rate constant.

Chapter 4 moves to a better experimental electrode structure; an all diamond macroelectrode (BDD electrode insulated in intrinsic diamond) and the effect of temperature, deposition potential and dissolved oxygen content on cathodic electrodeposition of crystalline lead oxide (PbO) is investigated. High resolution microscopic and crystallographic analysis is carried out to assess the morphology, composition and crystallinity of PbO.

In chapter 5 the effect of temperature on the electrochemical response of an all diamond microdisk electrode, where the mass transport characteristics are different to the macroelectrode set-up employed in chapters 3 and 4, is explored. The

response of the microelectrode is electrochemically examined under both ambient and laser heated conditions using both outer sphere ($Ru(NH_3)_6^{3+/2+}$) and inner sphere ($Fe^{2+/3+}$) redox mediators. A finite element model is built to understand the electrochemical response of microelectrode behaviour under elevated temperatures. Finally, the microdisk BDD electrode under laser heated conditions is employed to examine the oxidation characteristics of a neurotransmitter, dopamine, which is known to lead to surface fouling with other electrode materials.

Chapter 6 starts by functionalising an Au electrode surface using ferrocene labelled alkanethiols and methylene blue (MB) modified DNA. Then surface modification approaches for BDD, both electrochemically and photochemically, are explored and finally the electrochemical reponse of MB labelled DNA immobilsied on the BDD electrtode is investigated. Conclusions are summarised in chapter 7.

1.8 References

1. R. Balmer, J. Brandon, S. Clewes, H. Dhillon, J. Dodson, I. Friel, P. Inglis, T. Madgwick, M. Markham and T. Mollart, *J. Phys.: Condens. Matter*, 2009, 21, 3-5.

2. D. U. Braga, A. E. Diniz, G. W. Miranda and N. L. Coppini, *J. Mater. Process. Technol.*, 2002, 122, 127-138.

3. T. Ackemann, M. Alduraibi, S. Campbell, S. Keatings, P. L. Sam, H. Fraser, A. Arnold, E. Riis and M. Missous, *J. Appl. Phys.*, 2012, 112, 12310901-12310906.

4. P. W. May, *Philosophical Transactions of the Royal Society of London A: Mathematical, Physical and Engineering Sciences*, 2000, 358, 473-495.

5. S.-F. Wang, Y.-F. Hsu, J.-C. Pu, J. C. Sung and L. Hwa, *Mater. Chem. Phys.*, 2004, 85, 432-437.

6. E. Pace, A. Pini, G. Corti, F. Bogani, A. Vinattieri, C. Pickles and R. Sussmann, *Diamond Relat. Mater.*, 2001, 10, 736-743.

7. H. T. Hall, *Rev. Sci. Instrum.*, 1960, 31, 125-131.

8. M. Akaishi, H. Kanda and S. Yamaoka, *J. Cryst. Growth*, 1990, 104, 578-581.

9. K. E. Spear and J. P. Dismukes, *Synthetic diamond: emerging CVD science and technology*, John Wiley & Sons, 1994.

10. J. P. Lagrange, A. Deneuville and E. Gheeraert, *Diamond Relat. Mater.*, 1998, 7, 1390-1393.

11. J. Goss, P. Briddon, R. Jones and S. Sque, *Diamond Relat. Mater.*, 2004, 13, 684-690.

12. E. Brillas and C. A. M. Huitle, *Synthetic diamond films: preparation, electrochemistry, characterization and applications*, John Wiley & Sons, 2011.

13. M. Panizza and G. Cerisola, *Electrochim. Acta*, 2005, 51, 191-199.

14. M. Hupert, A. Muck, J. Wang, J. Stotter, Z. Cvackova, S. Haymond, Y. Show and G. M. Swain, *Diamond Relat. Mater.*, 2003, 12, 1940-1949.

15. T. N. Rao, I. Yagi, T. Miwa, D. Tryk and A. Fujishima, *Anal. Chem.*, 1999, 71, 2506-2511.

16. F. Bundy, *J. Chem. Phys.*, 1963, 38, 631-643.

17. W. Eversole, US Patents 3030187, 3030188, 1955.

18. B. Spitsyn, L. Bouilov and B. Derjaguin, *J. Cryst. Growth*, 1981, 52, 219-226.

19. S. Matsumoto, Y. Sato, M. Kamo and N. Setaka, *Jpn. J. Appl. Phys.*, 1982, 21, L183.

20. P. K. Bachmann, D. Leers and H. Lydtin, *Diamond Relat. Mater.*, 1991, 1, 1-12.

21. S. Wang and G. M. Swain, *J. Phys. Chem. C*, 2007, 111, 3986-3995.

22. F. P. Bundy, *J. Geophys. Res.: Solid Earth*, 1980, 85, 6930-6936.

23. J. Butler, Y. A. Mankelevich, A. Cheesman, J. Ma and M. Ashfold, *J. Phys.: Condens. Matter*, 2009, 21, 364201.

24. X. Jiang and C.-P. Klages, *Diamond Relat. Mater.*, 1993, 2, 1112-1113.

25. H. Schachner, H. Tippmann, B. Lux, K. G. Stjernberg and A. G. Thelin, US Patents 4707384, 1987.

26. K. Mallika and R. Komanduri, *Wear*, 1999, 224, 245-266.

27. C.-s. Yan, Y. K. Vohra, H.-k. Mao and R. J. Hemley, *Proc. Natl. Acad. Sci.* , 2002, 99, 12523-12525.

28. A. Tallaire, A. Collins, D. Charles, J. Achard, R. Sussmann, A. Gicquel, M. Newton, A. Edmonds and R. Cruddace, *Diamond Relat. Mater.*, 2006, 15, 1700-1707.

29. Y. Mokuno, A. Chayahara and H. Yamada, *Diamond Relat. Mater.*, 2008, 17, 415-418.

30. R. Sussmann, J. Brandon, G. Scarsbrook, C. Sweeney, T. Valentine, A. Whitehead and C. Wort, *Diamond Relat. Mater.*, 1994, 3, 303-312.

31. K. Kobashi, K. Nishimura, Y. Kawate and T. Horiuchi, *Physical review B*, 1988, 38, 4067.

32. C. P. Chang, D. L. Flamm, D. E. Ibbotson and J. Mucha, *J. Appl. Phys.*, 1988, 63, 1744-1748.

33. H. V. Patten, S. C. Lai, J. V. Macpherson and P. R. Unwin, *Anal. Chem.*, 2012, 84, 5427-5432.

34. J. V. Macpherson, *Phys. Chem. Chem. Phys.*, 2015, 17, 2935-2949.

35. M. Szameitat, X. Jiang and W. Beyer, *Appl. Phys. Lett.*, 2000, 77, 1554-1556.

36. H. Dyer and L. Du Preez, *J. Chem. Phys*, 1965, 42, 1898-1906.

37. J. F. Prins, *Phys. Rev. B*, 1988, 38, 5576-5584.

38. H. Spicka, M. Griesser, H. Hutter, M. Grasserbauer, S. Bohr, R. Haubner and B. Lux, *Diamond Relat. Mater.*, 1996, 5, 383-387.

39. J. Butler, M. Geis, K. Krohn, J. Lawless Jr, S. Deneault, T. Lyszczarz, D. Flechtner and R. Wright, *Semicond. Sci. Technol.*, 2003, 18, S67-S71.

40. R. Burns, V. Cvetkovic, C. Dodge, D. Evans, M.-L. T. Rooney, P. Spear and C. Welbourn, *J. Cryst. Growth*, 1990, 104, 257-279.

41. E. Gheeraert, A. Deneuville and J. Mambou, *Diamond Relat. Mater.*, 1998, 7, 1509-1512.

42. T. Yokoya, T. Nakamura, T. Matsushita, T. Muro, Y. Takano, M. Nagao, T. Takenouchi, H. Kawarada and T. Oguchi, *Nature*, 2005, 438, 647-650.

43. J.-P. Lagrange, A. Deneuville and E. Gheeraert, *Diamond Relat. Mater.*, 1998, 7, 1390-1393.

44. J. L. Anderson, L. A. Coury and J. Leddy, *Anal. Chem.*, 2000, 72, 4497-4520.

45. A. J. Bard and L. R. Faulkner, *Electrochemical methods: fundamentals and applications*, Wiley, 2001.

46. A. Fisher, *Electrode Dynamic*, Oxford University Press, 1996.

47. E. J. Dickinson, J. G. Limon-Petersen, N. V. Rees and R. G. Compton, *J. Phys. Chem. C*, 2009, 113, 11157-11171.

48. F. Opekar and P. Beran, *J. Electroanal. Chem. Interfacial Electrochem.*, 1976, 69, 1-105.

49. P. T. Kissinger and W. R. Heineman, *J. Chem. Educ*, 1983, 60, 702-706.

50. J. E. B. Randles, *Trans. Faraday Soc.*, 1948, 44, 327-338.

51. R. J. Forster, *Chem. Soc. Rev.*, 1994, 23, 289-297.

52. A. J. Bard, *J. Am.Chem.Soc.*, 2010, 132, 7559-7567.

53. W. Schmickler and E. Santos, *Interfacial Eelectrochemistry*, Springer, 2010.

54. H. Taube, *Electron Transfer Reactions of Complex Ions in Solution*, Elsevier, 2012.

55. C. Brett, M. O. Brett, A. M. C. M. Brett and A. M. O. Brett, *Electrochemistry: principles, methods, and applications*, Wiley, 1993.

56. D. C. Grahame, *Chem. Rev.*, 1947, 41, 441-501.

57. D. C. Grahame, *Zeitschrift für Elektrochemie, Berichte der Bunsengesellschaft für physikalische Chemie*, 1958, 62, 264-274.

58. G. M. Brown and N. Sutin, *J. Am.Chem.Soc.*, 1979, 101, 883-892.

59. T. W. Hamann, O. K. Farha and J. T. Hupp, *J. Phys. Chem. C*, 2008, 112, 19756-19764.

60. J. X. Wang, H. Inada, L. Wu, Y. Zhu, Y. Choi, P. Liu, W.-P. Zhou and R. R. Adzic, *J. Am.Chem.Soc.*, 2009, 131, 17298-17302.

61. A. Diaz, K. K. Kanazawa and G. P. Gardini, *J. Chem. Soc., Chem. Commun.*, 1979, 635-636.

62. A. Volkov, G. Tourillon, P.-C. Lacaze and J.-E. Dubois, *J. Electroanal. Chem. Interfacial Electrochem.*, 1980, 115, 279-291.

63. J. Yan, T. Wei, B. Shao, Z. Fan, W. Qian, M. Zhang and F. Wei, *Carbon*, 2010, 48, 487-493.

64. R. J. Geise, J. M. Adams, N. J. Barone and A. M. Yacynych, *Biosens. Bioelectron.*, 1991, 6, 151-160.

65. A. Ulman, *Chem. Rev.*, 1996, 96, 1533-1554.

66. J. C. Love, L. A. Estroff, J. K. Kriebel, R. G. Nuzzo and G. M. Whitesides, *Chem. Rev.*, 2005, 105, 1103-1170.

67. C. E. Chidsey and D. N. Loiacono, *Langmuir*, 1990, 6, 682-691.

68. Y. Yamamoto, H. Nishihara and K. Aramaki, *J. Electrochem. Soc.*, 1993, 140, 436-443.

69. C. D. Bain, E. B. Troughton, Y. T. Tao, J. Evall, G. M. Whitesides and R. G. Nuzzo, *J. Am.Chem.Soc.*, 1989, 111, 321-335.

70. M. Kraljić, Z. Mandić and L. Duić, *Corros. Sci.*, 2003, 45, 181-198.

71. S. V. Sasso, R. J. Pierce, R. Walla and A. M. Yacynych, *Anal. Chem.*, 1990, 62, 1111-1117.

72. K. Wu, J. Fei and S. Hu, *Anal. Biochem.*, 2003, 318, 100-106.

73. Y. Zhao, Y. Gao, D. Zhan, H. Liu, Q. Zhao, Y. Kou, Y. Shao, M. Li, Q. Zhuang and Z. Zhu, *Talanta*, 2005, 66, 51-57.

74. S.-M. Chen and K.-T. Peng, *J. Electroanal. Chem.*, 2003, 547, 179-189.

75. T. Łuczak, *Electrochim. Acta*, 2008, 53, 5725-5731.

76. D.-M. Zhou, H.-X. Ju and H.-Y. Chen, *J. Electroanal. Chem.*, 1996, 408, 219-223.

77. M. C. Henstridge, E. J. Dickinson, M. Aslanoglu, C. Batchelor-McAuley and R. G. Compton, *Sens. Actuators, B*, 2010, 145, 417-427.

78. G.-Z. Hu, D.-P. Zhang, W.-L. Wu and Z.-S. Yang, *Colloids Surf., B*, 2008, 62, 199-205.

79. J. Li and X. Lin, *Sens. Actuators, B*, 2007, 124, 486-493.

80. A. G. Güell, K. E. Meadows, P. R. Unwin and J. V. Macpherson, *Phys. Chem. Chem. Phys.*, 2010, 12, 10108-10114.

81. L. Zhang and X. Jiang, *J. Electroanal. Chem.*, 2005, 583, 292-299.

82. H. Luo, Z. Shi, N. Li, Z. Gu and Q. Zhuang, *Anal. Chem.*, 2001, 73, 915-920.

83. R. C. Koile and D. C. Johnson, *Anal. Chem.*, 1979, 51, 741-744.

84. A. N. Patel, P. R. Unwin and J. V. Macpherson, *Phys. Chem. Chem. Phys.*, 2013, 15, 18085-18092.

85. B. K. Swamy and B. J. Venton, *Analyst*, 2007, 132, 876-884.

86. M. Iwaki, S. Sato, K. Takahashi and H. Sakairi, *Nucl. Instrum. Methods Phys. Res.*, 1983, 209, 1129-1133.

87. G. M. Swain and R. Ramesham, *Anal. Chem.*, 1993, 65, 345-351.

88. G. M. Swain, *Adv. Mater.*, 1994, 6, 388-392.

89. T. Yano, D. Tryk, K. Hashimoto and A. Fujishima, *J. Electrochem. Soc.*, 1998, 145, 1870-1876.

90. Y. Zhang, S. Asahina, S. Yoshihara and T. Shirakashi, *Electrochim. Acta*, 2003, 48, 741-747.

91. T. Yano, E. Popa, D. Tryk, K. Hashimoto and A. Fujishima, *J. Electrochem. Soc.*, 1999, 146, 1081-1087.

92. C. Prado, S. J. Wilkins, F. Marken and R. G. Compton, *Electroanalysis*, 2002, 14, 262-272.

93. Y. C. Tsai, B. A. Coles, K. Holt, J. S. Foord, F. Marken and R. G. Compton, *Electroanalysis*, 2001, 13, 831-835.

94. A. Manivannan, D. Tryk and A. Fujishima, *Electrochem. Solid-State Lett.*, 1999, 2, 455-456.

95. A. Manivannan, M. Seehra and A. Fujishima, *Fuel Process. Technol.*, 2004, 85, 513-519.

96. A. Salimi, V. Alizadeh and R. Hallaj, *Talanta*, 2006, 68, 1610-1616.

97. A. Kraft, *Int. J. Electrochem. Sci*, 2007, 2, 355-385.

98. G. M. Swain, A. B. Anderson and J. C. Angus, *MRS Bull.*, 1998, 23, 56-60.

99. R. N. Adams, *Electrochemistry at solid electrodes*, 1969.

100. A. Manivannan, M. Seehra, D. Tryk and A. Fujishima, *Anal. Lett.*, 2002, 35, 355-368.

101. K.-W. Lee and W. Pickett, *Phys. Rev. Lett.*, 2004, 93, 2370031-2370034.

102. H. V. Patten, K. E. Meadows, L. A. Hutton, J. G. Iacobini, D. Battistel, K. McKelvey, A. W. Colburn, M. E. Newton, J. V. Macpherson and P. R. Unwin, *Angew. Chem. Int. Ed.*, 2012, 51, 7002-7006.

103. A. Correia and S. Machado, *Electrochim. Acta*, 1998, 43, 367-373.

104. A. Suzuki, T. A. Ivandini, K. Yoshimi, A. Fujishima, G. Oyama, T. Nakazato, N. Hattori, S. Kitazawa and Y. Einaga, *Anal. Chem.*, 2007, 79, 8608-8615.

105. J. Weng, J. Xue, J. Wang, J. Ye, H. Cui, F. Sheu and Q. Zhang, *Adv. Funct. Mater.*, 2005, 15, 639-647.

106. F. Shang, L. Zhou, K. A. Mahmoud, S. Hrapovic, Y. Liu, H. A. Moynihan, J. D. Glennon and J. H. Luong, *Anal. Chem.*, 2009, 81, 4089-4098.

107. T. Watanabe, Y. Honda, K. Kanda and Y. Einaga, *physica status solidi (a)*, 2014, 211, 2709-2717.

108. Z. J. Ayres, A. J. Borrill, J. C. Newland, M. E. Newton and J. V. Macpherson, *Anal. Chem.*, 2015, 88, 974-980.

109. L. A. Hutton, J. G. Iacobini, E. Bitziou, R. B. Channon, M. E. Newton and J. V. Macpherson, *Anal. Chem.*, 2013, 85, 7230-7240.

110. J. A. Bennett, J. Wang, Y. Show and G. M. Swain, *J. Electrochem. Soc.*, 2004, 151, E306-E313.

111. A. N. Patel, S.-y. Tan, T. S. Miller, J. V. Macpherson and P. R. Unwin, *Anal. Chem.*, 2013, 85, 11755-11764.

112. D. S. Knight and W. B. White, *J. Mater. Res.*, 1989, 4, 385-393.

113. S. Prawer and R. J. Nemanich, *Phil. Trans. R. Soc. A*, 2004, 362, 2537-2565.

114. S. Wang, V. M. Swope, J. E. Butler, T. Feygelson and G. M. Swain, *Diamond Relat. Mater.*, 2009, 18, 669-677.

115. H. Notsu, I. Yagi, T. Tatsuma, D. A. Tryk and A. Fujishima, *J. Electroanal. Chem.*, 2000, 492, 31-37.

116. I. Duo, C. Levy-Clement, A. Fujishima and C. Comninellis, *J. Appl. Electrochem.*, 2004, 34, 935-943.

117. H. Notsu, T. Fukazawa, T. Tatsuma, D. A. Tryk and A. Fujishima, *Electrochem. Solid-State Lett.*, 2001, 4, H1-H3.

118. H. Girard, N. Simon, D. Ballutaud, M. Herlem and A. Etcheberry, *Diamond Relat. Mater.*, 2007, 16, 316-325.

119. F. Liu, J. Wang, B. Liu, X. Li and D. Chen, *Diamond Relat. Mater.*, 2007, 16, 454-460.

120. S. Sque, R. Jones and P. Briddon, *Physical review B*, 2006, 73, 085313.

121. D. Takeuchi, H. Kato, G. Ri, T. Yamada, P. Vinod, D. Hwang, C. Nebel, H. Okushi and S. Yamasaki, *Appl. Phys. Lett.*, 2005, 86, 21031-21033.

122. B. M. Nichols, J. E. Butler, J. N. Russell and R. J. Hamers, *J. Phys.Chem. B*, 2005, 109, 20938-20947.

123. F. Maier, M. Riedel, B. Mantel, J. Ristein and L. Ley, *Phys. Rev. Lett.*, 2000, 85, 3472-3475.

124. A. Härtl, E. Schmich, J. A. Garrido, J. Hernando, S. C. Catharino, S. Walter, P. Feulner, A. Kromka, D. Steinmüller and M. Stutzmann, *Nat. Mater.*, 2004, 3, 736-742.

125. M. D. Porter, T. B. Bright, D. L. Allara and C. E. Chidsey, *J. Am.Chem.Soc.*, 1987, 109, 3559-3568.

126. D. K. Schwartz, *Annu. Rev. Phys. Chem.*, 2001, 52, 107-137.

127. R. E. Ruther, Q. Cui and R. J. Hamers, *J. Am.Chem.Soc.*, 2013, 135, 5751-5761.

128. A. L. Eckermann, D. J. Feld, J. A. Shaw and T. J. Meade, *Coord. Chem. Rev.*, 2010, 254, 1769-1802.

129. K. Kerman, D. Ozkan, P. Kara, B. Meric, J. J. Gooding and M. Ozsoz, *Anal. Chim. Acta*, 2002, 462, 39-47.

130. M. Wang, C. Sun, L. Wang, X. Ji, Y. Bai, T. Li and J. Li, *J. Pharm. Biomed. Anal.*, 2003, 33, 1117-1125.

131. S. E. Creager and K. G. Olsen, *Anal. Chim. Acta*, 1995, 307, 277-289.

132. J. J. Gooding, F. Mearns, W. Yang and J. Liu, *Electroanalysis*, 2003, 15, 81-96.

133. C. E. D. Chidsey, *Science*, 1991, 251, 919-922.

134. L. Tender, M. T. Carter and R. W. Murray, *Anal. Chem.*, 1994, 66, 3173-3181.

135. B. Ulgut and H. D. Abruna, *Chem. Rev.*, 2008, 108, 2721-2736.

136. P. Gründler, A. Kirbs and L. Dunsch, *ChemPhysChem*, 2009, 10, 1722-1746.

137. A. P. Abbott and N. E. Durling, *Phys. Chem. Chem. Phys.*, 2001, 3, 579-582.

138. P. Gründler, *In-situ Thermoelectrochemistry*, Springer Berlin Heidelberg, 2015.

139. S. R. Jacob, Q. Hong, B. A. Coles and R. G. Compton, *J. Phys. Chem. B*, 1999, 103, 2963-2969.

140. W. Ruther, J. Mcmahon and C. Melendres, *Apparatus for high temperature in situ laser Raman spectroelectrochemical studies of metal corrosion and passivation in aqueous environments*, Argonne National Lab., IL (USA), 1986.

141. L. Curtiss, J. Halley, J. Hautman, N. Hung, Z. Nagy, Y. J. Rhee and R. Yonco, *J. Electrochem. Soc.*, 1991, 138, 2032-2040.

142. R. G. Compton, B. A. Coles and F. Marken, *Chem. Commun.*, 1998, 2595-2596.

143. F. Marken, U. K. Sur, B. A. Coles and R. G. Compton, *Electrochim. Acta*, 2006, 51, 2195-2203.

144. F. Marken, S. L. Matthews, R. G. Compton and B. A. Coles, *Electroanalysis*, 2000, 12, 267-273.

145. P. Gründler and A. Kirbs, *Electroanalysis*, 1999, 11, 223-228.

146. P. Gründler, O. Frank, L. Kavan and L. Dunsch, *ChemPhysChem*, 2009, 10, 559-563.

147. P. Gründler, *Fresenius. J. Anal. Chem.*, 1998, 362, 180-183.

148. B. Miller, *J. Electrochem. Soc.*, 1983, 130, 1639-1640.

149. J. Valdes and B. Miller, *J . Phys. Chem.*, 1989, 93, 7275-7280.

150. C. Gabrielli, M. Keddam and J.-F. Lizee, *J. Electroanal. Chem. Interfacial Electrochem.*, 1983, 148, 293-297.

151. P. Gründler, T. Zerihun, A. Kirbs and H. Grabow, *Anal. Chim. Acta*, 1995, 305, 232-240.

152. F. Wachholz, J. Gimsa, H. Duwensee, H. Grabow, P. Gründler and G. U. Flechsig, *Electroanalysis*, 2007, 19, 535-540.

153. Y. V. Pleskov and Z. Rotenberg, *J. Electroanal. Chem. Interfacial Electrochem.*, 1978, 94, 1-4.

154. R. P. Akkermans, M. F. Suárez, S. L. Roberts, Q. Fulian and R. G. Compton, *Electroanalysis*, 1999, 11, 1191-1202.

155. J. F. Smalley, L. Geng, S. W. Feldberg, L. C. Rogers and J. Leddy, *J. Electroanal. Chem.*, 1993, 356, 181-200.

156. M. R. Mahoney and R. P. Cooney, *J. Phys. Chem.*, 1983, 87, 4589-4591.

157. R. Von Gutfeld, E. Tynan, R. Melcher and S. Blum, *Appl. Phys. Lett.*, 1979, 35, 651-653.

158. P. Chen and R. L. McCreery, *Anal. Chem.*, 1996, 68, 3958-3965.

159. T. Zerihun and P. Gründler, *J. Electroanal. Chem.*, 1996, 404, 243-248.

160. F. Marken, Y.-C. Tsai, A. J. Saterlay, B. A. Coles, D. Tibbetts, K. Holt, C. H. Goeting, J. S. Foord and R. G. Compton, *J. Solid State Electrochem.*, 2001, 5, 313-318.

161. M. A. Ghanem, H. Hanson, R. G. Compton, B. A. Coles and F. Marken, *Talanta*, 2007, 72, 66-71.

162. Y. C. Tsai, B. A. Coles, R. G. Compton and F. Marken, *Electroanalysis*, 2001, 13, 639-645.

163. J. Wang, G. U. Flechsig, A. Erdem, O. Korbut and P. Gründler, *Electroanalysis*, 2004, 16, 928-931.

164. A. H. Yang, K. Hsieh, A. S. Patterson, B. S. Ferguson, M. Eisenstein, K. W. Plaxco and H. T. Soh, *Angew. Chem.*, 2014, 126, 3227-3231.

165. C. Lau, S. Borgmann, M. Maciejewska, B. Ngounou, P. Gründler and W. Schuhmann, *Biosens. Bioelectron.*, 2007, 22, 3014-3020.

166. P. Gründler and L. Dunsch, *J. Solid State Electrochem.*, 2015, 19, 23-29.

167. B. C. Janegitz, R. A. Medeiros, R. C. Rocha-Filho and O. Fatibello-Filho, *Diamond Relat. Mater.*, 2012, 25, 128-133.

168. M. Li, G. Zhao, R. Geng and H. Hu, *Bioelectrochemistry*, 2008, 74, 217-221.

169. F. Montilla, E. Morallon, I. Duo, C. Comninellis and J. Vazquez, *Electrochim. Acta*, 2003, 48, 3891-3897.

170. S. Hrapovic, Y. Liu and J. H. Luong, *Anal. Chem.*, 2007, 79, 500-507.

171. L. A. Hutton, M. E. Newton, P. R. Unwin and J. V. Macpherson, *Anal. Chem.*, 2011, 83, 735-745.

172. E. A. McGaw and G. M. Swain, *Anal. Chim. Acta*, 2006, 575, 180-189.

173. R. Narayan, *Diamond-based materials for biomedical applications*, Elsevier, 2013.

174. S. Q. Lud, M. Steenackers, R. Jordan, P. Bruno, D. M. Gruen, P. Feulner, J. A. Garrido and M. Stutzmann, *J. Am.Chem.Soc.*, 2006, 128, 16884-16891.

175. P. E. Colavita, B. Sun, K.-Y. Tse and R. J. Hamers, *J. Am.Chem.Soc.*, 2007, 129, 13554-13565.

176. R. E. Ruther, M. L. Rigsby, J. B. Gerken, S. R. Hogendoorn, E. C. Landis, S. S. Stahl and R. J. Hamers, *J. Am.Chem.Soc.*, 2011, 133, 5692-5694.

177. H. Uetsuka, D. Shin, N. Tokuda, K. Saeki and C. E. Nebel, *Langmuir*, 2007, 23, 3466-3472.

178. S. Griveau, D. Mercier, C. Vautrin-Ul and A. Chaussé, *Electrochem. Commun.*, 2007, 9, 2768-2773.

179. D. Shin, B. Rezek, N. Tokuda, D. Takeuchi, H. Watanabe, T. Nakamura, T. Yamamoto and C. Nebel, *physica status solidi (a)*, 2006, 203, 3245-3272.

180. T. C. Kuo, R. L. McCreery and G. M. Swain, *Electrochem. Solid-State Lett.*, 1999, 2, 288-290.

181. S. Szunerits and R. Boukherroub, *J. Solid State Electrochem.*, 2008, 12, 1205-1218.

182. C. P. Andrieux and J. Pinson, *J. Am.Chem.Soc.*, 2003, 125, 14801-14806.

183. W. Yang, S. E. Baker, J. E. Butler, C.-s. Lee, J. N. Russell, L. Shang, B. Sun and R. J. Hamers, *Chem. Mater.*, 2005, 17, 938-940.

184. S. Szunerits, C. E. Nebel and R. J. Hamers, *MRS Bull.*, 2014, 39, 517-524.

185. W. Yang, O. Auciello, J. E. Butler, W. Cai, J. A. Carlisle, J. E. Gerbi, D. M. Gruen, T. Knickerbocker, T. L. Lasseter and J. N. Russell, *Nat. Mater.*, 2002, 1, 253-257.

186. D. Meziane, A. Barras, A. Kromka, J. Houdkova, R. Boukherroub and S. Szunerits, *Anal. Chem.*, 2011, 84, 194-200.

187. J. E. Field, *The Properties of Natural and Synthetic Diamond*, Academic Press London, 1992.

Chapter 2: Experimental

2.1 Materials and chemicals

2.1.1 CVD diamond

All the BDD samples used in this thesis are provided by Element Six Ltd., Ascot, UK, and synthesised using MPCVD. Details of diamond samples are listed in Table 2.1.

Table 2.1: List of diamond materials used in this thesis

Code	Type	[B] (atoms cm^{-3})	Thickness (μm)
MR14	BDD	3×10^{20}	630
MR11	BDD	3×10^{20}	200
	All diamond macrostructure	3×10^{20} in BDD region	500
	All diamond microstructure	3×10^{20} in BDD region	500

2.1.2 Chemicals

All solutions were prepared using Milli-Q water (resistivity 18.2 MΩ cm at 25 °C) and all reagents were used as received. pH measurements were carried out using a pH meter (PHM201 portable pH meter, Radiometer, Copenhagen, Denmark). Table 2.2 provides a list of the chemicals, formula, purity and suppliers used in this thesis.

Table 2.2: List of chemicals

Chemicals	formula	Purity	supplier
Ruthenium (III) hexaamine chloride	$Ru(NH_3)_6Cl_3$	98%	Acros Organics
Potassium hexachloroiridate (III)	K_3IrCl_6	98%	Sigma-Aldrich
Potassium ferricyanide (III)	$K_3[Fe(CN_6)]$	99%	Sigma-Aldrich
Potassium hexacyanoferrate (II) trihydrate	$K_4[Fe(CN_6)]\cdot 3H_2O$	≥98.5%	Sigma-Aldrich
Ruthenium (II) hexaamine chloride	$Ru(NH_3)_6Cl_2$	> 99%	Acros Organics
Potassium hexachloroiridate (IV)	K_2IrCl_6	98%	Sigma Aldrich
Potassium nitrate	KNO_3	99 %	Sigma-Aldrich
Lead (II) nitrate	$Pb(NO_3)_2$	99.99 %	Sigma-Aldrich
Dopamine hydrochloride	$C_8H_{12}NO_2Cl$	98%	Sigma-Aldrich
Potassium phosphate monobasic	KH_2PO_4	≥99.0%	Sigma-Aldrich
Potassium phosphate dibasic	K_2HPO_4	≥98%	Sigma-Aldrich
Potassium chloride	KCl	≥99.0%	Sigma-Aldrich
Concentrated sulfuric acid	H_2SO_4	≥95%	Sigma-Aldrich
6-(Ferrocenyl)hexanethiol	$C_{16}H_{22}FeS$	97%	Sigma-Aldrich
1-Pentanethiol	$C_5H_{12}S$	98%	Sigma-Aldrich
Ethanol	C_2H_6O	≥99.5%	Sigma-Aldrich
10-N-Boc-Amino-dec-1-ene	$C_{15}H_{29}NO_2$	N/A	Fluorochem Limited
Hydrochloric acid	HCl	35%	Sigma-Aldrich
1,4-Dixoane	$C_4H_8O_2$	99.8%	Sigma-Aldrich
Methanol	CH_3OH	99.8%	Sigma-Aldrich
Chloroform	$CHCl_3$	≥99%	Sigma-Aldrich

Ammonium hydroxide solution	NH_4OH	28%	Sigma-Aldrich
Sulphosuccinimidyl-4-(N-maleimidomethyl)cyclohexane-1-carboxylate	$C_{16}H_{17}N_2NaO_9S$	N/A	Sigma-Aldrich
Trifluoroacetic acid	CF_3CO_2H	>98%	Sigma-Aldrich
Dichloromethane	CH_2Cl_2	>99.8%	Sigma-Aldrich

2.1.3 Deoxyribonucleic acid

Both probe and target strand deoxyribonucleic acid (DNA) oligonucleotides were synthesized and provided by Dr. Robert Johnson, University of Utah, US. The surface (probe) strand is modified at the 3′ end (Figure 2.1a) with a thiol group, whilst the target strand is modified at the 5′ end (Figure 2.1b) with methylene blue (MB) redox mediator. Double stranded DNA (dsDNA) is anti-parallel, which means, once the probe DNA is immobilized, the 5′ MB redox mediator is close to the electrode surface after hybridisation. The NDA sequence information is listed below:

Probe DNA: 5′-CTACGCCACCAGCTCCA-Y-3′

Target DNA: 3′-GATGCGGTGGTCGAGGT-X-5′

where Y and X represent the thiol and MB modifications, respectively.

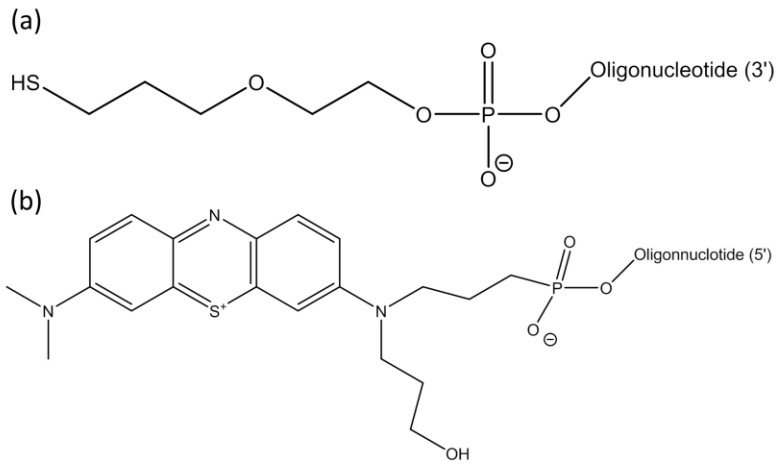

Figure 2.1: Structures of the modified (a) 3′ thiol group on the probe DNA and (b) 5′ MB group on the target DNA.

2.2 Electrode preparation

2.2.1 BDD disk preparation

1 mm diameter BDD disks (for the fabrication of glass sealed BDD electrode) and 5 mm × 5 mm BDD squares (for surface functionalisation) were cut from a MR14 diamond wafer using a laser micromachiner (wavelength: 355 nm, E-355H-3-ATHI-O system, Oxford Lasers, UK) at 100 % power, 20 kHz. The amorphous carbon formed during the laser cutting process was removed by boiling in concentrated sulphuric acid supersaturated with KNO_3 for 30 mins. BDD samples were then boiled in concentrated sulphuric acid only for another 30 minutes to remove any remaining KNO_3 salt, followed by sonication in distilled (DI) water for 15 mins. The resulting surface of BDD was oxygen terminated. Preparation of hydrogen terminated BDD will be discussed in section 2.4.5.

Ohmic contact was achieved by sputtering (E606 sputter/evaporator, Moorfields, UK) Ti (10 nm)/Au (300 nm) on the back (nucleation side) of the BDD samples, followed by annealing at 500 $^{\circ}$C for 4 hours, during which titanium carbide is formed.

2.2.2 Fabrication of BDD macroelectrode

2.2.2.1 Glass sealed BDD electrode

Back contacted BDD disks were sealed in a borosilicate glass capillary (i.d. 1.16 mm, o.d. 2 mm, Harvard Apparatus Ltd., UK) under vacuum. Electrical contact was made using a copper wire with silver epoxy (RS Components Ltd., Northants, UK) in contact with the BDD/Au surface. The end of the glass capillary was then polished using carbimet grit paper to expose the BDD surface. Finally, epoxy resin (Araldite, Bostik Findley, UK) was placed around the top of the capillary to fix the copper wire in position.[1]

2.2.2.2 BDD electrode for atomic force microscopy measurement

BDD electrode for atomic force microscopy (AFM) measurement was prepared in a slightly different way. A 1 mm diameter back contacted BDD disk and a Cu wire were mounted on a quartz slide which has been sputtered with Ti/Au using silver epoxy. Epoxy resin was employed to seal all the exposed areas (sputtered quartz slide, edges of BDD disk) except the 1 mm diameter BDD electrode.[2]

2.2.3 Laser heated electrochemical cell[3]

Laser heated electrochemical cell used in chapter 3 was fabricated using the following procedures. A 9 mm diameter MR11 disk BDD was laser machined from

the wafer, and back contacted in the same way described in section 2.2.1. In order to perform electrochemical measurements during pulsed heating, a custom-built electrochemical cell was designed and fabricated in-house, illustrated in Figure 2.2a. The cell comprised two parts, a Teflon container and a Perspex window, held together with nylon screws. The Perspex window contained a hole in the centre, across which the BDD disk was mounted (inside face) and held in place with adhesive Kapton tape (stable up to 1000 °C, R.S. Components Ltd., UK). The electrode area exposed to solution was reduced, also using Kapton tape, which contained a laser micromachined circular hole, 1 mm in diameter. A conductive track was made from the annealed Ti/Au contact on the back face of the BDD electrode (which is not in contact with solution) using silver conductive paint (R.S. Components Ltd., UK) to the top of the Perspex window, where electrical contact was made with a crocodile clip. All diamond macro- and micro- structures for laser heating experiments were prepared in the same way, and were used in chapter 4 and 5, respectively.

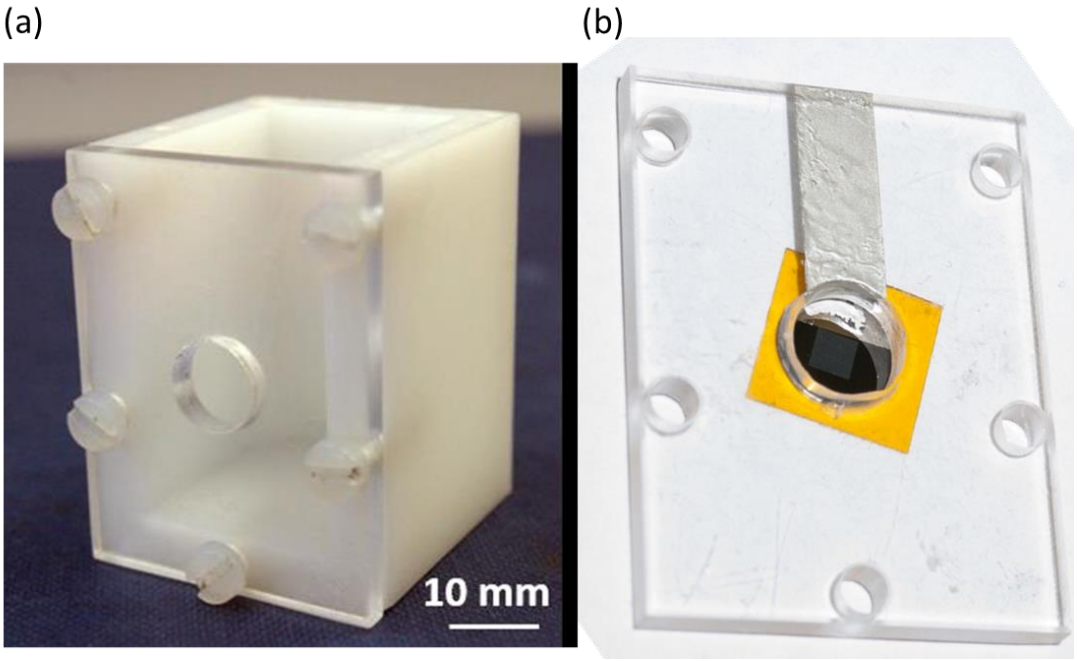

Figure 2.2: (a) Laser heated electrochemical cell; the Perspex window is secured on the Teflon cell using nylon screws. (b) 9 mm diameter BDD is mounted on the perspex window, and the electrode area is defined using a patterned Kapton mask. A conducting track is made at the back of diamond to make electrical contact.

2.3 Electrochemical measurements

Electrochemical measurements were made using either a CHI potentiostat (CH Instruments Inc., US), or an Ivium Compactstat (Ivium Technologies, Netherlands). A Pt gauge and either an Ag/AgCl or a saturated calomel electrode (SCE) were employed as the counter and reference electrodes, respectively.

2.3.1 Isothermal electrochemical cell

Isothermal experiments were carried out using a jacketed water bath, where the electrochemical cell, including all electrodes and solution, is placed. The electrochemical cell temperature was varied between 20 and 80 $^{\circ}$C. Open circuit

potential (OCP) measurements were carried out to determine the temperature coefficient, β,

$$\beta = \frac{\partial OCP}{\partial T} \tag{2.1}$$

for different redox couples employed. For OCP measurements two separate solutions, one held in ambient condition the other at elevated temperature, were employed. The two solutions were connected with a saturated KNO_3 salt bridge. Two conducting glass-sealed 1 mm diameter macrodisk BDD electrodes were placed in the separate solutions and connected via a high impedance digital voltmeter. OCPs were recorded as a function of the temperature difference, ΔT, between the two solutions.

2.3.2 Pulsed laser heating set-up

A diode laser (LM-D0296, LIMO, Germany) 914.7 nm, 3.8 kW cm^{-2}, was used for all pulsed temperature experiments, controlled by a laser diode controller (LDC1000, Laser Electronics Ltd., Lincolnshire, UK). The delivery lens focused the laser to a 1 mm diameter central circular spot on the back face of the BDD electrode. A dual-channel function generator (AFG3022B, Tektronix, US) was used as a master controller to ensure that the potentiostat and laser were synchronised when triggered. For macroelectrode experiments in chapters 3 and 4, the Ivium Compactstat was employed. For the microelectrode experiment in chapter 5, as the requirement for data sampling rate was increased due to the slow scan rate, the CV data was collected using a data acquisition (DAQ, NI USB-6211, UK) card controlled with custom LABVIEW code. For the majority of experiments in chapter 3 the CV potential scan rate was fixed at 100 mV s^{-1} (0.25 mV step potential). For

microelectrode experiments in chapter 5, the CV potential scan rate was fixed at 10 mV s^{-1} (0.01 mV step potential). Laser power density, P_d was varied between 0.3 and 3.8 kW cm^{-2}.

2.3.3 Temperature pulsed voltammetry

For the majority of experiments in chapters 3 and 5, cyclic voltammetry (CV) was performed simultaneously with pulsed laser heating *i.e.* temperature pulse voltammetry (TPV). For all TPV experiments the basic premise is the imposition of a pulsed laser to heat the surface of the electrode during CV measurements. In CV, for a chosen scan rate and potential step, the number of data points per second are defined by scan rate/potential step and the time between potential steps is given by (number of data points)$^{-1}$. For the CV experiments described herein the current is sampled immediately after each potential step. In TPV, the temperature pulse is superimposed on top of the CV and the current recorded, as shown schematically in Figure 2.3.

For the experiments in chapter 3 the laser was switched on and the electrode heated for 10 ms, and then switched off for 90 ms, with the cycle continuously repeated. For typical experimental parameters of 100 mV s^{-1} and 0.25 mV potential steps, current values were collected every 2.5 ms, with a total of 400 data points per second. For the microelectrode experiments in chapter 5, the laser was switched on for 10 ms and switched off for 990 ms. A 10 mV s^{-1} scan rate and 0.01 potential step was employed, so current values were collected every 1 ms and a total of 1000 data points per second were collected.

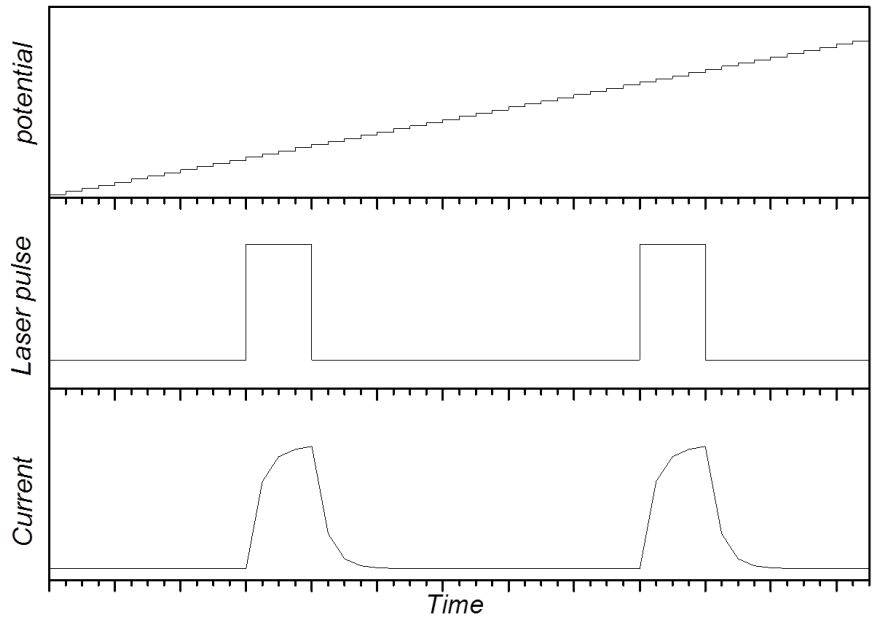

Figure 2.3: Schematic graphs showing the time dependence of (a) voltage steps taken by the digital potentiostat, (b) applied laser pulses and (c) change in current measured as a result of laser heating.

2.3.4 Differential pulse voltammetry[4]

Differential pulse voltammetry (DPV) is employed to minimise the influence of non-faradic process by applying a potential pulse during potential scan. The currents are recorded just before and at the end of each potential pulse, and the subtraction of two currents is recorded and plotted as a function of potential. Parameters, such as pulse amplitude, pulse width and period can be tuned to maximise the current response. DPV is typically used as a technique to improve the limit of detection (LOD) of species in the solution. Figure 2.4 illustrates the DPV technique.

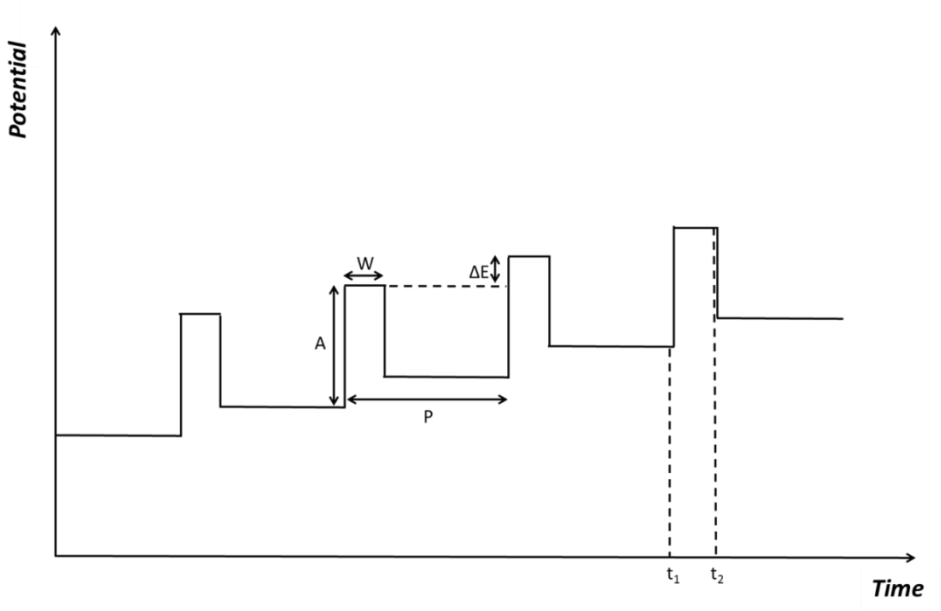

Figure 2.4: Schematic of DPV. A and W are the potential pulse amplitude and width, respectively. P is the period, and ΔE is the potential step for each potential pulse. t_1 and t_2 are the time when the current data are collected.

2.4 Instrumentation and techniques

2.4.1 Field emission scanning electron microscopy

Field emission scanning electron microscopy (FE-SEM) is a technique to probe surface composition and structure information by employing a focused electron beam scanning across the surface of interest.[5] An accelerating voltage (0-30 kV) is employed to generate the high energy electron beam and the interactions between electron and surface result in several types of signals, including backscattered electrons and secondary electrons. The former is obtained due to the elastic scattering of the incident electrons. Backscattered electrons are sensitive to surface composition as the intensity of backscattering electron is a function of the atomic number of the atom. The latter is more sensitive to surface structure and

topographical information, and images can be collected by an in-lens detector and a secondary electron (SE2) detector.

The in-lens detector is located in the same direction of the electron gun, so secondary electrons are collected with high efficiency and images can be obtained with high contrast. Therefore an in-lens detector is employed to characterise grain structures on the BDD surface. The SE2 detector is used to analyse surface topographical information. For example, nanoparticles (NPs) on BDD surface can be easily revealed by the SE2 detector.[6]

2.4.2 Energy-dispersive X-ray spectroscopy

Energy-dispersive X-ray (EDX) spectroscopy is equipped with the FE-SEM instrument, and employs either a focused high energy beam of charged particles such as electrons and protons or a beam of X-rays, to obtained localised element analysis and chemical characterisation due to the unique atomic structure of each element.[7] The high energy beam excites an electron in an inner shell, and at the same time creates an electron hole. Therefore, an electron from the outer high energy shell will transit to the inner shell to fill the hole, releasing X-rays. The energy and amount of X-rays is collected by an EDX spectrometer, illustrated in Figure 2.5. EDX spectroscopy provides element analysis as the energy of the emitted X-ray is the characteristic of the energy difference between two shells in a specific element.

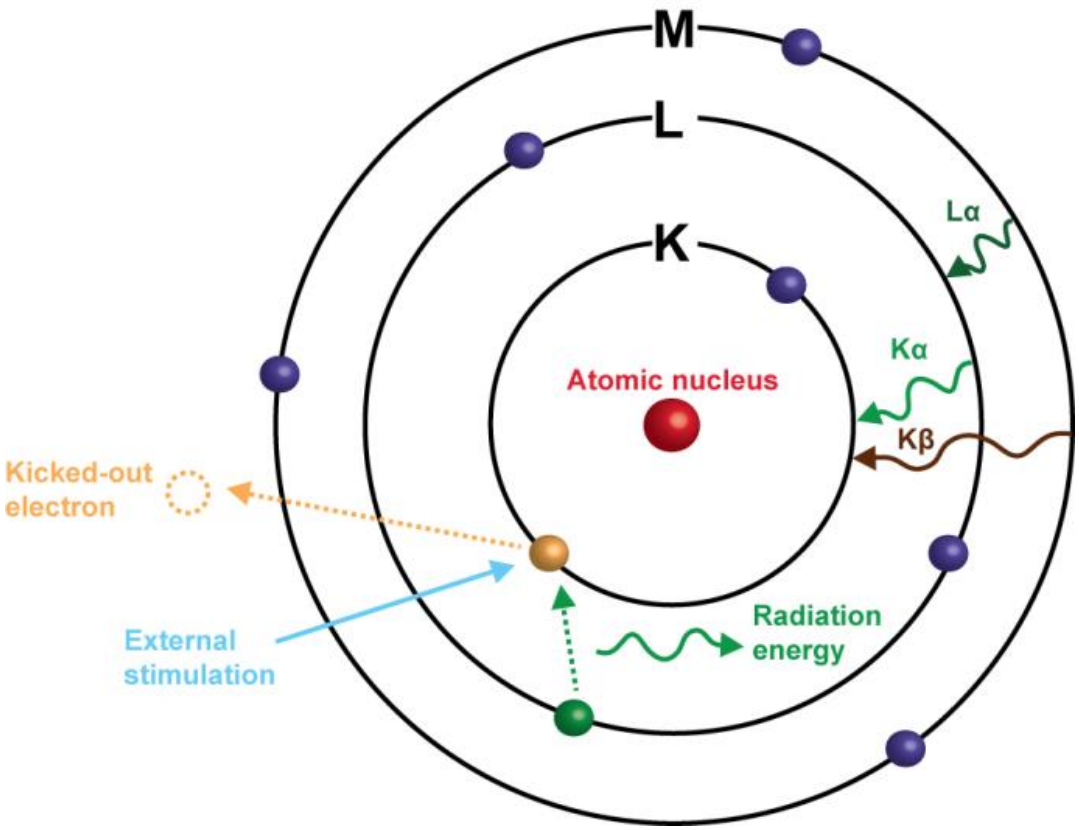

Figure 2.5: Principle of EDX. Electrons were kicked out by external high energy beam, outer shell electrons transit to inner shell, emitting X-rays.

2.4.3 Electron backscatter diffraction[8]

The crystallographic orientation of a BDD microelectrode in chapter 5 was recorded on electron backscatter diffraction (EBSD) equipped Zeiss Sigma FE-SEM system. The measurement was carried out at a 20 kV accelerating voltage with the sample tilted at 70°. Data analysis was performed using an Aztec 3.1 (Oxford Instruments, UK). The crystallographic orientation of a BDD grain is identified by the ‘colour key’ triangle, where the three corners with red, green and blue represent the three basic facets. High-index facets are represented by a mixture of the three colours.

2.4.4 Atomic force microscopy

AFM is a useful scanning probe microscopy technique to probe nanoscale information on the surface.[9] A sharp tip, which is fixed at the free end of a cantilever, scans across the sample surface. The interaction between the tip end and the surface is reflected by the change of the cantilever motion, which is recorded by shining a laser at the back of the cantilever and collecting the information from a photodiode. Figure 2.6 shows the schematic of an AFM system.

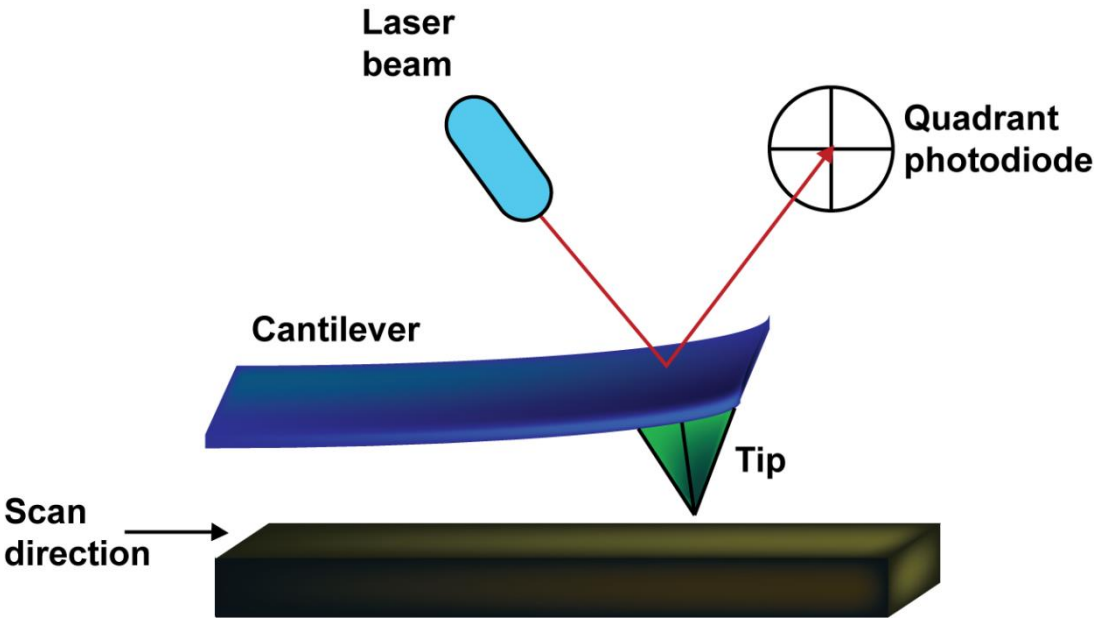

Figure 2.6: Schematic of AFM working principle. The tip scans across the surface. Laser is shone on the cantilever and reflected to the photodiode.

There are mainly two modes of AFM: contact mode and tapping mode. The former requires the tip to be 'dragged' across the surface and a constant force is maintained between the tip and the surface. The topographical information is measured by the deflection of the cantilever. For the tapping mode, the cantilever

oscillates at its resonant frequency, resulting in the tip oscillating when the tip is relatively 'far' away from the surface. The oscillating tip is then moved close to the surface, which affects the vertical oscillation of the tip. As the oscillating tip intermittently contacts the surface, an energy loss will be induced to the cantilever oscillation. The reduction in oscillation amplitude is used to probe surface features.

AFM measurements for the surface roughness of BDD in chapter 3 and for probing topographical information of metal/metal oxide deposits on BDD in chapter 4 were recorded *ex situ* in tapping mode using a Veeco Enviroscope AFM instrument (Bruker, UK). The size of the AFM image is typically limited to the micrometre range so it is useful as a probe of local topographical information. However, resolution in the *x*,*y* direction is controlled by the radius of curvature of the tip apex (typically ~ 10 - 200 nm), whilst *z* direction resolution is in the angstrom range.[9]

2.4.5 Contact angle measurements

A drop shape analyser is employed to distinguish the surface hydrophilicity,[10] *i.e.* if the diamond surface is hydrogen terminated or oxygen terminated. Surface functionality is of great importance, controlling not only the electrochemical response of redox mediators that are sensitive to surface chemistry (inner sphere) [11] but also subsequent modifications (chapter 6). A drop shape analyser (Krüss drop shape analyser system DSA100, Germany) was employed for all the contact angle measurements. The contact arises from the equilibrium between three phases: the solid phase (S), the liquid phase (L) and the gas phase (G). The contact angle was measured between the baseline, defined by the droplet solid interface, and the

tangent line for the ellipse fitted for the droplet shape profile, illustrated in Figure 2.7.

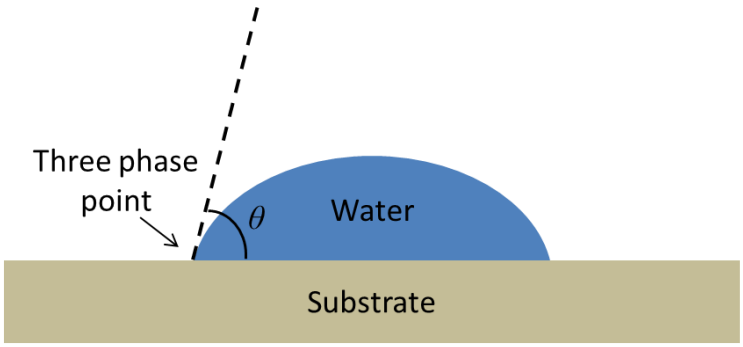

Figure 2.7: Schematic of contact angle measurements. Three phase point is the interface between water, solid and air, and θ is the contact angle.

2.5 References

1. L. Hutton, M. E. Newton, P. R. Unwin and J. V. Macpherson, *Anal. Chem.*, 2008, 81, 1023-1032.

2. L. A. Hutton, M. Vidotti, A. N. Patel, M. E. Newton, P. R. Unwin and J. V. Macpherson, *J. Phys. Chem. C*, 2010, 115, 1649-1658.

3. L. Meng, J. G. Iacobini, M. B. Joseph, J. V. Macpherson and M. E. Newton, *Faraday Discuss.*, 2014, 172, 421-438.

4. A. J. Bard and L. R. Faulkner, *Electrochemical methods: fundamentals and applications*, Wiley New York, 2001.

5. J. Goldstein, D. E. Newbury, P. Echlin, D. C. Joy, A. D. Romig Jr, C. E. Lyman, C. Fiori and E. Lifshin, *Scanning electron microscopy and X-ray microanalysis*, Springer Science & Business Media, 2012.

6. L. A. Hutton, M. E. Newton, P. R. Unwin and J. V. Macpherson, *Anal. Chem.*, 2011, 83, 735-745.

7. D. Shindo and T. Oikawa, *Energy Dispersive X-ray Spectroscopy*, Springer Japan, Tokyo, 2002.

8. A. J. Schwartz, M. Kumar, B. L. Adams and D. P. Field, *Electron backscatter diffraction in materials science*, Springer, 2009.

9. G. Binnig, C. F. Quate and C. Gerber, *Phys. Rev. Lett.*, 1986, 56, 930.

10. A. Marmur, *Soft Matter*, 2006, 2, 12-17.

11. M. C. Granger and G. M. Swain, *J. Electrochem. Soc.*, 1999, 146, 4551-4558.

Chapter 3: Laser heated boron doped diamond macroelectrode: effect of temperature on outer sphere electron transfer processes

Thermoelectrochemical experiments can reveal significant information about electrochemical processes compared to ambient only measurements. Typical thermoelectrochemistry is performed using resistively heated wires or laser heated electrodes, both of which can suffer drawbacks associated with the electrode material employed. Boron doped diamond (BDD) is ideal for thermoelectrochemical investigations due to its extremely high thermal conductivity and diffusivity, extreme resistance to thermal ablation (can withstand laser power densities, P_d, of GW cm^{-2} for nanosecond pulses) and excellent electrochemical properties (low background currents and wide potential window). In this chapter we describe the use of a pulsed laser technique to heat the rear of a 1 mm diameter conducting BDD disc electrode, which drives electrochemical solution reactions at the front face. Maximum average electrode temperatures of 90.0 ^{o}C were recorded experimentally and confirmed by finite element modelling (FEM). The effect of laser pulsed heating (maximum 3.8 kW cm^{-2}; 10 ms on and 90 ms off) on the cyclic voltammetric response of two fast (reversible) outer sphere electron transfer redox mediators ($Ru(NH_3)_6^{3+/2+}$ and $IrCl_6^{2-/3-}$) are investigated. In particular, we observe pulsed increases in the current, which increase with increasing P_d. The peak potential is shifted positively for the $Ru(NH_3)_6^{3+/2+}$ couple (in accordance with a positive temperature coefficient, β, +0.68 mV K^{-1}) and negatively for the $IrCl_6^{3-/2-}$ couple (β = - 0.48 mV K^{-1}). Scanning

backwards, in contrast to that observed for a macrodisc electrode in ambient solution, a cathodic peak is again observed for $Ru(NH_3)_6^{3+/2+}$ and an anodic peak for $IrCl_6^{3-/2-}$ couple. We attribute this response to the entropy of the redox reaction and the time-dependant change in mass transport due to the induced thermal gradients at the electrode/electrolyte interface. The observed responses are in qualitative agreement with FEM simulations.

3.1 Introduction

The effect of temperature, *T*, in electrochemistry is of great importance[1, 2] yet most electrochemical experiments are performed under ambient conditions. This is surprising since *T* plays a key role in determining the thermodynamics and kinetics of electron transfer processes,[3, 4] affects adsorption/desorption processes and double layer phenomena and is intrinsically linked to the mass transport properties of the system. It is also often the case that model systems proposed for real processes operating at elevated temperatures *e.g.* oxygen reduction reaction associated with fuel cells, are carried out under ambient conditions.[5, 6]

Thermoelectrochemistry[7] is the branch of electrochemistry where temperature is a controlled variable in the electrochemical experiment. The simplest means of controlling temperature is to use an isothermal approach, heating or cooling the system to the required temperature as appropriate. However, mass transport is often ill-defined due to uncontrolled thermal gradients in the solution, and systematically varying *T* is a slow process.[8] By moving to non-isothermal methodologies where heat is applied locally to the working electrode, a well-defined temperature gradient now exists at the electrode/electrolyte interface, meaning mass transport can be quantified in the system. It is also possible to heat and change the

temperature much faster by utilising short thermal pulses. Finally, the temperature at the electrode/electrolyte interface can be driven above the boiling point. As the electrode only sits at these elevated temperatures for brief periods of time, bubbling is avoided.

Different approaches to non-isothermal heating have been adopted[3] although the most popular in the literature are Joule heating and laser heating. In the former, the electrode can either be heated directly or indirectly, although the direct approach gives rise to the fastest thermal changes and is most widely used. Here the electrode is typically heated via application of an alternating current or radio frequency waves.[3] Thermal modulation by laser heating was proposed in 1975 by Barker and Gardner.[9] Since then laser heating using a pulsed laser has become a popular method of choice.[10-14] The lasers employed typically range in power densities, P_d, (mW cm^{-2} - GW cm^{-2}), wavelength (355 nm - 1064 nm) and pulse width (~10's of ps -10's of ms) and have been used to examine a variety of different temperature dependant electrochemical phenomena, ranging from electrode kinetics,[13, 14,15, 16] double layer structure elucidation[17] and surface cleaning.[10,18] Typically the laser is either focused onto the back face of the electrode[13, 14,18] or focused directly onto the front face, passing through solution[10,11,12,15] where energy will be lost, the amount dependant on the path length and absorption coefficient of solution. Local temperature increases typically vary from a few K to 500 K dependant on laser operation conditions.[12]

An important consideration in all thermoelectrochemical experiments is the geometrical arrangement and electrode material employed. Non-isothermal, Joule heated microwire electrodes have proven popular due to decreased Ohmic drop and higher rates of mass transport, compared to macroelectrodes.[3] In general, metal

electrodes such as Pt and Au are employed due to their high electrical and thermal conductivities. However, the electrode materials have limitations. For example, it has been shown that even after mild laser treatments (P_d > 1.5 W cm^{-2}) the metal electrodes roughen[11] and at high temperatures oxides form, making the material less inert, and electrochemical interpretation more complicated.[19] Furthermore, the usable potential region becomes narrower when the temperature increases, which for electrocatalytic materials such as Pt is especially a problem.[20] Glassy carbon electrodes have also been employed in both laser heated[21] and Joule heated experiments[22] but were not robust enough for high temperature electrochemistry. In some cases the electrode was even found to combust.[22]

Boron doped diamond (BDD) has emerged as an important electrode material due to its unique properties such as wide potential window, chemical and mechanical robustness and low background currents.[23] These arise from the electrochemical stability of the surface brought about by the sp^3 bonding configuration of this non-metallic material. Furthermore, large area free-standing polycrystalline BDD (pBDD) can now be grown using microwave plasma chemical vapour deposition (MW-CVD) techniques[24] making applications more widespread. As the boron doping level in diamond is increased, the resistivity decreases. The material becomes metal-like at B dopant concentrations > 1×10^{20} B atoms cm^{-3}.[23, 25] Crucially, BDD also possesses a very high thermal conductivity, *ca.* 600 W m^{-1} K^{-1} at 300 K,[26] for comparison the thermal conductivity of copper is *ca.* 400 W m^{-1} K^{-1}.[27] The thermal diffusivity of metallic pBDD is approximately 2 - 3 times higher than that of a metal; hence the entire electrode should rapidly attain a relatively uniform temperature, even when heated from the rear. Being mechanically robust, pBDD electrodes can be made very thin, and hence have a very low thermal mass. Thus high electrode

temperatures can be achieved with modest input powers. Diamond oxidises in air only if heated over *ca.* 700 °C.[28] Previous studies investigating laser damage to diamond have shown the laser damage threshold for intrinsic polished polycrystalline diamond to be typically in excess of 1.5 GW cm^{-2} for nanosecond (ns) pulses.[29]

In this chapter, given the notably favourable properties of conducting diamond, we examine the use of pBDD as an electrode material for thermoelectrochemical studies. In particular using pulsed laser heating methodology we examine the redox behaviour of two different fast electron transfer outer sphere redox species at a macrodisk pBDD electrode, in widely different potential ranges, under heated conditions.

3.2 Materials and methodology

3.2.1 Pulsed laser heating set-up

A 9 mm diameter disk of freestanding conducting pBDD synthesised by MW-CVD (boron dopant level ~ 3×10^{20} B atoms cm^{-3}), was grown by Element Six (Harwell, Oxford). The pBDD was removed from the growth substrate and polished (lapped) on both sides to give a surface finish of 1.25 ± 0.05 nm (measured over typical areas of 20 µm × 20 µm, *vide infra*). The resulting thickness of the electrode was 200 µm. The electrode was ohmically back contacted and the laser heated cell is fabricated in the same way as described in section 2.2.3, chapter 2. The experimental set-up is shown in Figure 3.1.

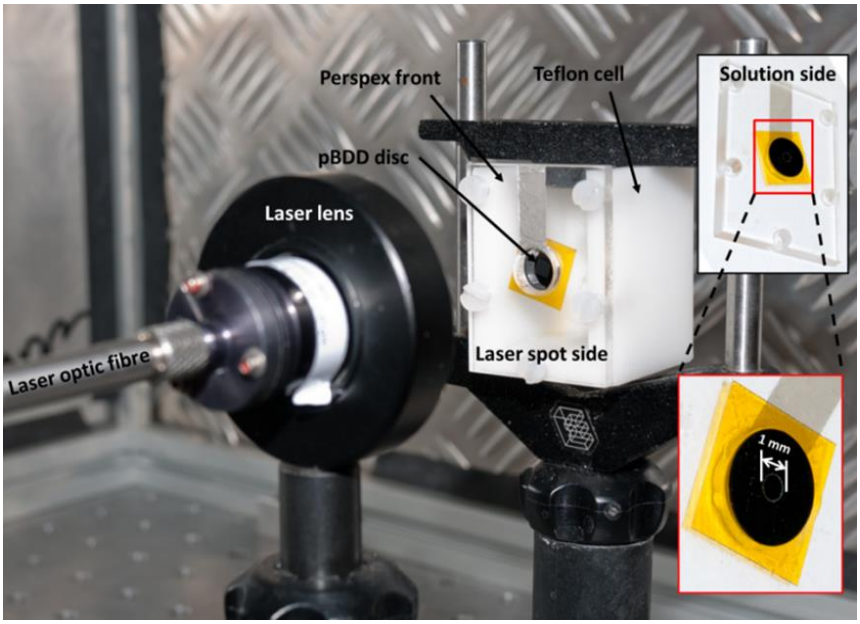

Figure 3.1: Photograph of the pulsed laser heating experimental set-up. The laser beam is focused by the laser lens onto the rear of the pBDD electrode held in the Perspex cell. Insets show the solution facing side of the electrochemical cell, detailing the black pBDD held in place with Kapton tape which also defines the active electrode area (1 mm disc).

3.2.2 Temperature pulsed voltammetry

In temperature pulsed voltammetry (TPV), the temperature pulse is superimposed on top of the CV and the current recorded, as shown schematically in Figure 2.3 in chapter 2. For the majority of experiments in this chapter the laser is switched on and the electrode heated for the shortest time possible, 10 ms, and then switched off for 90 ms, with the cycle continuously repeated. For typical experimental parameters of 100 mV s^{-1} and 0.25 mV potential step, current values are collected every 2.5 ms, with a total of 400 data points per second.

3.2.3 COMSOL simulations

A model for simulating the induced temperature profile upon application of the laser pulse as well as the effect of the fluctuating temperature on convection, diffusion and thermodynamics was carried out using COMSOL Multiphysics 4.3b (COMSOL, Sweden) finite element modelling (FEM) software. A *2D* geometry, shown in Figure 3.2 (not to scale) was built to describe the *2D* axisymmetric electrochemical cell. The model consists of the pBDD electrode, thickness 200 µm and 4.5 mm radius (domain a), mounted in Perspex (domain d), insulated with Kapton tape, thickness 100 µm, (domain b), which also defines the radius of the electrode (0.5 mm) in contact with solution (domain c). The radius and height of the modelled system is 12.5 mm. Each domain is occupied by material with a defined density (ρ), heat capacity (C_p), thermal conductivity (κ) and dynamic viscosity (μ), as detailed in Table 3.1. The pressure constraint point (P_{con}), which is necessary for the solved equations to have a unique solution, in Figure 3.2 was set to 1 atm. The location selected for this constraint was chosen such that the solution was not significantly perturbed. The boundary conditions are summarised in Table 3.2. In Table 3.2, P (W) and A (cm^2) represent the total boundary power and the active area and $\boldsymbol{n}$ is the unit normal vector. A no heat flux boundary condition is applied to boundary 2 (thermal insulator). No slip conditions were applied for boundaries 5 and 6. Gravity has an effect on the flow pattern of the fluid and thus a volume force (f_z) acting only in the *z*-dimension defined as

$$f_z = -\rho g \tag{3.1}$$

where g is the gravitational constant (~9.81 m s^{-2}), was employed.

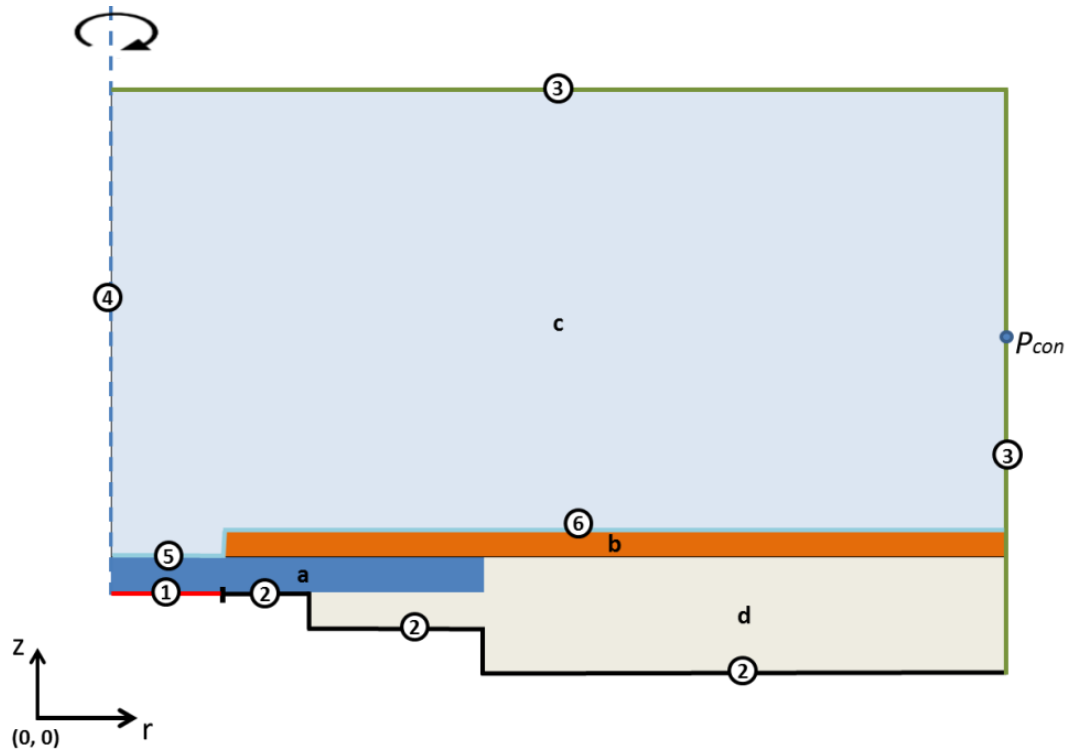

Figure 3.2: Schematic of the simulated geometry (not to scale) of the electrochemical cell consisting of pBDD (a), Kapton (b), water (c) and Perspex (d).

Heat transfer involves various mechanisms, such as thermal diffusion, thermal convection, thermal radiation, *etc*. These mechanisms often occur simultaneously in the system. Thermal diffusion of heat from a region of high temperature to low temperature is described by Equation 3.2, for both solids and liquids, where α_D, the thermal diffusivity ($m^2\ s^{-1}$) is given by Equation 3.3,

$$\frac{\partial T}{\partial t} = \alpha_D \nabla^2 T \tag{3.2}$$

$$\alpha_D = \frac{\kappa}{\rho C_p} \tag{3.3}$$

where t (s) represents time, and ∇^2 is the Laplace operator.

Table 3.1: Summary of the properties for the different domains used for the simulation of temperature at the diamond electrode/electrolyte interface

	Diamond[1]	Kapton[2]	Perspex[3]	Water[4]
Heat Capacity C_p (J kg^{-1} K^{-1})	$C_p = 3.2T - 473.6$ (275 K<T<500 K)	1090	1500	$12010-80.4\times T+0.310\times T^2-5.38\times10^{-4}\times T^3+3.63\times10^{-7}\times T^4$ (273.15 K<T<553.75K)
Density ρ (kg m^{-3})	3500	1420	1160	$838+1.40\times T-3.01\times10^{-3}\times T^2+3.72\times10^{-7}\times T^3$ (273.15 K<T<553.75K)
Thermal Conductivity κ (W m^{-1} K^{-1})	$-1.25T+1041.25$ (275 K<T<500 K)	0.12	50	$-0.869+8.95\times10^{-3}\times T-1.58\times10^{-5}\times T^2+7.98\times10^{-9}\times T^3$ (273.15 K<T<553.75K)
Dynamic Viscosity μ (Pa·s)	N/A	N/A	N/A	$1.38-2.12\times10^{-3}\times T+1.36\times10^{-4}\times T^2-4.65\times10^{-7}\times T^3+8.90\times10^{-10}\times T^4+9.08\times10^{-13}\times T^5+3.85\times10^{-16}\times T^6$ (273.15 K<T<413.15K)

[1]Manufacturer's data sheet (Element 6 Ltd.)

[2]Manufacturer's data sheet (R. S. Components Ltd.)

[3]Manufacturer's data sheet (Gilbert Curry Ltd.)

[4]Expression taken from COMSOL 4.3b software

Table 3.2: Summary of boundary conditions used for the simulation of temperature at the diamond electrode/electrolyte interface

Boundary	Boundary type	Equation
1	Boundary heat source	$-\boldsymbol{n}\cdot(-\kappa\nabla T)=P_d$ $P_d=\frac{P}{A}$
2	Thermal insulation	$-\boldsymbol{n}\cdot(-\kappa\nabla T)=0$
3	Ambient temperature	293.15 ^{o}C
4	Axis of symmetry	$\nabla T\cdot\boldsymbol{n}=0$
5, 6	No slip fluid boundary	$\boldsymbol{v}=0$
5	Butler Volmer kinetics	$k_f=k^0e^{\frac{-\alpha nF\left(E-\left(E^0+\beta\Delta T\right)\right)}{RT}}$ $k_b=k^0e^{\frac{(1-\alpha)nF\left(E-\left(E^0+\beta\Delta T\right)\right)}{RT}}$ $j=k_fC_{ox}-k_bC_{red}$

Convective flow of water in the system is treated as an incompressible flow of a Newtonian fluid which follows the Navier-Stokes equation, Equation 3.4,

$$\rho\left(\frac{\partial\boldsymbol{v}}{\partial t}+\boldsymbol{v}\cdot\nabla\boldsymbol{v}\right)=-\nabla p+\mu\nabla^2\boldsymbol{v}+f_z \tag{3.4}$$

where $\boldsymbol{v}$ (m s^{-1}) is the flow velocity, p (pa) is the pressure and ∇ is the grad operator.

A boundary heat source (boundary 1), reflecting P_d values in the range 0.3 kW cm^{-2} to 3.8 kW cm^{-2}, was employed to model the laser spot on the back of the diamond electrode. At t = 0 s, a laser pulse of 10 ms is applied to the centre of the electrode (1 mm in diameter), followed by 90 ms cooling time. The modelled temperature at the electrode electrolyte interface is the average temperature across the 1 mm diameter electrode surface.

Simulation of the effect of laser heating on TPV was performed by considering the effect of the temperature pulses and corresponding transient perturbations in T on the mass transport properties, kinetics and thermodynamics of the system, as described by Equations 3.5-3.8. Transport of dilute species in solution depends on convection, migration and diffusion. Migration was ignored due to the presence of excess supporting electrolyte (0.1 M KNO_3). In the fluid phase, the contribution of diffusion and convection is given by:

$$\frac{\partial C_i}{\partial t} = D_i \nabla^2 C_i - \boldsymbol{v} \nabla C_i \tag{3.5}$$

where D_i and C_i are the diffusion coefficient and concentration of the species respectively. The effect of changing T on D_i was calculated using the Stokes-Einstein equation:[30]

$$D_i = \frac{k_B T}{6\pi\mu r} \tag{3.6}$$

where k_B is the Boltzmann constant and r is the radius of the molecule. r for $Ru(NH_3)_6^{3+}$ was determined as 0.28 nm using Equation 3.6, and a literature value[31] for D at 298 K of 8.8×10^{-6} cm^2 s^{-1} and is assumed to be temperature independent. The T induced change in μ is accounted for in the water material characteristics, as described in Table 3.1.

Simple outer sphere electron transfer was modelled at the electrode/solution interface (boundary 5) using a modified Butler-Volmer kinetics. k_f and k_b are the reaction rates of the forward and back reactions respectively, which are derived from equation 1.3, 1.4, 1.6 and 1.7 in chapter 1.

$$k_f = k^0 e^{\frac{-\alpha n F\left(E-\left(E^0+\beta\Delta T\right)\right)}{RT}} \tag{3.7}$$

$$k_b = k^0 e^{\frac{(1-\alpha)nF\left(E-\left(E^0+\beta\Delta T\right)\right)}{RT}} \quad (3.8)$$

where α is the charge transfer coefficient, here assumed to be 0.5, E is the electrode potential, E_0 is the standard potential (-0.18 V *vs* SCE), R is the gas constant and ΔT is the change in temperature at the electrode/electrolyte interface.

3.3 Results and discussion

3.3.1 Temperature determination at the electrode/electrolyte interface

Verification of the time-dependant average temperature at the front face of the BDD electrode during the laser pulse experiments was made from both measurement of the OCP (Figure 3.3a) and thermal modelling (Figure 3.3b), described in section 3.2.3. β was calculated as -1.56 mV K^{-1} for $Fe(CN)_6^{3-}/Fe(CN)_6^{4-}$, from a plot of OCP versus ΔT (R^2 = 0.98) over the ΔT range of 40 °C. This value is in very good agreement with that determined previously, -1.6 mV K^{-1}.[34] With knowledge of β and the measured OCP, during laser heating, the corresponding interfacial electrode ΔT, versus time, t, behaviour can be determined; Figure 3.3 shows the OCP and ΔT data for a P_d of 0.6 kW cm^{-2}, 1.2 kW cm^{-2} and 3.2 kW cm^{-2} over a period of 90 ms (the laser is on for the first 10 ms). The data shows that during the laser pulse period, the temperature rises rapidly at the electrode surface. After the laser is turned off, the temperature decreases at a slower rate due to the lower value of thermal diffusivity for water, hindering heat transfer to bulk solution. For different P_d values in the range 0.3 kW cm^{-2} to 3.8 kW cm^{-2}, maximum T values at t_{10ms} at the electrode/electrolyte interface in the range 31.0 to 90.0 ^oC were

obtained. Specifically, 31.0 ^{o}C (0.3 kW cm^{-2}); 36.5 ^{o}C (0.6 kW cm^{-2}); 41.5 ^{o}C (0.9 kW cm^{-2}); 46.4 ^{o}C (1.2 kW cm^{-2}); 51.6 ^{o}C (1.6 kW cm^{-2}); 57.3 ^{o}C (1.9 kW cm^{-2}); 62.9 ^{o}C (2.2 kW cm^{-2}); 68.4 ^{o}C (2.5 kW cm^{-2}); 73.1 ^{o}C (2.9 kW cm^{-2}); 78.9 ^{o}C (3.2 kW cm^{-2}); 84.1 ^{o}C (3.5 kW cm^{-2}) and 90.0 ^{o}C (3.8 kW cm^{-2}). Figure 3.3b shows the ΔT profile determined from FEM simulations for a P_d of 0.6 kW cm^{-2}, 1.2 kW cm^{-2} and 3.2 kW cm^{-2} over 90 ms (the laser is on for the first 10 ms). Also given in the inset is a comparison of the recorded ΔT for the two methodologies; OCP (▪) and FEM modelling (•). As can be seen there is very good agreement between both methods of temperature determination. The employment of a higher P_d would allow even greater ΔT values to be reached.

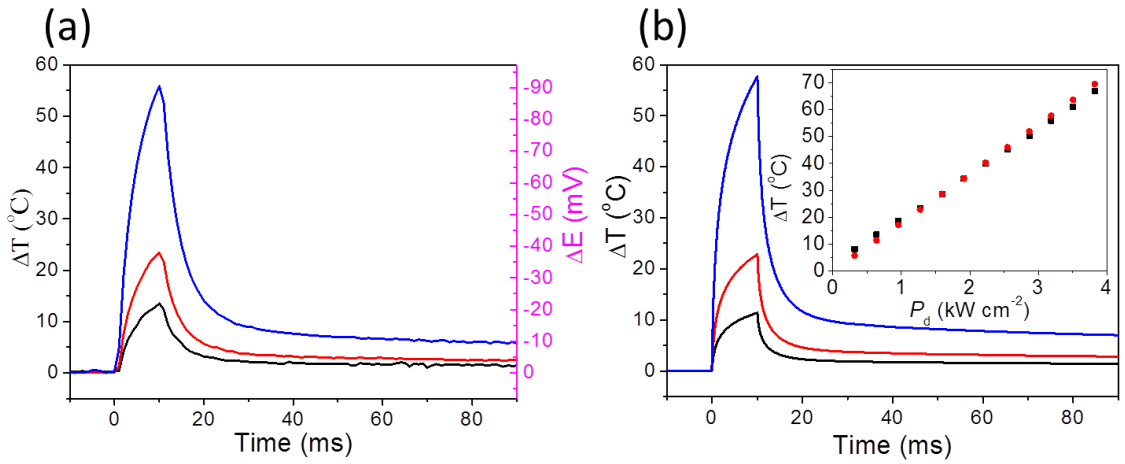

Figure 3.3: (a) OCP and associated temperature rise (ΔT) versus time for a 90 ms time period, recorded between a laser heated 1 mm diameter pBDD disc electrode and a 1 mm diameter pBDD disc electrode at ambient temperature (23 °C). Solution contained 0.5 mM $Fe(CN)_6^{4-}$ *and 0.5 mM* $Fe(CN)_6^{3-}$ *in 0.1 M* KNO_3*. The laser was pulsed at 0.6 kW* cm^{-2} *(black), 1.9 kW* cm^{-2} *(red) and 3.2 kW* cm^{-2} *(blue) for a 10 ms period and then switched off. The OCP data is converted to ΔT using the* $Fe(CN)_6^{4-}$ */* $Fe(CN)_6^{3-}$ *temperature coefficient = -1.56 mV* K^{-1}*. (b) Finite element modelled ΔT (at the electrode surface) of the laser heated pBDD electrode at* P_d *= 0.6 kW* cm^{-2} *(black), 1.9 kW* cm^{-2} *(red) and 3.2 kW* cm^{-2} *(blue). Insert shows maximum ΔT as a function of* P_d *for both experimental (black ■) and simulation (red ●).*

3.3.2 Temperature profile at the electrode surface

To visualise propagation of the thermal gradient through the pBDD electrode and into solution during the laser pulse as a function of time, thermal modelling was performed. Figure 3.4a shows the 2D temperature profile at t = 10 ms (*i.e.* at the end of the laser pulse) and Figure 3.4b shows the z axial temperature profile (the central axis of symmetry, r = 0) as a function of time, t = 0, 5, 10 and 20 ms for a P_d of (i) 1.2 kW cm^{-2} and (ii) 3.2 kW cm^{-2}, respectively. As Figure 3.4a shows, for both P_d

values, heat diffuses out from the laser heated zone hemispherically, diffusing much faster through the 200 μm thick pBDD than the surrounding solution, due to the higher thermal diffusivity of the conducting diamond. At both t = 5 ms and t = 10 ms (the end of the laser pulse), there is a small gradient in temperature through the BDD electrode which increases in absolute value as both P_d and t increases. The thermal gradient extends *ca.* 200 μm (1.2 kW cm^{-2}) and 230 μm (3.2 kW cm^{-2}) from the electrode surface into solution. At t = 20 ms, after the laser has been switched off for 10 ms, ΔT has decreased significantly in the electrode (with a uniform T obtained vertically through the pBDD). The water, however, as it retains heat more effectively, due to a higher C_p, has a higher T than that of the diamond (at a defined distance from the electrode) as the pBDD is able to cool itself more rapidly.

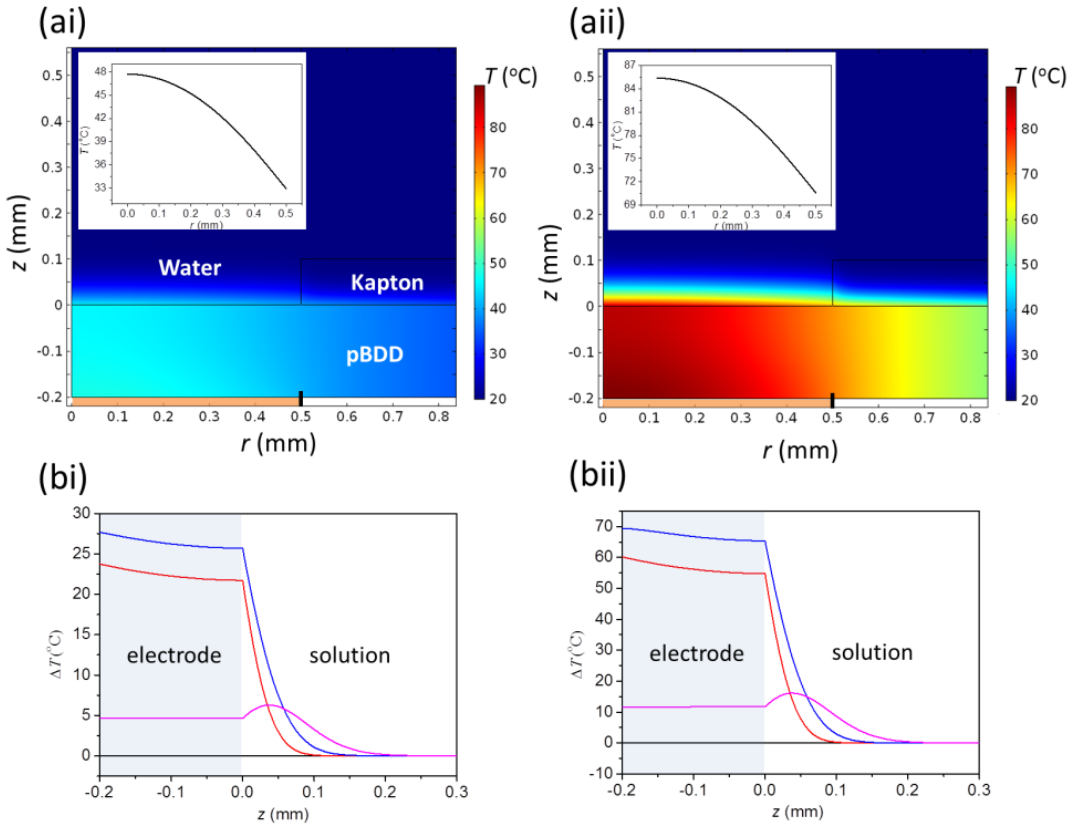

Figure 3.4: (a) 2D temperature profile at t = 10 ms and (b) z axial temperature profile through pBDD to solution at r = 0 mm for times of 0 ms (black), 5 ms (red), 10 ms (blue) and 20 ms (purple) at P_d of 1.2 kW cm^{-2} (i) and 3.2 kW cm^{-2} (ii). The insets to (a) show radial temperature profiles at z = 0 mm (electrode surface) at t = 10 ms. The laser heated boundary in (a) is marked by an orange band and occurs at z = -0.2 and 0 < r < 0.5.

3.3.3 Atomic force microscopy measurements of BDD surface before and after pulsed laser heating

With optical heating it is sensible to consider the laser damage threshold of the electrode material employed, especially as metallic pBDD absorbs very strongly at the wavelength (914 nm) of the diode laser employed herein. Previous studies indicate a laser damage threshold for intrinsic polycrystalline diamond typically to be in excess of 1.5 GW cm^{-2} for ns pulses,[29] which is far higher than the conditions

employed here. This is verified in Figure 3.5 which shows typical AFM images recorded in tapping mode at a scan rate of 20 µm s^{-1} before (a) and after (b) applying a P_d of 1.2 kW cm^{-2} (10 ms on, 90 ms off) for 120 cycles, typical to conditions employed herein. It can be seen from Figure 3.5a that the typical surface roughness of the pBDD electrode is 1.25 ± 0.05 nm before laser heating, compared to 1.3 ± 0.1 nm after. The AFM images in Figure 3.5 thus indicate no change in surface morphology at these modest heat fluxes. Note, this is in stark contrast to Pt electrodes which showed surface roughening with the electrode exposed to a P_d three orders of magnitude lower, for a similar timescale of exposure, but with ns laser pulses.[11] We are thus confident that much shorter and higher P_d pulses could be used in conjunction with BDD electrodes in order to establish significantly higher temperatures at the pBDD electrode/electrolyte interface.

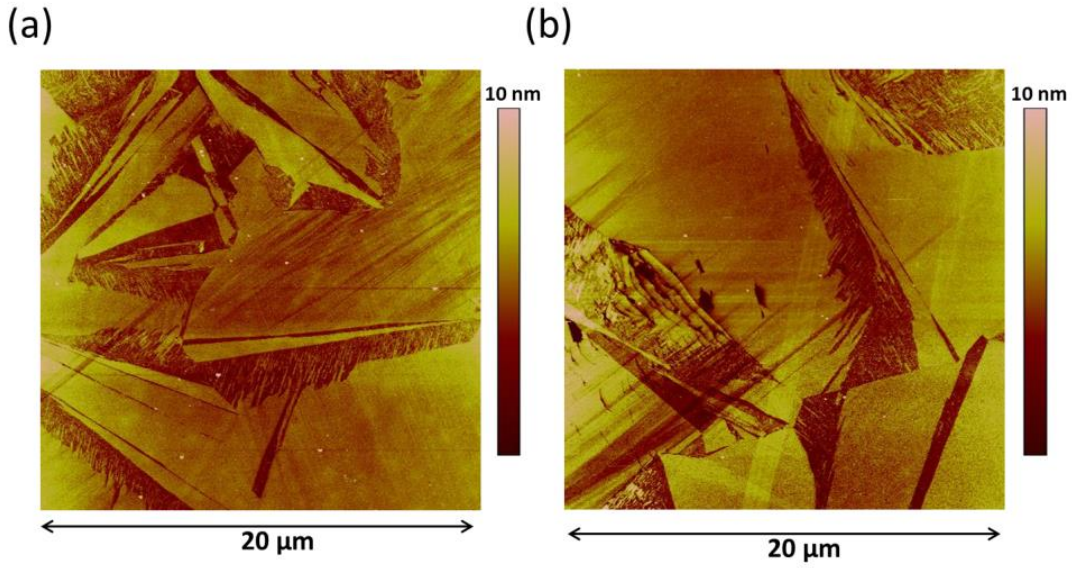

Figure 3.5: Typical tapping mode AFM images recorded at a scan rate of 20 µm s^{-1} before (a) and after (b) applying P_d of 1.2 kW cm^{-2} (10 ms on, 90 ms off) for 120 cycles.

3.3.4 Effect of temperature on non-Faradaic process

Initial experiments investigated the effect of pulsed temperature on the non-faradaic response of the electrode as a function of P_d (0, 0.6 kW cm^{-2}, 1.2 kW cm^{-2} and 3.2 kW cm^{-2}). Figure 3.6a shows the current-time response in 0.1 M KNO_3 with the electrode held at a constant potential of 0 V *vs* SCE for a P_d of 0.6 kW cm^{-2}, 1.2 kW cm^{-2} and 3.2 kW cm^{-2}, with an increased data sampling frequency of 1 kHz. The laser was pulsed on for 10 ms and off for 90 ms. Also shown is the current-time response (black square) under ambient conditions. It can be seen in Figure 3.6a that higher P_d and hence larger temperature changes produce bigger current transients. Figure 3.6b shows a zoomed out current-time trace recorded over 1 s. Each trace has a peak, which is associated with the laser pulse turning on and a reverse peak associated with the laser pulse turning off. The largest change in both cases occurs during the first ms and then the current transient decays.

Previous studies of the double layer using ns laser pulse techniques have shown that thermal heating leads to a virtually instantaneous restructuring of the double layer. The time constant of the data capture system employed herein is insufficient to probe such fast events, but still shows an effect. In particular, the current rise is associated with perturbation of the double layer resulting in a charging current, which decays with time in a similar fashion to a potential step experiment carried out under isothermal conditions. When the laser is turned off the temperature at the interface decreases to its original value, and due to restoration of the double layer, a current transient in the opposite direction is observed. The charge associated with the positive and negative current transients is approximately equal. For a P_d of 0.6 kW cm^{-2}, 1.2 kW cm^{-2} and 3.2 kW cm^{-2} , the charge transferred for both positive

and negative transients is 0.31 nC and 0.30 nC, 0.49 nC and 0.48 nC, 0.95 nC and 0.91 nC, respectively.

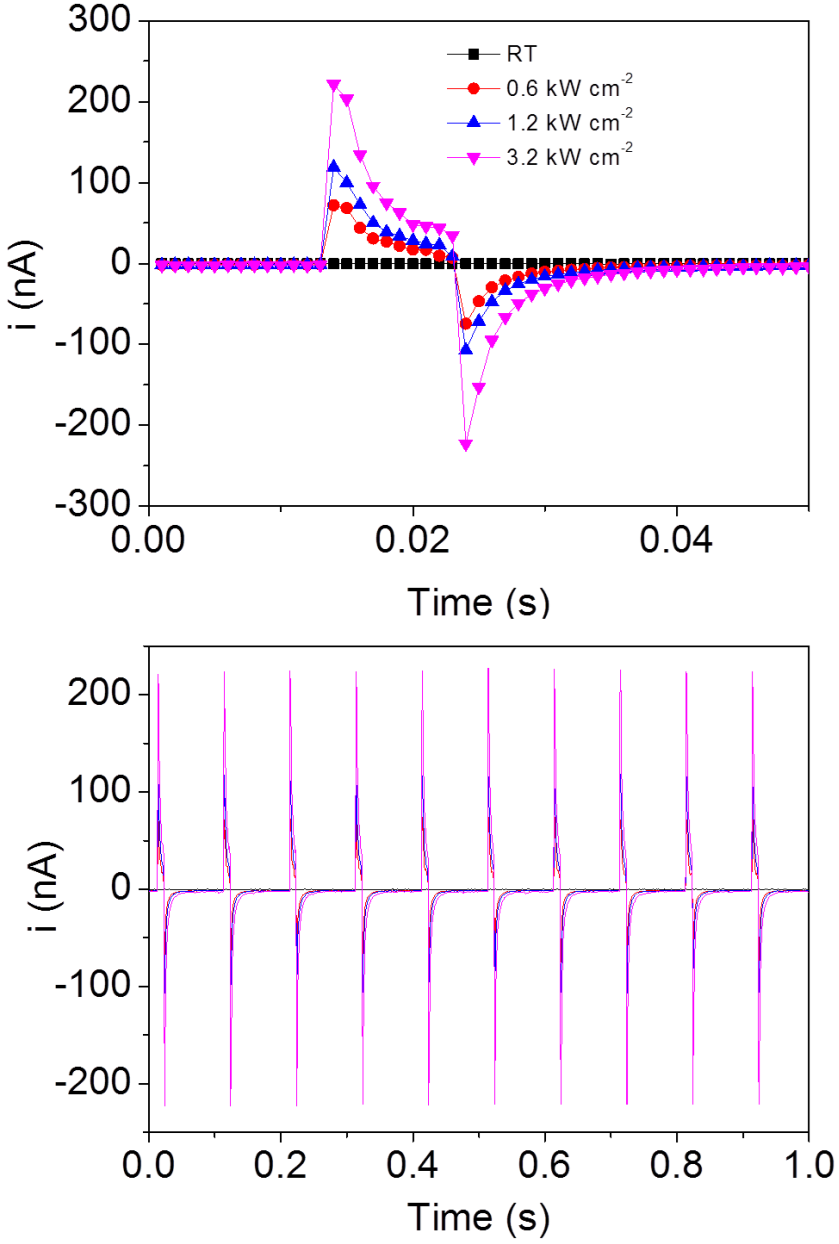

Figure 3.6: (a) Temperature pulsed chronoamperometry of pBDD in 0.1 M KNO_3 at room temperature (black ■) and P_d of 0 W cm^{-2} 0.6 kW cm^{-2} (red ●), 1.2 kW cm^{-2} (blue ▲), 3.2 kW cm^{-2} (purple ▼) at an applied potential of 0 V vs SCE. (b) Time-dependent current at the potential of 0 V vs SCE for a duration of 1 s.

3.3.5 Temperature pulsed voltammetry for the reduction of $Ru(NH_3)_6^{3+}$

Experiments investigating the effect of TPV on faradic processes were conducted by using a fast (reversible) one electron transfer outer sphere redox mediator, 1 mM $Ru(NH_3)_6^{3+}$ in 0.1 M KNO_3. Both experimental (i) and simulated (ii) TPVs are shown in Figure 3.7a and Figure 3.7b for the forward and backward scans, respectively, under temperature pulsed (P_d of 1.2 kW cm^{-2}, pulse on 10 ms, off 90 ms) conditions (red line). The ambient CV (black line) for $Ru(NH_3)_6^{3+}$ reduction and subsequent oxidation shows a peak-to-peak separation of 65 mV and a reductive peak current of 2.18 µA in accordance with that predicted using the Randles-Sevick equation, assuming an electrode diameter of 1 mm and D of 8.8 × 10^{-6} cm^2 s^{-1}.[31]

During TPV current spikes are obtained during laser heating, which decay during cooling, in a similar way to chronoamperometric transients produced during potential pulsing. A scan rate of 100 mV s^{-1} with a potential step of 0.25 mV is employed (sampling rate = 400 s^{-1}), resulting in 4 data points per laser pulse, where the last point records the largest current reading. Raw data is collected by the potentiostat (Figure 3.7a and b, red line) and then sampled by taking every 40^{th} point, resulting in the last sampling point during the laser pulse being plotted against potential. Figure 3.7c shows "sampled" TPV responses at P_d of 1.2 kW cm^{-2} (red line) and 2.5 kW cm^{-2} (green line).

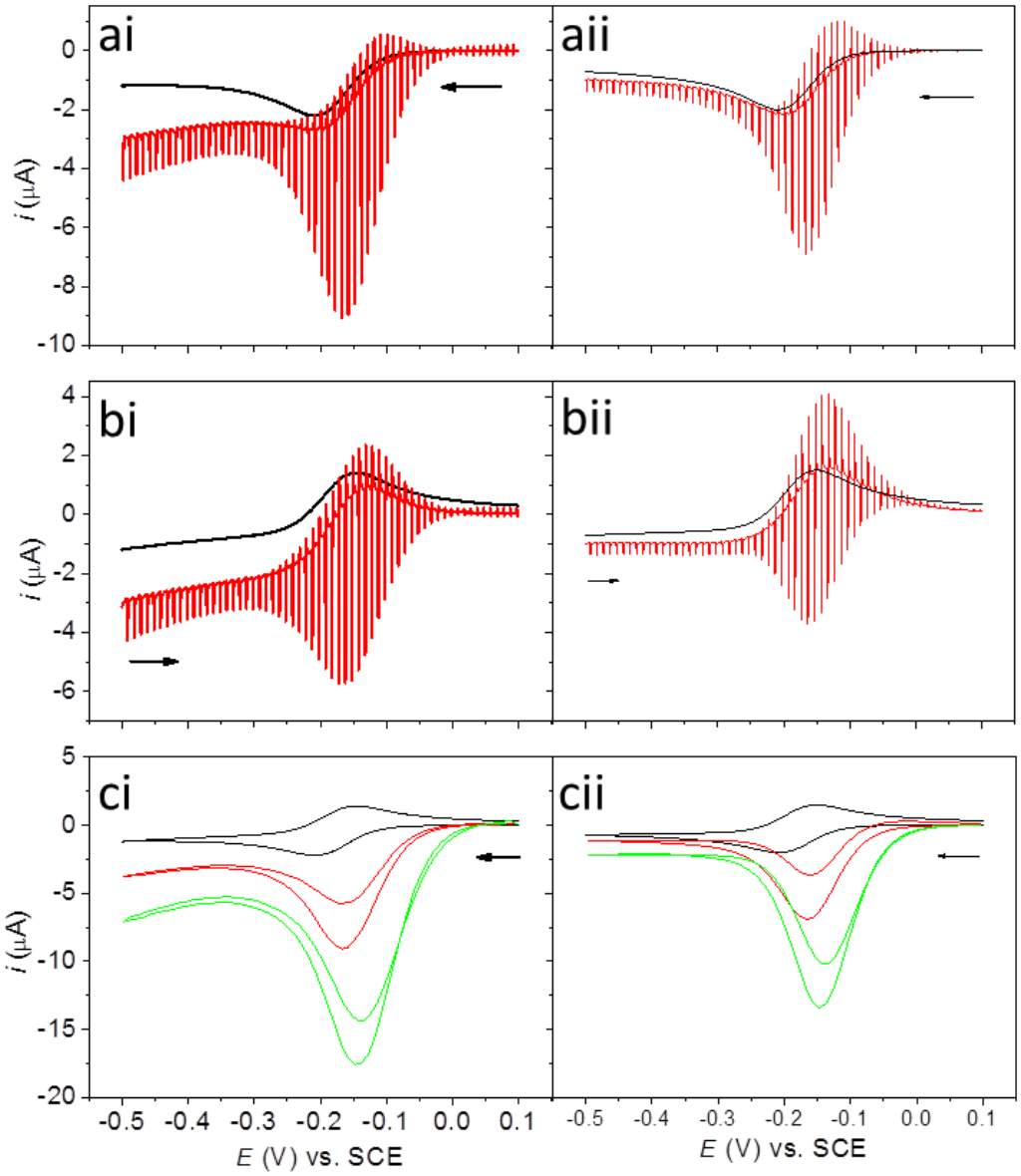

Figure 3.7: (i) Experimental and the (ii) simulated TPVs (red) at P_d of 1.2 kW cm^{-2} and ambient CV (black) recorded at a pBDD electrode in a solution containing 1 mM $Ru(NH_3)_6^{3+}$ in 0.1 M KNO_3 (a) forward scan and (b) backward scan at P_d of 1.2 kW cm^{-2}(red) and ambient CV (black). (ci) and (cii) "sampled" experimental and simulated TPVs at a P_d of 1.2 kW cm^{-2} (red), and 2.5 kW cm^{-2} (green), every 40th data point sampled. The CV recorded under ambient conditions (black) is not data sampled. Scan rate: 100 mV s^{-1}.

Three striking features are observed in the "data sampled" laser pulsed TPV, compared to the CV recorded under ambient condition; (1) the cathodic current for the forward scan increases as P_d increases. Specifically, the peak current has increased compared to that under ambient conditions by × 3.5 for 1.2 kW cm^{-2} and × 8.1 for 2.5 kW cm^{-2}. (2) The potential for the forward peak current shifts positively with increasing P_d (-0.168 V for 1.2 kW cm^{-2} and -0.148 V for 2.5 kW cm^{-2}) and; (3) a cathodic current is observed in magnitude for the backward scan, which increases in magnitude as the P_d is increased. β for the $Ru(NH_3)_6^{3+/2+}$ system, was calculated as +0.68 mV K^{-1} from a plot of OCP versus ΔT (R^2 = 0.99) over a ΔT range of 40 ^{o}C, shown in Figure 3.8, which is in close agreement with literature values.[11] From knowledge of β it is possible to calculate the change in entropy of the system, ΔS, through

$$\Delta S = nF\beta = 65.6 \text{ J K}^{-1}\text{mol}^{-1} \tag{3.9}$$

given n = 1.

The increase in cathodic (negative) current in the forward scan and observation of a cathodic current in the backward scan is due primarily to a combination of two factors, the entropy of the redox reaction and a change in mass transport due to the induced thermal gradient at the electrode/electrolyte interface. In these experiments, the temperature at the electrode/electrolyte interface is pulsed from ambient to hot repeatedly. Entropically, under steady-state conditions, a positive β indicates an additional cathodic current contribution to the ambient response (for both redox processes), near to the equilibrium potential.[35] Furthermore, the transient nature of the temperature increase also results in time-dependant

increases in mass transport, due to both diffusion and convective effects, which serves to enhance the current relative to ambient conditions.

By modelling all the contributions including temperature dependent E_o described in 3.2.3, qualitatively similar TPVs can be obtained, as shown in Figure 3.7ii. The small discrepancy between model and experimental is likely to be due to employment of a 2D axisymmetric model. This model does not account for the fact the laser strikes the electrode perpendicular to the direction of gravity, instead a computationally less time consuming parallel arrangement was assumed, which is likely to underestimate convective water flow effects. Figure 3.9 shows the Simulated TPV at P_d of 1.2 kW cm^{-2} at pBDD electrode for the reduction of 1 mM $Ru(NH_3)_6^{3+}$ for the (a) forward scan and (b) backward scan with (i) and without (ii) taking temperature dependent E_0 into consideration. It is clearly seen that β plays a crucial role in the temperature dependent electrochemical response of $Ru(NH_3)_6^{3+}$.

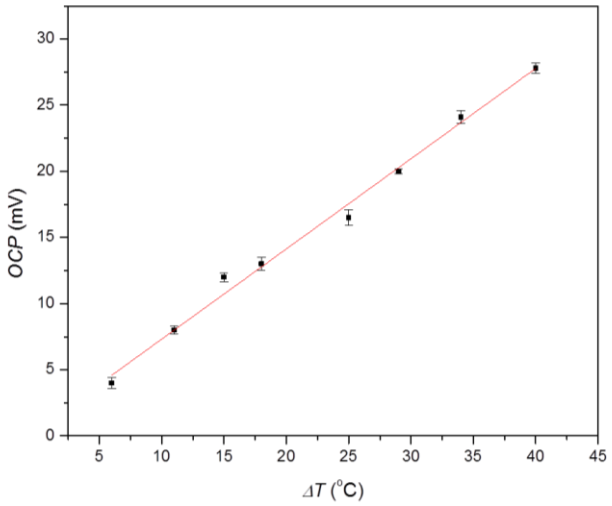

Figure 3.8: OCP as a function of ΔT between two identical 1 mm pBDD electrodes in 0.1 M KNO_3 solution containing 0.5 mM $Ru(NH_3)_6^{3+}$ and 0.5 mM $Ru(NH_3)_6^{2+}$. One of the pBDD electrodes was held at room temperature, while the other in a heated water bath.

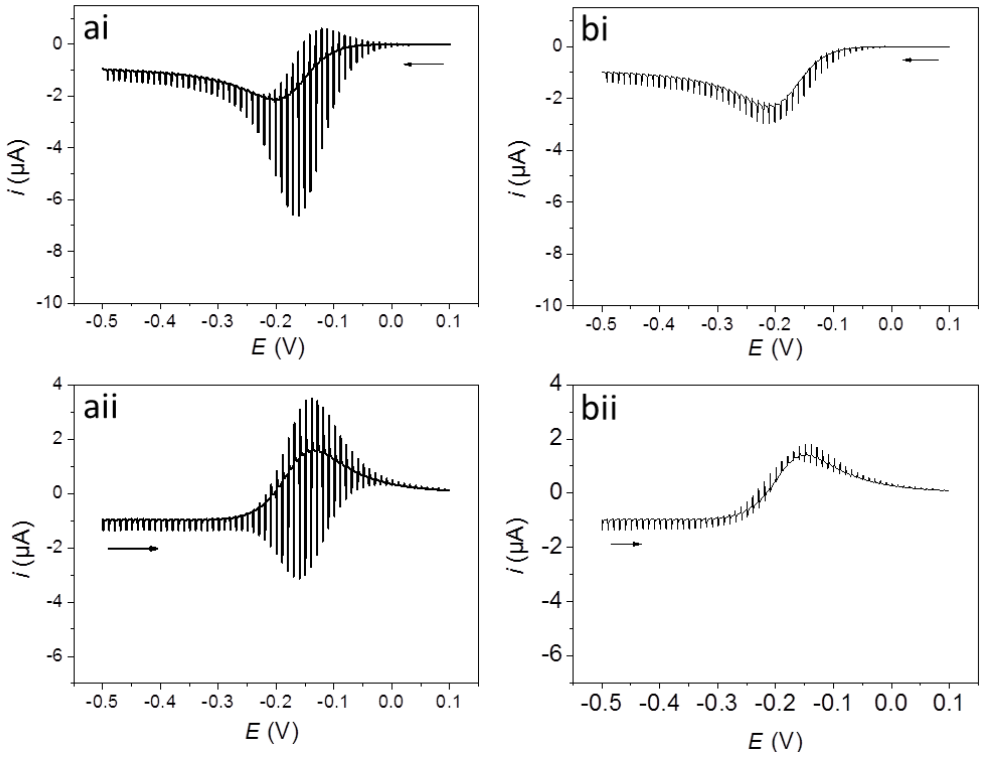

Figure 3.9: Simulated TPV at P_d of 1.2 kW cm^{-2} at pBDD electrode in 1 mM $Ru(NH_3)_6^{3+}$: (i) forward scan and (ii) backward scan with (a) and without (b) taking temperature dependent E_0 into consideration.

3.3.6 Temperature pulsed voltammetry for the oxidation of $IrCl_6^{3-}$

In order to further explore the effect of TPV on redox electrochemistry, another fast electron transfer (reversible) outer sphere redox mediator, $IrCl_6^{3-}$, was employed. Isothermal experiments gave a β value of -0.48 mV K^{-1} (R^2 = 0.99) for $IrCl_6^{3-/2-}$ (ΔS = -46.3 J K^{-1} mol^{-1}) recorded over a ΔT range of 35 ^oC, shown in Figure 3.10. Figure 3.11 shows a "data sampled" TPV (data collected as described for Figure 3.7c) for a pBDD electrode in a solution containing 1 mM $IrCl_6^{3-}$ in 0.1 M KNO_3, at a scan rate of 100 mV s^{-1} for P_d of 0.6 kW cm^{-2}, 1.2 kW cm^{-2}, 1.9 kW cm^{-2} and 2.5 kW cm^{-2}. Under ambient conditions the CV for $IrCl_6^{3-}$ oxidation and subsequent reduction shows a peak-to-peak separation of 70 mV and an oxidative peak current of 1.96 µA in agreement with Randles-Sevick predictions, assuming an electrode diameter of 1 mm and D of 7.5 × 10^{-6} cm^2 s^{-1}.[36] It can be seen in Figure 3.11 that (i) the anodic peak current for the forward scan increases as P_d increases; (ii) the potential for the forward peak current shifts negatively with increasing P_d, as expected for a negative β value (0.731 V for 0.6 kW cm^{-2}; 0.711 V for 1.2 kW cm^{-2}; 0.691 V for 1.9 kW cm^{-2}; and 0.681 V for 2.5 kW cm^{-2}) and; (iii) as P_d increases the "data sampled" back scan TPV shows a very small cathodic current at 0.6 kW cm^{-2}, which disappears at higher P_d, resulting in the observation of double peaked anodic currents at the two highest P_d values. The data shown is thus in qualitative agreement with that seen for the $Ru(NH_3)_6^{3+}$ TPV system (Figure 3.7).

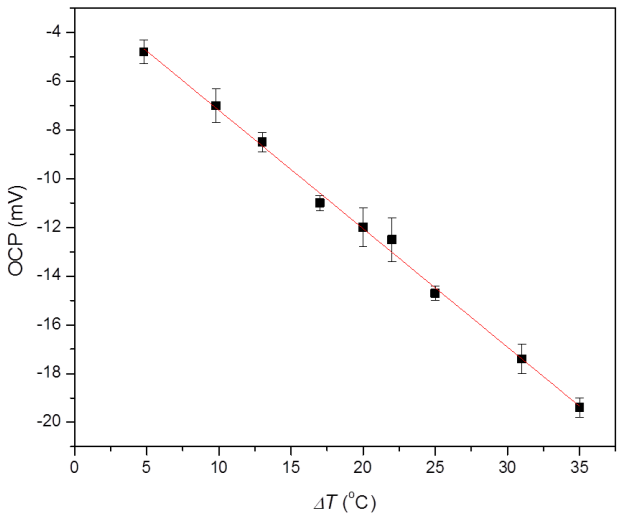

Figure 3.10: OCP as a function of ΔT between two identical 1 mm pBDD electrodes in 0.1 M KNO_3 solution containing 0.5 mM $IrCl_6^{3-}$ and 0.5 mM $IrCl_6^{2-}$. One of the pBDD electrodes was held at room temperature, while the other in a heated water bath.

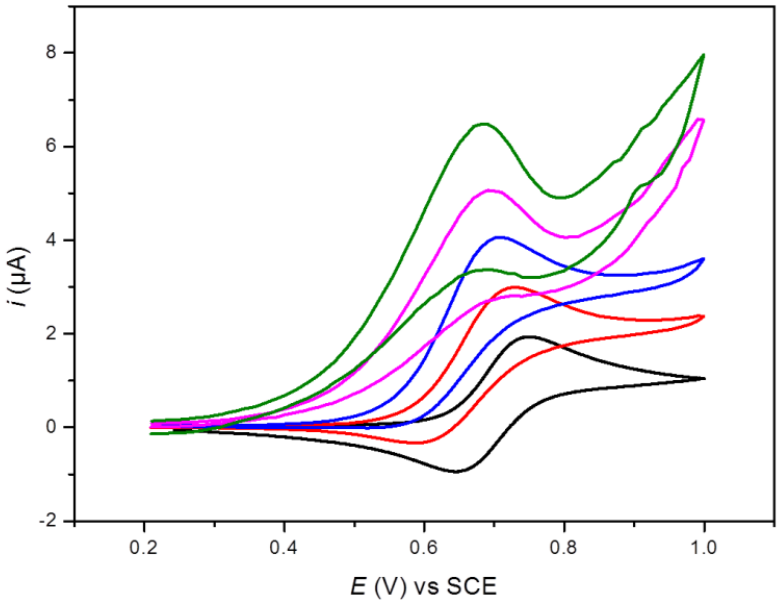

Figure 3.11: "Sampled" TPV using a pBDD electrode in a solution containing 1 mM $IrCl_6^{3-}$ in 0.1 M KNO_3, at P_d of 0.6 kW cm^{-2} (red), 1.2 kW cm^{-2} (blue) , 1.9 kW cm^{-2}(purple) and 2.5 kW cm^{-2} (green). Every 40^{th} data point is sampled. The CV recorded under ambient conditions (black) is not data sampled or subject to a laser pulse. Scan rate: 100 mV s^{-1}.

3.4 Conclusions

An electrochemical system combined with a pulsed laser setup is employed to examine the effect of temperature on the electrochemical response of pBDD electrodes. Conducting diamond is an ideal material for thermoelectrochemical studies due to its wide potential window, low background currents, very high thermal conductivity and diffusivity, mechanical robustness and ability to withstand P_d up to GW cm^{-2} without damage, for ns pulses. In these measurements, laser pulses of 10 ms duration (90 ms off) were delivered using a focused diode laser (maximum P_d 3.8 kW cm^{-2}) onto a ~ 1 mm spot on the rear side of a 200 μm thick pBDD electrode. The temperature attained at the pBDD electrode/electrolyte interface during this time period was assessed using both OCP measurements and FEM simulations; with both methods providing good agreement. A maximum temperature of 90.0 ^oC was achieved at the electrode/electrolyte interface using a P_d of 3.8 kW cm^{-2} for a heating time of 10 ms. Due to the high thermal diffusivity of pBDD, heat propagates into the electrode rapidly, without damage to the electrode surface, as evidenced by AFM. As diamond can withstand significantly greatly power densities, even higher temperatures can be attained quickly by moving to significantly higher power lasers.

Chronoamperometry measurements in supporting electrolyte were found to perturb the double layer, resulting in a positively peak-shaped charging current when the laser was on and restoration of the double layer, accompanied with a negative charging current, when the laser was turned off. The total charge transferred during the switch on and off periods was found to be approximately equal. In the presence of the fast electron transfer (reversible) outer sphere redox mediators, $Ru(NH_3)_6^{3+}$ (β

= +0.68 mV K^{-1}) and $IrCl_6^{3-}$ (β = -0.48 mV K^{-1}), TPV resulted in chronoamperometric-like current increases during the CV which enhanced the forward peak current, increasing with increasing P_d. The peak potentials were shifted positively for $Ru(NH_3)_6^{3+/2+}$ and negatively for $IrCl_6^{3-/2-}$, compared to the CV recorded under ambient conditions, in accordance with their entropic positive and negative β values, respectively. Scanning backwards cathodic ($Ru(NH_3)_6^{3+/2+}$) and anodic ($IrCl_6^{3-/2-}$) peaked current response were also observed (leading to the observation of a double peak). FEM showed striking qualitative agreement with the experimental data obtained and differences are most likely due to constraints imposed due to technical limitations of the approach used. pBDD is thus a promising electrode material for high temperature thermoelectrochemical measurements.

3.5 References

1. C. G. Ubah and E. Asselin, *ECS Trans.*, 2009, 19, 3-20.

2. J. Zhang, Z. Xie, J. Zhang, Y. Tang, C. Song, T. Navessin, Z. Shi, D. Song, H. Wang and D. P. Wilkinson, *J. Power Sources*, 2006, 160, 872-891.

3. P. Gründler, A. Kirbs and L. Dunsch, *ChemPhysChem*, 2009, 10, 1722-1746.

4. C. L. Forryan and R. G. Compton, *Phys. Chem. Chem. Phys.*, 2003, 5, 4226-4230.

5. S. H. Joo, S. J. Choi, I. Oh, J. Kwak, Z. Liu, O. Terasaki and R. Ryoo, *Nature*, 2001, 412, 169-172.

6. K. Gong, F. Du, Z. Xia, M. Durstock and L. Dai, *Science*, 2009, 323, 760-764.

7. P. V. Rysselberghe, *Electrochemical Affinity: Studies in Electrochemical Thermodynamics and Kinetics*, Paris, 1955.

8. G. G. Wildgoose, D. Giovanelli, N. S. Lawrence and R. G. Compton, *Electroanalysis*, 2004, 16, 421-433.

9. G. Barker and A. Gardner, *J. Electroanal. Chem. Interfacial Electrochem.*, 1975, 65, 95-100.

10. E. Hershenhart, R. L. McCreery and R. D. Knight, *Anal. Chem.*, 1984, 56, 2256-2257.

11. R. P. Akkermans, M. F. Suárez, S. L. Roberts, Q. Fulian and R. G. Compton, *Electroanalysis*, 1999, 11, 1191-1202.

12. J. L. Brennan and R. J. Forster, *J. Phys. Chem. B*, 2003, 107, 9344-9350.

13. J. F. Smalley, C. Krishnan, M. Goldman, S. W. Feldberg and I. Ruzic, *J. Electroanal. Chem. Interfacial Electrochem.*, 1988, 248, 255-282.

14. J. F. Smalley, S. W. Feldberg, C. E. Chidsey, M. R. Linford, M. D. Newton and Y. P. Liu, *J. Phys. Chem.*, 1995, 99, 13141-13149.

15. A. Yamakata, T. Uchida, J. Kubota and M. Osawa, *J. Phys. Chem. B*, 2006, 110, 6423-6427.

16. T. Hinoue, R. Harui, T. Izumi, I. Watanabe and H. Watarai, *Anal. Sci.*, 1995, 11, 1-8.

17. V. Climent, B. A. Coles and R. G. Compton, *J. Phys. Chem. B*, 2002, 106, 5988-5996.

18. T. Hinoue, N. Kuwamoto and I. Watanabe, *J. Electroanal. Chem.*, 1999, 466, 31-37.

19. M. R. Mahoney and R. P. Cooney, *J. Phys. Chem.*, 1983, 87, 4589-4591.

20. P. Gründler, A. Kirbs and T. Zerihun, *Analyst*, 1996, 121, 1805-1810.

21. F. Qiu, R. G. Compton, F. Marken, S. J. Wilkins, C. H. Goeting and J. S. Foord, *Anal. Chem.*, 2000, 72, 2362-2370.

22. P. Gründler, T. Zerihun, A. Möller and A. Kirbs, *J. Electroanal. Chem.*, 1993, 360, 309-314.

23. L. A. Hutton, J. G. Iacobini, E. Bitziou, R. B. Channon, M. E. Newton and J. V. Macpherson, *Anal. Chem.*, 2013, 85, 7230-7240.

24. R. Balmer, J. Brandon, S. Clewes, H. Dhillon, J. Dodson, I. Friel, P. Inglis, T. Madgwick, M. Markham and T. Mollart, *J. Phys.: Condens. Matter*, 2009, 21, 3-5.

25. J. P. Lagrange, A. Deneuville and E. Gheeraert, *Diamond Relat. Mater.*, 1998, 7, 1390-1393.

26. J. E. Field, *The properties of natural and synthetic diamond*, Academic Press London, 1992.

27. K. Yoshida and H. Morigami, *Microelectron. Reliab.*, 2004, 44, 303-308.

28. P. John, N. Polwart, C. Troupe and J. Wilson, *Diamond Relat. Mater.*, 2002, 11, 861-866.

29. R. Sussmann, G. Scarsbrook, C. Wort and R. Wood, *Diamond Relat. Mater.*, 1994, 3, 1173-1177.

30. E. L. Cussler, *Diffusion: mass transfer in fluid systems*, Cambridge, 2009.

31. J. V. Macpherson, D. O'Hare, P. R. Unwin and C. P. Winlove, *Biophys. J.*, 1997, 73, 2771-2781.

32. F. Qiu, R. G. Compton, B. A. Coles and F. Marken, *J. Electroanal. Chem.*, 2000, 492, 150-155.

33. H. V. Patten, K. E. Meadows, L. A. Hutton, J. G. Iacobini, D. Battistel, K. McKelvey, A. W. Colburn, M. E. Newton, J. V. Macpherson and P. R. Unwin, *Angew. Chem. Int. Ed.*, 2012, 51, 7002-7006.

34. A. Olivier, E. Merienne, J. Chopart and O. Aaboubi, *Electrochim. Acta*, 1992, 37, 1945-1950.

35. J. Valdes and B. Miller, *J. Phys. Chem.*, 1989, 93, 7275-7280.

36. J. V. Macpherson, C. E. Jones and P. R. Unwin, *J. Phys. Chem. B*, 1998, 102, 9891-9897.

Chapter 4: Elucidating the electrodeposition mechanism of lead/lead oxide nanocrystallite formation in aqueous solution

The *in-situ* production of ~nm thin crystalline lead oxide (PbO) structures *via* electrochemical deposition is demonstrated unequivocally for the first time, using boron doped diamond electrodes as the deposition platform. We show the effect of electrode potential, deposition time, presence of oxygen and temperature on the formation process. At room temperature, under both de-oxygenated and aerated conditions, high-resolution microscopy reveals a predominant nanoparticle (NP) morphology. In contrast, under laser-heating half-hexagon shaped "plates" result. Transmission electron microscopy reveals these "plates" to be crystalline β-PbO. Plate prominence, under heated conditions, increases as the driving potential and deposition time is increased. By de-oxygenating the solution and applying a driving potential such that hydroxide (OH^-) formation is not possible, only elemental Pb NPs are observed, in agreement with cyclic voltammetry data. We thus propose that Pb NPs form first which catalyse OH^- generation from either oxygen or nitrate reduction (potential dependant). The Pb NPs act as nucleation sites that in turn drive the formation of lead hydroxide, ($Pb(OH)_2$) which dehydrates to PbO. Hence by controlling temperature, potential and solution conditions, cathodic electrodeposition of Pb can lead to the preferential formation of PbO crystalline structures, *in-situ*.

4.1 Introduction

Lead oxide (PbO) has received interest as a material due to applications in energy (lead acid batteries)[1], carbon dioxide storage[2] and electrocatalysis.[3, 4] Chemical routes exist for the production of PbO, such as molten lead oxidation by oxygen gas[5] and thermal decomposition,[6, 7] but there is much to be gained by exploring electrodeposition strategies. This is due to the ready integration with electrode materials for electrocatalytic applications and the ability to tune the material properties by simply changing the deposition parameters such as potential, time and temperature.

For metal ions in solution, depending on the conditions of the experiment, it is normally the elemental metal that is electrodeposited, however, metal hydroxide formation *via* a precipitation route is also possible.[8, 9] Metal hydroxide formation occurs for the majority of metals except zinc where zinc ions in the presence of electrochemically produced hydroxide, convert to the more stable crystalline ZnO form, in solution.[10] In the case of lead, whilst anodic oxidation techniques are used commonly to produce lead dioxide, PbO_2[11, 12] (due to $Pb^{2+} \rightarrow Pb^{4+} + 2e^-$) cathodic electrodeposition has been reported to be capable of producing PbO.[13-17] However, the commonly held mechanism is that PbO is formed only after removal of freshly deposited lead from solution into an oxygen-containing atmosphere.[14, 15, 17]

Boron doped diamond (BDD)[18] is an excellent electrode material for electrodeposition studies, as it has an extended cathodic potential window, low background currents and insensitivity to oxygen reduction. Diamond also has an exceptionally high heat diffusivity, a product of a high thermal conductivity of 600 W m^{-1} K^{-1} at 300 K,[19] a low heat capacity (~500 J Kg^{-1} K^{-1}) and a high oxidation

temperature (~ 700 ^{o}C) in air.[20] Thus it is also an extremely useful platform for investigating metal deposition under elevated temperature conditions. Temperature is considered to be one of the most important variables in the industrial application of electrodeposition *i.e.* electroplating.[21-23] In contrast, many literature studies of metal electrodeposition often take place under ambient conditions.[24-26] Previous studies[27] aimed at investigating the effect of temperature in conjunction with BDD electrodes, studied only the voltammetry of outer sphere redox couples and employed a pulsed infrared (IR) laser, which heated from the rear.[28, 29] The non-isothermal approach is preferred over conventional isothermal heating methods, such as the water bath, due to improved mass transport control in the system and the ability to reach above 100 ^{o}C (in water) without boiling.[30]

In this work, we employ a pulsed IR laser set-up with a freestanding BDD macrodisk electrode[31, 32] to investigate whether it is possible to form PbO *in-situ* using electrochemical methods, and if so to determine the mechanism. The effect of temperature, potential and oxygen presence on the electrodeposition of Pb (from Pb^{2+}) under near neutral pH conditions is systematically explored. Deposition morphologies are analysed using field emission scanning electron microscopy (FE-SEM), atomic force microscopy (AFM), energy-dispersive X-ray (EDX) and transmission electron microscopy (TEM).

4.2 Experimental

4.2.1 Surface characterization

Microscopic studies were carried out *ex-situ* after electrodeposition. All de-oxygenated experiments under ambient conditions (T = 22 ± 1 ^{o}C) were carried out

in a nitrogen (N_2) purged glove box (Plas Labs, Mich, US). The solution was purged under N_2 gas before transferral to the glove box. After electrodeposition, the electrode was rinsed with de-oxygenated water and dried in the glove box to avoid any oxygen contamination. All the de-oxygenated experiments under laser-heated conditions were carried out after purging the solution with continuous N_2 gas for 30 mins and flowing N_2 gas during electrochemical measurements. After electrodeposition, the electrode was again rinsed in de-oxygenated water and dried in a N_2 atmosphere.

FE-SEM (Zeiss Supra55VP) was employed to characterise the electrode and the subsequent electrodeposition. FE-SEM images were recorded using a secondary electron detector at 2 kV to highlight the metal deposits on the BDD surface.[33] All AFM images were recorded *ex-situ* in tapping mode using an Enviroscope AFM instrument (Bruker, UK). For each deposition, at least three images were recorded in different areas of the surface for both AFM and FE-SEM measurements. EDX spectra were recorded using the EDX unit equipped with the FE-SEM instrument at a working distance of 10 mm and accelerating voltage of 7.5 keV. For high resolution TEM (HR-TEM) measurements, deposits on the BDD surface were mechanically removed using a blade and then dispersed in absolute ethanol (Fisher Scientific, 99.5 %), followed by centrifugation for 15 minutes (Eppendorf, 12 000 rpm). A drop of solution (4 µL) from the bottom of the ethanol solution containing the sedimented deposits was placed onto a lacey carbon TEM grid (Agar Scientific) and left until the ethanol had evaporated. HR-TEM was conducted using a JEM 2100 TEM (JEOL, LaB_6 filament, operated at 200 kV) equipped with selected area electron diffraction (SAED).

4.2.2 Non-isothermal laser heating set-up

For non-isothermal experiments, an all diamond co-planar macroelectrode (conducting diamond sealed in insulating diamond) was employed, synthesised by Element Six (Harwell, UK) using a modified procedure to that employed for the fabrication of the all diamond microelectrode arrays.[31] In brief, a freestanding circular wafer of ~ nm roughness Electroanalysis Grade[18] polycrystalline BDD, 4 mm in diameter, was laser machined (E-355H-3-ATHI-O system, Oxford Lasers, UK) to produce one 1 mm diameter cylinder protruding from the surface. Insulating diamond was then overgrown and polished back to reveal the co-planar BDD/insulating diamond, 1 mm diameter macrodisc electrode, shown in the schematic in Figure 4.1. A FE-SEM image of the all diamond macrostructure is shown in Figure 4.2. The final thickness of the structure was 500 μm. Prior to use, the BDD electrode was cleaned by boiling in concentrated sulphuric acid (H_2SO_4, Fisher Scientific, >95%) supersaturated with KNO_3 to remove impurities and amorphous carbon produced during laser ablation.[34] Electrical contact was made by sputtering Ti (20 nm)/Au (400 nm) on the edge of the backside (nucleation side) of the electrode and then annealing at 500 ^{o}C for 4 hours to create an ohmic contact.[35]

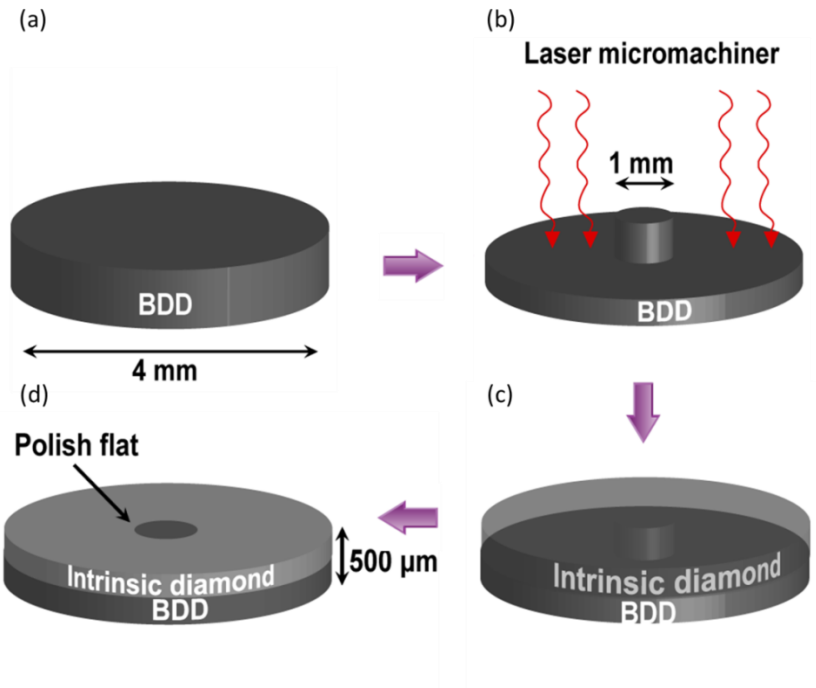

Figure 4.1: (a) 4 mm diameter CVD grown BDD disk; (b) Laser micromachining to etch away the surrounding BDD and produce a 1 mm diameter BDD cylinder protruding from the surface; (c) Intrinsic diamond overgrown on top of BDD; (d) Mechanical polishing to reveal the 1 mm BDD disk. The final thickness of the all diamond structure is 500 µm.

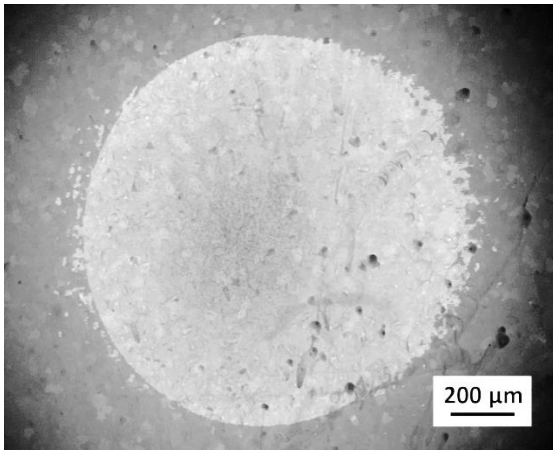

Figure 4.2: Secondary electron FE-SEM image of the all diamond structure; the brighter region in the image represents the BDD and the darker region is the intrinsic diamond. The slightly rough edge to the disk is likely to reflect the original cut of the laser to define the cylinder.

The BDD electrode was mounted in a Perspex window and sealed in place using Kapton tape (RS Components Ltd., UK) which exposed a 2 mm diameter circular window at the centre of which lay the 1 mm diameter BDD disc, sealed in insulating diamond. The fabrication procedure for the laser heating cell is similar to that employed in chapter 3, described in detail in section 2.2.3 chapter 2. The laser pulse duty cycle was deliberately chosen to be 20 ms on (10 ms laser pulse is employed in chapter 3) and 180 ms off as the all diamond structure is thicker (500 μm) than the MR11 BDD disk (200 μm) employed in chapter 3.

4.2.3 Electrochemical measurements

All electrodeposition experiments were carried out in a three-electrode system using an Ivium Compactstat. Cyclic voltammetry (CV) was carried out to determine the reduction potential for Pb deposition under both ambient and laser heated, de-oxygenated and aerated conditions. Differential pulse voltammetry (DPV) was employed during Pb stripping, over the potential range -1 V to 0 V, with DPV conditions of 2 mV potential step, 0.01 s pulse width and 50 mV pulse amplitude. To achieve a clean BDD surface in between measurements, the electrode was first anodically polarized at +1.4 V *vs* Ag/AgCl for 600 s and then polished with alumina powder (0.05 μm sized particles, micropolish, Buehler, Germany) on a DI water saturated polishing pad (Microcloth, Buehler, Germany). This procedure ensured no Pb remained on the electrode and provided a clean and reproducible surface for subsequent measurements.[33]

4.2.4 COMSOL modelling

Temperature at the electrode/electrolyte interface was simulated using COMSOL Multiphysics 4.3b (COMSOL, SE) finite element modelling (FEM) software, using the approach outlined in chapter 3 with slight modification on the dimensions to account for the all diamond electrode employed and laser on/off pulse time.

4.3 Results and discussion

4.3.1 Electrochemical characterisation of the all diamond BDD macro-disk electrode

The quality (*i.e.* absence of pin holes or defects in the intrinsic diamond layer) of the all diamond structure was assessed electrochemically for the reduction of 1 mM $Ru(NH_3)_6^{3+}$, shown in Figure 4.3. It can be seen from the CV that a peak to peak potential, ΔE_p, of 66 mV was obtained. The measured peak current was analysed by Randles Sevcik equation (equation 1.10, chapter 1) using the diffusion coefficient, D, for $Ru(NH_3)_6^{3+}$ of 8.8×10^{-6} cm^2 s^{-1}.[36] The calculated effective electrode radius for the all diamond structure is *ca.* 0.49 mm, in agreement with that measured using microscopy (Figure 4.2) which indicates that the intrinsic diamond serves as a suitable insulating layer and no pin holes or defects exist.

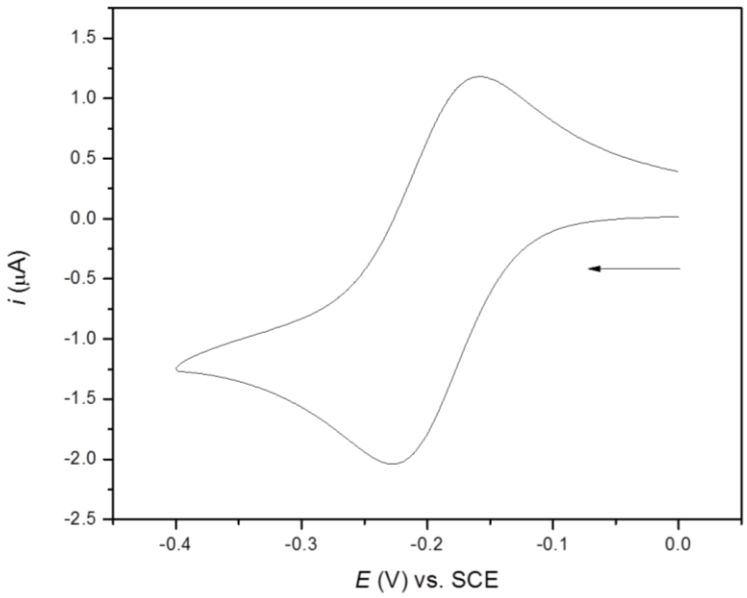

Figure 4.3: CV recorded using the all diamond BDD electrode in 0.1 M KNO_3 solution containing 1 mM $Ru(NH_3)_6^{3+}$ at a scan rate of 100 mV s^{-1}.

4.3.2 Temperature calibration at the BDD electrode/electrolyte interface under non-isothermal heating conditions

Pulsed laser heating (20 ms on, 180 ms off) induces a localised temperature increase at the BDD/solution interface, which can be quantified using open circuit potential (OCP*)* measurements (section 2.3.1, chapter 2), in an equimolar solution of $Fe(CN)_6^{3-}/Fe(CN)_6^{4-}$.[27] Figure 4.4a (red line) shows the OCP (right hand *y* axis) and the corresponding calculated average surface temperature (left hand *y* axis) over 10 s for laser power density, P_d, of 1.2 and 2.5 kW cm^{-2}. For each laser pulse the interfacial temperature increases rapidly whilst the laser is on, decreasing when the laser is off, forming a peak shaped temperature profile. The high thermal diffusivity[37] of diamond results in an instant temperature change at the electrode/electrolyte interface. However, the interfacial temperature does not cool to

ambient during the off period, as the solution close to the electrode is unable to dissipate heat sufficiently quickly due to its low thermal diffusivity. The interfacial temperature continues to rise until ~ 3 s, where an overall heat transfer equilibrium is reached with the surroundings. During this period, T at the electrode/electrolyte interface oscillates between 107.3 ± 12.3 ^{o}C for a P_d of 2.5 kW cm^{-2} and 72.5 ± 4.8 ^{o}C for a P_d of 1.2 kW cm^{-2}.

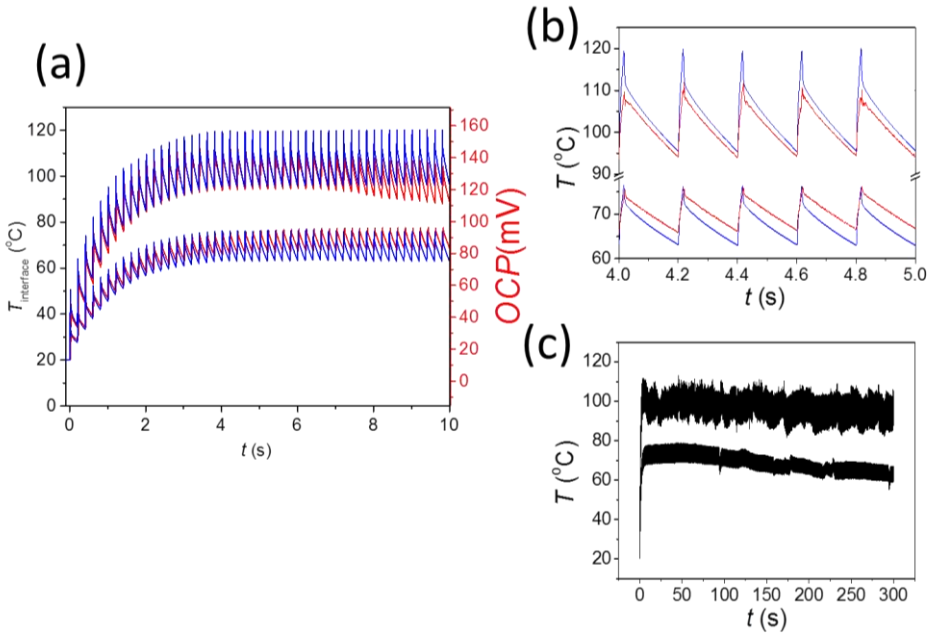

Figure 4.4: (a) Experimental (red) and modelled (blue) T at the electrode/electrolyte interface as a function of time for P_d of 1.2 kW cm^{-2} (lower) and 2.5 kW cm^{-2} (upper). T was obtained by measuring OCPs between a laser heated BDD electrode and a 1 mm glass sealed BDD electrode in an equimolar solution of 0.5 mM $Fe(CN)_6^{4-}$ and $Fe(CN)_6^{3-}$ in 0.1 M KNO_3. (b) and (c) are the zoomed-in and zoom-out plots of T at the electrode/electrolyte interface as a function of time, respectively.

In addition to experimental measurements, FEM simulations were undertaken to describe the temperature and fluid dynamics during laser heating, over a time period of 10 s. This data is shown in blue in Figure 4.4a. At short times, up to ~ 5 s,

there is very good correlation between the experimental and simulated data (see zoomed-in image in Figure 4.4b), where a steady-state has been achieved with the temperature oscillating between fairly constant limits (laser on-off); 107.5 ± 12.0 ^{o}C for 2.5 kW cm^{-2} and 69.5 ± 6.7 ^{o}C for 1.2 kW cm^{-2}. At longer time (5 - 10 s), the experimental data matches less well with the simulated data, especially when higher P_d was employed. Discrepancies between simulation and experimental may be attributed to the following: (i) The model assumed a 2D axis-symmetrical system with the electrode sitting in a parallel position at the bottom of the cell, in contrast to the experimental system where the electrode is positioned vertically; (ii) Bulk temperature heating after long-term pulsing of the laser.

Longer-term OCP experiments, over 300 s, equivalent to the timescale for Pb electrodeposition (*vide infra*) were also carried out as shown in Figure 4.4c at P_d of 1.2 and 2.5 kW cm^{-2}. The data shows the interfacial temperature reached a pseudo steady state but decreased slowly with time. This is likely to be due to the slight increase in temperature of the bulk solution with long-term heating, resulting in a decreased temperature difference, ΔT, between the laser heated electrode and the glass sealed electrode (placed ~ 3 cm away in the bulk solution).

4.3.3 Simulated temperature profile at the electrode surface

Temperature profile from the electrode surface towards bulk solution was simulated. Figure 4.5 shows the temperature profile for the 1st and 25th (5 s of pulsed laser heating) laser pulse at t = 20 ms (end of laser pulse), 100 ms (during the laser off period) and 200 ms (end of laser off period) at P_d of 1.2 kW cm^{-2}. It is seen that temperature profile changed significantly for the first 20 ms as the laser was on, after

which the temperature decreased across the electrode and solution. At the 25th laser pulse, higher temperature was obtained at the electrode surface with larger solution region being heated due to the diffusion of heat. This is caused by the heat accumulation at the interface due to the low thermal diffusivity of water. The temperature profile across the electrode and a small volume (around 100 μm thickness) of bulk solution maintained at a high temperature when the laser was switched off, which is in agreement with Figure 4.4. It can be seen from Figure 4.5 that the temperature distribution is more uniform in the diamond region than that in the water domain. This is due to the higher thermal diffusivity of the diamond.

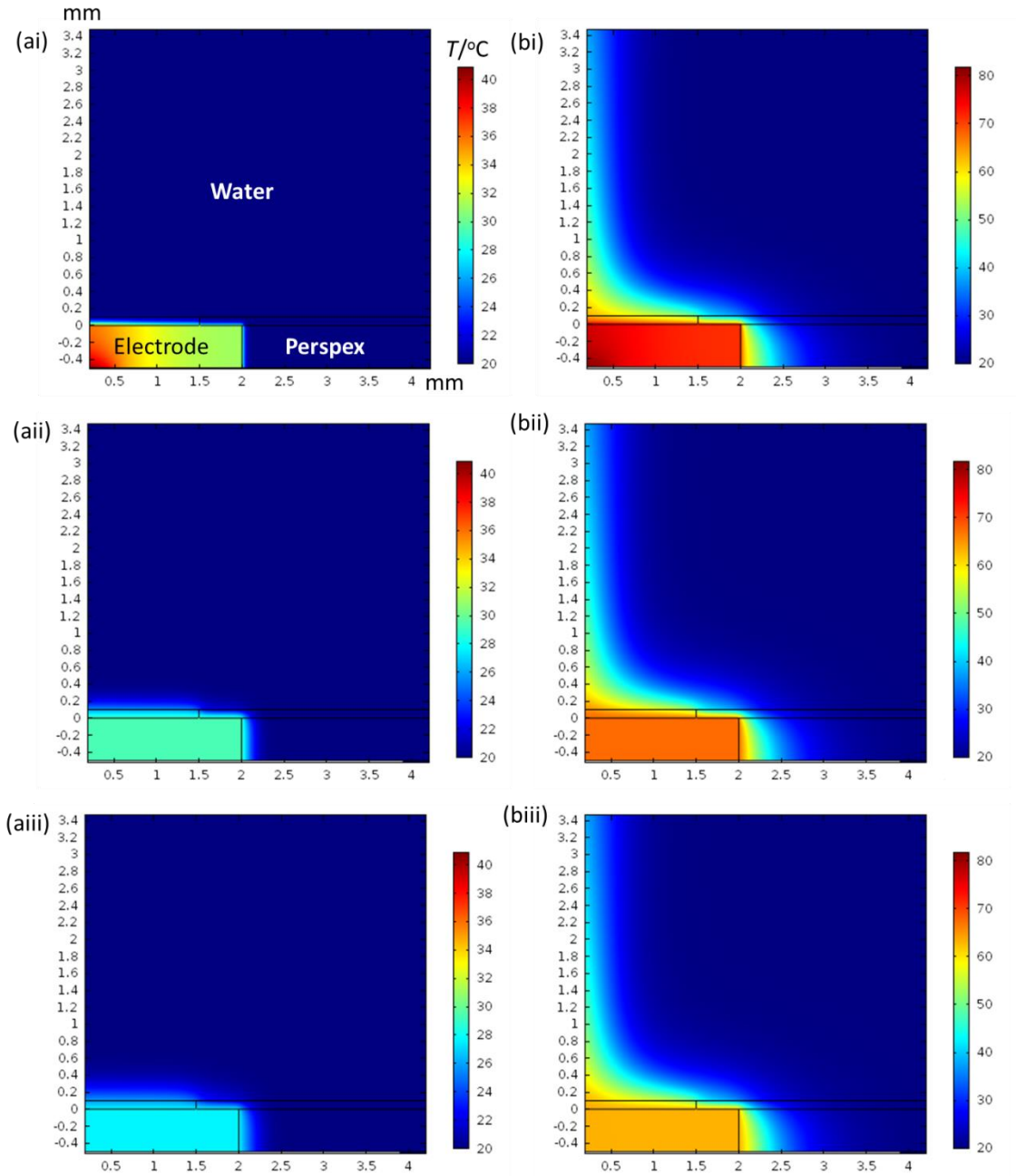

Figure 4.5: Simulated temperature profile at P_d of 1.2 kW cm^{-2} at (a) the 1st and (b) the 25th (after 5 s of pulsed laser heating) laser pulse for t = (i) 20, (ii) 100 and (iii) 200 ms. (ai) illustrated different domains. Domain for Kapton is located between water and Perspex.

4.3.4 Cyclic voltammetric studies of Pb deposition under ambient and de-oxygenated conditions

Initial CV experiments under ambient conditions, to explore the redox characteristics of Pb reduction and stripping, were carried out under both aerated and de-oxygenated solution conditions. Figure 4.6a shows CVs for the reduction of 100 µM Pb^{2+} in de-oxygenated (black) and aerated (red) solutions, running negatively from 0 V to -1.4 V and back to 0 V. Under de-oxygenation, a clear reduction wave is seen, with a half wave reduction potential, $E_{1/2,}$ at -0.76 V and charge, *Q*, for Pb^{2+} reduction of 1.49 µC (obtained by integrating between -0.6 V and -1.2 V). On the backward scan, a well-defined stripping peak is observed at *ca.* -0.52 V, indicating the anodic dissolution of Pb from the surface. *Q* for Pb stripping is calculated to be 1.42 µC, which is slightly smaller than that obtained for the reduction of Pb^{2+}.

In contrast, under aerated conditions, the CV is markedly different, most noticeable is the appearance of a large second wave with an $E_{1/2}$ at *ca.* -0.87 V, due we believe, to the reduction of oxygen (ORR). Whilst minimal sp^2 content BDD (as employed herein) is known to be inert towards ORR under these pH conditions,[38] during the scan Pb is first electrodeposited, which can serve as an electrocatalyst for ORR.[39] The ORR,

$$O_2(aq) + 2H_2O + 4e^- \rightarrow 4OH^-(aq) \qquad (4.1)$$

consumes dissolved oxygen and produces hydroxide ions (OH^-).

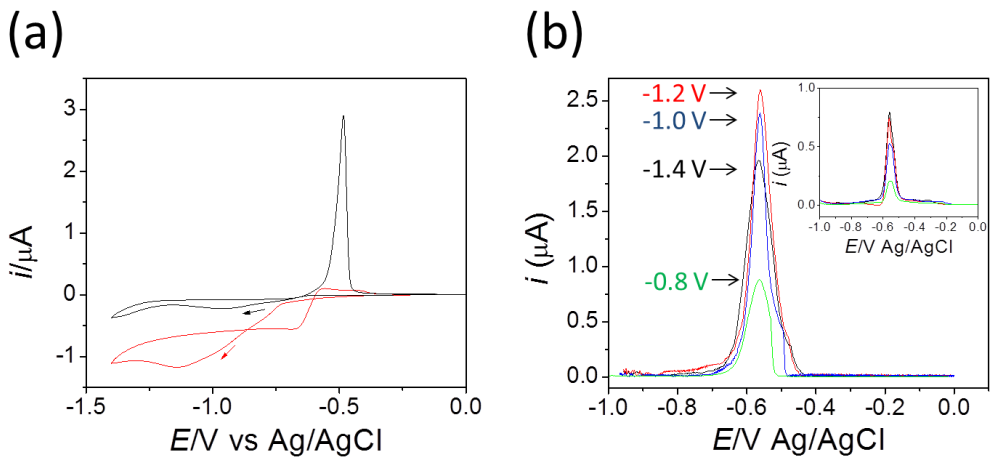

Figure 4.6: (a) CVs for the reduction of Pb^{2+} under ambient conditions at the BDD electrode in aerated (red) and de-oxygenated (black) 0.1 M KNO_3 solution containing 100 µM $Pb(NO_3)_2$. The scan rate was 50 mV s^{-1}. (b) DPVs (pulse width 0.01 s, pulse amplitude 50 mV, step size 2 mV) at room temperature after Pb deposition at the BDD electrode at different deposition potentials (i) -0.8 V (magenta); (ii) -1.0 V (blue); (iii) -1.2 V (red) and (iv) -1.4 V (black) in both aerated (inset) and de-oxygenated solutions. Deposition was carried out in 0.1 M KNO_3 solution containing 100 µM $Pb(NO_3)_2$ for 30 s.

Also evident is the significantly reduced stripping peak current (Q = 0.08 µC, ~ ×18 smaller than that under de-oxygenated conditions), suggesting that the amount of Pb that can be anodically dissolved from the surface has been reduced. This was further explored by investigating the size of the Pb DPV stripping peak current (and the area under the stripping peak) as a function of electrode driving potential under both aerated and de-oxygenated conditions, Figure 4.6b, for the same solution conditions as Figure 4.6a. These values are listed in Table 4.1. In all cases a deposition time of 30 s was employed and the electrode was held at potentials of (i) -0.8 V; (ii) -1.0 V; (iii) -1.2 V and (iv) -1.4 V. For the aerated case (inset to Figure 4.6b), the stripping current (and the peak area) associated with the removal of

electrodeposited Pb on the surface increases with increasing applied potential, however the peak currents are *ca.* 3 - 4 times smaller than those under de-oxygenated conditions (Figure 4.6b and Table 4.1). By de-oxygenating, the same trend of increasing Pb dissolution peak current with increasing applied potential is seen except at -1.4 V, the highest applied potential, where the amount of Pb stripped from the surface is actually smaller than that obtained at -1.0 V and -1.2 V.

Table 4.1: Pb DPV stripping peak current (and the area under the stripping peak) as a function of electrode driving potential under both aerated and de-oxygenated condition.

Deposition potential (V *vs* Ag/AgCl)	Peak current for aerated solution (μA)	Peak current for de-oxygenated solution (μA)
-0.8	0.21 (0.15×10^{-5})*	0.88 (4.43×10^{-6})
-1.0	0.53 (0.33×10^{-5})	2.39 (1.03×10^{-5})
-1.2	0.74 (0.51×10^{-5})	2.60 (1.08×10^{-5})
-1.4	0.79 (0.55×10^{-5})	1.96 (0.95×10^{-5})

* Area under the stripping peak

We believe these observations result from the generation of OH^- from the ORR (equation 4.1) at Pb deposits, and at higher driving potentials, from reduction of nitrate ions (equation 4.2),[40] present in excess in the solution.

$$NO_3^-(aq) + 7H_2O + 8e^- \rightarrow NH_4^+(aq) + 10\ OH^-(aq) \qquad (4.2)$$

Electrogeneration of OH^- is a common method in the literature to form metal hydroxides at electrode surfaces.[8, 9] $Pb(OH)_2$ is not known to be stable and is thought to transform via a dehydration mechanism to the more stable PbO form (equation 4.3), [15, 41, 42]

$$Pb(OH)_2 \rightarrow PbO(s) + H_2O \quad (4.3)$$

Formation of this inorganic Pb complex would mean that the amount of free Pb able to be anodically dissolved will be lower, depending on how much Pb is present in the passivated oxide form. Thus under aerated conditions, where equation 4.1 and equation 4.2 can act, at suitable applied potentials, less Pb on the surface would be expected than under the de-oxygenated case. The decrease in stripping current (and peak area) at the highest applied potential, under de-oxygenated conditions, could be attributed to OH^- formation due to equation 4.2.

CVs for the reduction of Pb^{2+} under laser heated conditions (1.2 kW cm^{-2}, pulsed laser on for 20 ms, and off for 180 ms, corresponding to an average local electrode temperature of 72.5 ^oC, *vide infra*) in both de-oxygenated (black) and aerated (red) solutions are shown in Figure 4.7. The CVs were run negatively from 0 V to -1 V and back to 0 V (*i.e.* not into the nitrate reduction region, equation 4.2). Under de-oxygenated conditions, during the cathodic scan, a diffusion limited current for the reduction of Pb^{2+} is obtained (~ 2.1 μA). The current magnitude is greatly increased (by 9 times) compared to that under de-oxygenated ambient conditions, indicating an enhancement in the mass transport rate at elevated temperatures, as expected. $E_{1/2}$ is -0.69 V, which shows a positive shift of 70 mV compared to de-oxygenated ambient conditions. β for the Pb^{2+}/Pb couple is reported as -0.359 mV K^{-1},[43] which from a thermodynamic perspective only, indicates a negative shift of the Pb reduction potential at elevated temperatures. Therefore our observation of a positive shift suggests that the increased ET kinetics for Pb

deposition under high temperature dominates over thermodynamic effects. In the anodic sweep, a Pb stripping peak at *ca.* -0.51 V is observed and the charge passed for Pb oxidation is 3.3 μC which is *ca.* 2.4 times the value obtained under de-oxygenated ambient conditions. This further confirms that more Pb has been deposited at elevated temperature (under de-oxygenated conditions) *Q* for Pb stripping (3.3 μC) is only slightly smaller than that obtained from Pb reduction (3.5 μC, calculated by integrating between -0.6 V and -1.0 V).

The emergence of the ORR is again obvious in the CV under heated, aerated conditions, where the ORR current is *ca.* 4 times larger than that under ambient conditions. The $E_{1/2}$ for ORR is *ca.* -0.73 V (compared to -0.87 V under ambient conditions), indicating that the ET kinetics for ORR is more facile at elevated temperatures. The stripping peak for Pb oxidation is again reduced greatly in magnitude under aerated, heated conditions with *Q* calculated to be 0.13 μC, which is ~ 24 times smaller than that obtained under de-oxygenated, heated conditions.

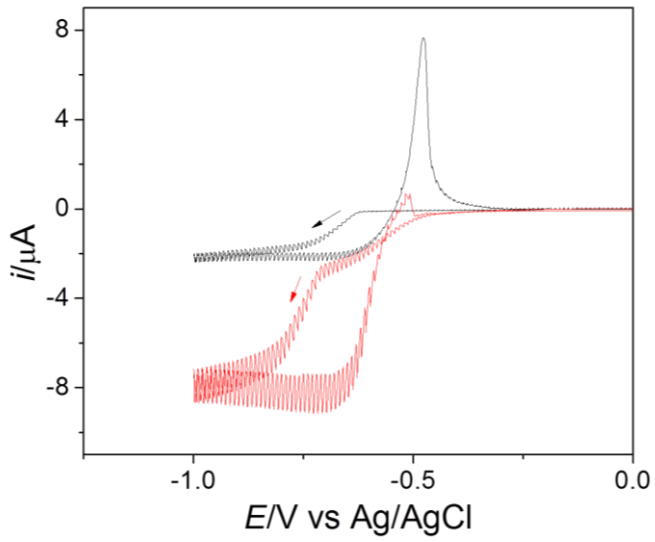

Figure 4.7: CVs for the reduction of Pb^{2+} at 72.5 ^{o}C (laser heated condition: 1.2 kW cm^{-2}, pulsed laser on for 20 ms, and off for 180 ms) at the BDD electrode in aerated (red) and de-oxygenated (black) 0.1 M KNO_3 solution containing 100 µM $Pb(NO_3)_2$. The scan rate was 50 mV s^{-1}.

4.3.5 Microscopic analysis

Ex-situ FE-SEM and TEM measurements were carried out to study the morphology and crystallinity of the Pb deposits on the BDD after Pb deposition under both de-oxygenated and aerated conditions at ambient and elevated temperatures, and under two different driving potentials (a) -1.0 V *vs* Ag/AgCl, where only ORR takes place and (b) -1.4 V *vs* Ag/AgCl, where ORR and nitrate reduction are possible. Note, for all experiments immediately after electrodeposition the BDD electrode was rinsed with **de-oxygenated DI water** and then dried immediately in N_2 atmosphere. This was to avoid any possible conversion of freshly deposited Pb, covered in a thin wet film of solution, into PbO upon removal from solution.[14]

Pb^{2+} concentration of 50 μM and deposition time of 300 s were chosen in order to produce significant deposits on the surface for analysis. Initial experiments (Figure 4.8) were carried out under laser heated conditions (P_d of 1.2 kW cm^{-2}, 72.5 ^oC, laser on for 20 ms, off for 180 ms) at two different driving potentials (a) -1.0 V and (b) -1.4 V and in the (i) absence and (ii) presence of dissolved oxygen. In the absence of oxygen and at a potential where OH^- formation is insignificant, *i.e.* -1 V, Figure 4.8ai shows that the BDD surface is dominated by Pb NPs with many of them agglomerating. The homogenous distribution of the Pb NPs indicates that the deposition process is independent of the boron doping level for different grains. The formation of agglomerated structures is attributed to the coalescence of NPs,[44] which reduces surface energy.

In contrast, under aerated conditions and under potential conditions where equation 4.1 contributes, the FE-SEM image shows a very different surface morphology (Figure 4.8aii). The BDD surface contains thin, half hexagonal 'plate' structures, with NPs density of *ca.* 8.2 NPs per μm^2 presented in the background. The "plates" have a density of 0.4 plates per μm^2 with a base diameter of 0.5 – 1.1 µm. A few of the "plates" stand vertically from the surface; however the majority lie flat. We believe the "plates" grow upwards from the surface (*vide infra*) and then either fall falt after reaching a certain size or as a result of the drying process in the N_2 atmosphere prior to imaging.[45]

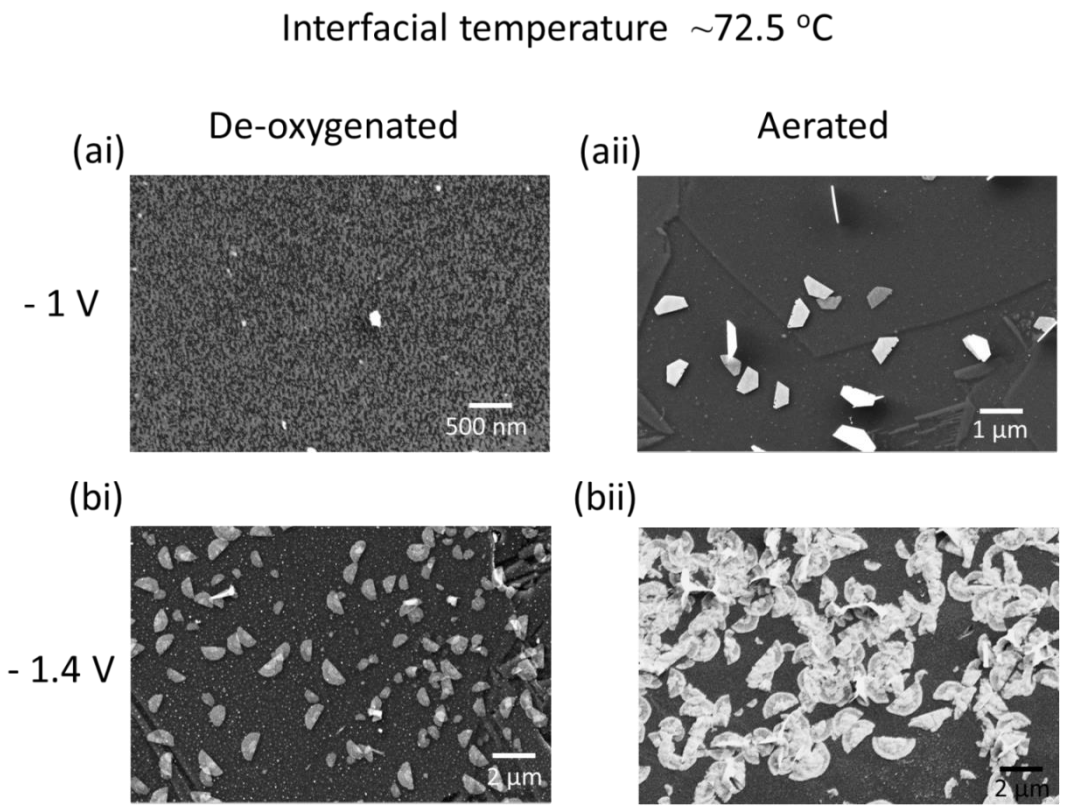

Figure 4.8: Typical secondary electron FE-SEM images after laser heated deposition at -1.0 V (a) and -1.4 V (b) vs Ag/AgCl in (i) de-oxygenated and (ii) aerated solutions. Laser heating conditions: P_d of 1.2 kW cm^{-2}, 72.5 ^oC, laser on for 20 ms off for 180 ms and deposition was carried out in 0.1 M KNO_3 solution containing 50 µM $Pb(NO_3)_2$ for 300 s.

By driving the deposition potential at -1.4 V for 300 s, where equation 4.2 is now possible, under de-oxygenated conditions, Figure 4.8bi again shows the presence of "plates" (in contrast to Figure 4.8ai**)**. The flat "plates" have become more hemispherical in shape and have a density of 0.7 plates per μm^2 with a base diameter of 0.3 – 1.1 µm. Pb NPs are also observed with a density of ~ 20 NPs per μm^2. It is thus probable that in the absence of oxygen the only route for OH^- production is via equation 4.2, which is only possible at the higher driving potential. The "plates" thus appear to correlate with OH^- electro-formation.

Under aerated conditions, where OH^- production will be increased due to both equation 4.1 and 4.2 operating, both the density and base diameter of the "plate" structures increase (Figure 4.8bii) with a density of *ca.* 1.2 plates per μm^2 and base diameter of 0.8 – 2 µm. The "plates" also seem to show 3D growth from the centre region of the flat hemisphere. A NP density of ~ 25 NPs per μm^2 was also observed, similar to that obtained under de-oxygenated conditions (Figure 4.8bi).

4.3.6 Composition and crystallographic analysis

In order to further confirm the composition and crystalline structure of the "plates", EDX and TEM analysis were carried out *ex-situ* after electrodeposition at -1.0 V for 300 s in 50 µM Pb^{2+} aerated solution under laser heated conditions (P_d of 1.2 kW cm^{-2}, 72.5 ^oC, laser on for 20 ms off for 180 ms), *i.e.* Figure 4.8aii. EDX spectra were collected from both the horizontal lying "plates" and the bare BDD surface. As the "plate" structure was not thick enough, the spectrum collected from a single plate was dominated by the carbon signal from the BDD, so overlapping "plates" were chosen for analysis. Figure 4.9 shows the EDX spectra collected on the overlap region of "plates" (black cross) and the background BDD surface (red cross). The inset FE-SEM image shows the spots for spectra collection. The spectrum from the background BDD surface (red) shows a large C peak at 0.277 keV, whereas the spectrum collected on the plate shows O and Pb peaks at 0.523 keV and 2.342 keV, respectively, which indicates the presence of both Pb and O in the "plates" structures.

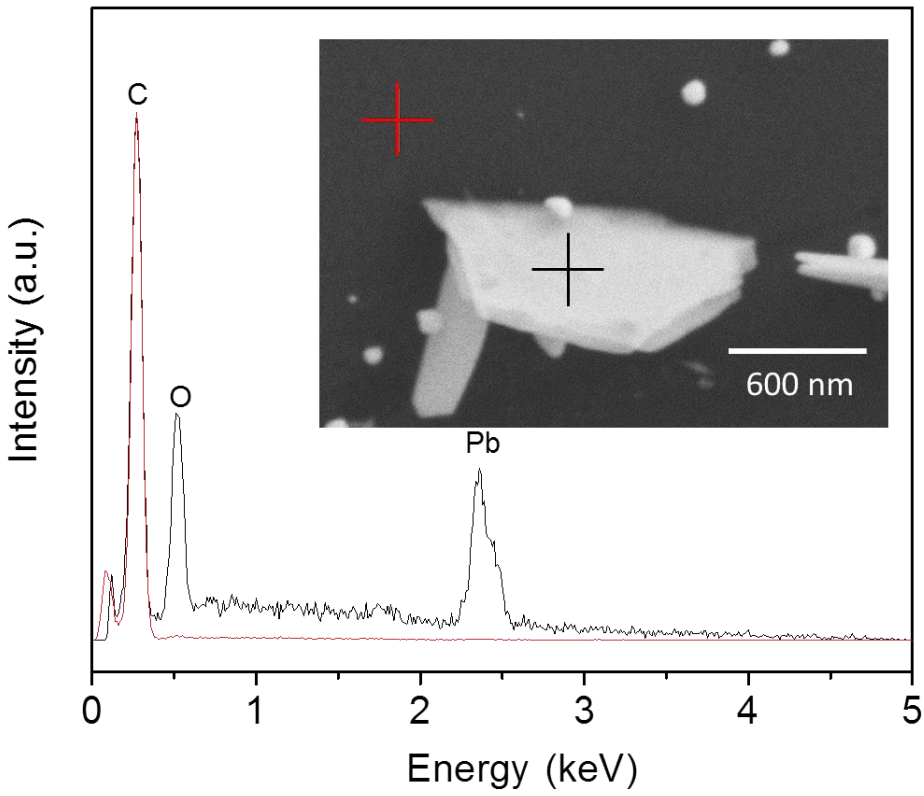

Figure 4.9: EDX spectra taken at a spot on the overlap between plate structures (black) and at a spot on the background BDD surface (red). Inset FE-SEM image highlights the spots where the EDX spectra were collected. Spectra and FE-SEM images were collected after electrodeposition at -1.0 V for 300 s in 0.1 M KNO_3 aerated solution containing 50 µM $Pb(NO_3)_2$ under laser heated conditions (P_d of 1.2 kW cm^{-2}, 72.5 ^oC, laser on for 20 ms off for 180 ms).

TEM analysis of an individual "plate" deposited under the same conditions to Figure 4.8aii and Figure 4.9 is shown in Figure 4.10, where "plate" structures with base diameter ranging from 0.7 to 1.0 µm were observed. The corresponding SAED pattern in Figure 4.10b shows a clear spot pattern, indicating the single crystal structure of the "plate", as evidenced by HR-TEM images in the Figure 4.10c. The calculated d-spacing's from the SAED pattern are consistent with standard values (Joint Committee on Powder Diffraction Standards (JCPDS) card, No. 76-1796) for

the orthorhombic β-PbO. Spots in the SAED pattern are indexed according to the JCPDS card of the orthorhombic β-PbO, showing the (200) and (210) facets. Thus both EDX and TEM prove unequivocally that the "plates" are crystalline PbO structures. It is not possible to analyse the NPs in this way due to the drifting effect when collecting the EDX spot data, and very low density and small size of NPs presented in the TEM grid. However, as the stripping peaks in Figure 4.6 and Figure 4.7 suggest that some of the deposited Pb must remain in the Pb form, we speculate that at least some of the NP structures are likely to be elemental Pb.

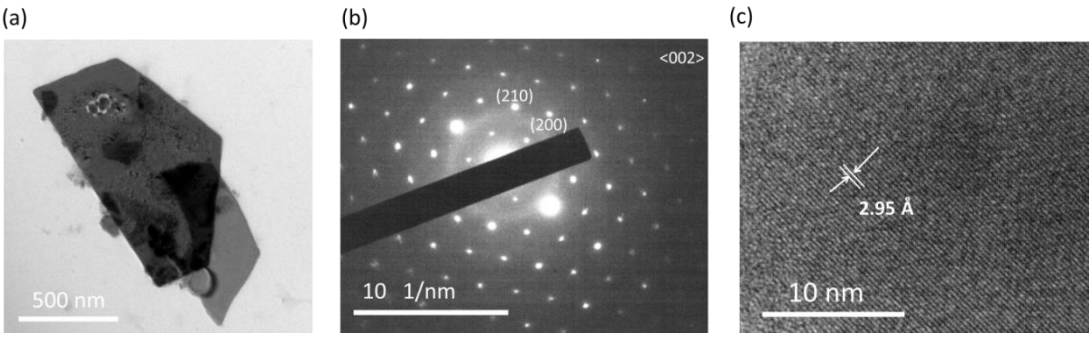

Figure 4.10: typical (a) TEM image and (b) SAED pattern of the "plate" structure. (c) HR-TEM image showing the crystallinity of the "plate" structure. TEM image and SAED pattern were collected after electrodeposition at -1.0 V for 300 s 0.1 M KNO_3 aerated solution containing 50 µM $Pb(NO_3)_2$ under laser heated conditions (P_d of 1.2 kW cm^{-2}, 72.5 ^oC, laser on for 20 ms off for 180 ms).

4.3.7 Mechanism for PbO formation

The formation mechanism of the crystalline PbO "plates" is worth investigating further. Figure 4.11a shows typical high resolution FE-SEM image of the "plates" formed after electrodeposition at -1.0 V for 300 s in 50 µM Pb^{2+} aerated solution under laser heated conditions (Figure 4.8aii) (P_d of 1.2 kW cm^{-2}, 72.5 ^oC,

laser on for 20 ms, off for 180 ms). The "plates" in these images lie flat on the surface, having fall flat, and three zoomed-in images of individual "plates" are shown in Figure 4.11a. Clearly evident are spherical vacancies at the base of the "plates", which we believe could highlight the original position of Pb NPs which catalyse the formation of the PbO crystal. Due to the different crystal structures between Pb NPs and PbO, there will be an increasing lattice strain (highly energetic interface) in the boundary between Pb and PbO which will lead to the separation of these two structures, and then the PbO "plates" fall flat.

At the initial electrodeposition stage, Pb NPs form on the electrode surface, which are capable of turning over oxygen, nitrate or water (potential dependant) to form OH^-. Those that are suitably spaced, sized and, or, of the correct morphology to promote efficient OH^- production, act as catalytic sites for local $Pb(OH)_2$ formation. This is due to a precipitation reaction between OH^-, which diffuses hemispherically away from the NP, and Pb^{2+}. The $Pb(OH)_2$ rapidly transforms to PbO, resulting in the "plate" crystal growth observed, as shown schematically in Figure 4.11b. Interestingly, Pb NPs have been observed at the base of PbO "plate" before,[17] and have also been postulated to act as nucleation sites, although the formation mechanism was different.[17] Our electrochemical (CV and stripping voltammetry) and microscopic data thus support the theory that under cathodic electrodeposition conditions both Pb NPs and crystalline β-PbO "plates" form directly in solution. This contrasts with the current thinking that it is the removal process from solution and exposure of the freshly deposited, wet Pb surface to an oxygen atmosphere that results in PbO formation.[14, 15]

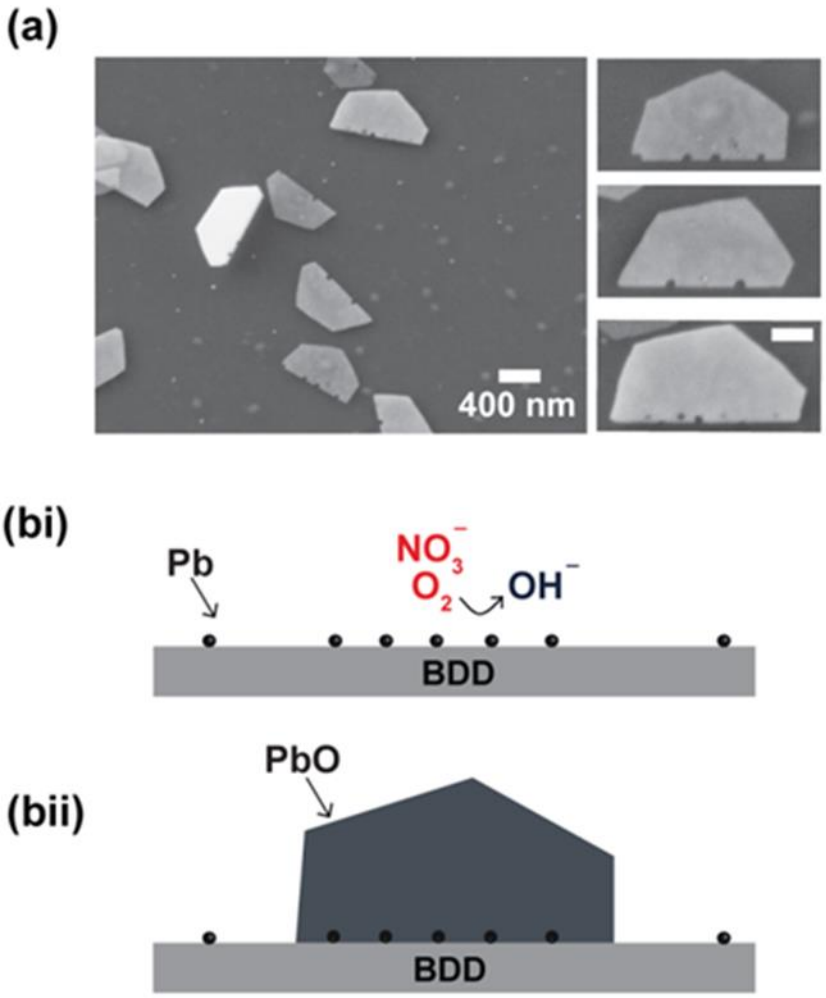

Figure 4.11: (a) Zoomed-in secondary electron FE-SEM images highlighting the "plate" structures. Scale bar in (a) is 400 nm. (b) Proposed mechanism for the formation of PbO "plate" structures.

4.3.8 Ambient deposition

Under heated conditions, the formation of the β-PbO "plates" is clearly evident. In contrast, when working under ambient conditions and even using parameters where OH^- formation is exacerbated, *i.e.* an oxygenated solution and -1.4 V driving potential (0.1 M KNO_3 containing 50 μM Pb^{2+}, 300 s deposition time), *ex-situ* AFM images showed only NPs presented on the BDD surface (Figure 4.12) with

the corresponding stripping voltammetry showing Pb stripping peak. This indicates that some of the NPs is in elemental Pb form and not passivated with PbO.

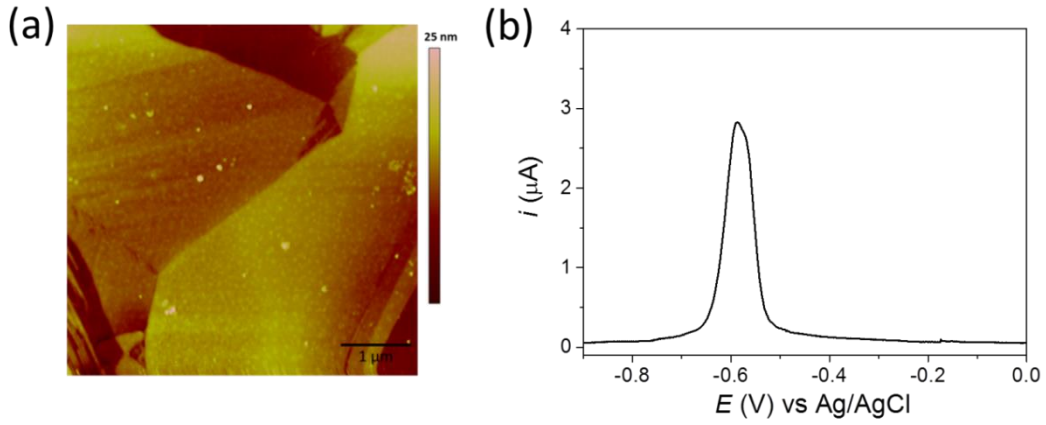

Figure 4.12: (a) Typical AFM image after Pb deposition under ambient conditions for 300 s. Pb deposition was carried out at -1.4 V vs Ag/AgCl in aerated 0.1 M KNO_3 solution containing 50 µM $Pb(NO_3)_2$. (b) The corresponding DPV (pulse width 0.01 s, pulse amplitude 50 mV, step size 2 mV) under ambient conditions after Pb deposition.

To investigate the timescale needed for "plate" structures to form under ambient conditions, deposition time was increased to 1800 s. Experiments were carried out in both de-oxygenated and aerated solutions at -1.4 V, as shown in Figure 4.13a and b, respectively. Under de-oxygenated conditions, both Pb NPs and a few PbO "plates" are present, with a NP density of 22 NPs per μm^2 and PbO "plate" density of 0.01 plates per μm^2 (base diameter of 1 – 5 µm). This indicates that "plate" formation is a much slower process under ambient conditions. Under aeration, the density of NPs is approximately the same ~ 23 NPs per μm^2 and the PbO "plates" have a density of 0.03 plates per μm^2 with base diameter of similar size (1 – 5 µm).

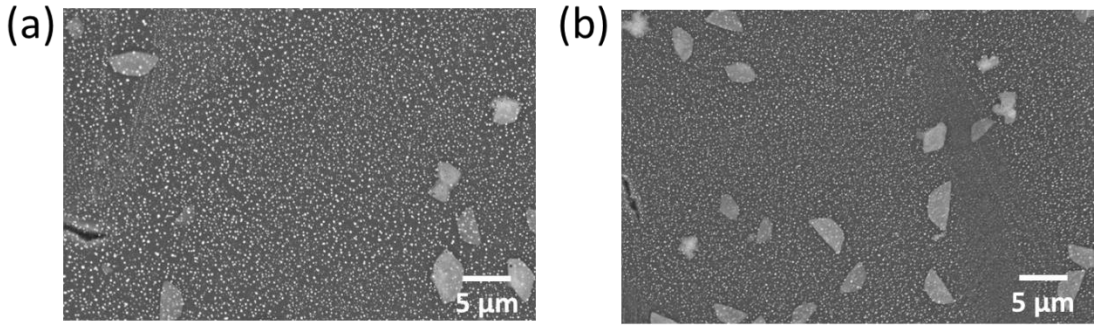

Figure 4.13: Typical secondary electron FE-SEM images after deposition at -1.4 V vs Ag/AgCl under ambient conditions in (a) de-oxygenated and (b) aerated solutions. Deposition was carried out in 0.1 M KNO_3 containing 50 µM $Pb(NO_3)_2$ solution for 1800 s.

4.3.9 Time-dependant microscopic analysis

Finally, time-dependant microscopic observations of the electrode surface were employed in order to follow the evolution of the morphology change of the structures on the BDD electrode. Deposition was carried out in an aerated 50 µM Pb^{2+} under laser heated (P_d of 1.2 kW cm^{-2}, 72.5 ^oC, laser on for 20 ms off for 180 ms) conditions for different times of (a) 10 s, (b) 50 s, (c) 100 s and (d) 300 s at an applied potential of -1.4 V, *i.e.* under conditions where PbO formation is favoured (Figure 4.8bii). The resulting *ex-situ* microscopic (FE-SEM and AFM) images are shown in Figure 4.14.

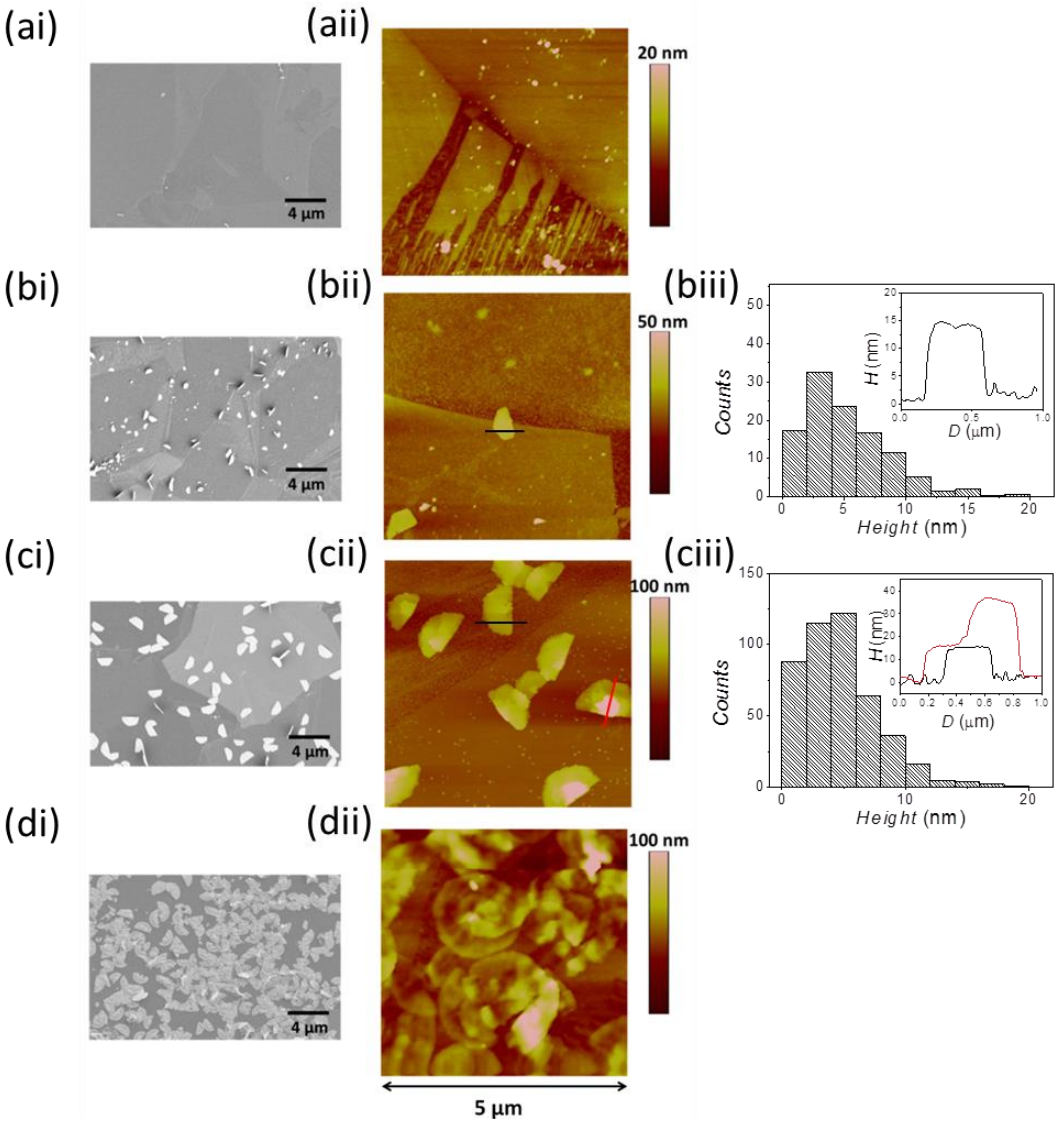

Figure 4.14: Typical secondary electron FE-SEM (i) and AFM (ii) images of the BDD surface after laser heated deposition at -1.4 V vs Ag/AgCl in 0.1 M KNO_3 aerated solution containing 50 µM $Pb(NO_3)_2$ for different times (a) 10 s, (b)50 s, (c) 100 s, (d) 300 s . (biii) and (ciii) are the histogram (data collected form an average of three AFM images) of NPs on BDD surface after electrodeposition for 50 s and 100 s, respectively. Insets in (biii) and (ciii) are the cross sectional plot of the "plate" structure highlighted in (bii) and (cii), respectively. Laser heated conditions were P_d of 1.2 kW cm^{-2}, 72.5 ^oC, laser on for 20 ms off for 180 ms.

After 10 s, the AFM image in Figure 4.14aii shows only NPs with a mean height of *ca.* 4.1 nm and 10 – 20 nm in diameter. Note height measurements in AFM are more accurate than lateral measurements, as the latter may overestimate the true particle width. As the deposition time increases to 50 s, both FE-SEM and AFM images confirm the presence of β-PbO "plates", showing the crystallisation process operates on a relatively fast timescale. The FE-SEM image again shows both the "upright" and flat "plate" structures. Plate density is *ca.* 0.08 plates per μm^2 with a base diameter ranging from 300 to 500 nm. A cross-sectional view of the "plate" (highlighted in the AFM image in Figure 4.14bii) is plotted (inset in Figure 4.14biii), showing the thickness of the structure is *ca.* 14.8 nm, and the "plate" surface is relatively flat (1 – 2 nm roughness). Histogram of NP distribution in Figure 4.14biii shows that the NPs have a mean diameter of 4.3 nm, which is similar to the size obtained at the time of 10 s deposition.

As the deposition time increases to 100 s, the "plates" increase in size with a base diameter ranging from 500 to 800 nm and a density rising to 0.44 plates per μm^2. Some of the "plate" structures retain a similar thickness (*ca.* 15.1 nm) to those grown for 50 s deposition (inset in Figure 4.14ciii, black). However, others show 3D growth from the centre of the "plate" structure as can be clearly seen in the cross sectional plot (inset in Figure 4.14ciii, red). A histogram of NP distribution in Figure 4.14ciii shows that mean diameter of NPs is *ca.* 5.2 nm, and the number of NPs has increased significantly. PbO "plate" formation is dominant after 300 s deposition as shown in Figure 4.14d. In this case, "plates" have a base diameter of 0.8 – 2 μm, overlapping with each other substantially and show significant growth over the surface of the "plates".

The move from a defined half hexagonal structure to hemispherical to 3D growth from the planar surface is interesting. The shape of the plate suggests growth takes place preferentially at the thin edges. We can speculate that the once the crystalline structure reaches a certain size it may fall over. Once this happens three dimensional supply of Pb^{2+} ions is now constrained and preferential growth can no longer proceed as it did. Instead, nucleation takes place on the surface of the "plate".

4.4 Conclusions

A systematic study was undertaken to determine if and under what conditions it was possible to form PbO structures *in-situ via* electrochemical reduction of Pb^{2+}. An all diamond co-planar BDD macrodisk electrode was utilised as the substrate electrode and experiments were conducted under both ambient and laser heated conditions (interfacial temperature = 72.5 ^{o}C), in the absence and presence of dissolved oxygen and under different applied potential conditions. Two electrode potentials were employed, -1.0 V, where ORR is possible on freshly deposited Pb and -1.4 V, where ORR and nitrate reduction occurs. Both reduction routes result in hydroxide formation.

Under aerated conditions a smaller Pb stripping peak was obtained than under de-oxygenated conditions. The size of the stripping peak under both conditions increased when laser heating the interface. Under heating, FE-SEM and AFM revealed the presence of both NPs and "plates" on the electrode surface. "Plates" were absent when the solution was de-oxygenated and an applied potential of -1 V was employed. Under ambient conditions irrespective of the applied

potential no “plates” were observed, unless significantly longer deposition times were implemented (*i.e.* 1800 s not 300 s) in the present of oxygen.

EDX and TEM studies revealed the “plates” to be crystalline β-PbO. PbO was thus proposed to form directly in solution from freshly deposited Pb NPs acting as catalytic nuclei for the localised production of OH^- (the BDD surface itself does not turn over ORR). The OH^- in turn reacts with Pb^{2+} *via* a precipitation mechanism to form unstable $Pb(OH)_2$ which dehydrates quickly to PbO; a process accelerated under laser heated conditions. The fact that Pb stripping was observed from the BDD surface in the presence of NPs and PbO “plates”, suggested that at least some (if not all) of the NPs were still in the elemental Pb form and capable of dissolution from the surface at the expected Pb/Pb^{2+} dissolution potential. The reason for why some NPs stay as Pb nuclei whereas others promote the formation of PbO “plates” or themselves may become passivated with PbO is still not fully understood.

The results presented confirm that *in-situ* formation of crystalline PbO structures is possible *via* cathodic electrodeposition and hydroxide generation route. By controlling temperature, electrode potential, dissolved oxygen content and deposition time, precise control of the morphology of the resulting structures can be achieved. Finally, the nm thin crystalline PbO “plate” structures lend themselves perfectly for further investigation using high resolution electrochemical imaging techniques.[46]

4.5 References

1. F. Cheng, J. Liang, Z. Tao and J. Chen, *Adv. Mater.*, 2011, 23, 1695-1715.

2. J. Jianguo, C. Maozhe, Z. Yan and X. Xin, *J. Hazard. Mater.*, 2009, 161, 1046-1051.

3. H. Karami, M. A. Karimi, S. Haghdar, A. Sadeghi, R. Mir-Ghasemi and S. Mahdi-Khani, *Mater. Chem. Phys.*, 2008, 108, 337-344.

4. G. L. Clark and R. Rowan, *J. Am.Chem.Soc.*, 1941, 63, 1302-1305.

5. T. Blair, *J. Power Sources*, 1998, 73, 47-55.

6. C. S. Lim, Z. Sofer, O. Jankovský, H. Wang and M. Pumera, *RSC Advances*, 2015, 5, 101949-101958.

7. E. A. Peretti, *J. Am. Ceram. Soc.*, 1957, 40, 171-173.

8. S. P. E, D. Liu, R. A. Lazenby, J. Sloan, M. Vidotti, P. R. Unwin and J. V. Macpherson, *J. Phys. Chem. C*, 2016, 120, 16059-16068.

9. S. Peulon and D. Lincot, *J. Electrochem. Soc.*, 1998, 145, 864-874.

10. M. Skompska and K. Zarębska, *Electrochim. Acta*, 2014, 127, 467-488.

11. X. Li, D. Pletcher and F. C. Walsh, *Chem. Soc. Rev.*, 2011, 40, 3879-3894.

12. P. N. Bartlett, T. Dunford and M. A. Ghanem, *J. Mater. Chem.*, 2002, 12, 3130-3135.

13. I. Zhitomirsky, L. Gal-Or, A. Kohn and H. Hennicke, *J. Mater. Sci. Lett.*, 1995, 14, 807-810.

14. S. Sawatani, S. Ogawa, T. Yoshida and H. Minoura, *Adv. Funct. Mater.*, 2005, 15, 297-301.

15. J. Cheng, X. Zou, Y. Su, G. Yang and X. Lue, *Funct. Mater. Lett.*, 2009, 2, 185-191.

16. P. Ren, X. Zou, J. Cheng, H. Zhang, F. Li, M. Wang and G. Zhu, *J. Nanosci. Nanotechnol.*, 2009, 9, 1487-1490.

17. Y. Kwon, H. Lee and J. Lee, *Nanoscale*, 2011, 3, 4984-4988.

18. L. A. Hutton, J. G. Iacobini, E. Bitziou, R. B. Channon, M. E. Newton and J. V. Macpherson, *Anal. Chem.*, 2013, 85, 7230-7240.

19. J. E. Field, *The properties of natural and synthetic diamond*, Academic Press London, 1992.

20. P. John, N. Polwart, C. Troupe and J. Wilson, *Diamond Relat. Mater.*, 2002, 11, 861-866.

21. C. Ramírez, E. M. Arce, M. Romero-Romo and M. Palomar-Pardavé, *Solid State Ionics*, 2004, 169, 81-85.

22. J. M. Elliott, G. S. Attard, P. N. Bartlett, N. R. Coleman, D. A. Merckel and J. R. Owen, *Chem. Mater.*, 1999, 11, 3602-3609.

23. H. Natter and R. Hempelmann, *J. Phys. Chem.*, 1996, 100, 19525-19532.

24. L. P. Bicelli, B. Bozzini, C. Mele and L. D'Urzo, *Int. J. Electrochem. Sci*, 2008, 3, 356-408.

25. T. M. Day, P. R. Unwin, N. R. Wilson and J. V. Macpherson, *J. Am.Chem.Soc.*, 2005, 127, 10639-10647.

26. R. M. Penner, *J. Phys. Chem. B*, 2002, 106, 3339-3353.

27. L. Meng, J. G. Iacobini, M. B. Joseph, J. V. Macpherson and M. E. Newton, *Farad. Discuss.*, 2014, 172, 421-438.

28. J. F. Smalley, S. W. Feldberg, C. E. Chidsey, M. R. Linford, M. D. Newton and Y. P. Liu, *J. Phys. Chem.*, 1995, 99, 13141-13149.

29. J. F. Smalley, C. Krishnan, M. Goldman, S. W. Feldberg and I. Ruzic, *J. Electroanal. Chem. Interfacial Electrochem.*, 1988, 248, 255-282.

30. P. Gründler, A. Kirbs and L. Dunsch, *ChemPhysChem*, 2009, 10, 1722-1746.

31. M. Pagels, C. E. Hall, N. S. Lawrence, A. Meredith, T. G. Jones, H. P. Godfried, C. J. Pickles, J. Wilman, C. E. Banks and R. G. Compton, *Anal. Chem.*, 2005, 77, 3705-3708.

32. M. B. Joseph, E. Bitziou, T. L. Read, L. Meng, N. L. Palmer, T. P. Mollart, M. E. Newton and J. V. Macpherson, *Anal. Chem.*, 2014, 86, 5238-5244.

33. L. A. Hutton, M. E. Newton, P. R. Unwin and J. V. Macpherson, *Anal. Chem.*, 2011, 83, 735-745.

34. N. R. Wilson, S. L. Clewes, M. E. Newton, P. R. Unwin and J. V. Macpherson, *J. Phys. Chem. B*, 2006, 110, 5639-5646.

35. K. Das, V. Venkatesan, K. Miyata, D. Dreifus and J. Glass, *Thin Solid Films*, 1992, 212, 19-24.

36. J. V. Macpherson, D. O'Hare, P. R. Unwin and C. P. Winlove, *Biophys. J.*, 1997, 73, 2771-2781.

37. J. Graebner, S. Jin, G. Kammlott, J. Herb and C. Gardinier, *Nature*, 1992, 359, 401 - 403.

38. J. V. Macpherson, *Phys. Chem. Chem. Phys.*, 2015, 17, 2935-2949.

39. R. Adžić, A. Tripković and N. Marković, *J. Electroanal. Chem. Interfacial Electrochem.*, 1980, 114, 37-51.

40. R. Tenne, K. Patel, K. Hashimoto and A. Fujishima, *J. Electroanal. Chem.*, 1993, 347, 409-415.

41. P. Veluchamy and H. Minoura, *J. Mater. Sci. Lett.*, 1996, 15, 1705-1707.

42. J. Cheng, X. Zou, W. Song, X. Meng, Y. Su, G. Yang, X. Lü, F. Zhang and M. Cao, *CrystEngComm*, 2010, 12, 1790-1794.

43. S. G. Bratsch, *J. Phys. Chem. Ref. Data*, 1989, 18, 1-21.

44. J. Ustarroz, J. A. Hammons, T. Altantzis, A. Hubin, S. Bals and H. Terryn, *J. Am.Chem.Soc.*, 2013, 135, 11550-11561.

45. N. D. Nikolic and K. I. Popov, *Electrodeposition and Surface Finishing*, Springer, 2014.

46. N. Ebejer, M. Schnippering, A. W. Colburn, M. A. Edwards and P. R. Unwin, *Anal. Chem.*, 2010, 82, 9141-9145.

Chapter 5: Laser heated boron doped diamond microelectrode: fundamental investigation and into temperature

In this chapter, an all diamond microstructure: a 50 μm diameter micro-disk boron doped diamond (BDD) sealed in insulating diamond, combined with a pulsed laser set-up, heating the diamond from the rear side, is employed. As boron doped diamond has a very high absorptivity for visible and infrared (IR) light, laser heating is very efficient and it is possible to significantly, rapidly and controllably modify the temperature at the BDD/electrolyte interface. The effect of pulsed heating on the cyclic voltammetric response of simple outer and inner sphere redox mediators ($Ru(NH_3)_6^{3+/2+}$ and $Fe^{2+/3+}$) is investigated. The effect of temperature on the oxidation of dopamine, an electroactive species which is known to form an insulating film on the surface as a result of electrolysis, is then probed. Under ambient conditions the electrode shows fouling behaviour (decreased limiting current, i_{lim}). Interestingly, under laser heated (at P_d of 3.8 kW cm^{-2}) conditions, the fouling is significantly minimized with only 4 % decrease in i_{lim} after 10 CV cycles.

5.1 Introduction

Temperature has been considered to be one of the significant factors that affects the fundamentals of electrochemistry,[1] including mass transport, electron transfer (ET) kinetics and thermodynamics. Electrode processes, such as

adsorption/desorption of reactant, intermediate and product,[2] construction of double layer,[3] are also temperature dependent. As shown in chapter 3, the pulsed laser approach to electrode heating enables the study of temperature as an independent variable with advantages, such as rapid temperature change at electrode surface, higher temperatures (above 100 ^{o}C) achievable and well-defined temperature gradient and mass transport.

Boron doped diamond (BDD), as an electrode material, exhibits a superior electrochemical response[4] (as discussed in chapter 1), and it also has exceptional thermal properties, such as high thermal diffusivity (3 - 11 cm^2 s^{-1}), which is 2 - 3 times higher than that of the metal[5] and high absorptivity for visible and infrared (IR) light. Chapter 3 described the effect of temperature on both mass transport and ET kinetics for outer sphere redox couples at a macrodisc electrode under pulsed heating conditions. In this chapter an all diamond microelectrode[6] (fabricated in a similar way as the all diamond macroelectrode used in chapter 4), combined with a pulsed IR laser focused on the rear of the diamond structure, was employed. Working with microelectrodes has the advantage that a steady-state current is always obtained under a suitably high driving potential and the steady-state analysis is thus simpler than for a macroelectrode system. A similar effect can be produced by rotating a macrodisc electrode.[7] Studies of a rotating disc electrode under controlled temperature conditions found the cyclic voltammetry (CV) signature was significantly affected by the temperature dependent entropy change (ΔS) of the electrode reaction.[7] In this chapter we explore the effect of laser pulsed heating on

the CV response of an all diamond microelectrode towards the electrolysis of both an outer sphere complex ($Ru(NH_3)_6^{3+/2+}$) and an inner sphere one ($Fe^{2+/3+}$).

Electrochemistry plays a vital role in the development of electrode materials and technologies for the detection of biological agents in the environment.[8] A common problem is, however that electrode materials are subject to fouling by the intermediate or product of biomolecule electrolysis. These species tends to absorb on electrode surface and lead to inhibition of the ET process.[9, 10] This is obviously disadvantageous as it is detrimental to the sensitivity and stability of the electrode,[11, 12] affecting the subsequent quantitative analysis. One common example is dopamine, a well-known surface fouling inner-sphere ET neurotransmitter.[13] The oxidation process for dopamine, as shown in Figure 1.12, chapter 1, happens through a complex 2-electron 2-proton process,[14-16] and leads to the product, dopaminequinone, which spontaneously forms leucodopaminechrome. Finally, polymerisation of a melanin-like compound is formed, which suppresses the ET process.[17] Surface fouling phenomena for the oxidation of dopamine has been found in both metal electrodes, such as Au,[18] Pt[19] and conventional carbon electrodes, such as glassy carbon.[20]

Recent studies[21] have shown BDD exhibits resistance to fouling compared to conventional electrode materials. For example, BDD showed superior electrochemical response towards the oxidation of dopamine with the least fouling effect, although still evident (20 % decrease in peak current, i_p) compared to that obtained at glassy carbon electrode (38 % decrease) and highly oriented pyrolytic graphite (HOPG) (43 % decrease).[21] Another crucial feature of BDD as a biosensor

is the potential for long term use compared to all other electrodes, as it can be cleaned in-situ by polarisation[22, 23] and ex-situ by mechanical polishing.

For any ET process that is inner sphere, the kinetics can be enhanced by suitably changing the surface chemistry or chemical identity of the electrode.[24] Regarding the former, researchers have investigated (1) modified electrodes[20, 25-28] and (2) electrode polarisation.[29] For example, it has been found that electrode sensitivity for the oxidation of dopamine[20, 26, 27] and serotonin [26, 30] can be improved by modifying a glassy carbon electrode with Au nanoparticles (NPs)[25-27] or carbon nanotubes.[20, 28] Whilst anodic or cathodic polarisation has been employed to change the surface chemistry of an electrode,[29] it is also used extensively as a means to remove fouled products from an electrode surface, such as phenolic films deposited on Pt electrode.[22] Besides, it has been employed as a technique for reducing fouling at BDD electrodes[23] and carbon nanotube modified microelectrodes.[31] In this chapter, for the first time, we focus on the effect of temperature, induced by the pulsed heating, on the electrochemical response of dopamine oxidation on the BDD microelectrode. An initial molecular dynamic (MD) model is built to study the dopamine absorption/desorption processes at elevated temperatures on the BDD surface with different terminations.

5.2 Materials and methodology

5.2.1 Electrode material

An all diamond co-planar array of BDD microelectrodes (50 μm diameter per electrode, 9 mm overall diameter of substrate and 500 μm in thickness), shown

schematically in Figure 5.1, was synthesised by Element Six (Harwell, UK) using a modified procedure to that employed elsewhere.[6] The fabrication of the structure is similar to that for the all diamond macroelectrode (section 4.2.2, chapter 4). The all diamond structure was back contacted by sputtering Ti (10 nm)/Au (300 nm) and the surface was masked off using Kapton tape with a 1 mm circular hole in the centre to reveal a 50 µm diameter electrode, which is shown in schematically in Figure 5.2a. A FE-SEM image of the microelectrode is shown in Figure 5.2b where it can be seen that the BDD is polycrystalline with grain sizes ranging from 5 µm to 20 µm.

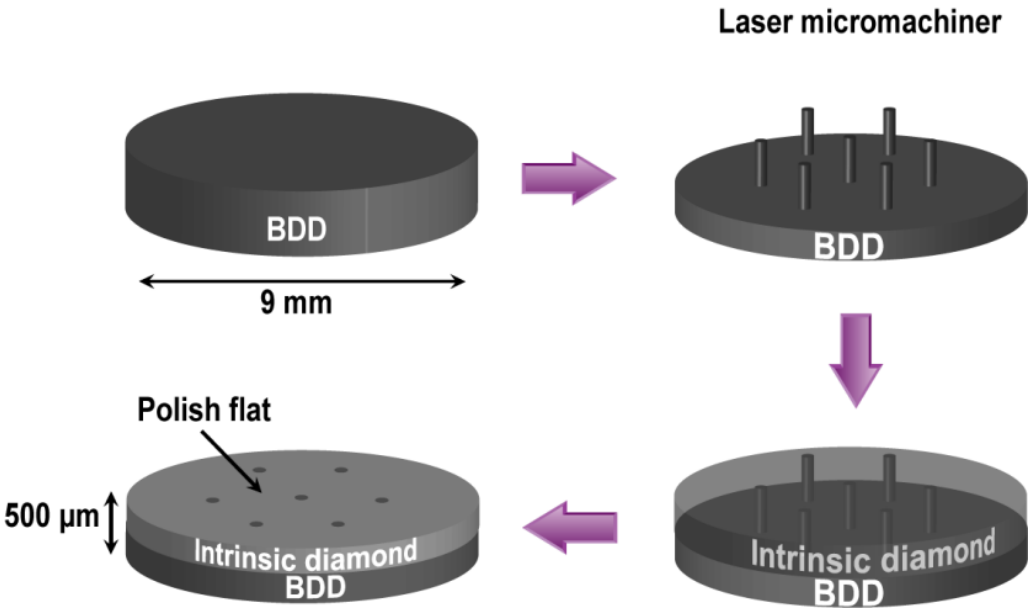

Figure 5.1: (a) 9 mm diameter CVD grown BDD disk; (b) Laser micromachining to etch away the surrounding BDD and produce 50 µm diameter cylinder array protruding from the surface; (c) Intrinsic diamond overgrown on top of BDD; (d) Polish to reveal the 50 µm diameter BDD array. The final thickness of all diamond structure is 500 µm.

The micro-disk BDD electrode has a measured diameter of 48.2 µm. The contrast of the BDD in the FE-SEM indicates the difference in boron doping level at

different crystallographic orientations.[32] The lighter grain indicates less boron uptake, and more boron uptake makes the grain darker. The boron doping level in both grains is > 10^{20} B atoms cm^{-3}, which makes the BDD metallic in nature. The ratio of the light and dark grain ($R_{l/d}$) in the BDD region is *ca.* 7:3. The all diamond microstructure was mounted on the cell for laser heating experiments in the same way as described in chapters 3 and 4.

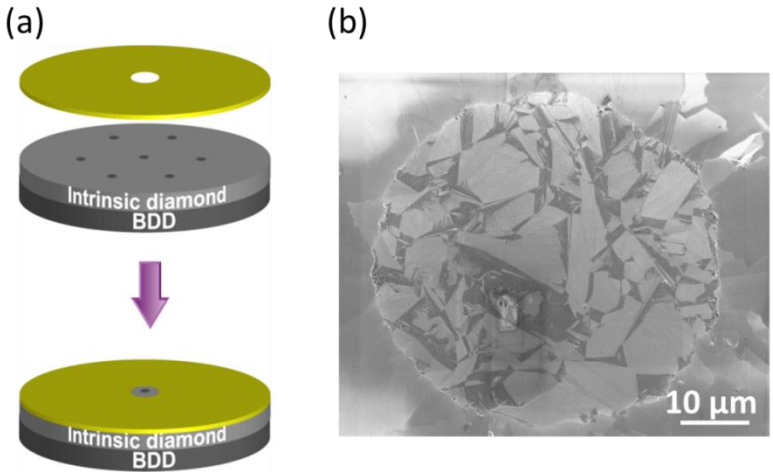

Figure 5.2: (a) Single BDD micro-disk electrode defined by Kapton tape masking off the other arrays with 1 mm diameter circular hole in the centre. (b) Typical SEM image of micro-disk structure.

5.2.2 Temperature pulsed voltammetry (TPV)

CV was performed simultaneously with pulsed laser heating *i.e.* TPV. For all TPV experiments the basic premise is the imposition of a pulsed laser to heat the surface of the electrode during CV measurements. For all microelectrode experiments, the laser was repeatedly switched on for 10 ms and off for 990 ms. A

10 mV s^{-1} scan rate and 0.01 potential step was employed, so current values were collected every 1 ms so a total of 1000 data points per second were collected.

5.2.3 COMSOL simulation

Temperature at the electrode/electrolyte interface and TPVs for the reduction of $Ru(NH_3)_6^{3+}$ were simulated using COMSOL Multiphysics 4.3b (COMSOL, SE) finite element analysis (FEA) software. The approach is outlined in chapter 3 but with slight modification on the dimension of the diamond, where a diamond structure with thickness of 500 µm and diameter of 9 mm is employed. The diameter of BDD microelectrode is 48.2 µm and a pulsed external energy input (laser on for 10 ms, off for 990 ms) is employed.

5.3 Results and discussion

5.3.1 Electrochemical characterisation of the all diamond BDD microelectrode at ambient condition

The BDD microelectrode was firstly assessed electrochemically under ambient conditions for the reduction of 1 mM $Ru(NH_3)_6^{3+}$ to examine the material quality (whether pin holes or defects exist) of the microelectrode structure. CVs from both experimental (red) and finite element simulation (black) for the reduction of $Ru(NH_3)_6^{3+}$ on BDD microelectrode at a scan rate of 10 mV s^{-1} are shown in Figure 5.3.

The CV shows a typical microelectrode signature with a limiting current (i_{lim}) of *ca.* - 8.25 nA, at the potential of - 0.35 V *vs* Ag/AgCl. The i_{lim} for a disk microelectrode is determined by equation 1.11 in chapter 1. The theoretical i_{lim}, taking the radius (24.1 μm) from the SEM image and the diffusion coefficient, *D*, (8.8×10^{-6} cm^2 s^{-1}) of $Ru(NH_3)_6^{3+}$ from literature,[33] is calculated to be - 8.18 nA, which is slightly smaller than the experimental value. This is probably due to the mass transport contribution from the slightly rough edge of the micro-disk (shown in the FE-SEM image in Figure 5.2), which reflects the original cut of the laser to define the cylinder.

The ΔE_p, using equation 1.12 in chapter 1, is calculated to be 63 mV, indicating a reversible process for the reduction of $Ru(NH_3)_6^{3+}$ on the BDD microelectrode. The simulated CV shows good agreement with the experimental data, and only exhibits a very small discrepancy on the i_{lim} (- 8.22 nA compared to - 8.25 nA obtained experimentally), which is likely caused by either the non-faradic (background) process or the faradic process contributed from the rough edge of the microdisk electrode, resulting in slightly larger i_{lim} experimentally. The simulated half wave potential, $E_{1/2}$, for the reduction of $Ru(NH_3)_6^{3+}$ is - 173 mV, which is in good agreement with that (- 175 mV) obtained from experimental data.

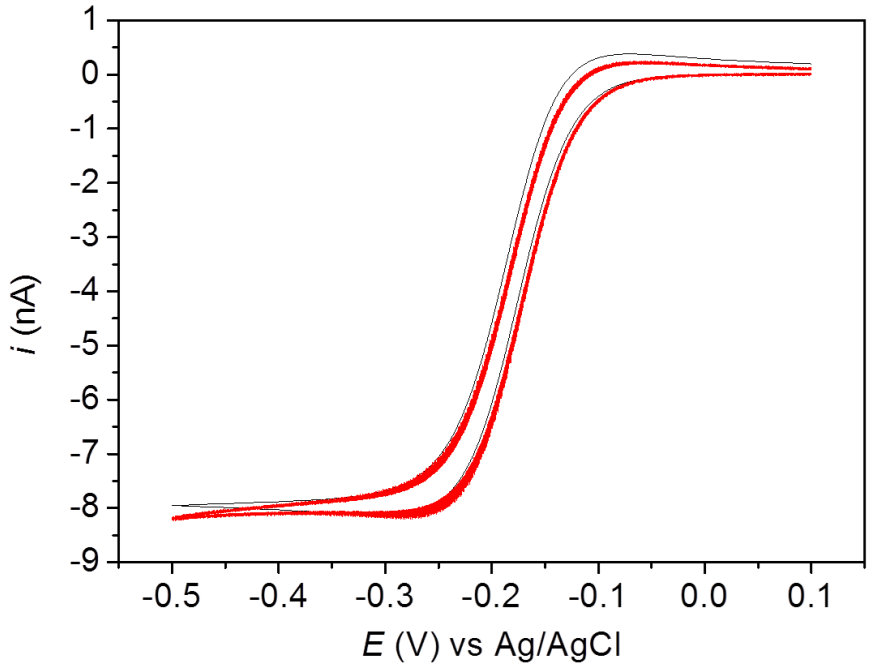

Figure 5.3: Experimental (red) and simulated (black) CVs for the reduction of 1 mM $Ru(NH_3)_6^{3+}$ *on a BDD microelectrode. Scan rate is 10 mV* s^{-1}.

5.3.2 Temperature determination at electrode/electrolyte interface

Prior to laser heated CV experiments, the temperature at the electrode/electrolyte interface was modelled. Figure 5.4 shows the average temperatures at the electrode surface at different laser power densities (P_d's). Interfacial temperature increased rapidly when the laser was switched on due to the high thermal diffusivity (3 - 11 cm^2 s^{-1}) of the diamond, which delivers heat from the rear to the solution side quickly. The temperature reached its maximum at t = 10 ms, followed by a significantly decrease as the laser was switched off. During the cooling off period (990 ms), the temperature decreased at a slow rate due to the large heat capacity of water, hindering heat transfer from electrode surface to the bulk

water. Highest average interfacial temperature at t = 10 ms was obtained for different P_d's. Specifically, 47.1 ^{o}C (1.2 kW cm^{-2}); 68.4 ^{o}C (2.5 kW cm^{-2}); 105.5 ^{o}C (3.8 kW cm^{-2}). The average interfacial temperatures at the microelectrode is slightly larger than that (46.4 ^{o}C (1.2 kW cm^{-2}), 62.9 ^{o}C (2.5 kW cm^{-2}), 90.0 ^{o}C (3.8 kW cm^{-2})) obtained at the macroelectrode in chapter 3, which is likely caused by the homogenous thermal distribution across the microelectrode (48.2 µm in diameter) surface (laser spot is 1 mm in diameter which is comparable with the size of the macroelectrode).

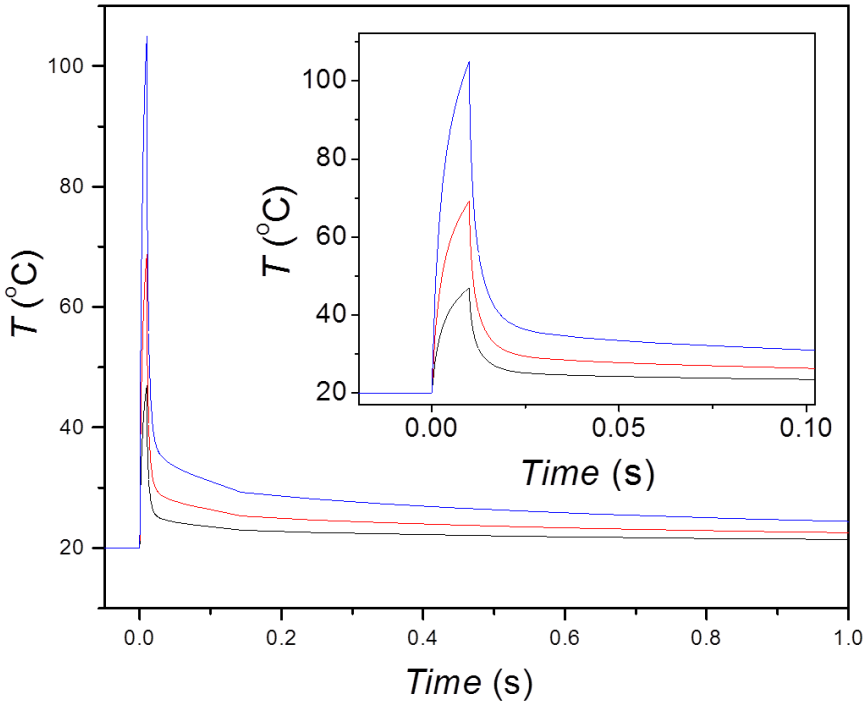

Figure 5.4: Simulated average temperatures at a BDD microelectrode surface for a single laser pulse at P_d of 1.2 (black), 2.5 (red) and 3.8 (blue) kW cm^{-2}. The laser was switched on for 10 ms and off for 990 ms. Inset shows the zoomed-in image of the laser pulse region.

5.3.3 Thermoelectrochemical response of a surface insensitive redox mediator ($Ru(NH_3)_6^{3+}$) on the BDD microelectrode

Initial high temperature experiments were carried out for the reduction of the fast ET outer sphere redox couple, $Ru(NH_3)_6^{3+}$, at the BDD microelectrode, as shown in Figure 5.5. A laser power density of 1.2 kW cm^{-2} was employed corresponding to an average local temperature of 47.1 ^{o}C. It can be seen from Figure 5.5a the CV exhibits a limiting current response with current spikes superimposed on top of the CV due to the applied pulsed laser, periodically heating and cooling the electrode surface. For a more detailed illustration, the CV was split into two components: the forward (Figure 5.5b) and backward (Figure 5.5c) scans.

In the microelectrode CV measurements, a scan rate of 10 mV s^{-1} was employed with a potential step of 0.001 mV, which provides a total of 10 current sampling points per laser pulse (10 ms). Raw data is collected and then sampled by taking the 10^{th} point for each laser pulse, corresponding to the last sample at the end of each laser pulse. TPV is then constructed, which is illustrated in Figure 5.5bii and cii for the forward and backward scan, respectively. The plot of 'sampled' current as a function of potential is shown in Figure 5.5d. For comparison the CV (blue line) under ambient conditions is shown.

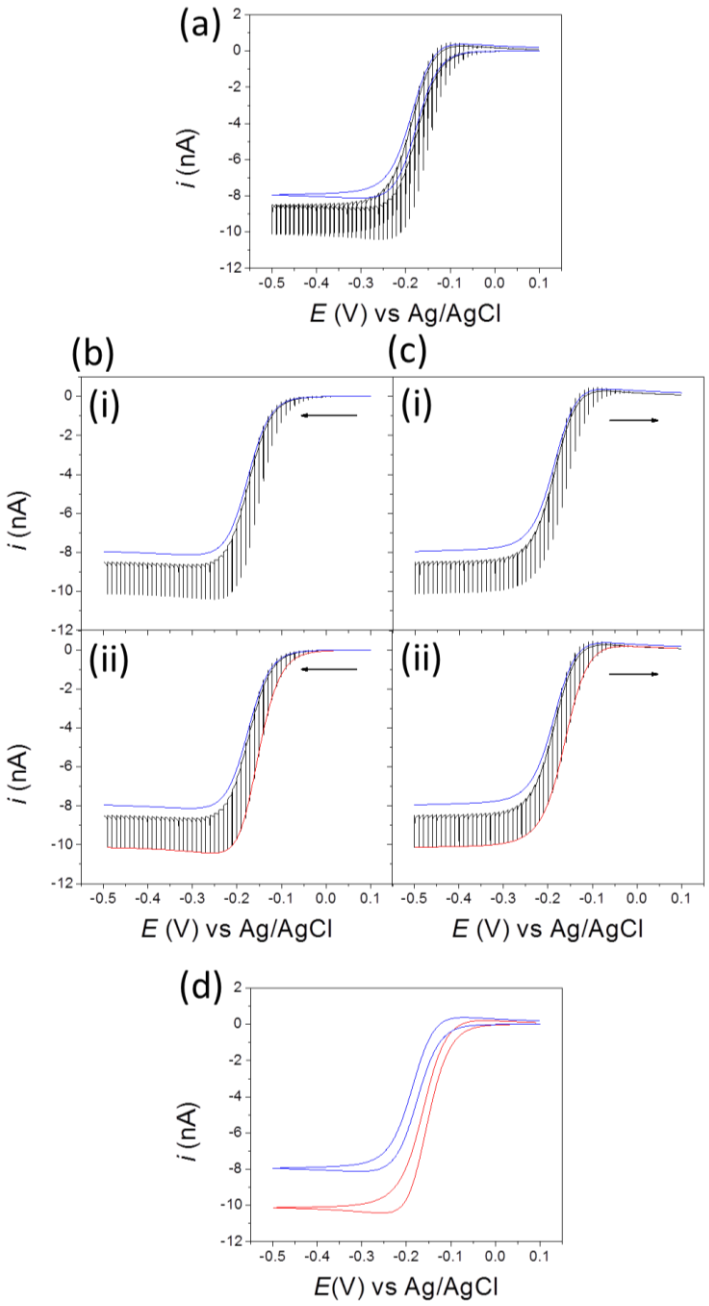

Figure 5.5: (a) Pulsed laser heated CV (P_d of 1.2 kW cm^{-2}, laser on for 10 ms, off for 990 ms) for the reduction of 1 mM $Ru(NH_3)_6^{3+}$ at a BDD microelectrode, scan rate 10 mV s^{-1}. (bi) and (ci) represent the forward and backward scans. (bii) and (cii) shows the 'sampled' TPV data by taking the current value at the end of each 10 ms laser pulse. (d) The TPV is constructed by plotting the 'sampled' current as a function of potential. For comparison the CV (blue line) under ambient conditions is shown.

Figure 5.6 shows both experimental (a) and simulated (b) TPVs (*i.e.* current values obtained at the end of each laser pulse were plotted against potential) for the reduction of 1 mM $Ru(NH_3)_6^{3+}$ on a BDD microelectrode at P_d of (a) 1.2 and (b) 2.5 kW cm^{-2}, respectively, corresponding to average surface temperatures of 47.1 and 68.4 ^oC. TPVs in Figure 5.6a exhibit typical limiting current response, similar to that obtained under ambient conditions. However two distinct features were observed, *i.e.* the increased i_{lim} (10.2 nA for 1.2 kW cm^{-2} and 12.1 nA for 2.5 kW cm^{-2}) and the positive shift of the $E_{1/2}$ (shown in Table 5.1).

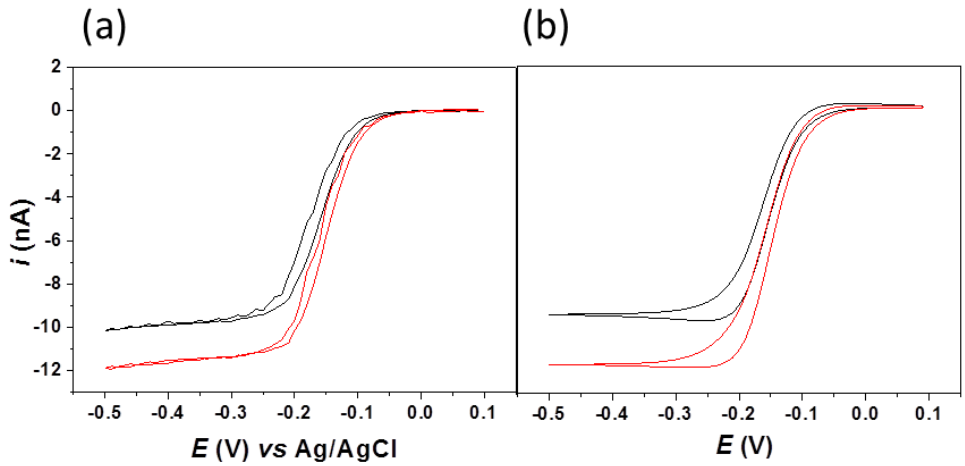

Figure 5.6: (a) Experimental and (b) simulated TPVs for the reduction of 1 mM $Ru(NH_3)_6^{3+}$ on a BDD microelectrode at P_d of 1.2 (black) and 2.5 (red) kW cm^{-2}. Scan rate is 10 mV s^{-1}.

The former is due to the enhanced mass transport rate of redox species towards electrode surface, as a result of the thermal enhancement of the diffusion (Stokes-Einstein equation 3.6 in chapter 3). Note the enhancement in limiting current observed at the microelectrode is less than that (peak current) observed at the macroelectrode (Figure 3.7, chapter 3) due to the increased diffusional flux of species to a microelectrode. The positive shift in $E_{1/2}$ is due to the positive sign of β

for the $Ru(NH_3)_6^{3+/2+}$ system,[7] which was calculated as +0.68 mV K^{-1} from a plot of open circuit potential (OCP) versus ΔT (R^2 = 0.99) over a ΔT range of 60 ^oC (Figure 3.8, chapter 3), which is in close agreement with literature values.[34]

The simulated TPVs in Figure 5.6b show good agreement with the experimental data. The current does not quite reach plateau for the experimental data and this may be due to the background processes from the BDD microelectrode. The shift in $E_{1/2}$ for the simulated CVs (controlled by β) again agrees well with that observed experimentally, as shown in Table 5.1.

Table 5.1: Experimental and simulated $E_{1/2}$'s vs Ag/AgCl for the reduction of $Ru(NH_3)_6^{3+}$ at ambient and laser heated conditions

Laser P_d	Experimental	Simulation
ambient	-173 mV	-175 mV
1.2 kW cm^{-2}	-158 mV	-158 mV
2.5 kW cm^{-2}	-148 mV	-145 mV

5.3.4 Thermoelectrochemical response of a surface sensitive redox process (Fe^{2+})

Surface sensitive (inner sphere) ET processes are strongly influenced by the heterogeneity and surface termination of the electrode surface.[29, 35] Studies were then focused on the effect of temperature on the electrochemical response of Fe^{2+}, which has been shown to be surface sensitive in the literature.[35] Figure 5.7 shows 'sampled' TPVs for the oxidation of 1 mM Fe^{2+} at P_d of 1.2 (47.1 ^oC, blue) and 2.5 (68.4 ^oC, red) kW cm^{-2}, respectively. For comparison the ambient CV (black line) is also

shown in Figure 5.7. It can be seen that limiting current increased with the increasing of P_d, resulting from the enhanced mass transport, with specifically, 6.2 nA at ambient conditions, 8.5 nA at 1.2 kW cm^{-2} and 10.6 nA at 2.5 kW cm^{-2}. A negative shift of $E_{1/2}$ for the oxidation of Fe^{2+} was observed, which is listed in Table 5.2 for different P_d's.

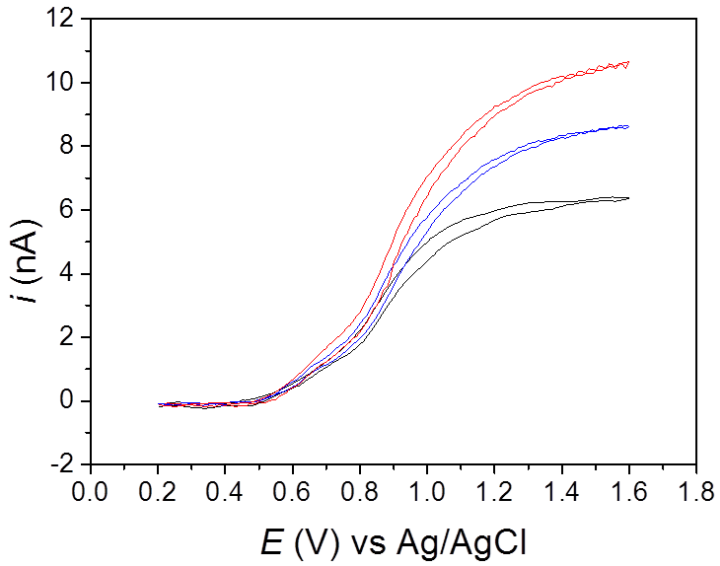

Figure 5.7: Ambient CV (black) and 'sampled' TPVs for the oxidation of 1 mM Fe^{2+} on a BDD microelectrode at P_d of 1.2 (47.1 °C, blue) and 2.5 (68.4 °C, red) kW cm^{-2}. Scan rate is 10 mV s^{-1}.

β for the $Fe^{2+/3+}$ system was experimentally determined as -1.72 mV K^{-1} (section 2.3.1, chapter 2) which is close to the literature value.[36] Using this β value the calculated $E_{1/2}$'s for the different surface temperatures are listed in Table 5.2. As can be seen the calculated $E_{1/2}$ is slightly larger than the experimental data. The negative shift of $E_{1/2}$ is caused by a combination of temperature dependent formal potential (β) and ET kinetics. The slight difference between experimental and

calculated $E_{1/2}$ indicates the contribution from thermodynamic is dominant (contribution from the temperature enhanced ET process is relatively small).

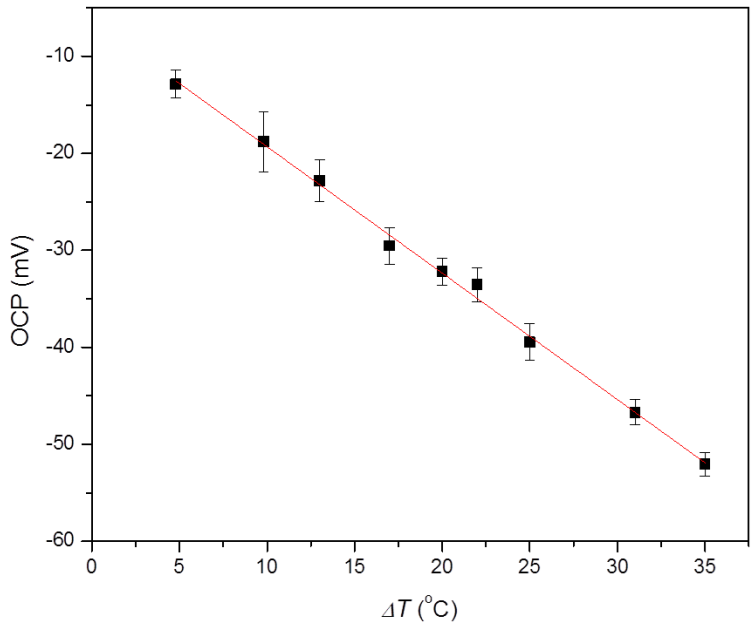

Figure 5.8: OCP between two identical 1 mm pBDD electrode in 0.1 M $HClO_4$ solution containing 0.5 mM Fe^{3+} and 0.5 mM Fe^{2+}. One of the pBDD electrodes was held at room temperature, while the other in a heated water bath.

Table 5.2: $E_{1/2}$ vs Ag/AgCl for the oxidation of Fe^{2+} at ambient and laser heated conditions. Note E_o for the $Fe^{2+/3+}$ couple is 741 mV vs standard hydrogen electrode (SHE) in perchlorate medium on Pt electrode[37] and it is electrode material dependent (inner sphere redox couple)

Laser P_d	Experimental	Calculated $E_{1/2}$
Ambient	679 mV	*N/A*
1.2 kW cm^{-2}	669 mV	677 mV
2.5 kW cm^{-2}	659 mV	665 mV

The actual shape of the CV is unusual. Clear evidence from the CV and TPVs in Figure 5.7 is the observation of a small 'shoulder current' (i_s) prior to the larger limiting current. i_s under ambient conditions is 1.08 nA, which is *ca.* 18 % of i_{lim} (6.2 nA). This could indicate there are two different rates of ET occurring on the electrode surface, with the shoulder current representing the faster rate. The ratio is 19.6 % and 19.1 % for P_d of 1.2 and 2.5 kW cm^{-2}, respectively. Previous studies[38] have shown the BDD surface to be heterogeneous towards ET processes due to the differently doped crystal facets of polycrystalline BDD. This material has been grown thick enough and then polished flat so that the facets have a size in the range 5 - 20 μm (Figure 5.2). The reason for different doping levels is due to the different crystallites of BDD uptaking boron at different rates. It is reported boron is more incorporated (about 10 times) into (111) surface than the (100) facet.[39, 40]

The oxygen surface terminations of the differently doped crystal facets is different,[29] which could also have an effect on the resulting ET kinetics of an inner sphere species.[29] However, after growth the surface is polished flat for electrochemical studies resulting in a different crystallography for the electrode surface than the as-grown ones (as shown in Figure 1.2c and d, chapter 1). Electron backscatter diffraction (EBSD) was thus employed to determine the resulting crystallography of the polished polycrystalline material, as shown in Figure 5.9. It can be seen that after polishing the surface is dominated by one crystal plane, (110), which is known to have ether and ketone surface terminations.[41] Due to the observation of dominant (110) facet on the BDD surface from the EBSD data, surface termination is unlikely to explain the shoulder current presented in the CV

and TPVs, thus it could be due to the different boron dopant levels in different grians (evidenced by the contrast in the SEM image) which result in different local density of states at the electrode surface. It has previously been observed on BDD using high resolution electrochemical imaging techniques, that k_0 at highly doped facets (darker grains) is *ca.* 4 times compared to that in the less highly doped facets (lighter grains). Thus the shoulder current at the less positive potential could be due to contributions from the highly doped grains. The FE-SEM image showed the ratio of the darker to lighter grains is *ca.* 3:7, *i.e.* the darker, more conducting grains occupy ~ 30 % of the surface.

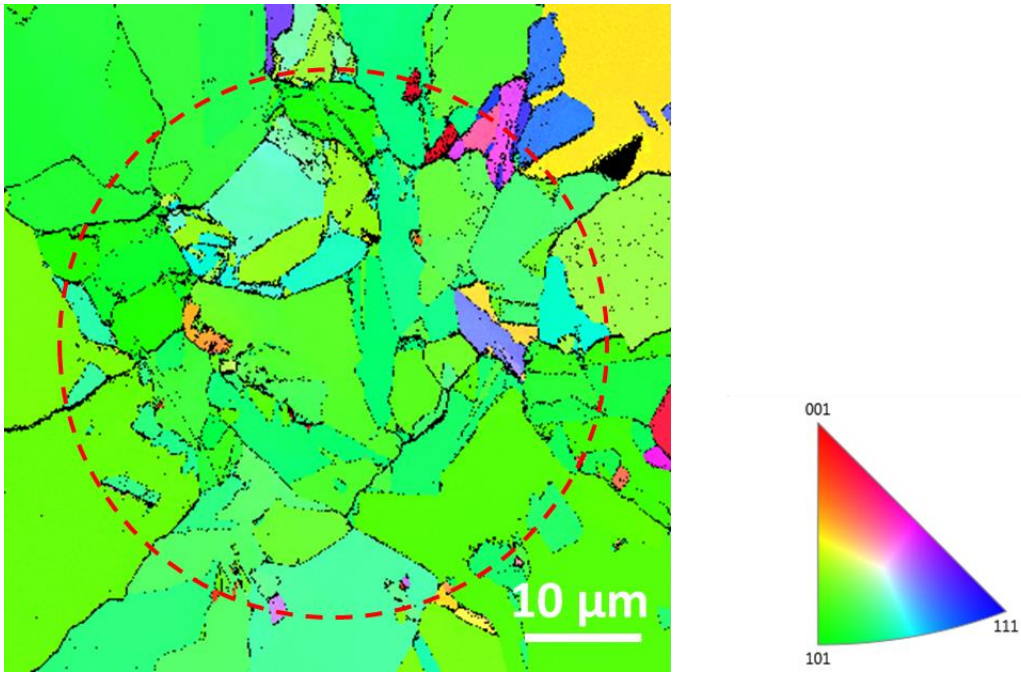

Figure 5.9: EBSD image with the colour coded orientation map on the BDD microelectrode. Red dash line highlights the boundary between BDD and intrinsic diamond. The corresponding SEM image is shown in Figure 5.2b.

5.3.5 Effect of temperature on the oxidation of dopamine

It is well known that the electro-oxidation of dopamine leads to rapid fouling and contamination of the electrode surface due to the adsorption of dopamine product.[42] Consecutive CVs and TPVs (10 cycles) were employed to assess the extent to which the electrode fouled during dopamine oxidation.

Consecutive CVs and TPVs are recorded with 5 seconds quiet time interval and are shown in Figure 5.10 for the oxidation of 1 mM dopamine (10 mM phosphate buffer, pH 7.2) at a scan rate of 10 mV s^{-1}, at ambient conditions (a), P_d of 1.2 (b), 2.5 (c) and 3.8 (d) kW cm^{-2}, respectively. Using equation 1.11 provided in the chapter 1, the theoretical i_{lim} was calculated to be 10.3 nA, using a D of 5.8 $\times 10^{-6}$ cm^2 s^{-1} [43] and n of 2 for the oxidation of 1 mM dopamine. The value is in close agreement with the experimental i_{lim} (10.1 nA) for the 1st CV at ambient conditions.

Significant changes in electrochemical response were observed after the first cycle, with decreased i_{lim} and positively shifted $E_{1/2}$. The former indicates the blocking due to the absorption of dopamine product on the electrode surface and the latter indicates hindered ET process. The limiting current for the 10th CV is 52.8 % of that from the initial CV, which is presented in Figure 5.11 and the $E_{1/2}$ shifted positively from 683 mV (1st CV) to 741 mV (10th CV), showing the deterioration of electrode response, which could be due to surface chemistry where dopaminergic compounds absorbing on 'active sites' on the BDD surface, resulting in decreased i_{lim} and sluggish ET process.

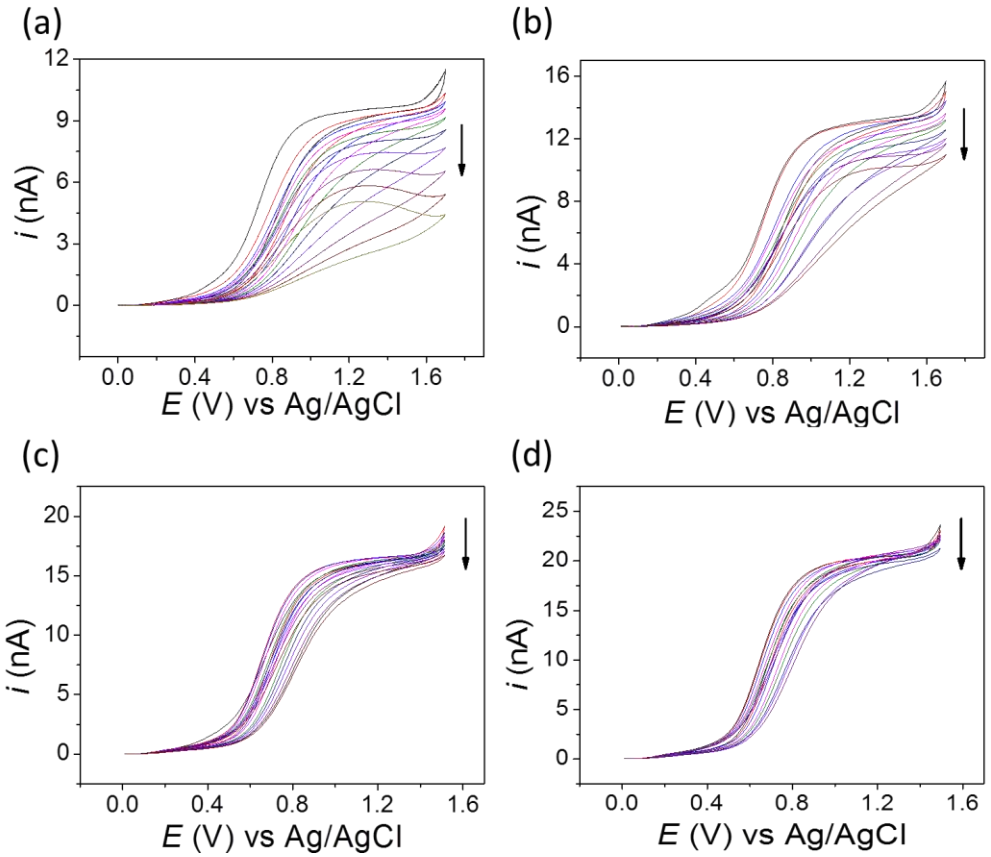

Figure 5.10: 10 consecutive CVs in ambient condition (a) and 'sampled' TPVs on BDD microelectrode for the oxidation of 1 mM dopamine (10 mM phosphate buffer, pH 7.2) at P_d of 1.2 (b), 2.5 (c) and 3.8 (d) kW cm^{-2}. Scan rate 10 mV s^{-1}.

Experiments were then carried out to assess the effect of temperature on the fouling effect on the BDD surface for the electro-oxidation of dopamine. Note that during the 5 second interval no pulsed laser heating was applied. Under laser heated conditions, increased i_{lim}'s (13.5 nA for 1.2 kW cm^{-2} (47.1 °C), 17.5 nA for 2.5 kW cm^{-2} (68.4 °C) and 21.2 nA for 3.8 kW cm^{-2} (105.5 °C)) and slightly negative shifted $E_{1/2}$ (670 mV for 1.2 kW cm^{-2}, 658 mV for 2.5 kW cm^{-2} and 643 mV kW cm^{-2}) for the 1st cycle were observed, where the former indicates the enhanced mass transport and the latter shows increased ET kinetics and thermodynamics at elevated

temperatures. Interpreting the effect of β on the dopamine oxidation is difficult as equal molar of both the oxidised and reduced form of dopamine is needed in order to measure β. The successive $i_{lim,}$ for all P_d's, decreased in magnitude, but only by a small extent, compared to that in ambient conditions, indicating the blocking effect is less prominent, which is possibly due to the increased diffusion of dopamine product at elevated temperatures.[44]

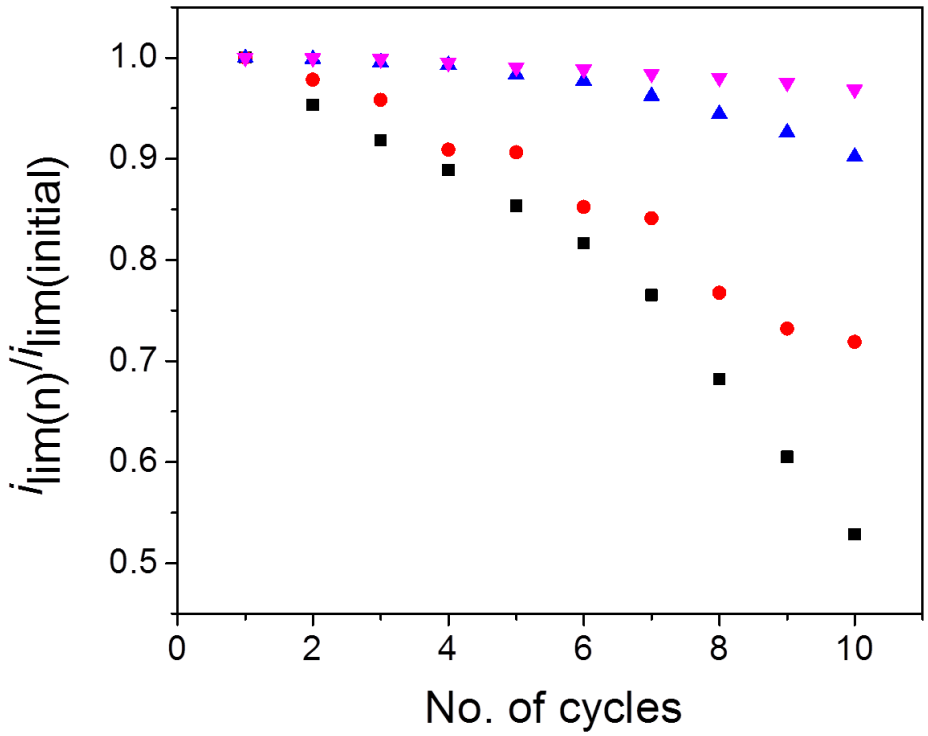

Figure 5.11: $i_{lim(n)}/i_{lim(initial)}$ as a function of number of cycles for the oxidation of 1 mM dopamine (data collected from Figure 5.10). Ambient: ■; 1.2 kW cm^{-2}: ●; 2.5 kW cm^{-2}: ▲; 3.8 kW cm^{-2}: ▼;

A plot of $i_{lim(n)}/i_{lim(initial)}$ as a function of number of cycles, n, (shown in Figure 5.11) allows an easy comparison at the different temperatures. The plots show that the oxidation of dopamine under ambient condition is most affected by the

fouling since after 10 cycles i_{lim} decreased to *ca.* 52.8 % of the initial i_{lim}. However, under laser heated conditions, the decrease in i_{lim} is significantly minimised; *i.e.* the 10^{th} i_{lim} is 73%, 90 % and 96 % of initial i_{lim} for P_d of 1.2, 2.5 and 3.8 kW cm^{-2}, respectively. The results show the BDD electrode exhibits superior resistance to fouling at elevated temperature compared to ambient conditions, indicating the dopaminergic compounds have a stronger adsorption affinity at room temperature[44] compared to that at elevated temperatures, though the reaction rate for dopamine oxidation is more favourable at high temperature.

5.4 Molecular dynamic simulations

In addition to experiments, a simple MD simulation was carried out to assess the effect of temperature (room temperature, 25 ^{o}C and P_d of 20 kW cm^{-2}, 68.4 ^{o}C) on the dopamine absorption/desorption processes at a diamond surface with different terminations (hydrogen (C-H), ether (C-O-C) and ketone (C=O)). A single crystalline (100) facet of diamond is chosen to simplify the MD simulation, though as shown in the EBSD image (Figure 5.9), the (110) facet dominates the electrode surface. However, the (100) facet contains similar surface groups (C-H, C-O-C, C=O) to the (110) facet[29] and hence at a first approximation the dopamine surface interactions should be comparable.

5.4.1 Model equilibration

All simulations were carried out using GROMACS v.4.6.5 software package.[45] Diamond slabs and dopamine were energy minimised separately for 5000 steps. Dopamine was equilibrated firstly in vacuum for 500 ps, followed by in a 15 nm^3 water box for 500 ps in the *NVT* (fixed number of particles, volume and temperature) ensemble, and then for 1 ns in the *NAPzT* (fixed number of particles, cross-sectional area, pressure in the *z*-direction and temperature) ensemble using a time step of 2 fs and coordinates saved every 10 ps (5000 steps), where T = 25 ^{o}C and P = 1 bar. 150 pre-equilibrated dopamine molecules were inserted randomly into the simulation box above and below the diamond slab. The box was then solvated with 14600 water molecules and 150 counter ions (Cl^-) to maintain electroneutrality of the system using the Gromacs genion tool. The solvated systems were energy minimised at room temperature (25 ^{o}C) and laser temperature (68.4 ^{o}C) for 5000 steps and then equilibrated for 100 ps in the *NAPzT* ensemble. Harmonic restraints of 1000 kJ mol^{-1} nm^{-2} were placed on all dopamine molecules during equilibration to ensure they remained at fixed positions. The final simulation box has *xyz*-dimensions of 7.13 × 7.13 × 12.45 nm^3, with the centre of the diamond slab positioned at the centre of the box.

5.4.2 Model running

All harmonic restraints placed on the dopamine molecules during equilibration were removed and the simulations were run at room temperature (25 ^{o}C) and laser heated conditions (P_d = 1.2 kW cm^{-2}, *i.e.* 68.4 ^{o}C) for each surface for

20 ns in the *NAPzT* ensemble, where the first 15 ns of all simulations were considered as the equilibration phase and the remaining 5 ns was used for subsequent analysis. Simulations were run using a time step of 2 fs with coordinates saved every 100 ps (50000 steps). *NAPzT* ensemble is used as it matches closely to the experimental conditions.

5.4.3 Analysis

The simulations were analysed using tools available in GROMACS, visual molecule dynamics (VMD) and locally written scripts. All MD trajectories were visualised using VMD. Figure 5.12 shows an illustrative VMD snapshot of dopamine molecules adsorbed on (100) H-terminated diamond surface at room temperature when the system is equilibrated. H-terminated diamond surface is employed to compared with oxygen terminated surface for dopamine absorption/desorption process at elevated temperature. The number of dopamine molecules adsorbed per time frame was counted over the last 5 ns using geometric criteria, where a dopamine molecule was considered adsorbed if the z-coordinate of the centre of mass was within 0.7 nm of the diamond surface (on either top or bottom face). This geometric cut-off was chosen as it matches to the adsorption distance calculated in a previous single dopamine-diamond MD adsorption study.[46] The average and standard deviation of adsorbed dopamine molecules was calculated from the last 2 ns.

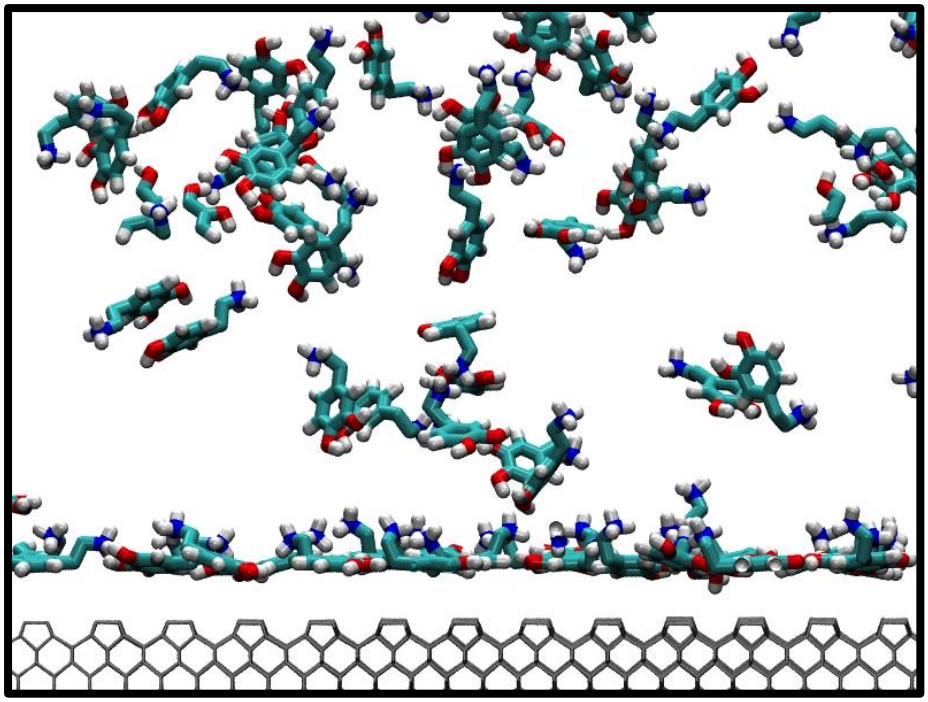

Figure 5.12: Illustrative VMD snapshot of dopamine molecules adsorbed on (100) H-terminated diamond surface at room temperature when the system is equilibrated.

5.4.4 MD simulation results

Figure 5.13 shows the plots of dopamine adsorption over time on three different surfaces of (100) diamond (a) H-terminated, (b) C-O-C-terminated and (c) C=O-terminated diamond at room temperature (25 ^{o}C, black) and laser heated conditions (68.4 ^{o}C, green). It is observed fewer dopamine molecules adsorb in both H- (43 ± 1) and C=O- (55 ± 1) terminated diamond surface at the high temperature (68.4 ^{o}C) compared to that (55 ± 2 for H-terminated and 75 ± 1 for C=O-terminated surface) obtained room temperature, which is in agreement with the experimental data, where less fouling was observed under laser heated conditions. It can also be seen that dopamine adsorbs more favourably to oxygen terminations (75 ± 1 dopamine molecules for C-O-C- and C=O- terminated surface at 25 ^{o}C) than

hydrogen termination (55 ± 2 dopamine molecules for H-terminated surface at 25 ^{o}C). This is helpful for future experiments to study the dopamine adsorption/desorption processes on diamond surface by anodic/cathodic polarisation, which modifies the density of surface oxygen groups.

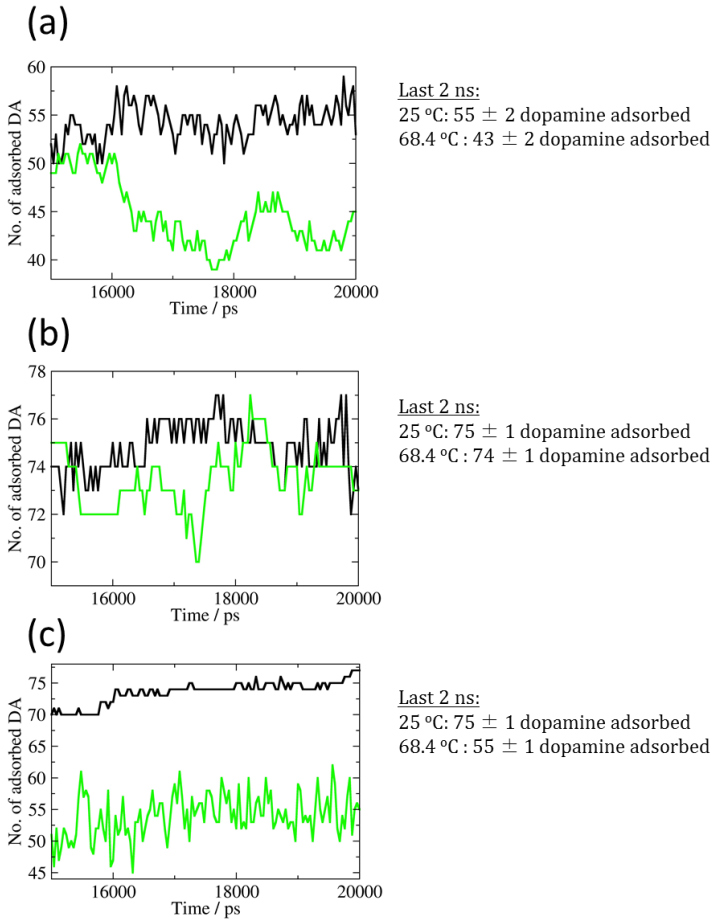

Figure 5.13: Plots of dopamine adsorption over time on three different surfaces (a) H-terminated, (b) C-O-C--terminated and (c) C=O--terminated diamond at ambient conditions (25 ^{o}C, black) and laser heated conditions (68.4 ^{o}C, green).

5.4.5 Future MD simulation work

The MD simulation was carried out on an inert diamond surface, where surface atoms have partial charges that cancel each other out, hence there is no overall charge. MD simulation implemented with additional surface charges to mimic a diamond electrode surface is needed. A mixture of surface termination (C-H, C-O-C, C=O) on the same diamond surface, different crystal facets and absorption/desorption processes of dopamine product molecules are of interest to further study the system.

5.5 Conclusions

An all diamond microelectrode was fabricated and firstly characterised electrochemically using an outer sphere fast ET redox mediator, $Ru(NH_3)_6^{3+}$, to assess the quality of the structure under ambient conditions. Experimental CV was then compared with finite element simulation and good agreement was obtained, indicating the high quality (no pin holes or defects) of the fabricated microelectrode structure.

A pulsed heating technique, as described in chapters 3 and 4, was employed, as a fast controllable heat source. In these measurements, laser pulses of 10 ms duration (990 ms off) were delivered onto a ~ 1 mm spot on the rear side of the BDD microelectrode. Due to the superior thermal diffusivity of diamond, heat propagates to the electrode surface (solution side) rapidly. Average temperature at the electrode/electrolyte interface was obtained, *i.e.* 47.1 ^{o}C (1.2 kW cm^{-2}); 68.4 ^{o}C (2.5 kW cm^{-2}); 105.5 ^{o}C (3.8 kW cm^{-2}).

The effect of temperature on the electrochemical response of both an outer sphere ($Ru(NH_3)_6^{3+}$) and an inner sphere (Fe^{2+}) redox mediator on the BDD microelectrode were studied. Increased i_{lim}'s were observed in both cases, due to the enhanced mass transport rate at elevated temperatures. TPV showed a positive shift in $E_{1/2}$ for the reduction of $Ru(NH_3)_6^{3+}$ due to the positive sign of β (+0.68 mV K^{-1}), in accordance with the simulated TPV, whereas a negative shift in $E_{1/2}$ for the oxidation of Fe^{2+} was evidenced, which was caused by a combination of the enhanced ET kinetics and the negative sign of β (-1.72 mV K^{-1}). Interestingly, CV and TPVs for the oxidation of Fe^{2+} exhibited 'shoulder currents'. This we believe is due to the heterogeneity of the polycrystalline nature of the BDD surface, where highly doped grains exhibits superior ET process compared to less heavily doped grains.

The pulsed laser heating system was then moved to study a well-known surface fouling redox mediator, dopamine. Consecutive CVs at ambient conditions for the oxidation of dopamine on the BDD microelectrode showed decreased i_{lim} ($i_{lim(10)}$ is 52.8 % of $i_{lim(initial)}$), as an evidence for the surface fouling resulting from the dopamine product. Minimised fouling (only decrease by 4 % in i_{lim} at P_d of 3.8 kW cm^{-2} over ten cycles) was achieved by TPV, where temperature pulses was applied during potential scans. Thus BDD is promising for high temperature thermoelectrochemical measurements for the surface sensitive (fouling) bio-molecules.

MD simulations on H-terminated and ketone-terminated diamond (100) facet indicate less dopamine molecules absorption under heated conditions, which is in

good agreement with experimental data and provide guidance for future experiments on examining the surface fouling effect of dopamine oxidation on the polycrystalline BDD with different surface functional groups.

5.6 References

1. P. Gründler, In-situ Thermoelectrochemistry, Springer Berlin Heidelberg, 2015.

2. A. Zolfaghari and G. Jerkiewicz, J. Electroanal. Chem., 1997, 420, 11-15.

3. L. Fokkink, A. De Keizer and J. Lyklema, J. Colloid Interface Sci., 1989, 127, 116-131.

4. J. V. Macpherson, Phys. Chem. Chem. Phys., 2015, 17, 2935-2949.

5. L. Meng, J. G. Iacobini, M. B. Joseph, J. V. Macpherson and M. E. Newton, Faraday Discuss., 2014, 172, 421-438.

6. M. Pagels, C. E. Hall, N. S. Lawrence, A. Meredith, T. G. Jones, H. P. Godfried, C. J. Pickles, J. Wilman, C. E. Banks and R. G. Compton, Anal. Chem., 2005, 77, 3705-3708.

7. J. Valdes and B. Miller, J. Phys. Chem., 1989, 93, 7275-7280.

8. A. P. Turner, Chem. Soc. Rev., 2013, 42, 3184-3196.

9. J. Wang, Electroanalysis, 2005, 17, 7-14.

10. M. Musameh, J. Wang, A. Merkoci and Y. Lin, Electrochem. Commun., 2002, 4, 743-746.

11. S. V. Sasso, R. J. Pierce, R. Walla and A. M. Yacynych, Anal. Chem., 1990, 62, 1111-1117.

12. R. J. Geise, J. M. Adams, N. J. Barone and A. M. Yacynych, Biosens. Bioelectron., 1991, 6, 151-160.

13. J. Ghilane, F. Hauquier and J.-C. Lacroix, Anal. Chem., 2013, 85, 11593-11601.

14. K. Wu, J. Fei and S. Hu, Anal. Biochem., 2003, 318, 100-106.

15. Y. Zhao, Y. Gao, D. Zhan, H. Liu, Q. Zhao, Y. Kou, Y. Shao, M. Li, Q. Zhuang and Z. Zhu, Talanta, 2005, 66, 51-57.

16. S.-M. Chen and K.-T. Peng, J. Electroanal. Chem., 2003, 547, 179-189.

17. J. Huang, Y. Liu, H. Hou and T. You, Biosens. Bioelectron., 2008, 24, 632-637.

18. T. Łuczak, Electrochim. Acta, 2008, 53, 5725-5731.

19. D.-M. Zhou, H.-X. Ju and H.-Y. Chen, J. Electroanal. Chem., 1996, 408, 219-223.

20. M. C. Henstridge, E. J. Dickinson, M. Aslanoglu, C. Batchelor-McAuley and R. G. Compton, Sens. Actuators, B, 2010, 145, 417-427.

21. A. N. Patel, S.-y. Tan, T. S. Miller, J. V. Macpherson and P. R. Unwin, Anal. Chem., 2013, 85, 11755-11764.

22. R. C. Koile and D. C. Johnson, Anal. Chem., 1979, 51, 741-744.

23. A. N. Patel, P. R. Unwin and J. V. Macpherson, Phys. Chem. Chem. Phys., 2013, 15, 18085-18092.

24. A. J. Bard, J. Am.Chem.Soc., 2010, 132, 7559-7567.

25. L. Zhang and X. Jiang, J. Electroanal. Chem., 2005, 583, 292-299.

26. J. Li and X. Lin, Sens. Actuators, B, 2007, 124, 486-493.

27. G.-Z. Hu, D.-P. Zhang, W.-L. Wu and Z.-S. Yang, Colloids Surf., B, 2008, 62, 199-205.

28. H. Luo, Z. Shi, N. Li, Z. Gu and Q. Zhuang, Anal. Chem., 2001, 73, 915-920.

29. L. A. Hutton, J. G. Iacobini, E. Bitziou, R. B. Channon, M. E. Newton and J. V. Macpherson, Anal. Chem., 2013, 85, 7230-7240.

30. A. G. Güell, K. E. Meadows, P. R. Unwin and J. V. Macpherson, Phys. Chem. Chem. Phys., 2010, 12, 10108-10114.

31. B. K. Swamy and B. J. Venton, Analyst, 2007, 132, 876-884.

32. L. Hutton, M. E. Newton, P. R. Unwin and J. V. Macpherson, Anal. Chem., 2008, 81, 1023-1032.

33. J. V. Macpherson, D. O'Hare, P. R. Unwin and C. P. Winlove, Biophys. J., 1997, 73, 2771-2781.

34. R. P. Akkermans, M. F. Suárez, S. L. Roberts, Q. Fulian and R. G. Compton, Electroanalysis, 1999, 11, 1191-1202.

35. B. D. Aaronson, C.-H. Chen, H. Li, M. T. Koper, S. C. Lai and P. R. Unwin, J. Am.Chem.Soc., 2013, 135, 3873-3880.

36. S. G. Bratsch, J. Phys. Chem. Ref. Data, 1989, 18, 1-21.

37. Z. Samec and J. Weber, J. Electroanal. Chem. Interfacial Electrochem., 1977, 77, 163-180.

38. H. V. Patten, K. E. Meadows, L. A. Hutton, J. G. Iacobini, D. Battistel, K. McKelvey, A. W. Colburn, M. E. Newton, J. V. Macpherson and P. R. Unwin, Angew. Chem. Int. Ed., 2012, 51, 7002-7006.

39. N. R. Wilson, S. L. Clewes, M. E. Newton, P. R. Unwin and J. V. Macpherson, J. Phys. Chem. B, 2006, 110, 5639-5646.

40. G. Janssen, W. Van Enckevort, W. Vollenberg and L. Giling, Diamond Relat. Mater., 1992, 1, 789-800.

41. B. L. Mackey, J. N. Russell, J. E. Crowell, P. E. Pehrsson, B. D. Thoms and J. E. Butler, J. Phys. Chem. B, 2001, 105, 3803-3812.

42. S.-M. Chen and W.-Y. Chzo, J. Electroanal. Chem., 2006, 587, 226-234.

43. M. E. Rice and C. Nicholson, Anal. Chem., 1989, 61, 1805-1810.

44. L. Guo, Y. Zhang and Q. Li, Anal. Sci., 2009, 25, 1451-1455.

45. H. J. Berendsen, D. van der Spoel and R. van Drunen, Comput. Phys. Commun., 1995, 91, 43-56.

46. J. R. Webb, Ph.D thesis, University of Warwick, 2015.

Chapter 6: Electrochemically active self-assembled monolayer and DNA immobilisation on gold and diamond surfaces

The electrochemical detection of single nucleotide polymorphism (SNP) has gained great interest recently. The eventual aim of this work is to build a system where an SNP can be detected electrochemically using a thermal heating approach. However, to achieve this goal several milestones need to be met. The first one includes proving that redox labelled self-assembled monolayer (SAM) and Deoxyribonucleic acid (DNA) can be immobilised on an electrode surface; in initial studies a gold (Au) electrode is used. The electrochemical response of surface bound ferrocene (Fc) derivatives and methylene blue (MB) modified DNA is examined using cyclic voltammetry (CV). Proof-of-concept covalent modification of a diamond surface is then carried out both electrochemically and photochemically. The successful immobilisation of 10-N-Boc-Amino-dec-1-ene (tert-Butyloxycarbonyl (t-BOC) protected amine alkene molecule) is confirmed by X-ray photoelectron spectroscopy (XPS). The electrochemical response of MB labelled DNA grafted on a diamond surface is then investigated, which provides guidance for optimising experimental parameters for electrochemically detecting SNPs in DNA duplex based on melting curve analysis (which would be the subject of future work).

6.1 Introduction

A single nucleotide polymorphism (SNP)[1] is a deoxyribonucleic acid (DNA) sequence variation occurring commonly within a population, where one nucleotide base has been substituted for another. Detecting SNPs in DNA is extremely important for genomic research as SNPs are often implicated in many different genetic diseases.

There are different methods to detect SNPs but many are reliant on the basic premise that a target of interest will form a fully-complementary duplex with a probe DNA strand in the absence of an SNP, but will contain a single-base mismatch in the presence of an SNP. The consequence of this is that the melting temperature of probe bound to SNP-containing target DNA is lower than an SNP-free DNA because of the instability of mismatched base pairs.[1, 2] To monitor the melting of the DNA, fluorescent labels[3, 4] are often employed. One of the main drawbacks of the fluorescent technique is the time taken to perform the analysis, as conventional temperature cycling is often slow and inefficient. In this work we plan to investigate an alternative strategy, pulsed laser heating, to interrogate DNA melting. The advantages of the pulse laser heating over conventional heating techniques, such as well controlled and quantifiable heat pulses (up to 100 ^{o}C) and rapid temperature change,[5] have already been outlined in chapter 3.

Recently, surface immobilised, redox molecule-labelled DNA sensors[6-8] have been developed to offer many advantages such as a low background current, compatibility with microfluidics and microelectronics, and easy preparation. The most common electrode material used for DNA immobilisation is gold (Au),[6-9]

where the grafting process is achieved *via* the interaction between a thiol modified DNA and the gold surface. However, the weak interaction between the thiol and gold at high temperature results in poor stability.[7, 10] Boron doped diamond (BDD), as an electrode material, has gained great interest for surface functionalisation[11] due not only to its exceptional electrochemical response (chapter 1), but its robustness and bio-compatibility. Recent progress has been made for controllable and reliable covalent grafting of different functional groups on the diamond surface. These approaches include chemical,[12] photochemical,[13, 14] and in the case of BDD, electrochemical modification.[15, 16]

Covalent grafting of the diamond surface leads to the formation of robust and stable bio-interface[10] as the nature of the covalent bond between diamond and surface molecule (*e.g.* C-C bond strength 346 kJ mol^{-1}) [17] is stronger than that of the thiol and gold interaction (strength ~ 188 kJ mol^{-1}).[18] In combination with the pulsed laser heating technique, the potential is provided for distinguishing SNPs in DNA duplex by means of melting curve analysis.

The concept is shown schematically in Figure 6.1. Probe single stranded DNA (ssDNA) is firstly immobilised on the electrode surface, followed by hybridisation with redox labelled target ssDNA. The redox label, which is held in close proximity to the surface (*ca.* 1-2 nm) can be oxidised or reduced when the potential at the electrode surface is changed. By applying the pulsed laser heating, denaturation of double stranded DNA (dsDNA) occurs, the redox labelled ssDNA diffuses away from the surface and the redox label cannot be oxidized or reduced. The Faradaic current is measured as a function of temperature applied to the electrode, with the fraction of DNA denatured at the electrode surface a function of

its thermodynamic stability. Thus, different melting curves (current temperature curves) can be obtained for SNP-free and SNP-containing dsDNA, where the SNP-containing DNA is easier to denature at the electrode surface.

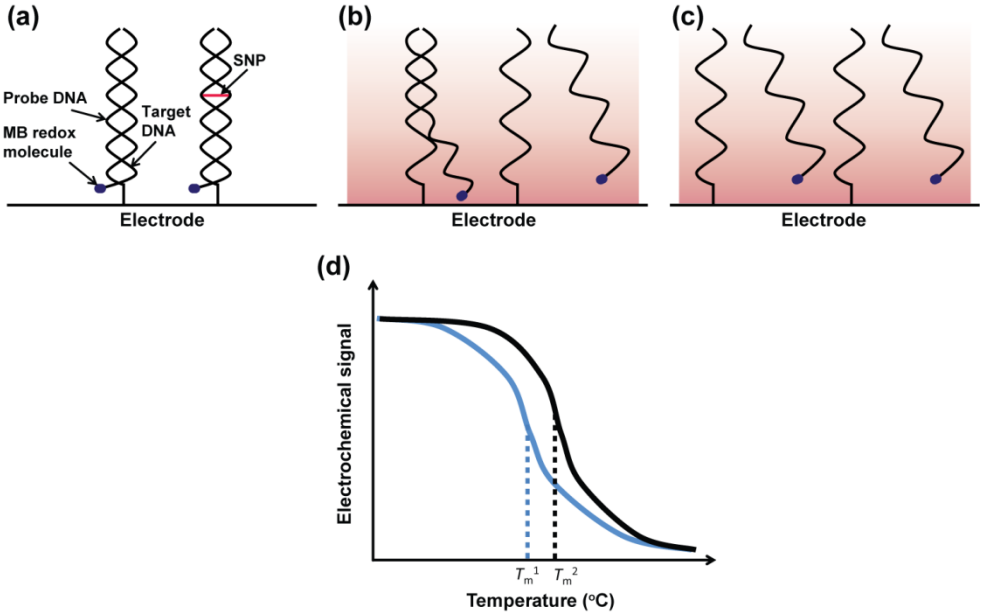

Figure 6.1: Schematic of the concept for the electrochemical discrimination of SNPs in DNA duplex. (a) Electrochemically active DNA immobilisation on the electrode surface; (b) Both SNP-free and SNP-containing DNA duplex denaturation after heating but at different rates; (c) Electrochemically active redox molecule diffuses away from the electrode surface; (d)Electrochemical current as a function of temperature (DNA melting curve) for both SNP-free (black line) and SNP-containing (blue line) DNA duplex.

In this chapter, we firstly investigate approaches to tether electrochemically active self-assembled monolayer (SAM) and DNA to gold surfaces. Verification of functionalisation is achieved using cyclic voltammetry (CV). Different functionalisation strategies (electrochemical and photochemical) are then carried out to graft SAM onto a diamond surface. The functionalisation is assessed using both

surface sensitive spectroscopic technique (X-ray photoelectron spectroscopy, XPS) and CV. The approaches employed in this chapter provide further guidance for detecting SNPs in DNA duplex based on the electro-thermal melting curve analysis.

6.2 Preparation of SAM on the gold electrode

1.5 cm × 2.5 cm Si/SiO_2 substrates (525 µm n-type Si with 300 nm thermally grown SiO_2 on both sides, IDB technologies Ltd., UK) were firstly cleaned in piranha solution (a 3:1 (*v*/*v*) mixture of concentrated (95 %) sulfuric acid and 30 % hydrogen peroxide) at 60 ^{o}C for 10 mins. The substrates were then rinsed by deionised (DI) water, followed by oxygen plasma treatment at 100% power and 7 × 10^{-4} bar for 2 mins using a plasma cleaner (K1050X, Quorum technologies, UK). The substrates were then mounted on the evaporation plate, and areas (1 mm in diameter as the electrode with a 50 µm width conducting gold track to make contact) exposed to evaporation were defined by a Kapton shadow mask, illustrated in Figure 6.2. Evaporation of Cr (3 nm), followed by Au (60 nm) was carried out using a thermal evaporator (Minilab 060 platform, Moorfield, UK).

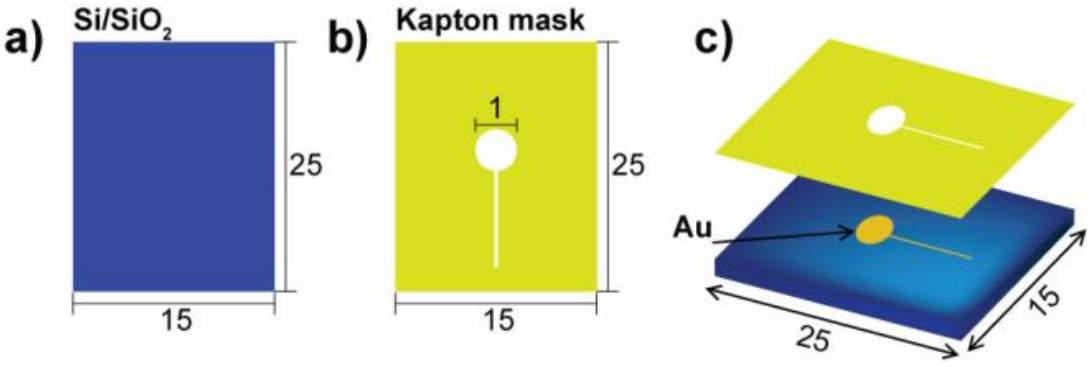

Figure 6.2: Schematic of the gold electrode preparation; (a) Si/SiO_2 substrate; (b) Kapton mask used to define electrode area; (c) Cr/Au evaporation on Si/SiO_2 substrate. Unit: mm.

For comparison, both commercial (2 mm diameter) and evaporated gold electrodes (1 mm diameter) were employed for SAM immobilisation. Gold electrodes were immersed in absolute ethanol containing 0.1 mM 6-(ferrocenyl) hexanethiol (Fc-SAM molecule) and 0.9 mM 1-pentanethiol (spacer molecule) for 24 hours, followed by rinsing in absolute ethanol and drying in nitrogen (N_2) gas. A schematic of the Fc-SAM and spacer molecules modified gold electrode is illustrated in Figure 6.3.

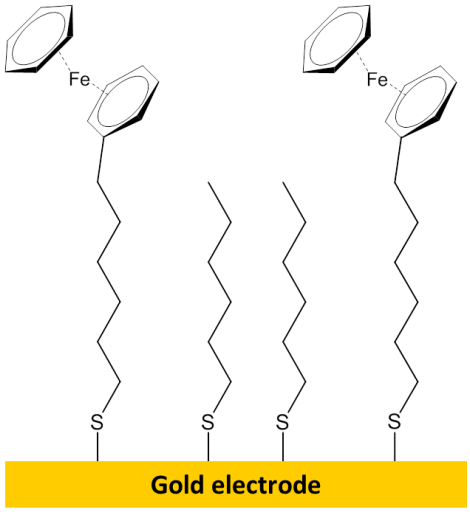

Figure 6.3: Schematic of the 6-(Ferrocenyl) hexanethiol modified gold electrode with 1-pentanethiol as the spacer molecule.

6.3 Preparation of DNA modified gold electrode

Both probe and target ssDNA information is listed in Figure 2.1 in chapter 2. The surface (probe) ssDNA is modified at the 3′ end with a thiol group, whilst the target ssDNA is modified at the 5′ end with a methylene blue (MB) redox molecule. dsDNA is anti-parallel, which means, once the probe ssDNA is immobilised on the

electrode surface, the 5′ MB redox mediator is in close vicinity to the electrode surface after hybridisation (as shown schematically in Figure 6.4).

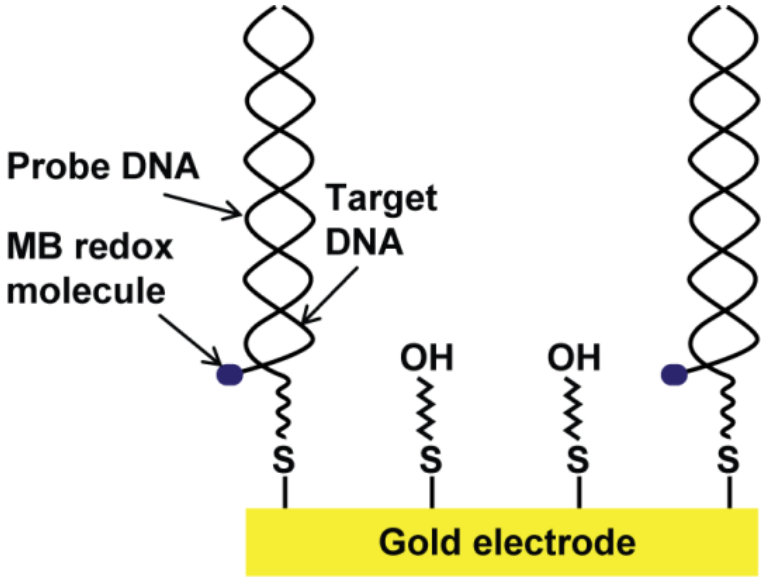

Figure 6.4: Schematic of MB labelled DNA immobilised on gold electrode with MCH as the spacer molecule.

Gold electrodes were immersed in 10 mM phosphate buffer (1 M KCl, pH 7.3) containing 1 µM mixture of both the probe ssDNA and a spacer molecule, mercaptohexanol (MCH) for 24 hours (Figure 6.4). The ratios of probe ssDNA to MCH concentrations ($R_{PD/MCH}$) were varied as 1:10, 1:5, 1:1 and 1:0. Gold electrodes were then rinsed with buffer, followed by immersing in 10 mM phosphate buffer (1 M KCl, pH 7.3) containing 1 µM MB modified target ssDNA. DNA hybridisation was achieved by heating the solution to 80 °C and then slowly cooling to room temperature over a period of 2 hours. dsDNA modified gold electrodes were then rinsed and stored in buffer.

6.4 Photochemical modification of BDD

6.4.1 Attempt to synthesis trifluoroacetamide-protected 10-aminodec-1-ene (TFAAD)

In order to achieve covalent immobilisation of the probe ssDNA molecule on the diamond surface, a linker molecule, acting as the bridge between the surface and the probe ssDNA, is needed. The photochemical grafting of a protected ω-alkenylamine[19, 20] SAM appears attractive and a synthetic route used by Hamers (but originated by Wymann) was identified as a means to prepare the desired linker molecule, *N*-(dec-9-en-1-yl)-2,2,2-trifluoroacetamide **1** (Figure 6.5). This trifluoroacetamide, sometimes referred to as "trifluoroacetamide-protected 10-aminodec-1-ene (TFAAD)" or "trifluoroacetic acid protected 10-aminodec-1-ene (TFAAD)" and its derived amine **2** continue to be used to immobilise DNA and other biomolecules on silicon and diamond surfaces. However, the synthesis of this molecule involves sodium azide in dichloromethane (DCM, Figure 6.5). With concerns on the safety, we chose to investigate the possibly less hazardous, although nonetheless imperfect alternative diphenyl phosphoryl azide (DPPA) for Curtius rearrangement to dec-9-en-1-yl isocyanate **3**, followed by the addition of trifluoroacetic acid (TFA) as Strother *et al.*'s method (Figure 6.6).[21, 22]

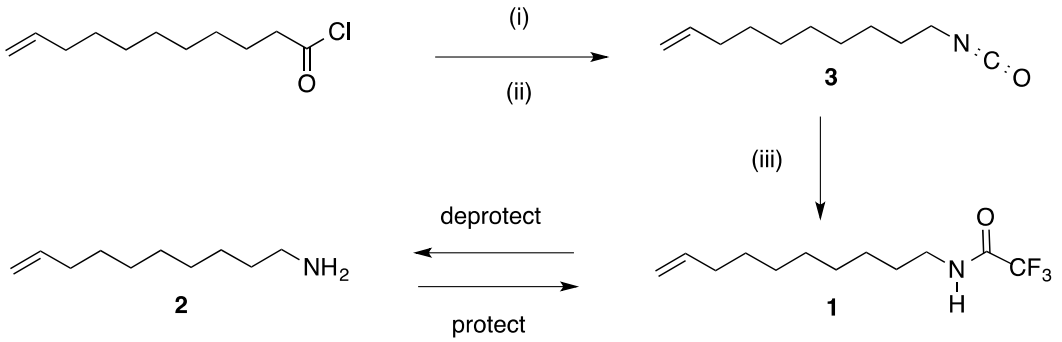

Figure 6.5: Literature reagents and conditions: (i) NaN_3, H_2O, CH_2Cl_2, $Bu_4N^+Br^-$, 0 °C; (ii) aqueous workup; (iii) CF_3CO_2H, CH_2Cl_2, reflux 6 h.

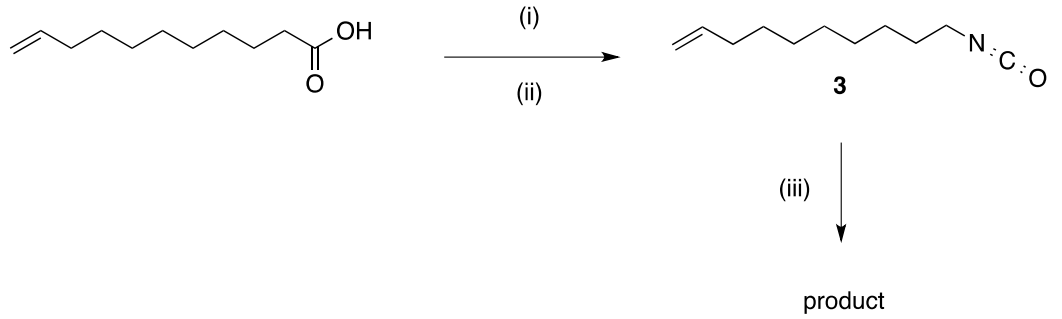

Figure 6.6: Our reagents and conditions: (i) DPPA, toluene, 0 °C then 90 °C, 4 h; (ii) aqueous workup; (iii) CF_3CO_2H, CH_2Cl_2, reflux 6 h.

A small scale procedure was devised that uses DPPA in the non-participatory solvent toluene (b.p. 110–111 °C)[23] and triethylamine (Figure 6.6). The reaction was heated and followed by infrared spectroscopy (IR, Figure 6.7) showing the presence of an azide moiety (2171 cm^{-1})[24] and the Curtius rearranged isocyanate **3** (2269 cm^{-1}). Aqueous workup gave **3** as a solution in toluene which was dried overnight with $MgSO_4$. The filtered toluene solution was treated with 1.1 eq. of TFA[21, 22] and then refluxed overnight. The product was isolated as a solid from the cooled mixture by aqueous workup and rotary evaporation under reduced pressure. The appearance of a white solid was surprising since Strother *et al.*'s preparation, albeit on a larger

scale, reported *N*-(dec-9-en-1-yl)-2,2,2-trifluoroacetamide **1** as an oil. Purification by flash silica gel chromatography gave a white solid (20 mg) whose 1H NMR data (Figure 6.8) was consistent with that of another compound, 1,3-bis(dec-9-en-1-yl)urea (Figure 6.9) and this indicates the unsuccessful synthesis of TFAAD.

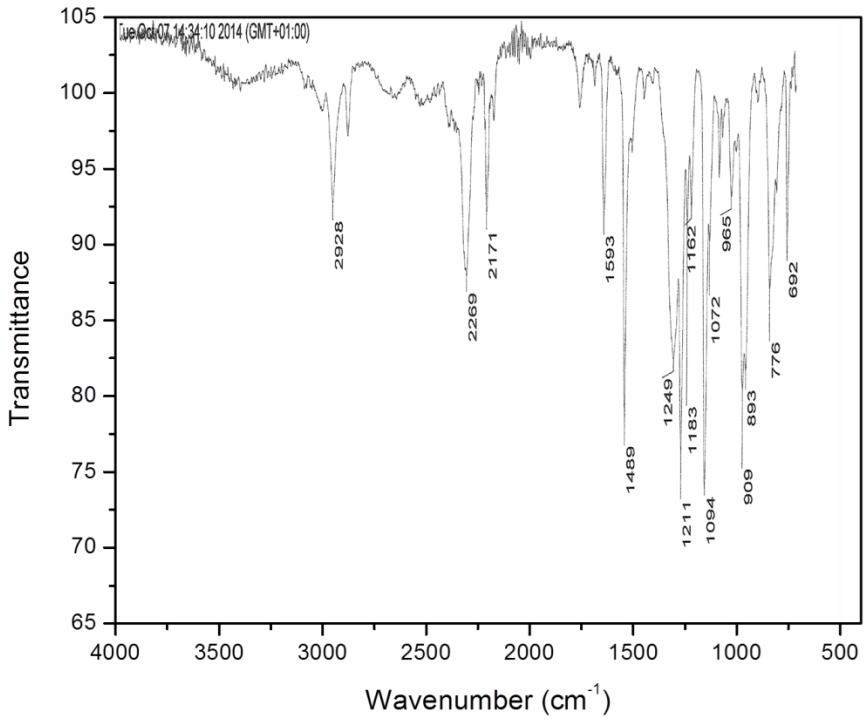

Figure 6.7: IR spectroscopy after the reaction of DPPA with triethylamine in the non-participatory solvent toluene.

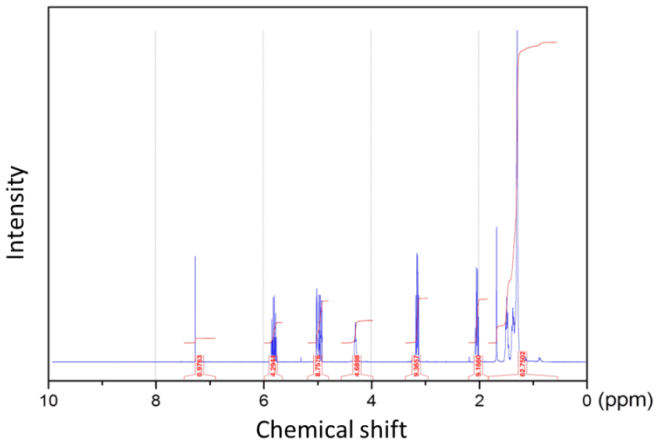

*Figure 6.8: 1H NMR on the product of reaction between dec-9-en-1-ylisocyanate **3** and trifluoroacetic acid.*

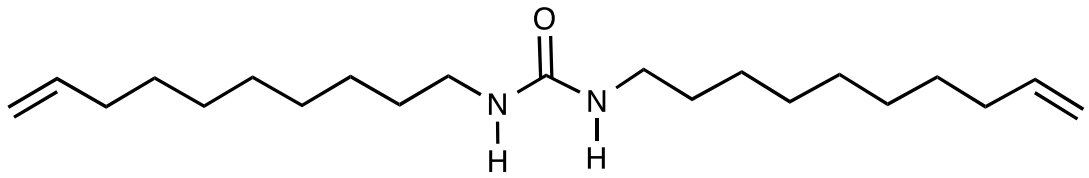

Figure 6.9: Structure of product isolated from reaction in Figure 6.6, 1,3-bis(dec-9-en-1-yl)urea.

6.4.2 Preparation of DNA modified BDD using an alternative linker molecule, 10-N-Boc-Amino-dec-1-ene

Upon the unsuccessful preparation of TFAAD, an alternative molecule, 10-N-Boc-Amino-dec-1-ene (tert-Butyloxycarbonyl (t-BOC) protected amine alkene molecule), was employed. This molecule exhibits a protected amine and has been employed before as the linker to tether DNA to Si[25, 26] and diamond surfaces.[13, 26]

Hydrogen termination is essential for the photochemical modification of BDD due to its negative electron affinity[27] (NEA, section 1.3, chapter 1).

Hydrogenation was achieved by placing the BDD substrates in a chemical vapour deposition (CVD) reactor, where a hydrogen (H_2) plasma is generated using 1 KW power, at 50 Torr for 10 mins.[28] A home-built cell, illustrated in Figure 6.10, was employed for photochemical modification under N_2 atmosphere.[10] 4 µL t-BOC protected amine alkene molecule was placed on the diamond surface and then covered with a fused silica window (UQG optics, UK), trapping a thin film of liquid on the surface. The cell was illuminated by a pen-ray mercury lamp (254 nm, 2 mW cm^{-2} at 0.75 inch, ultraviolet product Ltd., UK) for 12 hours. Diamond substrates were then sonicated in methanol (5 mins) and chloroform (5 mins), followed by drying under N_2 gas.

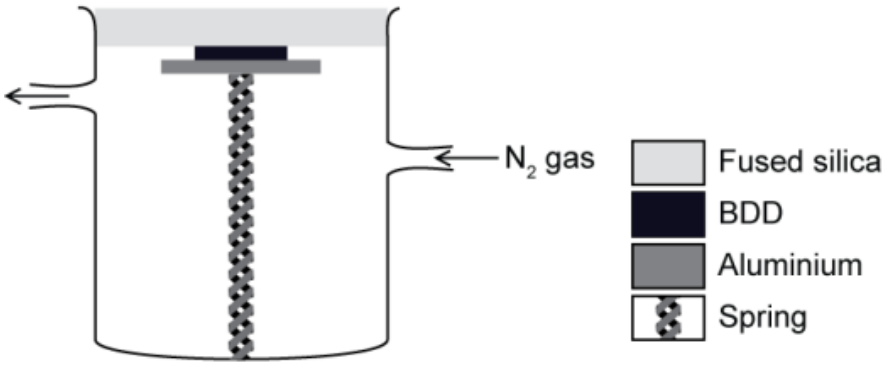

Figure 6.10: Schematic of the home-built photochemical modification cell. A thin film of reactive molecule, 10-N-Boc-Amino-dec-1-ene, is trapped and secured by the fused silica. An UV source is placed ca. 1 cm above the cell. N_2 gas is constantly flowed into the cell during the photochemical experiment.

The de-protection was achieved by immersing the substrates into a 1:3 (*v/v*) mixture of TFA and DCM for 2 hours and then immersing in 10 % NH_4OH solution for 30 seconds to leave the primary amine (Figure 6.11), which then reacted with the crosslinker, 0.5 mM sulphosuccinimidyl-4-(N-maleimidomethyl)cyclohexane-1-

carboxylate (SSMCC) in 10 mM phosphate buffer (1 M KCl, pH 7.3). For DNA grafting, the substrates were then immersed in 10 mM phosphate buffer (1 M KCl, pH 7.3) containing 1 µM thiol modified 3′ probe ssDNA overnight (illustrated schematically in Figure 6.12) followed by rinsing with buffer for 5 mins to dissolve any physisorbed probe ssDNA. DNA hybridisation was achieved by placing the probe ssDNA modified diamond in 10 mM phosphate buffer (1 M KCl, pH 7.3) containing 1 µM MB modified target ssDNA overnight, followed by rinsing with buffer for 5 mins.

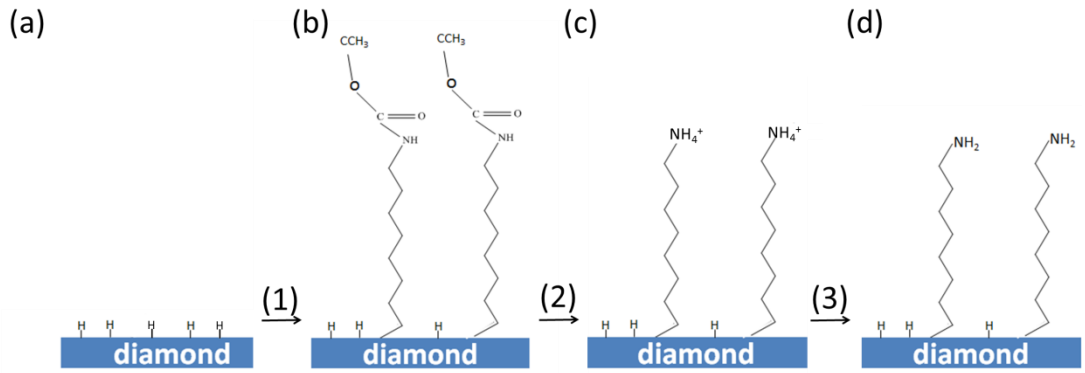

Figure 6.11: Schematic of surface modification of BDD (1) Photochemical grafting of 10-N-Boc-Amino-dec-1-ene; (2) De-protection by placing diamond sample in 1:3 (v/v) TFA in DCM for 2 hours; (3) 10 % NH_4OH aqueous solution for 30 seconds to reveal the primary amine.

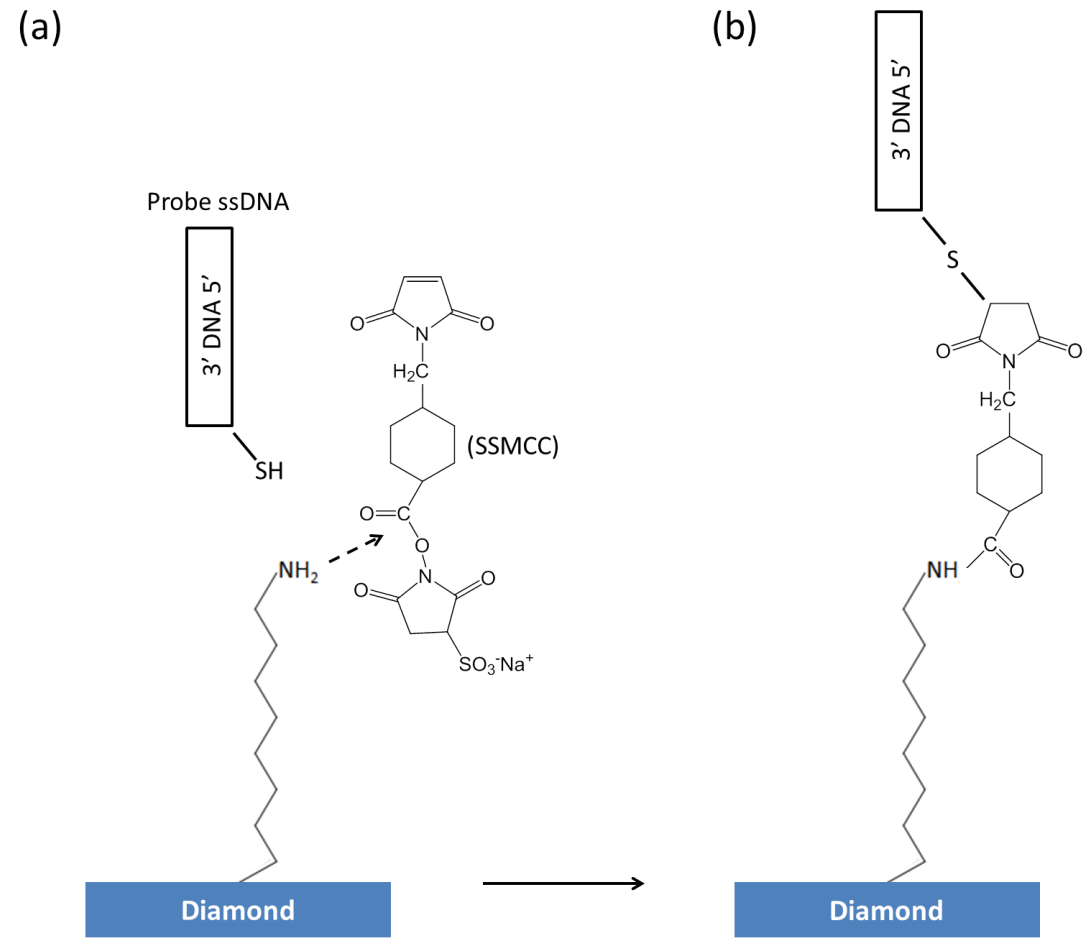

Figure 6.12: Probe ssDNA immobilisation on the diamond surface.

6.4.3 XPS measurements

XPS measurements were performed using a Kratos Axis Ultra DLD photoelectron spectrometer, with the sample being illuminated using a monochromated Al k_α x-ray source. The measurements were conducted at room temperature and at a take-off angle of 90° with respect to the surface parallel. The survey and core level spectra were recorded using pass energies of 160 eV and 20 eV (resolution approx. 0.4 eV) from a 1 mm diameter spot size, respectively. The data were analysed in the CasaXPS package, using Shirley backgrounds and mixed Gaussian-Lorentzian lineshapes and asymmetry parameters where appropriate.

6.5 Results and discussion

6.5.1 Electrochemical characterisation of the Fc-SAM modified commercial gold electrode

Figure 6.13a shows the CVs at different scan rates for the oxidation of Fc-SAM immobilised on a commercial gold electrode (2 mm in diameter). Well defined peaks for Fc oxidation and reduction are observed with $E_{1/2}$ at *ca.* 307 mV, which is in good agreement with literature value (*ca.* 305 mV)[29] of a surface bound Fc derivative. In the case of surface bound electrochemistry, where both the oxidised and reduced forms of chemical species are strongly adsorbed to the electrode surface, the peak current, i_p, is proportional to the scan rate, v.[30] Figure 6.13b shows the linear dependence of i_p with v (R^2 = 0.998), indicating the successful immobilisation of the Fc-SAM on the gold surface.

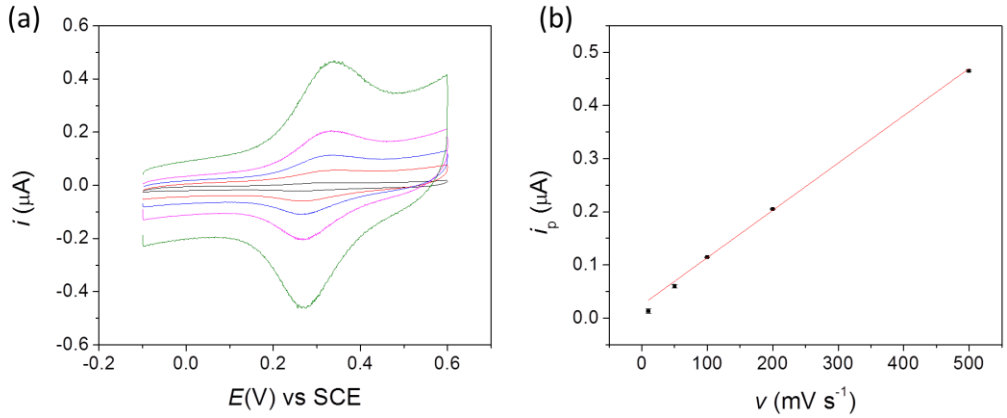

Figure 6.13: (a) CVs of the Fc-SAM modified commercial gold electrode (2 mm diameter) in 0.1 M $HClO_4$ electrolyte at different scan rates: 10 mV s^{-1} (black), 50 mV s^{-1} (red), 100 mV s^{-1} (blue), 200 mV s^{-1} (pink), 500 mV s^{-1} (green). (b) Plot of i_p as a function of v for the Fc-SAM modified commercial gold electrode.

The surface coverage, Γ, of the electrochemically active Fc derivative is calculated from equation 6.1,

$$\Gamma = \frac{Q}{nFA} \tag{6.1}$$

where Q is the charge passed for the oxidation or reduction of the Fc derivative. Γ calculated from the CV is *ca.* 1.2×10^{-10} mol cm^{-2} (average value calculated from CVs with different scan rates), which is 27 % of the closely packed monolayer of Fc derivative on the electrode surface.[31] Low surface coverage has been observed previously which is due to the nature of the gold electrode surface, with factors such as surface roughness and cleanliness reducing thiol gold bond formation.[32]

Figure 6.13a gives a peak-to-peak separation, ΔE_p, of 54 mV, which is independent of v. Ideally ΔE_p for surface bound redox molecules is 0 mV at slow scan rates.[30] Previous reports have observed larger than 0 mV ΔE_p for surface bound molecules which has been attributed to factors such as the structure and density of the surface molecules[33] and changes in the solvation of the redox centre.[34] The independence of ΔE_p as a function of v indicates fast electron transfer (ET) rates for the surface bound Fc derivative.

Immobilisation of Fc-SAM was then carried out on an evaporated gold electrode, and Figure 6.14a shows the resulting CVs at different scan rates. An increased peak current (1.18 µA at 500 mV s^{-1}) is obtained compared to that at the commercial gold electrode (0.47 µA at 500 mV s^{-1}). The surface coverage of the Fc-SAM is calculated to be 4.1×10^{-10} mol cm^{-2}. This value is close to that for full monolayer coverage (4.6×10^{-10} mol cm^{-2}).[35] The background current at the evaporated gold electrode is much smaller compared to that obtained at the

commercial gold electrode. This is due to the reduced surface roughness of the evaporated gold electrode. $E_{1/2}$ for the oxidation of Fc is 305 mV, similar to that (307 mV) obtained at the commercial gold electrode. ΔE_p (50 mV) is again independent of *v*, indicating a fast ET process between the surface bound Fc-SAM and the electrode. The linear dependence (R^2=0.99) of i_p as a function of *v* (Figure 6.14b) shows the behaviour of a typical surface bound redox molecule.

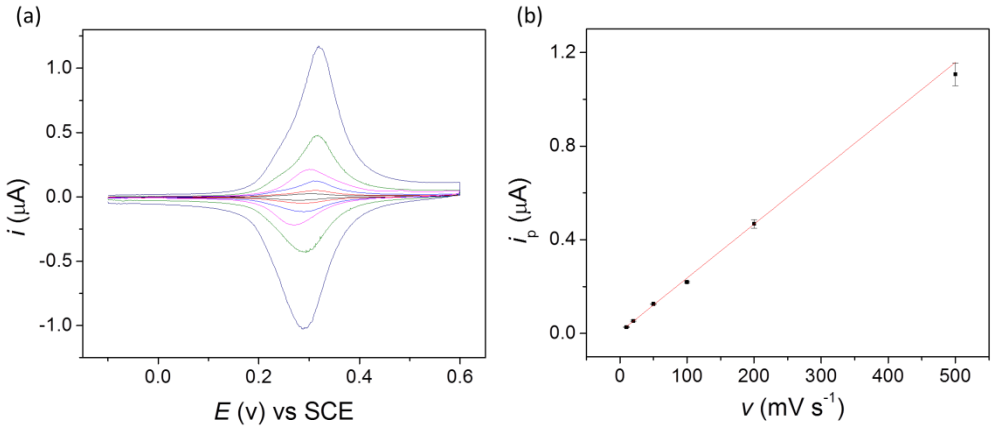

Figure 6.14: (a) CVs of the Fc-SAM modified evaporated gold electrode (1 mm diameter) in 0.1 M $HClO_4$ electrolyte at different scan rates: 10 mV s^{-1} (black), 20 mV s^{-1} (red), 50 mV s^{-1} (blue), 100 mV s^{-1} (pink), 200 mV s^{-1} (green), 500 mV s^{-1} (navy). (b) Plot of i_p as a function of v for the Fc- SAM modified evaporated gold electrode.

6.5.2 DNA immobilisation on the evaporated gold electrode

Upon the successful immobilisation and high surface coverage of the Fc-SAM on the evaporated gold surface, redox labelled DNA modification was carried out using a two-step process (Figure 6.4): (1) thiol modified probe ssDNA immobilisation on the gold electrode. This was performed by placing the gold electrodes in 10 mM phosphate buffer (1 M KCl, pH 7.3) containing 1 μM mixture

of the probe ssDNA and an alkanethiol spacer molecule, MCH, with different ratios ($R_{PD/MCH}$=1 : 0, 1 : 1, 1 : 5 and 1 : 10). Spacer molecules on electrode surface lead to the reduction of the surface density of the probe ssDNA, and enhance the accessibility of (2) MB labelled target ssDNA. Figure 6.15 shows the CVs at different scan rates for the reduction of MB modified DNA.

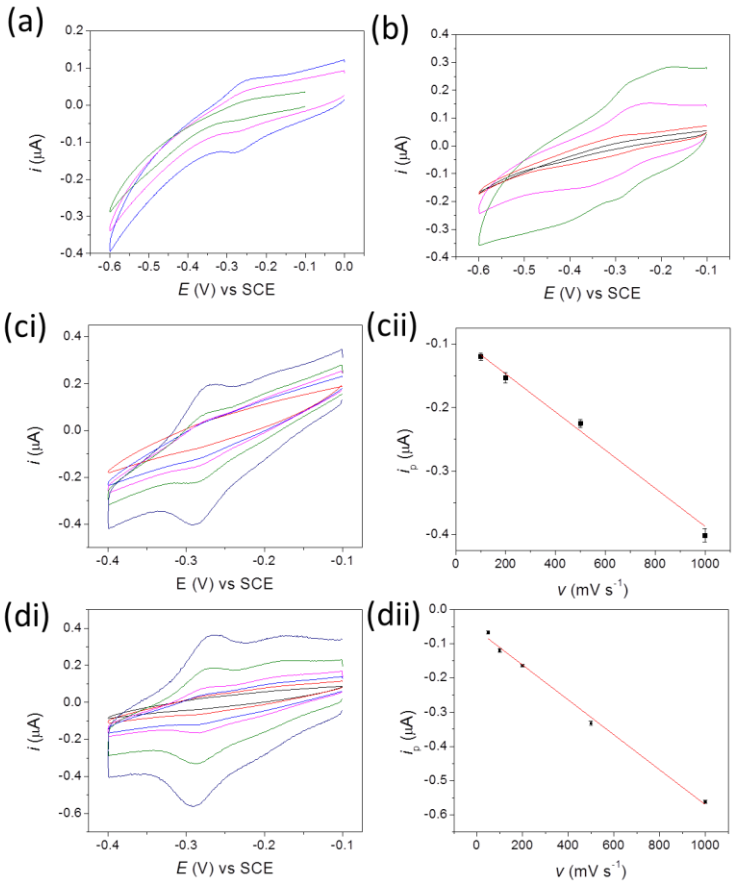

Figure 6.15: CVs of MB modified DNA immobilised on the evaporated gold electrode (1 mm diameter) in 10 mM phosphate buffer (1 M KCl, pH 7.3) at different scan rates: 20 mV s^{-1} (black), 50 mV s^{-1} (red), 100 mV s^{-1} (blue), 200 mV s^{-1} (pink), 500 mV s^{-1} (green), 1000 mV s^{-1} (navy). The ratios of probe ssDNA and MCH ($R_{PD/MCH}$) are (a) 1:0, (b) 1:1, (c) 1:5 and (d) 1:10. (cii) and (dii) Plots of i_p as a function of v for the MB modified DNA immobilised on the evaporated gold electrode.

At larger $R_{PD/MCH}$ (1 : 0 and 1 : 1), peak currents for the reduction of MB modified DNA are only observed at higher scan rates (200 mV s^{-1} and 500 mV s^{-1} shown in Figure 6.15a and b). Surface coverages of electrochemically active MB are calculated to be 1.2×10^{-12} and 1.5×10^{-12} mol cm^{-2}, which is smaller than the reported value (5.2×10^{-12} mol cm^{-2}).[8] This is possibly due to the absence (or small amount) of spacer molecules on the gold surface, resulting in closely packed probe ssDNA, confining the hybridisation process. The surface coverage of active DNA molecules is *ca.* 2 orders of magnitude smaller than the Fc-SAM modified gold surface (4.1×10^{-10} mol cm^{-2}), which is probably caused by the bulky structure of the DNA molecule (a few nm in diameter) compared to the alkyl chain spacing (0.5 nm in diameter).[33] $E_{1/2}$ at higher $R_{PD/MCH}$ (1: 0 and 1: 1) for the reduction of MB is - 265 mV and - 267 mV, respectively. ΔE_p is again independent of scan rate (24 mV and 22 mV for $R_{PD/MCH}$ of 1: 0 and 1: 1), indicating a fast ET process.

At smaller $R_{PD/MCH}$ (1: 5 and 1: 10), peak currents observed from the CVs are more pronounced with a linear dependence of i_p as a function of v (Figure 6.15cii and dii), serving as the evidence for the successful tethering of the MB modified DNA to the gold surface. The surface coverages are calculated to be 4.5×10^{-12} and 4.7×10^{-12} mol cm^{-2}, which is in close agreement with the literature value (5.2×10^{-12} mol cm^{-2}) for loosely packed DNA immobilised on an electrode surface.[8, 36] Enhanced surface coverage at smaller $R_{PD/MCH}$ indicates that spacer molecules play a crucial role in the ET process between the redox centre and the electrode surface. It is reported that an enhanced electrochemical response was observed at a loosely packed surface, where the motional movement of immobilised, bulky dsDNA was possible.[37]

$E_{1/2}$'s at smaller $R_{PD/MCH}$ (1: 5 and 1: 10) for the reduction of MB is - 263 mV and - 265 mV, respectively. Decreased ΔE_p's (17 mV and 15 mV for $R_{P/MCH}$ of 1: 5 and 1: 10) are obtained, indicating an increased ET process for the loosely packed surface compared to that obtained at closely packed surface (larger $R_{PD/MCH}$). This can be explained by the surface bound ET kinetic equation 1.14 in chapter 1, where the ET rate constant, $k_{0,}$ increases exponentially as the separation between redox centre and the electrode surface is decreased. In the case of the loosely packed surface, immobilised MB molecules are more accessible to the electrode surface compared to that at a densely packed surface.

Stability studies of the DNA modified gold surface were carried out by cycling the denaturation and hybridisation processes. Denaturation was carried out by heating the dsDNA modified electrode at 90 ^{o}C for 10 mins in 10 mM phosphate buffer (1 M KCl, pH 7.3). The CV after denaturation (Figure 6.16a) shows no obvious faradaic process. After re-hybridisation with the MB labelled target ssDNA, the CVs in Figure 6.16b show a typical surface bound electrochemical response with a linear dependence (R^2 = 0.98) of i_p as a function of v. However, a significant decrease in surface coverage (1.3×10^{-12} mol cm^{-2}) was obtained, which is possibly due to the desorption (unstable non-covalent interaction between the thiol and gold[18]) of probe ssDNA from the electrode surface at high temperatures.[7]

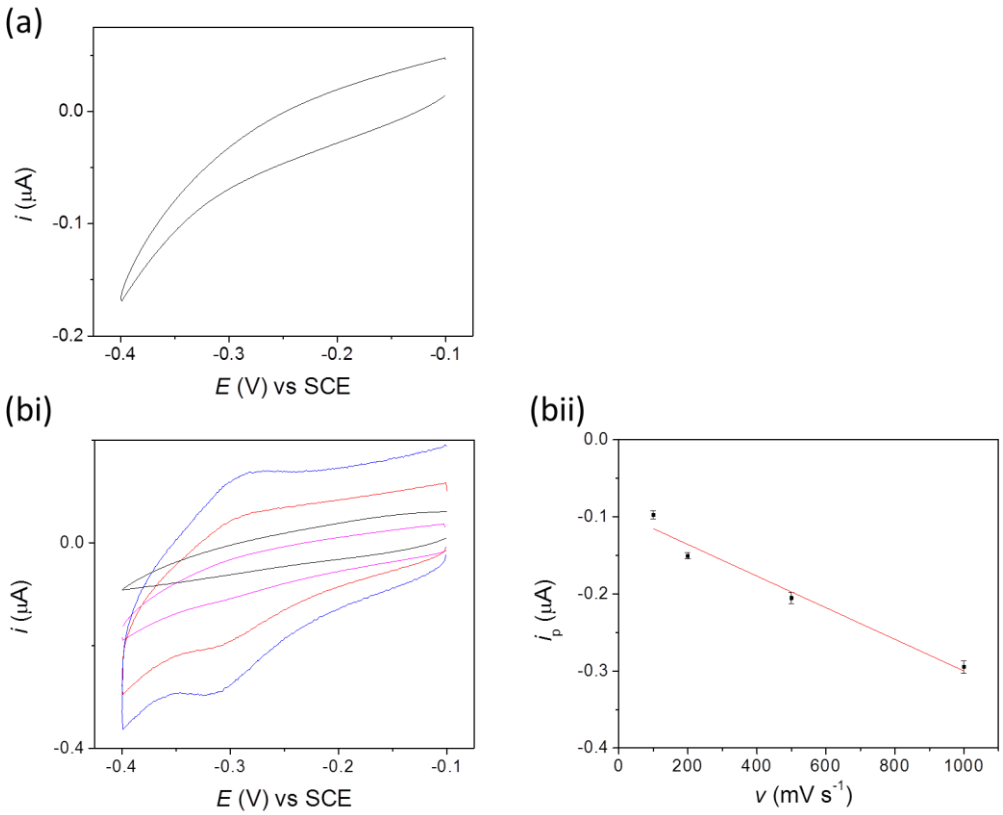

Figure 6.16: (a) CV of the evaporated gold electrode (1 mm diameter) after denaturation. Denaturation was achieved by immersing the dsDNA modified gold electrode in 10 mM heated (90 ^{o}C) phosphate buffer (1 M KCl, pH 7.3) for 10 mins. (bi) CVs of evaporated gold electrode (1 mm diameter) after re-hybridisation with MB modified target ssDNA at different scan rates: 100 mV s^{-1} (black), 200 mV s^{-1} (pink), 500 mV s^{-1} (red), 1000 mV s^{-1} (blue). Re-hybridisation was carried out by immersing the probe ssDNA modified gold electrode in 1 μM MB modified target ssDNA in 10 mM phosphate buffer (1 M KCl, pH 7.3). (bii) Plot of i_p as a function of v for the dsDNA modified gold electrode.

6.5.3 Electrochemical modification of BDD

Since the first report on the modification of a diamond surface by electrochemical reduction of aryldiazonium salt by McCreery et al,[38] a wide range of

functional groups, such as -COOH, -NO_2,[38, 39] have been introduced to the diamond surface, enabling further bio-sensing applications.

Electrochemical modification of BDD was carried out by the reduction of 1 mM 4-nitrophenyl diazonium (the nitro (-NO_2) group can be further reduced to primary amine (-NH_2) group for binding with DNA molecules) in acetonitrile solution, and Figure 6.17a shows two consecutive CVs on a 1 mm diameter BDD electrode. The 1st CV exhibits a cathodic peak current of *ca.* - 3.0 µA at 0.18 V, indicating the reduction and grafting of nitrophenyl diazonium on the diamond surface, illustrated schematically in Figure 6.18. A significantly decreased reduction peak current (- 0.8 µA) is observed for the 2nd CV, indicating the blocking effect, which is attributed to multi-layer formation of nitrophenyl molecules on the electrode surface (Schematic in Figure 6.18e), similar to that reported previously on a glassy carbon electrode.[40]

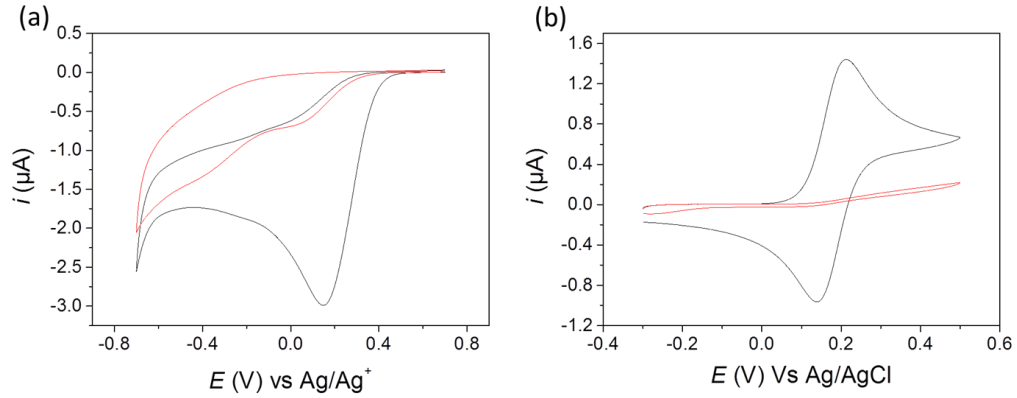

Figure 6.17: (a) Two consecutive CVs of a 1 mm diameter BDD electrode for the reduction of 1 mM 4-nitrophenyl diazonium in 0.1 M NBu_4BF_4 acetonitrile solution (black 1st scan, red 2nd scan); (b) CVs of a 1 mm diameter BDD electrode for the oxidation of 1 mM $Fe(CN)_6^{4-}$ in 0.1 M KNO_3 before (black) and after (red) electrochemical modification (two consecutive CVs in 1 mM 4-nitrophenyl diazonium).

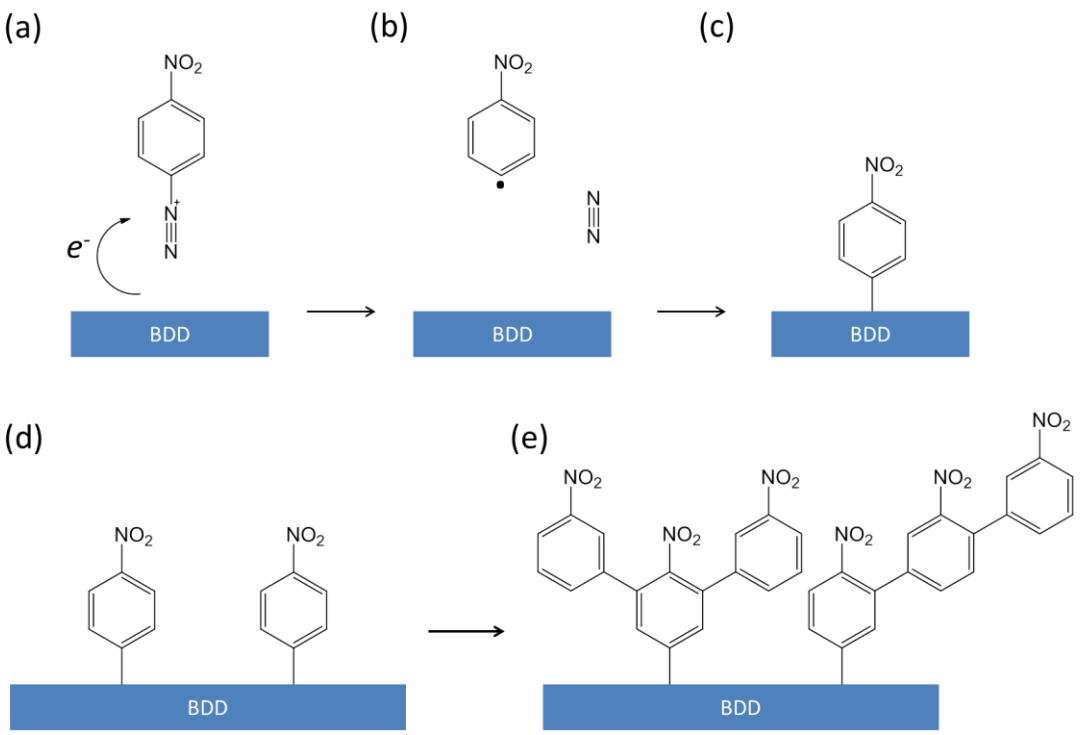

Figure 6.18: Electrochemical reduction of 4-nitrophenyl diazonium on the diamond surface and subsequent multi-layer formation.

Surface functionalisation is further assessed using a redox mediator, $Fe(CN)_6^{4-}$ in bulk solution and the CVs for the oxidation of $Fe(CN)_6^{4-}$ before and after nitrophenyl modification are shown in Figure 6.17b. Prior to modification, the CV shows a typical diffusion limited response with an anodic peak current at *ca.* 1.58 µA and ΔE_p of 68 mV. However, after modification, the CV exhibits only a non-faradic (capacitance) response, indicating the blocking effect from the surface molecules for this ET process. This is most likely due to the formation of nitrophenyl multi-layers on the diamond surface. Therefore, the electrochemical modification route is excluded for the subsequent redox labelled DNA immobilisation on the diamond surface due to the hindered ET process between the electrode and redox molecule.

6.5.4 Photochemical modification of BDD

Photochemical modification of hydrogen terminated diamond with alkene-containing organic molecules was developed by Hamers and co-workers.[10] The modification process employed an ultraviolent (wavelength, λ = 254 nm) light irradiating on hydrogen terminated diamond, where the surface was covered by a liquid thin film of surface active molecules, illustrated schematically in Figure 6.11.

Figure 6.19 shows the contact angle measurements before and after hydrogen termination. Prior to hydrogenation, the diamond sample (cleaned in boiled concentrated acid) is hydrophilic, evidenced by the small contact angle (35.5^o << 65^o, Figure 6.19a). After hydrogen termination, the surface exhibits a hydrophobic nature (contact angle: 88.3^o, Figure 6.19b). The hydrogen terminated diamond substrate was then used for subsequent photochemical modification using the t-BOC protected amine alkene molecule and XPS was employed to analyse the surface chemistry. Figure 6.20 shows the survey XPS spectra for a hydrogen terminated and surface molecule modified diamonds. The intensities were normalised against C *1s* peak at 284.6 eV. It can be seen that the O *1s* signal is enhanced slightly after the modification process compared to that at the hydrogen terminated surface. The presence of N *1s* signal, at 400.8 eV, further confirms the successful grafting of t-BOC protected amine alkene molecule (consists of C-N- bond structure, Figure 6.21c) on the diamond surface.

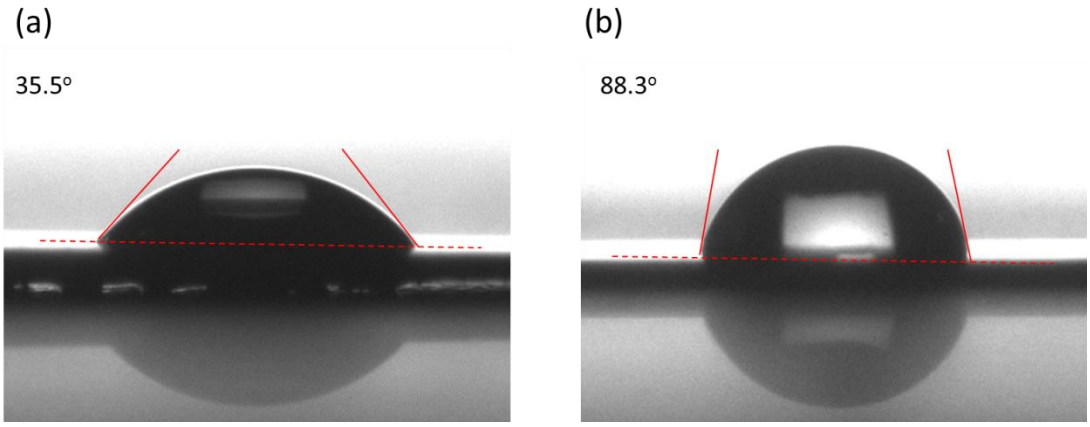

Figure 6.19: Contact angle measurements on a diamond surface before (a) and after (b) hydrogen termination.

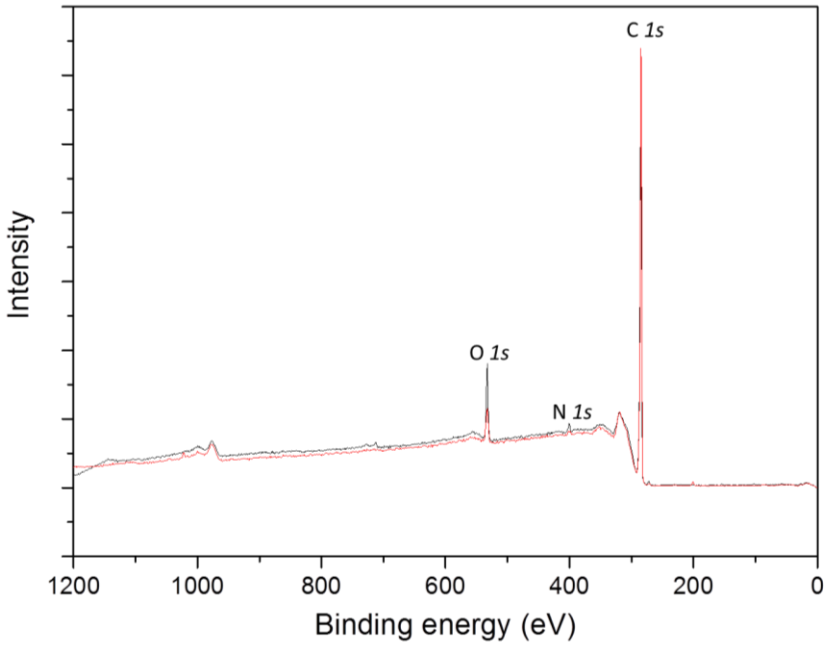

Figure 6.20: XPS survey spectra of a hydrogen terminated (red) and t-BOC protected amine alkene molecule (black) modified diamond surface.

Angle resolved C *1s* and N *1s* XPS spectra were employed to provide further information on surface chemistry, shown in Figure 6.21a and b, respectively. The C *1s* spectra exhibit a prominent peak at 284.6 eV, which is attributed to the sp^3

carbon. Peak 2, positioned at 285.24 eV, represents hydrocarbon (C-H), which is due to either the hydrogen termination nature of the surface or the methylene group originated from the surface molecule (Figure 6.21c). Peak 3 and 4 corresponds to the alcohol group (C-OH) and carbon-nitrogen bond (C-N-), which are originated from the bond structure of the surface molecule, 10-N-Boc-Amino-dec-1-ene (Figure 6.21c). At higher binding energies, peak 5 and 6 are attributed to the carbonyl (C=O) and carboxyl (COOH) groups, respectively. The peak positions for different surface chemical structures are listed and compared with literature values in Table 6.1. N *1s* spectra (Figure 6.21b) exhibit a prominent peak at 400.8 eV, which is attributed to the presence of nitrogen (Figure 6.21c) on the surface. This further confirms the successful immobilisation of the t-BOC protected amine alkene molecule on the diamond surface.

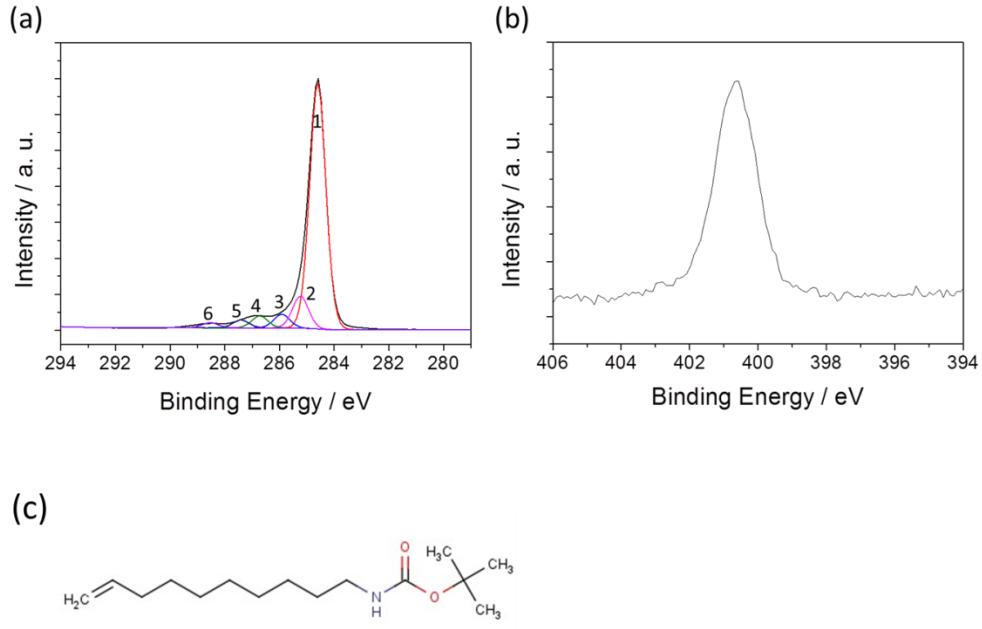

Figure 6.21: Angle resolved XPS spectra for (a) C 1s and (b) N 1s after photochemical modification by the t-BOC protected amine alkene molecule; (c) Molecular structure of 10-N-Boc-Amino-dec-1-ene

Table 6.1: Peak positions for different surface chemical structures for the C 1s XPS spectra on the diamond surface.

	1	2	3, 4	5	6
Bond structure	sp^3 carbon	hydrocarbon	C-O-, C-N-	C=O	-O-C=O-
Energy range (eV)[41, 42]	284.6	+0.6 - 0.9*	+1 - 2*	+2.9 - 3.8*	+3.7 - 4.3*
Peak position (eV)	284.6	285.24	285.92, 286.72	287.42	288.54

*Position relative to sp^3 carbon peak

6.5.5 DNA immobilisation on BDD

Upon the successful grafting of the t-BOC protected amine alkene molecule, dsDNA was then immobilised on diamond surface (Figure 6.12, section 6.4.2) and the electrochemical response of the MB labelled DNA was assessed by CV (Figure 6.22a). The CV shows a peak current of - 0.026 μA for MB reduction with $E_{1/2}$ at *ca.* - 258 mV, which is shifted positive slightly compared to that (-265 mV, Figure 6.15) at gold electrode. The surface coverage of electrochemical active MB is calculated to be 1.1×10^{-12} mol cm^{-2} (equation 6.1), smaller than that (4.7×10^{-12} mol cm^{-2}, $R_{PD/MCH}$ = 1:10) obtained at the gold electrode. This is most likely due to either the low efficiency of photochemical modification process compared to thiol-gold interaction or high efficiency of photochemical grafting but resulting in closely packed surface molecules and probe ssDNA, confining the hybridisation process. Further experiments investigating the photochemical modification time and the introduction of spacer molecules are needed to optimise the grafting efficiency and subsequent electrochemical response.

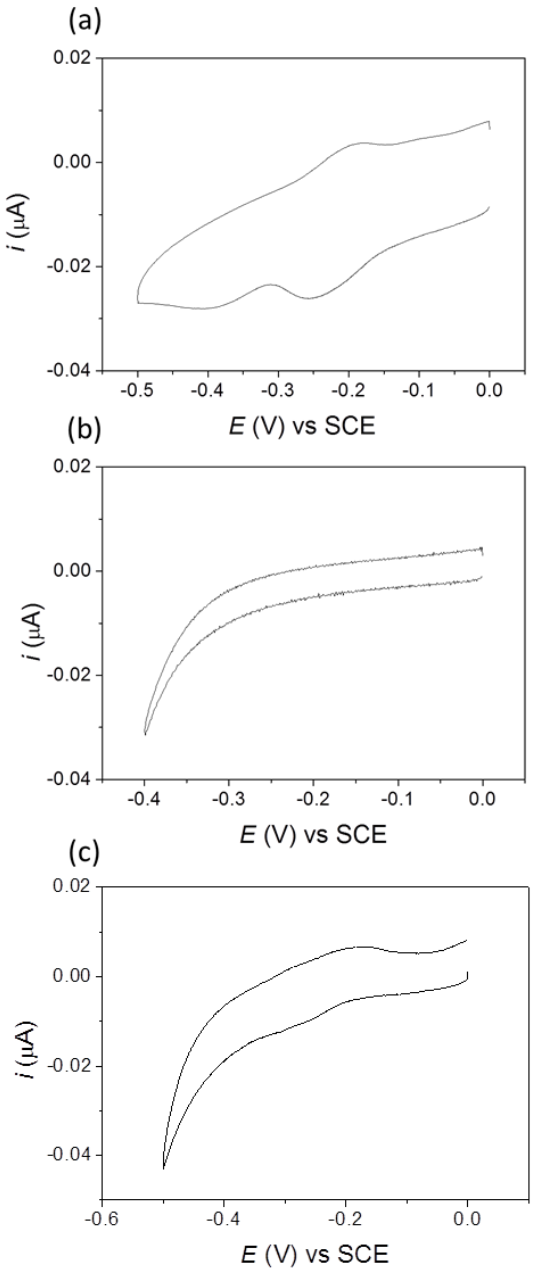

Figure 6.22: (a) CVs of MB modified DNA immobilised on a 1 mm diameter BDD electrode in 10 mM phosphate buffer (1 M KCl, pH 7.3). (b) CV of a 1 mm diameter BDD electrode after denaturation. Denaturation was achieved by immersing the DNA modified electrode in 10 mM heated (90 ^{o}C) phosphate buffer (1 M KCl, pH 7.3) for 10 mins. (c) CV after re-hybridisation with MB modified target ssDNA. Re-hybridisation was carried out by immersing the electrode in 10 mM phosphate buffer (1 M KCl, pH 7.3) containing 1 μM target ssDNA.

A stability test was carried out by cycling the denaturation and hybridisation processes. CVs after denaturation and re-hybridisation are shown in Figure 6.22b and Figure 6.22c, respectively. The CV after denaturation exhibits only background (non-faradic) process, whilst after re-hybridisation, a reduction peak current (- 0.016 µA) is observed, but it is smaller in size compared to that (- 0.026 µA) obtained for the 1st cycle. The calculated surface coverage of electrochemically active MB is 0.2 × 10^{-12} mol cm^{-2}, which is *ca.* 5 times smaller compared to the initial hybridisation process. The proof-of-concept experiment of covalent grafting dsDNA on the diamond surface provides guidance for further exploration on optimising photochemical modification parameters. Subsequent electrochemical melting curve analysis (Figure 6.1) to discriminate SNPs in dsDNA will be investigated.

6.6 Future work

The t-BOC protected amine alkene molecule has been successfully immobilised on the diamond surface. The concept of redox labelled DNA molecules grafted on a diamond electrode has been demonstrated electrochemically using CV. However, further investigations on the reproducibility and stability of the redox labelled DNA grafting on the diamond electrode are required. The surface coverage of the redox molecule (MB) needs to be optimised by tuning the photochemical modification time (density of surface molecules), introduction of spacer molecules inert to the probe ssDNA (increase the separation of probe ssDNA on the surface), DNA immobilisation and hybridisation time, *etc.*

The melting temperature of a dsDNA is affected by the existing SNPs in the dsDNA structure and can be interrogated electrochemically (Figure 6.1); as the DNA

duplex melts and the electrochemically labelled target ssDNA diffuses away from the surface, the electrochemical current signal will be lost. Experiments investigating the difference in melting curves between an SNP-free and an SNP-containing dsDNA, in combination with a pulsed laser heating system, will be carried out.

Another intriguing perspective of redox labelled DNA grafting on the diamond surface is to investigate the ET process. Contradictory findings have revealed different mechanisms for the ET process between a gold electrode and the redox centre.[43-47] These include: (1) intercalation of the redox molecule with dsDNA, enabling directional ET process;[43, 44] (2) conjugation of the redox molecule through the long and flexible carbon chain;[45, 46] (3) ET process occurs through tunnelling from the electrode surface and redox molecule.[47] Further experiments, exploring the effect of length and density of surface linker molecules and position of the redox centre integrated to the DNA on the electrochemical response, will be investigated.

6.7 Conclusions

In this chapter, redox labelled (Fc derivative) alkanethiols have been successfully immobilised on gold electrodes *via* thiol gold interaction, which was confirmed by CV. The surface coverage of electrochemically active Fc-SAM immobilised on commercial and evaporated gold electrodes was calculated to be 1.2×10^{-10} and 4.1×10^{-10} mol cm^{-2}, respectively. MB labelled DNA modified evaporated gold electrode has been investigated and the highest surface coverage (4.7×10^{-12} mol cm^{-2}) was obtained when the ratio of probe ssDNA to MCH was 1: 10.

Covalent grafting of the surface linker molecule, 10-N-Boc-Amino-dec-1-ene on a diamond surface was achieved *via* a photochemical approach, and verification of the functionalisation process was examined by XPS. MB labelled DNA was then grafted on the diamond surface and a surface coverage of 1.1×10^{-12} mol cm^{-2} was obtained. The successful grafting of MB labelled DNA on diamond provides the possibility for SNP detection based on melting curve analysis.

6.8 References

1. E. Palecek and M. Bartosik, *Chem. Rev.*, 2012, 112, 3427-3481.

2. A. Sassolas, B. D. Leca-Bouvier and L. J. Blum, *Chem. Rev.*, 2008, 108, 109-139.

3. A. Star, E. Tu, J. Niemann, J.-C. P. Gabriel, C. S. Joiner and C. Valcke, *Proc. Natl. Acad. Sci.*, 2006, 103, 921-926.

4. D. Gerion, F. Chen, B. Kannan, A. Fu, W. J. Parak, D. J. Chen, A. Majumdar and A. P. Alivisatos, *Anal. Chem.*, 2003, 75, 4766-4772.

5. L. Meng, J. G. Iacobini, M. B. Joseph, J. V. Macpherson and M. E. Newton, *Farad. Discuss.*, 2014, 172, 421-438.

6. C. Fan, K. W. Plaxco and A. J. Heeger, *Proc. Natl. Acad. Sci.*, 2003, 100, 9134-9137.

7. A. H. Yang, K. Hsieh, A. S. Patterson, B. S. Ferguson, M. Eisenstein, K. W. Plaxco and H. T. Soh, *Angew. Chem.*, 2014, 126, 3227-3231.

8. C. G. Pheeney and J. K. Barton, *J. Am.Chem.Soc.*, 2013, 135, 14944-14947.

9. T. G. Drummond, M. G. Hill and J. K. Barton, *Nat. Biotechnol.*, 2003, 21, 1192-1199.

10. W. Yang, O. Auciello, J. E. Butler, W. Cai, J. A. Carlisle, J. E. Gerbi, D. M. Gruen, T. Knickerbocker, T. L. Lasseter and J. N. Russell, *Nat. Mater.*, 2002, 1, 253-257.

11. S. Szunerits, C. E. Nebel and R. J. Hamers, *MRS Bull.*, 2014, 39, 517-524.

12. S. Q. Lud, M. Steenackers, R. Jordan, P. Bruno, D. M. Gruen, P. Feulner, J. A. Garrido and M. Stutzmann, *J. Am.Chem.Soc.*, 2006, 128, 16884-16891.

13. P. E. Colavita, B. Sun, K.-Y. Tse and R. J. Hamers, *J. Am.Chem.Soc.*, 2007, 129, 13554-13565.

14. R. E. Ruther, M. L. Rigsby, J. B. Gerken, S. R. Hogendoorn, E. C. Landis, S. S. Stahl and R. J. Hamers, *J. Am.Chem.Soc.*, 2011, 133, 5692-5694.

15. H. Uetsuka, D. Shin, N. Tokuda, K. Saeki and C. E. Nebel, *Langmuir*, 2007, 23, 3466-3472.

16. S. Griveau, D. Mercier, C. Vautrin-Ul and A. Chaussé, *Electrochem. Commun.*, 2007, 9, 2768-2773.

17. J. Huheey, *Inorg. Chem.*, 1993, 326-330.

18. R. G. Nuzzo, B. R. Zegarski and L. H. Dubois, *J. Am.Chem.Soc.*, 1987, 109, 733-740.

19. A. B. Sieval, R. Linke, G. Heij, G. Meijer, H. Zuilhof and E. J. R. Sudhölter, *Langmuir*, 2001, 17, 7554-7559.

20. T. Strother, T. Knickerbocker, J. N. Russell, J. E. Butler, L. M. Smith and R. J. Hamers, *Langmuir*, 2002, 18, 968-971.

21. T. Strother, R. J. Hamers and L. M. Smith, *Nucleic acids res.*, 2000, 28, 3535-3541.

22. N. Kaur, J. G. Delcros, B. Martin and O. t. Phanstiel, *J. Med. Chem.*, 2005, 48, 3832-3839.

23. N. S. Sudarshan, N. Narendra, H. P. Hemantha and V. V. Sureshbabu, *J. Org. Chem.*, 2007, 72, 9804-9807.

24. L. J. Bellamy, *The infrared spectra of complex molecules*, Chapman and Hall, London, 3rd edn., 1975.

25. G.-J. Zhang, J. H. Chua, R.-E. Chee, A. Agarwal, S. M. Wong, K. D. Buddharaju and N. Balasubramanian, *Biosens. Bioelectron.*, 2008, 23, 1701-1707.

26. J. A. Streifer, H. Kim, B. M. Nichols and R. J. Hamers, *Nanotechnology*, 2005, 16, 1868.

27. C. E. Nebel, B. Rezek, D. Shin, H. Uetsuka and N. Yang, *J. Phys. D: Appl. Phys.*, 2007, 40, 6443.

28. L. A. Hutton, J. G. Iacobini, E. Bitziou, R. B. Channon, M. E. Newton and J. V. Macpherson, *Anal. Chem.*, 2013, 85, 7230-7240.

29. K. Weber, L. Hockett and S. Creager, *J.Phys. Chem. B*, 1997, 101, 8286-8291.

30. A. L. Eckermann, D. J. Feld, J. A. Shaw and T. J. Meade, *Coord. Chem. Rev.*, 2010, 254, 1769-1802.

31. G. K. Rowe, M. T. Carter, J. N. Richardson and R. W. Murray, *Langmuir*, 1995, 11, 1797-1806.

32. L. S. Curtin, S. R. Peck, L. M. Tender, R. W. Murray, G. K. Rowe and S. E. Creager, *Anal. Chem.*, 1993, 65, 386-392.

33. R. E. Ruther, Q. Cui and R. J. Hamers, *J. Am.Chem.Soc.*, 2013, 135, 5751-5761.

34. H. Finklea, *Electroanalytical Chemistry: a Series of Advances, Vol 19*, CRC press, 1996.

35. A. Bond, E. McLennan, R. Stojanovic and F. Thomas, *Anal. Chem.*, 1987, 59, 2853-2860.

36. C. G. Pheeney and J. K. Barton, *Langmuir*, 2012, 28, 7063-7070.

37. A. Abi and E. E. Ferapontova, *J. Am.Chem.Soc.*, 2012, 134, 14499-14507.

38. T. C. Kuo, R. L. McCreery and G. M. Swain, *Electrochem. Solid-State Lett.*, 1999, 2, 288-290.

39. S. Szunerits and R. Boukherroub, *J. Solid State Electrochem.*, 2008, 12, 1205-1218.

40. J. K. Kariuki and M. T. McDermott, *Langmuir*, 2001, 17, 5947-5951.

41. D. Ballutaud, N. Simon, H. Girard, E. Rzepka and B. Bouchet-Fabre, *Diamond Relat. Mater.*, 2006, 15, 716-719.

42. S. Ghodbane, D. Ballutaud, F. Omnès and C. Agnes, *Diamond Relat. Mater.*, 2010, 19, 630-636.

43. E. M. Boon, D. M. Ceres, T. G. Drummond, M. G. Hill and J. K. Barton, *Nat. Biotechnol.*, 2000, 18, 1096-1100.

44. E. L. Wong and J. J. Gooding, *Anal. Chem.*, 2006, 78, 2138-2144.

45. Y.-T. Long, C.-Z. Li, T. C. Sutherland, M. h. Chahma, J. S. Lee and H.-B. Kraatz, *J. Am.Chem.Soc.*, 2003, 125, 8724-8725.

46. A. A. Gorodetsky, O. Green, E. Yavin and J. K. Barton, *Bioconjugate Chem.*, 2007, 18, 1434-1441.

47. K. Habermüller, M. Mosbach and W. Schuhmann, *Fresenius. J. Anal. Chem.*, 2000, 366, 560-568.

Chapter 7 Conclusions

The work in this thesis investigated the thermoelectrochemical response of BDD as an electrode material. BDD is ideal for thermoelectrochemical investigations due to a combination of its exceptional electrochemical response (extended solvent window, reduced capacitance, *etc.*) and excellent thermal properties (high thermal diffusivity and extreme resistance to thermal ablation (can withstand laser power densities, P_d, of GW cm^{-2} for nanosecond pulses). In this thesis, an infrared (IR) pulsed laser was employed to deliver heat to the rear of the BDD electrode, which drives electrochemical reactions at the front face. Investigations of thermo-electrochemistry on BDD have been carried out from fundamental studies, including the effect of temperature on mass transport, ET kinetics and thermodynamics of both inner sphere and outer sphere molecules, to applications in the effect of temperature on surface fouling molecules and metal/metal oxide deposition processes. Finally, proof-of-concept covalent immobilisation of electrochemically active SAM and DNA on gold and diamond electrodes was investigated. This is with an eventual view to performing temperature assisted electrochemical SNP analysis.

A 200 μm thickness BDD (1 mm diameter electrode area defined by Kapton tape), in combination with a pulsed laser heating set-up, was employed in chapter 3 firstly to determinate the average temperature at electrode/electrolyte interface. The interfacial temperature was obtained to be 90.0 ^oC for a single 10 ms laser pulse at P_d of 3.8 kW cm^{-2}, although higher interfacial temperature can be achieved by tuning the laser pulse width and P_d. Temperature determined by finite element simulation

showed good agreement with experimental data. The effect of temperature on electrochemical response of two outer sphere redox mediators, $Ru(NH_3)_6^{3+/2+}$ and $IrCl_6^{2-/3-}$ was then investigated. The CV signature for both redox mediators showed an enhanced current response, which was due to the enhanced mass transport rate at elevated temperatures.

Intriguingly, temperature has different effects on the position of peak potential for these two redox mediators. In the case of the $Ru(NH_3)_6^{3+/2+}$ couple, the peak potential shifted positively, due to the positive temperature coefficient (β, +0.68 mV K^{-1}). A negative shift of the peak potential was observed for the oxidation of $IrCl_6^{3-}$, which was due to the negative sign of β (-0.48 mV K^{-1}). Scanning backwards, in contrast to that observed for a macrodisc electrode in ambient solution, a cathodic peak was observed for $Ru(NH_3)_6^{3+/2+}$. We attributed this response to the change in entropy for the redox reaction and the time-dependent change in mass transport due to the induced thermal gradient at the electrode/electrolyte interface. Finite element simulation results showed qualitative agreement with the experimental data.

In chapter 4 we systematically investigated the effect of electrode potential, presence of dissolved oxygen and temperature on the electrodeposition of crystalline β-PbO, from nitrate solutions (pH ~ 6.4), on BDD using CV, combined with microscopic and crystallographic techniques. Under laser-heated conditions (interfacial temperature = 72.5 ^{o}C, P_d of 1.2 kW cm^{-2}, laser on for 20 ms and off for 180 ms) after 300 s deposition at - 1 V *vs* Ag/AgCl in 50 µM Pb^{2+} aerated solution, hexagonal "plate" structures were observed, in addition to NPs. The chemical composition and crystallographic information of the "plates" were confirmed as crystalline β-PbO using EDX and TEM, whilst the NPs were postulated to be Pb.

The morphology of the plate ranges from flat hexagon to flat hemisphere to 3D roughed hemisphere, depending on the deposition parameters such as deposition potential, time, presence of dissolved oxygen and temperature. β-PbO was proposed to form directly in solution from freshly deposited Pb NPs acting as nuclei sites for the localised production of OH^-, either from the reduction of oxygen, nitrate or water (all take place at different potentials). The OH^- in turn reacts with Pb^{2+} *via* a precipitation mechanism to form unstable $Pb(OH)_2$ which dehydrates rapidly to β-PbO. The study in this chapter thus enabled conditions for the controllable synthesis of β-PbO. With high resolution electrochemical imaging techniques it would be possible to investigate the electrocatalytic activity of these interesting structures.

In chapter 5, a BDD microelectrode was employed to study the effect of temperature on the electrochemical response of both an outer sphere ($Ru(NH_3)_6^{3+}$) and an inner sphere (Fe^{2+}) redox mediator, in combination with finite element simulation. Increased limiting currents were observed in the CVs for both the reduction of $Ru(NH_3)_6^{3+}$ and the oxidation of Fe^{2+}. Half wave potential, $E_{1/2}$, for the reduction of $Ru(NH_3)_6^{3+}$ shifted positively due to the positive sign of β, similar to that obtained in chapter 3 for BDD macroelectrode. In the case of Fe^{2+}, $E_{1/2}$ shifted negatively due to the negative sign of β (-1.72 mV K^{-1}). Intriguingly, a 'shoulder current' was observed in the CV and TPVs for the oxidation of Fe^{2+}, which we attributed to the heterogeneity of the polycrystalline nature of the BDD surface, where highly doped grains exhibits superior ET process compared to less heavily doped grains. The effect of crystallographic orientation was excluded using EBSD. The pulsed laser heating system was then moved to investigate a well-known surface fouling redox mediator, dopamine. Minimised fouling (i_{lim} decreased only by 4 % at P_d of 3.8 kW cm^{-2} over 10 cycles) was achieved by employing TPV. BDD is thus

promising for thermoelectrochemical measurements and as a means to reduce surface fouling effects.

In chapters 4 and 5, all diamond macro- and micro- electrodes (intrinsic diamond overgrown on BDD) were employed. All diamond structures were assessed electrochemically to reveal the good quality (no pin holes or defects in the intrinsic BDD region) of the overgrowth structure. The robustness of the all diamond structures provides a promising platform for electroanalytical applications in aggressive media and in thermoelectrochemical studies.

Surface functionalisation of both gold and BDD electrodes was investigated in chapter 6. Surface coverages of electrochemically active Fc-SAM (4.1×10^{-10} mol/cm^2) and MB labelled DNA (4.7×10^{-12} mol/cm^2) were obtained on evaporated gold electrodes using CV measurements. Covalent grafting of a surface linker molecule, 10-N-Boc-Amino-dec-1-ene on a diamond surface was achieved using photochemical approach. MB labelled DNA was then grafted on the diamond surface and a surface coverage of 1.1×10^{-12} mol/cm^2 was obtained. The successful grafting of MB labelled DNA on diamond surface provides the possibility for SNP detection under laser heated conditions based on melting curve analysis.